CHARGE TRANSPORT IN SELENIUM BASED AMORPHOUS XEROGRAPHIC PHOTORECEPTORS

by

SAFA OSMAN KASAP, B.Sc.(Eng.), M.Sc., D.I.C.

A thesis submitted for the degree of Doctor of
Philosophy of the University of London

November, 1982

Department of Electrical Engineering
Imperial College of Science and Technology
London S.W.7.

ABSTRACT

Time-of-Flight experiments were carried out on the following Se based amorphous xerographic photoreceptors: (i) pure Se; (ii) Se + y ppm Cℓ ($y \lesssim 90$ at.); (iii) $Se_{1-x}As_x$ + y ppm Cℓ ($x \lesssim 0.005$, $y \lesssim 60$ at.); (iv) $Se_{1-x}Te_x$ + y ppm Cℓ ($x \lesssim 0.08$, $y \lesssim 90$ at.). The drift mobility μ and the mean drift lifetime τ of the charge carriers were measured, where possible, as a function of applied electric field, temperature and composition.

Mobility-temperature data at various applied fields on these systems have been discussed within the framework of shallow trap controlled transport mechanisms. Drift data indicate that in undoped amorphous Se (a-Se), hole transport is controlled by a discrete set of traps at ~ 0.29 eV above E_V whereas electron transport is limited by the localized tail states below E_C and/or a discrete set of traps at ~0.35 eV below E_C.

Doping of a-Se with Cℓ introduces an additional set of shallow hole traps; at ~0.45 eV above E_V. Alloying a-Se with As affects the electron transport by increasing the extent of the localized tail states below E_C. As addition seems to neutralize the Cℓ induced hole traps at ~0.45 eV above E_V.

Addition of Te to a-Se introduces shallow hole traps at ~0.43 eV above E_V and electron traps at ~0.5 eV below E_C. These are likely to be Te_1^- and Te_3^+ defect centres respectively.

The microscopic mobility in these systems is probably determined by nearly diffusive motion in extended states, $\mu_0 \approx 0.1 - 0.3$ $cm^2 V^{-1} s^{-1}$, both for holes and electrons.

Hole lifetime τ_h in a-Se depends on the origin of Se as well as on preparation conditions. Its behaviour with temperature and Te content in a-$Se_{1-x}Te_x$ indicates that τ_h is inversely proportional to the hole drift mobility μ_h.

The hole lifetime in the system $Se_{1-x}As_x$ + y ppm Cℓ can be effectively controlled by simultaneous doping with As and Cℓ. Alloying with As reduces the lifetime whereas Cℓ addition enhances it.

Electron drift parameters, particularly the lifetime τ_e, have been found to be sensitive to the origin of Se and impurities. There was no detectable electron transport signal when a-Se and a-Se/Te alloys were doped with Cℓ.

ACKNOWLEDGEMENTS

I am grateful to Dr. C. Juhasz for his help, guidance and encouragement throughout the course of the project.

I wish to thank members of the Materials Section for helpful suggestions and discussions, and Professor J.C. Anderson for his interest in this work.

Special thanks are due to Dr. R. Rollason of Gestetner (Byfleet) Ltd. for preparing some of the samples and also for the many useful discussions.

I am grateful to the Science Research Council and Mr. Lindsay Malcolm of Gestetner Ltd. for providing financial support.

Finally, I wish to thank Miss Cynthia Collins for her adept typing of the thesis.

CONTENTS

LIST OF TABLES

Page No.

CHAPTER 1

INTRODUCTION

§1.1 AMORPHOUS SEMICONDUCTORS

During the last two decades the research activity in amorphous semiconductors (a-semiconductors) has increased enormously due not only to their increasing technological or commercial importance but also to the scientific interest in the subject. Applications of amorphous semiconductors either realized or anticipated include a very wide spectrum such as[†] electrophotographic photoreceptors, switching and memory devices, continuous dynode electron multipliers (channeltron), optical mass memories, phase contrast holograms, high energy particle detectors, infrared lenses, ultrasonic delay lines and microfiche transparencies. The discovery of the Ovshinsky switching effect in amorphous chalcogenide glasses (Ovshinsky 1968) and the development of xerography (see §1.2) attracted much research interest into the electrical and optical properties of amorphous semiconductors although the pioneering research work had been started at the Ioffe Institute in Leningrad by B.T. Kolomiets and co-workers in the fifties and early sixties (see, for example, Kolomiets 1964). Yet the theories and experiments on non-crystalline materials still remain discussed mainly in the appropriate journals and conferences.

An amorphous solid has been defined in many review articles on the subject as that in which there is no long range order. The experimental and theoretical evidence on amorphous solids indicate clearly the presence of short range order similar to that occurring in the corresponding crystalline forms of the solid. Short range order exists if for any atom of the solid the bond length, bond angle and coordination number are well defined within certain limits. Short range order is, therefore, determined by the

---

[†] See, for example, Ovshinsky and Fritzsche 1973, Fritzsche 1973a, Goodman 1973, Mort 1973a, Ovshinsky 1977, Allison and Thomson 1976, Allan 1977

chemical bonding requirements of the constituent atom and thus depends on its chemical nature. For example in a-Si almost every Si atom is surrounded by four neighbouring atoms 2.35Å away, exactly the same atomic separation as in the crystal. Even the second neighbours are essentially at the same distance as in the crystal, but there is a spread in separation which reflects bond angle deviations of about ±10° (e.g. de Neufville 1975). This spread becomes more and more significant as the distance from the central atom increases and at distances of the order of the tenth neighbour or so the atoms are located essentially at random. Therefore, pure a-Si can be said to possess short range order up to about 5Å (see Figs. 2.6, 2.7 in §2.2 for short range order in a-Se). The perseverance of short range order in amorphous solids was first recognized by Ioffe and Regel nearly twenty years ago (Ioffe and Regel 1960).

1.1.1 Structure and Classification of a-Semiconductors

The presence of short range order alone in an amorphous solid means that there are an infinite number of configurations for the structure, in contrast to one unique configuration[†] for the corresponding crystal if it exists. Therefore, most structural studies on amorphous solids have considered the range of short range order or the extent of order. In the discussion above on a-Si this was about 4-5Å. Information on the structure is obtained from a variety of experiments like, X-ray, electron and nuetron diffraction, EXAFS (Extended X-ray Absorption Fine Structure), and Infrared (IR) and Raman Spectroscopy. Some of these techniques have been used on a-Se and their results and conclusions are discussed in §2.2. An important parameter which carries much information on the structure is the radial distribution function (RDF), J(r), which gives a one-dimensional description of the atomic distribution in the material. J(r) is defined as follows. Given an atom as

---

[†] for a solid which has N > 1 number of crystalline phases insert N for 'one unique'

an arbitrary origin,then $J(r)dr$ is the number of atoms in a shell of thickness dr at a distance r. If $\rho(r)$ is the atomic density at a distance r from the origin then $J(r)$, by definition, is

$$J(r) = 4\pi r^2 \rho(r) \qquad (1.1)$$

The RDF or $J(r)$ is normally obtained from diffraction studies by measuring the dependence of the diffracted intensity $I(\theta,\lambda)$ on the Bragg angle θ and/or on the wavelength λ of the beam (X-ray, etc.). If $S \equiv \frac{4\pi}{\lambda} \sin\theta$ then the RDF is given by (e.g.Grigorovici 1974, Omar 1975, Ch. 2)

$$J(r) \equiv 4\pi r^2 \rho = 4\pi r^2 \rho_0 + \frac{2r}{\pi} \int_0^\infty S\left[\frac{I(S)}{f^2(S)} - 1 \right] \sin Sr \, dS \qquad (1.2)$$

where ρ_0 is the macroscopic average atomic density and $f(S)$ is the atomic scattering factor. It can be seen that $J(r)$ is obtained by Fourier transforming the scattered intensity and thus its accurate evaluation requires the whole spectrum of $I(S)$. There are many difficulties involved in generating a reliable RDF from $I(\theta,\lambda)$. Besides the corrections arising from the experimental procedure used, e.g. background intensity corrections, there are also difficult corrections associated with data analysis, e.g. termination corrections to the Fourier integral.

The RDFs obtained on a-semiconductors (see, for example, Grigorovici, 1973) show clearly the perseverance of short range order (see Figs. 2.6, 2.7 for a-Se) and the absence of any long range periodicity. In addition to these basic facts, the experimental evidence suggests small radial and strong bond angle distortions in local arrangements. Further it has been found that the higher order (second or more) neighbours appear mostly in a configuration which differs from that found in any existing crystal. This will become apparent in §2.2.

The physical models used in describing the structure of amorphous semiconductors must predict not only the RDF but also account for the results of other experiments, for example IR or Raman spectroscopy. There are essentially two types of structural models used (see reviews by Grigorovici 1973, Weaire 1976, Fritzsche 1981). In the microcrystalline model the a-semiconductor consists of randomly oriented crystallites so that the broadening of diffraction rings is essentially a size effect. The necessary crystal sizes are of the order of 10-15Å. In the homogeneous continuous network model the a-semiconductor is considered to consist of a homogeneous network of atoms linked together by the same types of chemical bonds as in the corresponding crystal, but without long range order. This model was first suggested by Zachariasen in 1932 for a binary glass A_2B_3. A continuous random network model for a binary system is constructed so that the 8-N valence coordination rule proposed by Mott 1969 is satisfied. The application of these models to a-Se is discussed in §2.2. Note that in the microcrystalline model it is not essential for the crystallite structure to represent the corresponding crystal. It may be deformed or a polymorph.

Inorganic amorphous semiconductors may be divided into two distinct categories; ionic and covalent. Examples of ionic amorphous semiconductors are MnO_2, V_2O_5 and other transition metal oxides. Covalent amorphous semiconductors may be subdivided into four groups (Friztsche 1973b)(i) Tetrahedral amorphous semiconductors, e.g. Si, Ge, InSb, (ii) Tetrahedral glasses of the type $A^{II}B^{IV}C_2^{V}$, e.g. $CdGe_xAs_2$, $ZnSi_xP_2$, (iii) Lone pair (chalcogenide) semiconductors which can be elemental, e.g. Se, Te, or in compound form e.g. As_2Se_3 As_2S_3, (iv) Others, e.g. B, As. Mott and Davis 1979 use a scheme of classification that is based on grouping materials having the same short range structural coordination.

1.1.2 Charge Transport in Amorphous Semiconductors[†]

The first semiquantitative concepts in generalizing the theory of crystalline semiconductors to amorphous materials were put forward by Mott (1967, 1968), and Cohen, Fritzsche and Ovshinsky (1969), who argued that the sharp band edges (and singularities) in the electronic band structure of crystalline semiconductors (see, for example, van Hove 1953 or Blakemore 1974, ch. 3) are purely the consequence of long range order[†]. Mott, used the earlier work of Anderson (1958) on localization as a starting notion to suggest that in disordered structures the one electron eigenfunctions ψ_E (corresponding to the one electron energy, E), if they exist, are either extended through the whole structure or localized in a region whose dimensions are not greatly in excess of the interatomic spacing. It was argued that the density of states N(E), still remaining a valid concept as long as the one electron Schrodinger equation has solutions, is continuous but the extended states are divided from the localized states by some critical energy E_C.

Fig. 1.1a and b show the density of states N(E) vs energy E spectrum for an ideal crystalline semiconductor and for an ideal amorphous semiconductor which has a continuous random network structure (see section 1.1.1) without any defects, e.g. dangling bonds. Consider the density of states function for the ideal a-semiconductor. The sharp-band edges and any singularities have disappeared and instead there are band tails in which the states are localized. At the bottom of the conduction band (CB) and at the top of the valence band (VB) these are separated from the extended states by sharp energies E_C and E_V respectively. $E_C - E_V$ is an 'energy band gap' between the extended states. Because of the perseverance of the short range order the

---

[†] For general reviews on electronic properties of amorphous semiconductors see, for example, Cohen 1970, Owen 1970, Fritzsche 1971, Adler 1971, Fritzsche 1973b, Mott 1973, Owen and Spear 1976, Ovshinsky and Adler 1978, Mott 1977a,b, Mott and Davis 1979 (Ch.6), Adler 1980, 1981, Yonezawa and Cohen 1981. For reviews on charge transport see, for example, Davis 1971, Mott 1972, Brenig 1974, Spear 1974, Emin 1976, Mott 1981 and references therein.

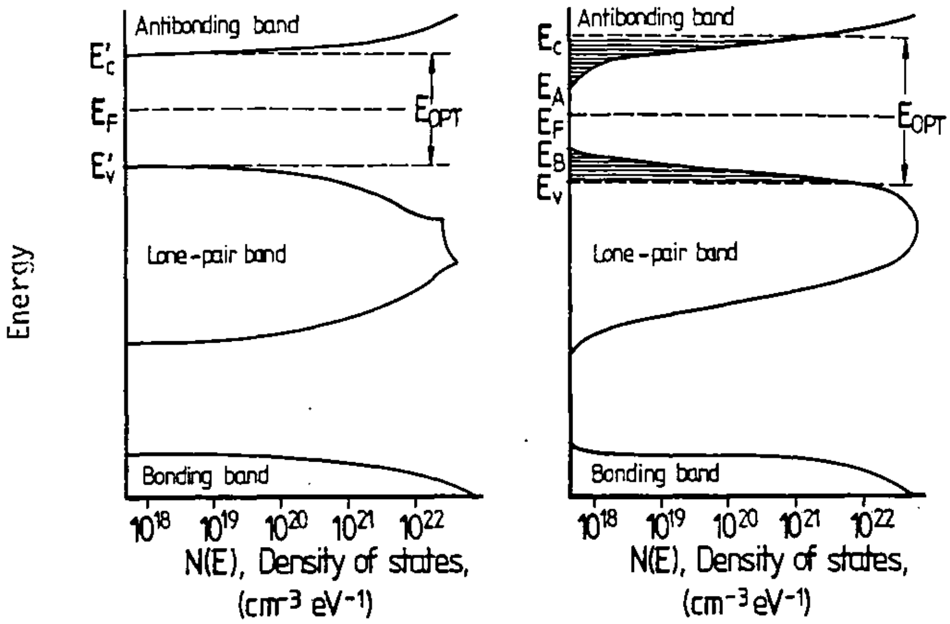

(a) (b)

Fig. 1.1: Sketch of the electronic density of states N(E) of (a) perfect crystalline chalcogen solid, and (b) and ideal amorphous chalcogen solid. E_F is the Fermi energy, E_{OPT} is the approximate value of the optical band gap. E_C and E_V in (b) are the conduction and valence band mobility edges. (From Ovshinsky and Adler 1978).

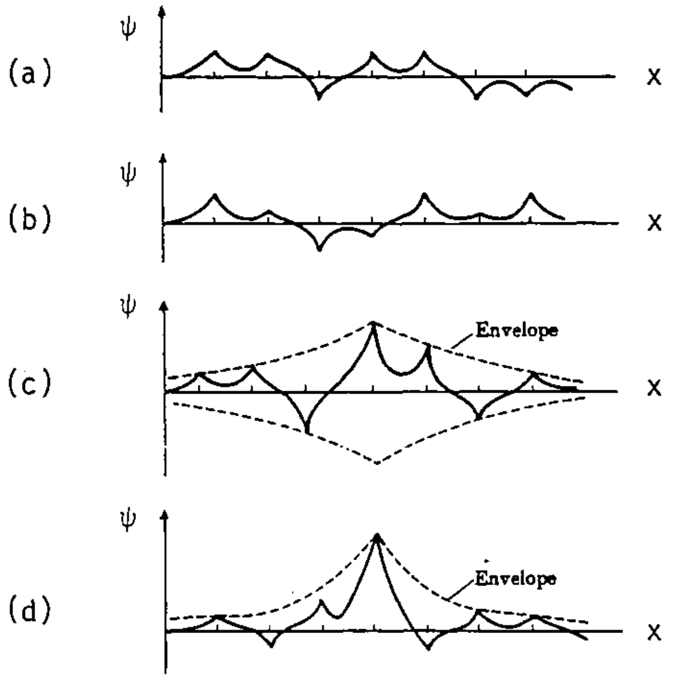

Fig. 1.2: Forms of the electron wavefunction $\psi(x)$ in the Anderson lattice for (a) mean free path $\sim a$; (b) states are just non-localized, $E \gtrsim E_C$; (c) states are just localized, $E \lesssim E_C$; (d) strong localization. (From Mott and Davis 1979 Ch. 2).

gross features of the crystalline spectrum are still preserved. The tails of localized states shown have been extended to E_A below E_C and E_B above E_V. Their extent depends on the degree of disorder but may be typically 0.1-0.3 eV (Mott and Davis 1979, p.216). The actual form of N(E) in the tails is not expected to be proportional to $E^{\frac{1}{2}}$ as in the crystal.

A more rigorous definition of a localized state has been proposed by Mott 1968. If the configurationally averaged d.c. conductivity $\langle\sigma_E\rangle$ at zero absolute degrees vanishes for eigenstates of energy E then these states are localized. Otherwise, they are extended. σ_E is given by the Kubo-Greenwood formula (Mott and Davis 1979, Ch. 2)

$$\sigma_E = \frac{2\pi e^2 \hbar^2 \Omega}{m^2} \; |D_E|^2_{AV} \; [N(E)]^2 \qquad (1.3)$$

where Ω is the volume, $D_E \equiv \langle E'|\frac{\partial}{\partial x}|E\rangle$ and the suffix AV denotes averaging D_E over all states E and all states E' such that E = E'.

The form of the extended and localized wavefunctions for an electron in an Anderson lattice[†] are shown in Fig.1.2 following the descriptions of Mott and Davis 1979 (Ch. 2). The forms were first conjectured by Mott 1968. For an electron above E_C although the wavefunction is extended its phase coherence length ξ may be short, i.e. $\xi \lesssim a$, where a is the average interatomic separation. The wavefunctions near E_C can be written as

$$\psi_{ext} = \sum_n A_n \, \phi(\underset{\sim}{r} - \underset{\sim}{R}_n) \qquad (1.4)$$

where $\phi(r)$ is an atomic wavefunction and A_n have random phases and amplitudes. This description is often called the random phase model (RPM). For a localized electron below E_C, its wavefunction is expected to be

---

[†] Anderson lattice is generally described as a three-dimensional periodic array of potential wells of random depth spread over an energy range, V_o.

$$\psi_{loc} = \exp(-\alpha r) \sum_n A_n \, \phi(\underset{\sim}{r} - \underset{\sim}{R}_n) \qquad (1.5)$$

where α is a localization parameter which has been proposed to behave as $[(E_C-E)/E_C]^{2/3}$. Thus the spatial extent of the localized states in the tail varies with energy.

Conduction of electrons excited to the CB of an ideal a-semiconductor may be divided into three transport processes.

(1) Conduction in states $E \gg E_C$:

Since the excited electron is energetic it will have a a mean free path $\bar{\ell} \gg a$ and the conventional scattering theory through equation

$$\mu = \frac{e\langle\tau\rangle}{m^*} \qquad (1.6)$$

where $\langle\tau\rangle$ is an appropriately averaged relaxation time (e.g. Smith 1978 Ch.5, Kireev 1978 Ch. 4) may be used to determine the mobility due to electrons having $E \gg E_C$.

(2) Conduction in extended states near E_C:

This is often called the Ioffe and Regel diffusion regime. According to Cohen 1970 the transport is essentially diffusive in nature similar to Brownian motion. The electron is envisaged as 'jumping' or tunnelling from site to site with an electronic frequency ν_{el}, conserving energy at each jump, in contrast to the hopping regime where the electron exchanges energy with a phonon in each hop. The mobility is given by the Einstein relationship[†]

$$\mu = \frac{eD}{kT} \qquad (1.7)$$

where D is the diffusion constant which can be written as (see. e.g. Wert and Thomson 1970, Ch. 4)

[†] $\mu = \frac{eD}{kT}$ is a general relationship which does not depend on any crystal structure; see, for example, Smith 1978 (Ch. 7) or Allison 1971 (Ch. 6).

$$D = \frac{1}{6} \nu a^2 \tag{1.8}$$

where ν is the probability per unit time that an electron will 'jump' to a neighbouring site, i.e. jump frequency and a is the average interatomic distance. Thus near E_C the extended state mobility is

$$\mu_{ext} = \frac{1}{6} \frac{e\nu_{el} a^2}{kT} \tag{1.9}$$

where ν_{el} is an 'electronic frequency'.

Writing $\nu_{el} \sim \frac{\hbar^2}{ma^2}$, μ_{ext} can be estimated at room temperature as

$$\mu_{ext} \sim \frac{1}{6} \left(\frac{e}{kT} \right) \frac{\hbar}{m} \sim 6 \ \mathrm{cm}^2 \ \mathrm{V}^{-1} \ \mathrm{s}^{-1} \tag{1.10}$$

Alternatively the mobility μ_{ext} can be calculated from RPM (e.g. Hindley 1970) or from the minimum conductivity σ_{min} (Mott and Davis 1979, p. 219).

A lower limit for μ_{ext} in the diffusion regime, according to Cohen may be as small as 10^{-2} cm^2 V^{-1} s^{-1}.

(3) Conduction in a tail of localized states:

Below E_C the electron is localized, i.e. 'trapped' and it can only move by phonon assisted hopping at temperatures above zero. Since hopping means tunnelling to another state via interaction with a phonon the transition probability per unit time ν and thus D in this regime will be temperature dependent.

If two states are separated by a distance R in space and by $W = \Delta E_{hop}$ in energy the probability per unit time, ν, that an electron will hop from one to the other by interacting with a phonon is (e.g. Mott and Davis, 1979, Ch.2, or see reviews by Davis 1971, Spear 1974)

$$\nu = \nu_{ph} \exp \left\{ -2\alpha R - \frac{W}{kT} \right\} \tag{1.11}$$

where ν_{ph} is a factor called the 'phonon frequency' and α is the 'decay rate' of the localized wavefunction. R and W will depend on N(E).

For strong localization, i.e. $\alpha a_E >> 1$ where a_E is the separation of states of energy E (defined quantitively by $a_E^{-3} \equiv N(E)\ V_0$ where V_0 is a parameter characterizing disorder) then nearest neighbour hopping will dominate since the probability per unit time ν will drop sharply for $R > a_E$. This type of nearest neighbour hopping is called Millér and Abrahams (1960) hopping. The mobility due to hopping at states around an energy E is then

$$\mu(E) = \nu_{ph} \frac{eR_0^2(E)}{kT} \exp[-2\alpha R_0 - \frac{W}{kT}] \qquad (1.12)$$

where $R_0(E)$ is the average nearest neighbour separation, i.e. $\approx a_E$, and the hopping energy W is $\sim[\frac{4}{3}\pi R_0^3\ N(E)]^{-1}$.

Assuming the CB tail shape to be of algebraic form,

$$N(E) = N_c \left[\frac{E-E_A}{\Delta E}\right]^n \qquad (1.13)$$

where N_c is the density of states at E_C, $\Delta E \equiv E_C - E_A$ and n an index, leads to the largest population of electrons occuring at some energy E_m in the tail where E_m (for details see Grant and Davis 1974 or Mott and Davis 1979, Ch. 6) lies above E_A by nkT;

$$E_m = E_A + nkT \qquad (1.14)$$

Then the main contribution to the mobility will be expected to come from electrons hopping around E_m where the density of states is

$$N_m = N(E_m) = [\frac{nkT}{\Delta E}]^n N_c \qquad (1.15)$$

If localization is not strong, i.e. $\alpha a_E \lesssim 1$ the electron may jump further than R_0 to find a state which is closer in energy, i.e. it will try to decrease W. This type of hopping is called variable range hopping and is more likely to be the transport process in the tail (see Mott and Davis 1979, Ch. 6, Grant and Davis 1974). It was first suggested by Mott 1969, for hopping near the Fermi-level in a Fermi glass. The hop energy W can be related to the hop distance by

$$W = [\frac{4}{3}\pi R^3 N(E)]^{-1} \qquad (1.16)$$

Consider hopping around E_m, i.e. $N(E) = N(E_m)$ in eqn. (1.16), the hopping probability ν, eqn. (1.11), may be maximized either with respect to the hopping range R or to W (Hill 1971a). The hop energy W is then

$$W \doteq \frac{3}{4}(\frac{8}{9})^{3/4}\left[\frac{(kT)^{3-n}(\Delta E)^n \alpha^3}{\pi n^n N(E_c)}\right]^{1/4} \qquad (1.17)$$

The mobility due to these electrons at E_m is

$$\mu_{hop} = C\,\nu_{ph}\,T^{-\frac{(n+3)}{2}} \exp[-BT^{-(\frac{n+1}{4})}] \qquad (1.18)$$

where B is a constant of the form

$$B = 3\,(\frac{8}{9})^{3/4}\left[\frac{(\Delta E)^n \alpha^3}{\pi N(E_c) n^n k^{n+1}}\right]^{1/4} \qquad (1.19)$$

ν_{ph} is a 'phonon frequency' and C is a constant independent of the temperature. Note that ν_{ph} may contain an additional temperature dependence.

Because of the uncertainty in the magnitude and temperature dependence of the pre-exponential factor in eqn. (1.18), it is difficult to estimate the variable range hopping mobility in the band tail. The use of nearest neighbour hopping formula, eqn. (1.12), on the other hand with some typical values, e.g. R_o = 3-4Å, $\nu_{ph} \lesssim 10^{13}\ s^{-1}$ (c.f. $\nu_{el} \sim 10^{15}\ s^{-1}$) gives a hopping mobility $\mu_{hop} \lesssim 10^{-1}\ cm^2\ V^{-1}\ s^{-1}$. μ_{ext} however was $\sim 6\ cm^2\ v^{-1}\ s^{-1}$. It was therefore suggested (e.g. Cohen et al 1969 and Cohen 1970) that at E_C there is a sharp mobility drop of about $\sim 10^2$. Since there will be a similar sharp drop in the hole mobility across E_V in the valence band tail, E_C-E_V defines a 'mobility gap'. The energies E_C and E_V are termed mobility shoulders or mobility edges.

Direct experimental evidence for the existence of a mobility edge comes from the electron drift mobility vs temperature data of LeComber and Spear 1970 on a-Si. A change in the activation energy was observed from $E_t = 0.19$ eV above $T \cong 250K$ to $W = 0.09$ eV below $T \cong 250K$. This behaviour, when compared with $\log\sigma$ vs T^{-1} data which also showed a 'kink' at $T \cong 250K$, was interpreted as a transition from trap controlled extended state transport regime above E_c to a hopping regime in the band tail below E_c.

It is well known that in crystalline semiconductors, impurities, lattice defects and many other types of flaws (see, e.g. Blakemore 1974, Ch. 4.1) introduce discrete or a distribution of traps in the band gap. An electron captured by such a trap is localized. The density of states diagram in Fig. 1.1b for an ideal non-crystalline semiconductor was based on an ideally bonded continuous random network model described in section 1.1.1. Structural defects, such as dangling bonds or variations in the normal structural bonding (NSB) requirements, e.g. over-coordination, in amorphous semiconductors also lead to states in the (mobility) gap (see recent reviews by Fritzsche1977 or Ovshinsky and Adler 1978). In Ch. 2, for example, it will be shown that under- and over-coordinated Se atoms which have NSB requirements corresponding to a valency of 2 give rise to two types of states in the gap. Besides the tails in the CB and VB there may therefore be discrete or some distribution of localized states in the mobility gap.

One density of states model for a-semiconductors is the Mott and Davis (Davis and Mott 1970) model which is shown in Fig. 1.3a. Besides the tails at the CB and VB due to disorder there is a distribution of localized states (of ∿0.1 eV wide) at the Fermi level arising from defects, e.g. dangling bonds. The latter states were proposed ad hoc to account for the 'pinning' of the Fermi level[†] observed and some photoluminescence data. Charge transport in this model in addition to those described above can also occur amongst

---

[†] By 'pinning' it is implied that the Fermi level cannot be shifted easily by the addition of impurities.

the states around the Fermi level. The mobility at low temperatures is then determined by variable range hopping near E_F.

There are also other density of states models proposed ad hoc by various authors. For example, in the Mott and Spear model (e.g. Spear 1974b) for a-Si there are two overlapping peaks in the density of states function corresponding to donor, E_Y, and acceptor E_X, states arising from defects. These peaks are located below and above the Fermi level; Fig. 1.3b (Mott 1972).

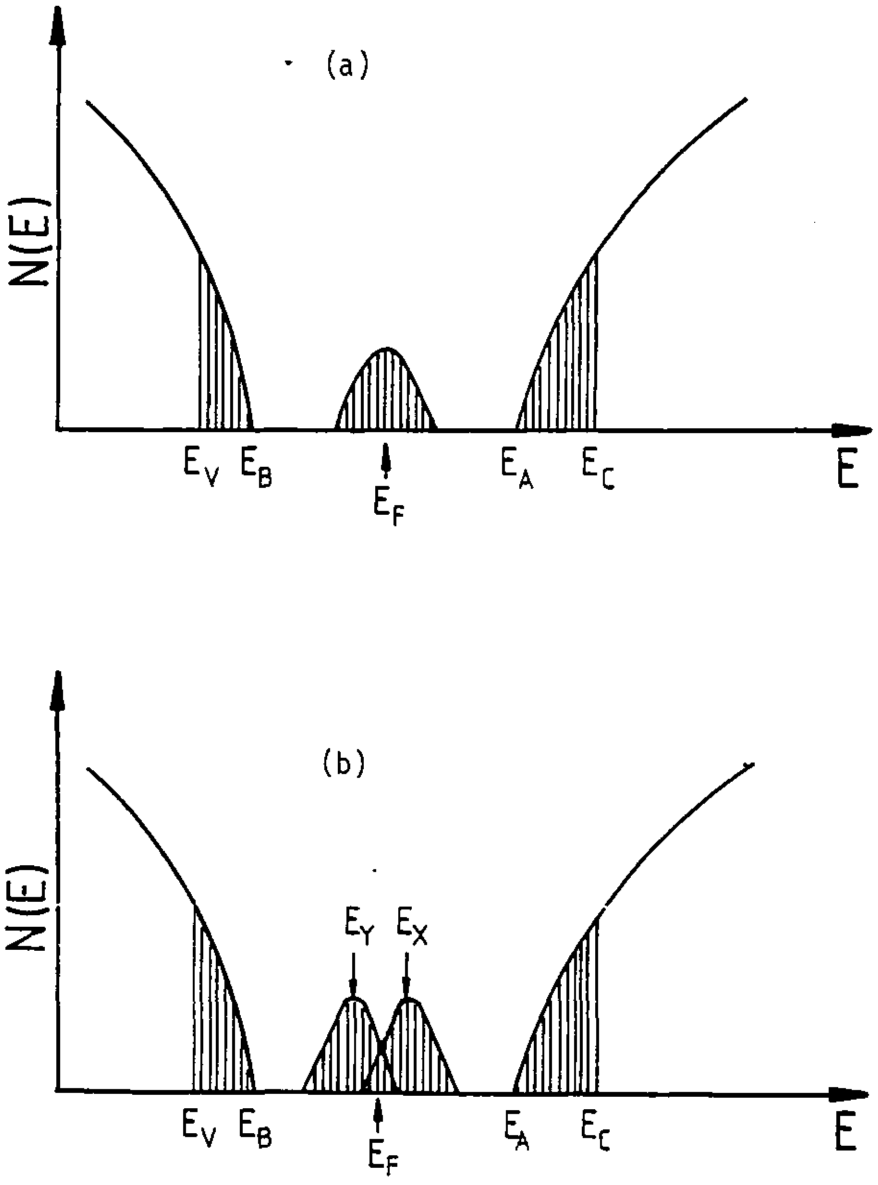

Fig. 1.3: Density of states N(E) vs energy E for an amorphous semiconductor in (a) Davis and Mott model, (b) Mott model. Localized states are shaded vertically.

§1.2 AMORPHOUS SELENIUM, XEROGRAPHY AND THIS PROJECT

Selenium whether in the crystalline or amorphous phase has a special attraction in solid state research due not only to its commercial importance but also to its very interesting physical properties (Stuke 1974). For example, trigonal selenium is the simplest Reststrahlen displaying elemental crystal (Zallen and Lucovsky 1974). It has photoconductive and piezoelectric properties. Its d.c. conductivity and thermoelectric power is relatively insensitive to impurities but depends on temperature and lattice deformations (pressure).

The commercial importance of selenium lies in its wide use as a xerographic photoreceptor (e.g. Schaffert 1975, Ch. 2). It is also used in photocells (e.g. Stuke 1974) and rectifier diodes (e.g. Champness et al 1969).

Many photocopying machines employ a-Se based photoreceptors. So, it is not surprising to find a large number of papers published on the properties of a-Se systems. It is instructive to summarize briefly the xerographic process to understand some of the research interest in a-Se.

Xerography[†] is the most highly developed form of electrophotography in present commercial use. Fig.1.4 (p.27) illustrates the sequential steps involved in generating a copy (for details see,for example, reviews by Schaffert 1975, Chs. 1 and 2, Tabak et al 1973, Lukovsky and Tabak 1974, Jain 1975, Weigl 1977). These process steps are essentially those that take place in commercial machines employing reusable photoreceptors.

Step 1: Sensitization (Charging) of the Photoreceptor

The photoconductor typically consists of a vacuum-deposited layer of Se, approximately 40-60 μm thick on an $A\ell$ substrate. Sensitization is accomplished by depositing electric charges onto the surface of the photoconductor by means of corona discharging. Fields required for sensitization are typically 10^5 V cm^{-1}.

[†] The xerographic technique was invented by Carlson 1938

Step 2: Exposure and Latent Image Formation

The sensitized photoreceptor is exposed to a light and dark image pattern. In light struck areas, the surface potential of the photoconductor is reduced due to a photoconductive discharge. Since the current can only flow normal to the film surface, this step produces an electrostatic potential distribution which replicates the light-dark pattern of the image.

Step 3: Development of the Image

The most common technique is the cascade method. The developer used in this technique consists of a mixture of black (or coloured) toner particles typically 10 μm in diameter and carrier beads, typically 100 μm in diameter. Toner particles are charged triboelectrically in this process and are preferentially attracted by either the surface field at light-dark boundaries, or in systems employing a development electrode, by the absolute potential in the dark areas. They adhere to the photoconductor, forming a visible image corresponding to the latent electrostatic image.

Step 4: Image Transfer

The image developed in Step 3 can be transferred onto paper by using electrostatic transfer, wherein the paper is appropriately charged and the toner particles are attracted to the paper. An alternative process is an adhesive transfer.

Step 5: Print Fixing

The powder image on the paper is made permanent by fusing or melting the plastic-based toner particles into the surface of the paper. This can be accomplished by heat, heat and pressure, or by solvent vapours.

Step 6: Cleaning

Following the transfer process, there is some toner still left on the photoreceptor. This is removed by either mechanical, cloth web or brush, or mechanical and electrostatic means.

Step 7: Image Erasure

This step removes any potential differences on the photoreceptor by flooding it with sufficiently intense light to drive the surface potential to some uniformly low value (typically ~100V corresponding to fields $\sim 10^4$ V cm^{-1}). At this stage the photoreceptor is ready for another print cycle.

A photoreceptor has to satisfy several important conditions before it can qualify as a commercially viable xerographic photoreceptor.

Ideally the surface potential does not decay appreciably following the sensitization step. This condition requires a large dark resistivity $\rho \gtrsim 10^{12}$ Ω cm (due to a lack of intrinsic mobile carriers), a negligible charge injection at the free surface and at the substrate interface (Se/Aℓ interface), and no lateral surface conduction. These conditions are also required in the latent image formation step so that the electrostatic image is not neutralized.

In Step 2, the light exposed areas have their charges neutralized. Specifically, for positive surface potential, photogenerated electrons neutralize the positive surface charge while free holes drift across the photoreceptor layer to neutralize the induced negative charge on the Aℓ substrate. Ideally Step (2) requires each absorbed photon to result in the transport of one electronic charge unit through the photoreceptor. Therefore this requirement depends not only on the photogeneration efficiency but also on the charge transport parameters like the effective drift mobility μ and the effective deep trap capture time, τ.

Other photoreceptor requirements are: there is no change in the photoreceptor characteristics with cycling, e.g. no fatiguing, negligible residual potential, and the properties of the photoreceptor are the same everywhere on the photoreceptor surface, e.g. no partially crystallized surface regions.

In studying charge transport limitations in photoreceptors, the xerographically important parameters are the range $r \equiv \mu\tau$, the Schubweg

$s \equiv \mu\tau F$ and the transit time $t_T \equiv \frac{L^2}{\mu V}$ of a photogenerated carrier (see §3.2). The Schubweg is the distance a carrier travels before being trapped whereas the range is the Schubweg per unit field. If some of the photogenerated carriers while traversing the sample suffer deep trapping then there will be a residual potential on the surface due to these deep trapped carriers. Over many consecutive cycles, the accumulative build-up of the trapped charge can lead to undesirably high residual voltages causing serious deterioration in the copy quality. If Q_t is the total trapped charge, assumed to be uniform, and C is the geometrical capacitance of the photoreceptor then the residual surface potential V_{res} will be

$$V_{res} = \frac{Q_t}{2C} \tag{1.20}$$

Q_t will depend on the ratio $\frac{t_T}{\tau}$ or $\frac{L}{s}$. However, t_T in the xerographic process is not a unique quantity because it depends on the electric field which decays as more and more surface charges are neutralized[†]. In addition not all the carriers will be generated near the surface so L will also be different for different carriers. Thus V_{res} cannot be expressed in a simple manner in terms of V, L, μ and τ. The simplest relation obtained is (Warter 1969).

$$V_{res} = \frac{L^2}{2\mu\tau} \tag{1.21}$$

which assumes that the photogenerated charge is about CV, near the surface and does not disturb the internal field $\frac{V}{L}$.

For a-Se photoreceptors such range limitations on xerographic performance play an important role since τ is a sensitive function of preparation conditions, impurities etc. (see §2.5).

[†] Transit time t_T for a carrier which has to traverse a distance L under the influence of a non-uniform electric field F(x) may be defined by the relation (Scharfe and Tabak 1969) $t_T = \int \frac{dx}{\mu F(x)}$.

Another charge transport effect is called the transit time limitation which becomes important when the longest transit times occurring in the xerographic process become comparable with the time it takes to develop the latent electrostatic image. This limitation is for example of interest in As_2Se_3 photoreceptors.

The purpose of this project was to study the charge transport mechanism in some most widely employed selenium based amorphous xerographic photoreceptors by means of the Time-of-Flight (TOF) technique. The following commercially important amorphous photoreceptor systems were investigated:

(i) pure Se
(ii) Se + y wt. ppm Cℓ ($y \lesssim 40$)
(iii) Se/0.5 wt. % As
(iv) Se/0.5 wt. % As + y wt. ppm Cℓ ($y \lesssim 40$)
(v) $Se_{1-x}Te_x$ ($x \lesssim 0.032$)
(vi) $Se_{1-x}Te_x$ + y wt. ppm Cℓ ($x \lesssim 0.078$)

Although the systems in (i) to (v) have been studied separately by different authors at one time or another, there seems to be no comprehensive collection of transport data. One systematic study (Tabak and Hillegas 1972) for example comprises the first four cases where data have been taken on the drift mobilities, carrier lifetimes and ranges at room temperatures. There are also differences in the experimental techniques and results obtained between different researchers.

In Chapter 2, the properties of a-Se and some of its light compositional alloys relevant to this project are critically discussed. Due to a large number of published articles on a-Se and its alloys it was not possible to provide an exhaustive literature review and thus mainly recent selections were preferred. Note that this chapter also has introductions to a number of important theories and discussions which are of general applicability to other similar amorphous structures, e.g. glass transition, crystallization, charged defects (the so-called D^+ and D^- centres).

In Chapter 3, the principles of the Time-of-Flight technique are presented and the general theory of transient conduction is discussed. It must be remembered that the TOF technique is still a relatively new experimental research tool for studying charge transport (see §4.2) and therefore its theory is not readily available in general texts on solid state research.

In conventional experimental research on transport in high conductivity semiconductors, at least two or more experiments are normally required before any conclusions can be drawn on charge transport. These are conductivity and thermoelectric power and/or Hall mobility measurements. The former is rendered free of contact effects by using the four probe method (Allison 1971 Ch.6) Thus the behaviour of the carrier mobility and free carrier density with temperature and/or impurities can be readily determined. Even the use of these conventional techniques on trigonal Se have not been sufficient to characterize its conduction mechanism. It has been found necessary to measure the mobility by other means (e.g. acoustoelectric current saturation technique; §2.5).

In the case of a-Se its high resisitivity ($\rho \gtrsim 10^{14}$ Ω cm; e.g. Lakatos and Abkowitz 1971) precludes the four probe method although some limited thermoelectric work has been carried out (§2.5). The Time-of-Flight technique on the other hand has been proved to be extremely useful in studying charge transport not only in a-Se and in its monoclinic allotrope but also in many other low mobility solids which satisfy the conditions stated in §3.2.

In Chapter 4 the experimental details of the TOF system constructed, sample preparation and characterization are described. In addition the latter part of this chapter includes important experimental data obtained from Differential Scanning Calorimetry (DSC). Such thermal studies are not only invaluable in yielding quantitative data on thermal properties but also in providing indirect information on the structure.

In Chapter 5, the results of the TOF transport measurements are presented in sections according to material composition. The discussion in each section cannot be treated in isolation inasmuch as the eventual picture or model of charge transport and the effects of impurities must be consistent and comprehensive. The discussions are quantified by numerical analysis.

In Chapter 6, the conclusions drawn by virtue of the results and discussions of Chapter 5 are summarized and suggestions for future work are outlined.

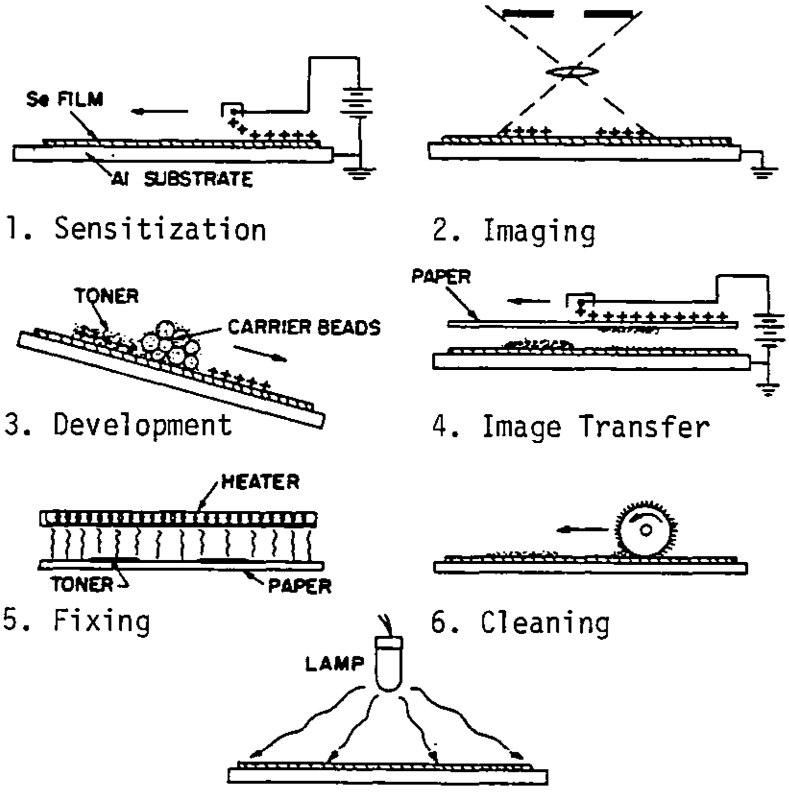

1. Sensitization
2. Imaging
3. Development
4. Image Transfer
5. Fixing
6. Cleaning
7. Image erasure

Fig. 1.4: Schematic illustration of the process steps in reusable xerography (From Tabak et al 1973)

CHAPTER 2

PROPERTIES OF a-Se AND THE EFFECTS OF IMPURITIES

§2.1 INTRODUCTION

In the previous introductory chapter we mentioned the importance of a-Se and the reasons for the research interest into its properties. Although there has been an extensive investigation of most of its physical properties there are still unresolved theoretical problems. Firstly, there are several possible different physical models for its structure. Therefore it is not surprising that the details of the crystallization process are also unresolved. These are discussed in the next section. Secondly, the electrical conduction mechanism has not been conclusively identified. For example, its transient charge transport mechanism as determined from TOF experiments has been interpreted in terms of a shallow trap controlled conduction, multiple trapping in a distribution of traps, and a hopping process. Its I-V characteristics obtained from similar d.c. measurements have been attributed to space charge limited currents (SCLC) and emission limited currents; two diverse conduction mechanisms. The existence of SCLC however would require an ohmic contact (an infinite reservoir of charge carriers) which would not allow TOF measurements (Abkowitz and Scher 1977). So, this is another paradox which has not been settled.

The problem of interpreting experimental data to determine the effects of adding impurities to a-Se is difficult and the most probable interpretation, sometimes based on a comparative study, is preferred.

There have been many review articles on the properties of a-Se[†]. There are, in fact, regular books published on selenium which also include reviews on the amorphous phase (see, for example, Zingaro and Cooper 1974 and Gerlach and Grosse 1979). An extensive collection of data on the physical and chemical

---

[†] Some recent articles may be found in Lucovsky 1979 on the structure, Enck and Pfister 1976, Owen and Spear 1976, and Owen and Marshall 1977, Pfister and Scher 1978, Pfister 1979 on electronic states and charge transport. Mott and Davis 1979 (Ch. 10) also review a-Se.

behaviour of the various phases of selenium may be found in Cooper, Bennett and Broxton 1974. In the following sections we will survey the relevant a-Se literature to obtain a reasonable picture of its physical properties.

§2.2 STRUCTURE

2.2.1 Background

Three crystalline allotropes of selenium are known to exist, namely trigonal, α-monoclinic, and β-monoclinic, as sketched in Fig. 2.1. Trigonal Se consists of screw-like spiral chains which run parallel in a hexagonal symmetry. The atoms of each individual chain are held together by covalent bonding, and the chains probably by van der Waals forces. So the molecular unit for the trigonal phase is a chain (Fig. 2.2a). The monoclinic allotropes are based on eight-member, i.e. Se_8, puckered ring molecular units (Fig. 2.2b) which are packed in two different patterns to give either the α or the β phases (Fig. 2.1b). In β-monoclinic selenium the molecular units stack parallel to each other whereas in α-monoclinic polymorph there are two stacking directions. The Se_8 ring may be viewed as a bent chain.

In the trigonal crystal, a selenium atom has two nearest neighbours (at a distance[†] $r = 2.32$Å) with which it forms strong intramolecular (primary) covalent bonds (≈ 0.94 eV per bond). It has four next nearest neighbours on different chains at a distance $R = 3.46$ Å. Since this is shorter than the van der Waals diameter ($2R_v$) of about 4 Å the intermolecular (secondary) bonds cannot be attributed to van der Waals forces alone[#]. In fact any consideration of intermolecular forces must, therefore, include overlap of atomic orbitals

---

[†] Lattice parameters may be found in Abdullaev et al 1969, Unger and Cherin 1969 and Kaplow et al 1968.

[#] The radius of an outer electron in an isolated Se atom may be calculated approximately from $r_{av} = a_0 Z^{*-1} n^2[1.5 - \ell(\ell+1)/(2n^2)]$ with $Z^* = 3.4$ from the first ionization energy).Thus $r_{av} \approx 3.6$ A. This is nearly the same as the intermolecular distance so we may expect substantial interchain interaction between (hybridized) orbitals.

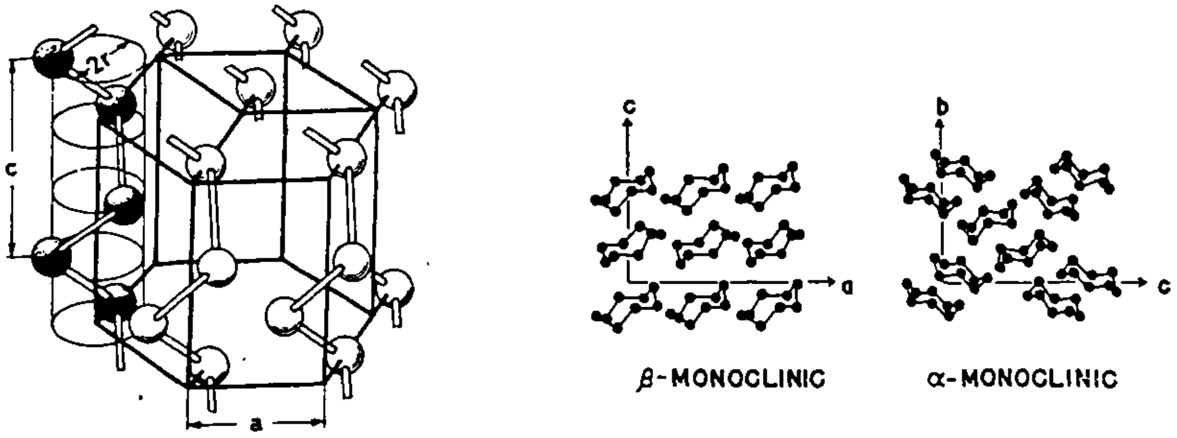

(a) Trigonal Selenium (b) Monoclinic Selenium

Fig. 2.1: Crystalline modifications of Selenium

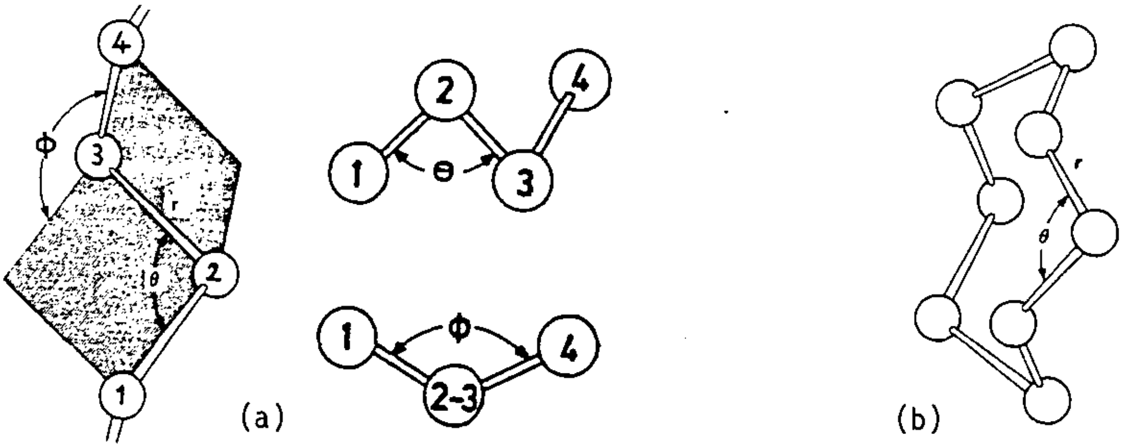

Se chain molecule and the definition of the dihedral angle ϕ.

Se_8 ring molecule

Fig. 2.2: Se chain and ring molecular units. θ and r are the bond angle and length respectively.

Table T2.1: Density and Intermolecular Separation for Various Phases of Se

	γ-Se	α-Se	β-Se	a-Se
Density (g/cm^3) :	4.819	4.389	4.4	4.285
Intermolecular Separation (Å) :	3.46	3.53	3.48	?

NOTATION: γ: trigonal, α = α-monoclinic, β: β-monoclinic

a: amorphous

(probably hybridized) of atoms on different chains (see, for example, Martin, Lucovsky and Helliwell 1976 and Robertson 1976). Note that the energy of the intermolecular bond with the second nearest neighbour is ≈0.08 eV. In the next section we will discuss the bonding and coordination aspects of selenium. The bond angle θ in the trigonal crystal is about 105° whereas the dihedral angle ϕ is 102°. This angle which has recently received considerable attention in structural studies on a-Se is sketched in Fig. 2.2a. It is defined as the angle between two adjacent bonding planes. Therefore its definition involves four atoms, say 1,2,3 and 4, so that it is observed as shown in Fig. 2.2a by looking down the bond connecting atoms 2 and 3. In the crystal, the positions of all the atoms are fixed by the symmetry and the two parameters θ and r, consequently the magnitude of ϕ is constrained as a function of bond length and angle. In the trigonal form, the dihedral angle rotates in the same sense in moving along a chain to give a spiral pitch of three atoms. In the Se_8 molecular unit however, its sign alternates in moving around the ring.

The monoclinic selenium crystals have an intramolecular bond length of 2.34 Å and a bond angle and dihedral angle essentially similar to that in the trigonal phase. Both α and β forms have neighbours on different molecules 3.53 Å apart but in β-monoclinic selenium the shortest distance between atoms in adjacent molecules is only 3.48 Å.

The trigonal crystal phase has been reported to be the most stable form of selenium up to the melting point of ≈218°C, so most physical and chemical data on selenium in books and tables refer to this phase. The monoclinic allotropes revert monotropically to the trigonal modification (details in Abdullaev et al 1969). The densities of the various forms of Se and the shortest intermolecular distances are given in Table T2.1 (p.30).

The structure of amorphous selenium is believed to depend on the method of preparation. The RDF of a-Se, as obtained from X-ray or Neutron diffraction, differs in detail between samples prepared by deposition at different substrate temperatures (Richter 1972) and also between evaporated and bulk quenched (vitreous) specimens (Kaplow et al 1968, Chang and Romo 1967). A long-standing notion on the structure of a-Se was that this modification contained a mixture of both rings, Se_8, and polymer chain, Se_n, molecular units (Fig. 2.2a and b). The evidence for this structural view came from several different sources.

The existence of a long chain polymer component in melt quenched a-Se was inferred from the high viscosity of the liquid (Eisenberg and Tobolsky 1960), whereas the existence of Se_8 rings was assumed from the partial dissolution of vitreous Se in CS_2 by Briegleb 1929. It was demonstrated by Briegleb that Se_8 molecules could be differentially dissolved out from bulk quenched samples in CS_2 and therefore the dependence of the ring fraction on the melt temperature could be obtained. According to Briegleb's data about 40% of the atoms are in Se_8 rings at the melting point and the ring fraction decreases with temperature in an Arrhenius fashion.

The comparative study of the vibrational spectra of the amorphous and crystalline phases of selenium obtained from infra-red (IR) and Raman spectroscopy lead several authors (Lucovsky et al 1967, Ward 1972, Gorman and Solin 1976) to conclude the existence of a significant fraction of Se_8 rings in a-Se. Figs. 2.3 and 2.4 show the IR transmittance data of Lucovsky 1969 and the Raman scattering data of Ward 1972 respectively. The features attributed specifically to Se_8 rings included polarised features in the Raman response denoted by A_1 modes at 113 cm^{-1} and 250 cm^{-1} (main peak). The latter is due to the totally symmetric bond stretching vibrational mode of the Se_8 ring and the former corresponds to the bond bending mode. The weak shoulder at 239 cm^{-1} was associated with the Se_n polymeric chain. The assignments of the features in the IR spectrum to Se_8 rings comprised the main peak at 254 cm^{-1} and low frequency active mode at 95 cm^{-1}. The band at 135 cm^{-1} was the only feature directly attributable to polymeric chains. Zallen and Lucovsky 1974 have discussed the various assignments in detail.These notions were consequently used to study the structural effects of alloying Se (see Schottmiller

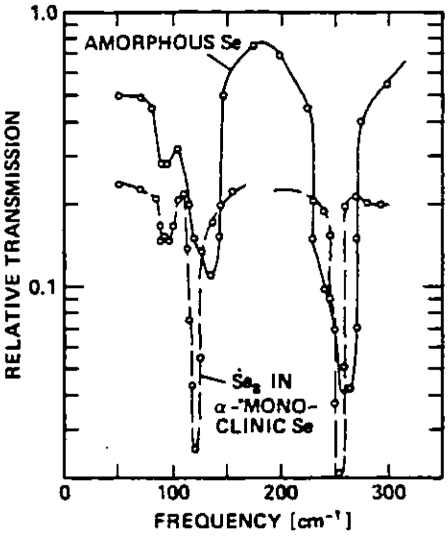

Fig. 2.3: Infrared transmittance of α-monoclinic and a-Se (Lucovsky 1969).

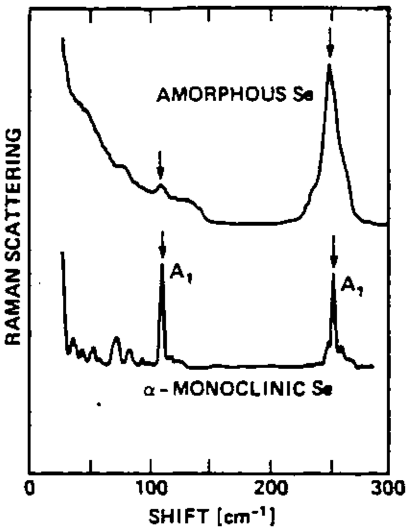

Fig. 2.4: Raman scattering of α-monoclinic and a-Se. The A_1 modes of α-monoclinic Se of 113 and 250 cm^{-1} are identified (Ward 1972).

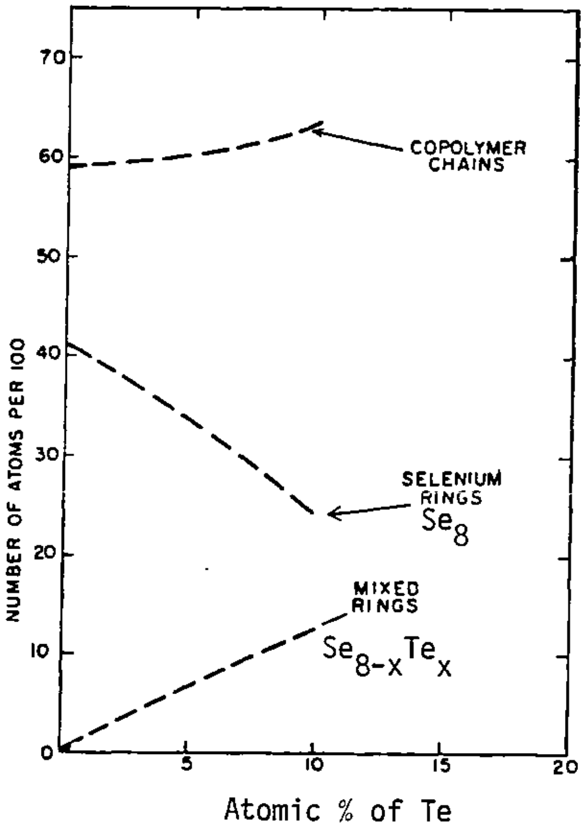

Fig. 2.5: Atomic distributions in Se-Te alloys as proposed by Schottmiller et al 1970

et al 1970, Ward 1972, Ohsaka 1975). Fig. 2.5, for example, shows one of the conclusions of Schottmiller et al on the effects of alloying Te. It seems that the addition of Te to a-Se reduces the fraction of Se_8 rings but introduces a new species; $Se_{8-x}Te_x$ mixed rings.

Theoretical studies in finding the best RDF fit to that obtained experimentally were based on models containing the two molecular units found in the crystalline polymorphs. Firstly, consider the features of the experimental RDFs reported. Fig. 2.6a shows the RDFs for evaporated a-Se samples taken from the X-ray diffraction work of Richter 1972 and Fig. 2.6b shows those taken from the neutron diffraction experiments of Hansen et al 1975. The latter authors questioned the accuracy of the RDFs of some of the previous experiments, viz. the works of Henninger et al 1967, Moscinski et al 1973, Richter 1972 and Renninger et al 1974, by showing the necessary data corrections needed for an accurate analysis (e.g. truncation corrections). Nevertheless peak positions are not expected to be seriously affected for distances < 10 Å so the following reported observations are valid.

The first peak occurs at 2.32 Å and contains two atoms. Therefore the bond length and coordination number are the same as those in the crystalline forms.

The second peak position seems to depend somewhat on the preparation method and has a relatively broad area. Its position between r_2 = 3.55 - 3.70 Å and large coordination number 6-7 (Kaplow 1968 and Hansen et al 1975) suggest that it is probably associated with intermolecular spacings.

There is no peak at the interchain distance of 3.46 Å of trigonal selenium.

From about 4 Å to the next common peak at about 5.75 Å the RDF behaviour is different in the two forms of a-Se. According to Richter, who uses planar zig-zag chains in interpreting the RDF, this behaviour may be attributed to different stacking arrangements. The arrows over the peaks show the expected spacings based on atomic distances within a flat chain. Note that the three remaining dominant peaks are located at approximately the positions

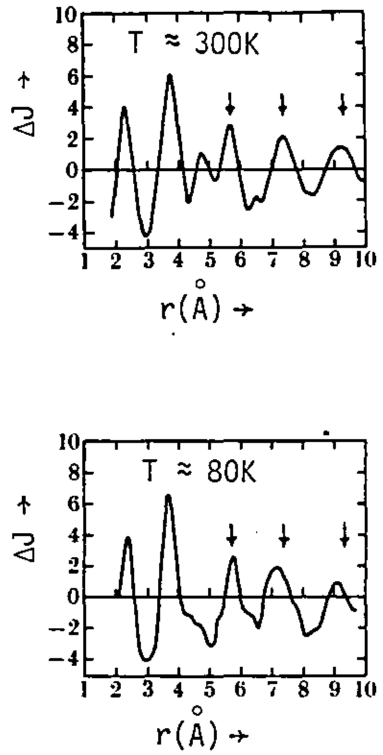

(a) Differential RDF, ΔJ for a-Se evaporated and investigated at two different temperatures. The arrows mark distances in the Richter model of flat zig-zag Se chains. ΔJ from X-ray work of Richter and co-workers (see Richter 1972)

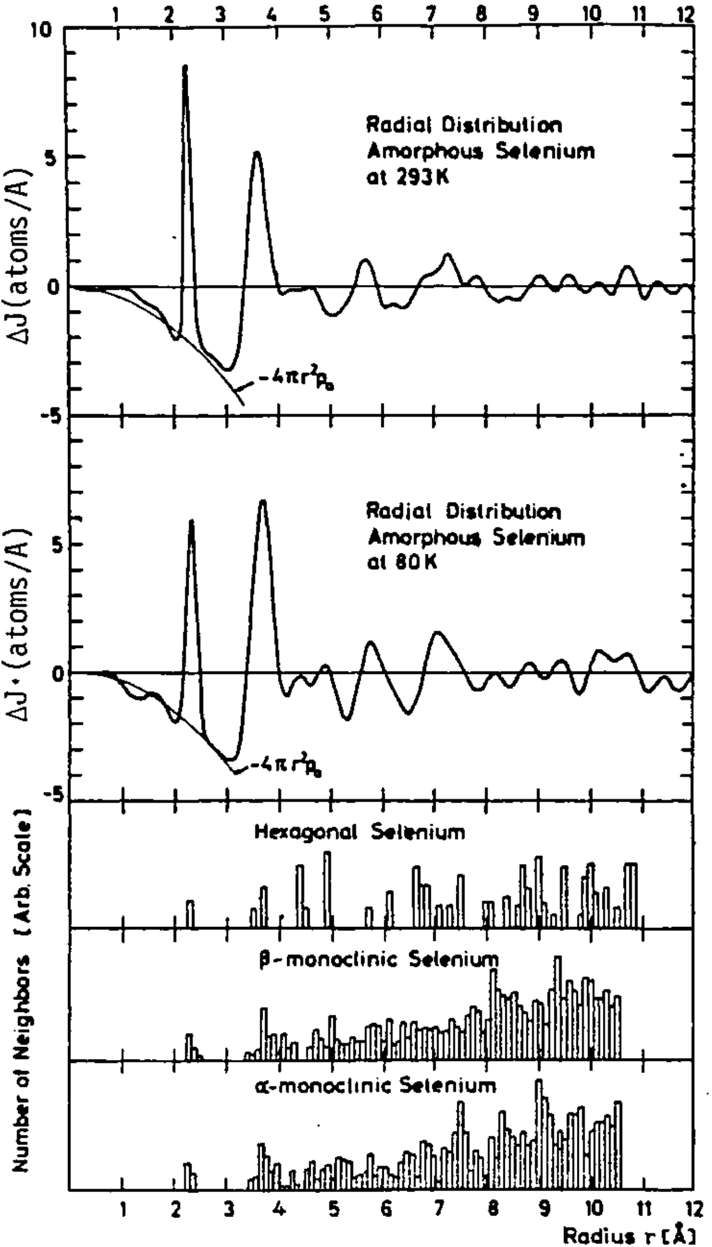

(b) Differential RDF for a-Se from neutron diffraction work of Hansen et al 1975. Also shown, schematically, the number of surrounding atoms in the three crystalline phases.

Fig. 2.6: Differential RDF, $\Delta J \equiv 4\pi r^2[\rho(r) - \rho_0]$, for a-Se

Fig. 2.7: RDF for amorphous and partially crystallized films.

A : $4\pi r^2\rho_0$

B : As deposited (amorphous) film

C : Partially annealed film

D : Peak positions for fully annealed film

From the X-ray work of Samantaray and Nigam 1976.

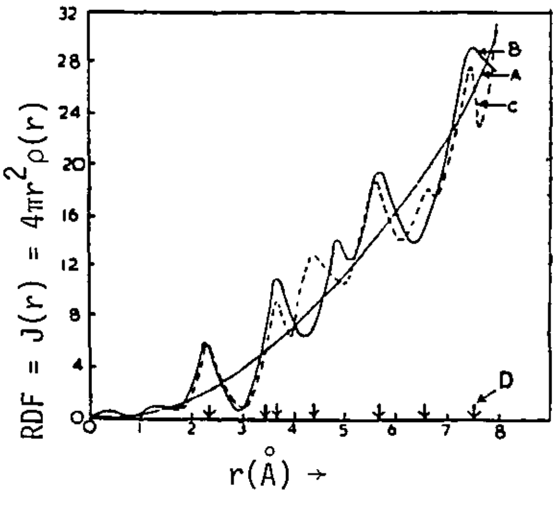

predicted from the Richter model.

There have been several models proposed to explain the RDF of a-Se. The model of Long et al 1976 will be discussed in section 2.2.2. As mentioned, Richter used layers of flat zig-zag chains in which the structural unit was the isosceles triangle of the helical chain of trigonal Se to explain the various features of the RDF. He identified three types of a-Se, called a-Se I, II and III, which had the flat chains stacked in different ways. This planar chain model of a-Se excludes closed ring structures.Hansen et al 1975 doubted Richter's model by pointing out that on crystallization the dihedral angle must change to that in the spiral chains of the trigonal crystal. The energy barrier for this rotation is about 0.43 eV per atom, considerably larger than the crystallization energy of ≈0.07 eV per atom.

Kaplow et al 1968 essentially used a microcrystalline model in which small perturbations from the atomic positions in trigonal or monoclinic Se were considered. Using Monte Carlo calculations they showed that, relatively small displacements, of the order of 0.20 Å, in the monoclinic modifications provided a good fit to a-Se RDF. But the peaks at 5.7 Å and 7.2 Å (Fig. 2.6) could not be matched accurately. When Kaplow et al also considered the evidence for Se_8 rings from IR and Raman spectroscopy they concluded that a-Se consists predominantly of Se_8 rings with nearly 95% of the atoms in a ring symmetry.

Satow et al 1978 also used the microcrystalline model to interpret their experimental RDF of a-Se. They used a mixture of trigonal and monoclinic microcrystals in the 0.15:0.85 ratio, so the preferred species were Se_8 rings.

In contrast to a mainly Se_8 ring structure Henninger et al 1967, as a result of their neutron diffraction experiments, have concluded that the structure of a-Se can be pictured as polymeric chains in random orientation. Richter and Herre 1958, on the other hand, suggested that vitreous Se is a mixture of long chains and Se_6 rings.

It can be seen that the RDF studies have not been able to provide a unique structural model for a-Se. Further support for the existence of Se_8 rings in a-Se comes from other differential dissolution experiments. Apparently, the Soviet group of workers, Geller, Karalunetz, Kolomiets and Popov (see Popov 1976, Popov et al 1977) have shown that CH_2I_2 dissolves only the monomeric, Se_8, ring molecules. Therefore, these researchers were able to obtain the temperature dependence of the ring fraction in quenched Se samples.

It must be remarked that when a-Se is heated it crystallizes to the trigonal phase. Its RDF changes gradually to that of polycrystalline trigonal form (see, for example, Samantaray and Nigam, 1976) as shown in Fig. 2.7. Any structural model of a-Se must also account for the crystallization process and also for the enthalpy involved in this structural ordering.

2.2.2 Recent Advances

According to Lucovsky 1979, Keezer and Geils at Xerox Laboratories have studied the dissolution of three polymorphic forms of selenium in CS_2, with some surprising conclusions. They found that (i) α-monoclinic Se readily dissolved in CS_2, and that the rate of dissolution was not affected by illumination, (ii) trigonal Se was insoluble under all of the experimental conditions explored and (iii) a-Se was soluble but only in the presence of illumination with photon energies, $\hbar\omega$, exceeding 2.3 eV. Since ambient room light levels were found to be sufficient to provide the required illumination, Briegleb's results quoted previously must be excluded from any study of a-Se structure, simply because the state of illumination was not controlled. Similar dissolution results of Popov and co-workers (1976, 1977) of a-Se in CH_2I_2 must also be doubted because there was no report of any illumination control in their experiments.

As a result, any work which has used Briegleb's work as input data into its model must also be suspect. This includes, for example, the much quoted selenium Polymerization P versus Temperature T curve of Eisenberg and Tobolsky 1960.

In this context, note that Keezer, Lucovsky and Martin 1975, studied the IR spectrum of Se samples quenched from liquids equilibrated at different temperatures (at ~222°C and 402°C) and found that both the stretching, 200-300 cm^{-1}, and bending, 90-150 cm^{-1}, modes, including the distinct 95 cm^{-1} feature, showed identical absorption. A similar finding was reported for the Raman spectrum by Brodsky et al 1972. These two findings contradict Briegleb's data which predict half as many Se_8 rings at 402°C than at 222°C.

Vibrational spectra of a-Se as interpreted in early work by assigning modes to Se_8 monomers or Se_∞ polymeric chains has been shown to be incorrect (see Brodsky et al, 1972, Martin, Lucovsky and Helliwell, 1976, Meek 1976, Lucovsky 1979). For molecular solids the spectra would be expected to be similar if two conditions are satisfied (Lucovsky 1979); (1) the solids must be based on the same molecular species, in other words, the intramolecular local order and chemical bonding must be the same, and (2) the intermolecular forces must be of similar magnitude. If these conditions are not met then the spectra of the amorphous and crystalline forms may be quite different even if both phases are based on the same molecular building unit but with significantly different intermolecular forces. This situation occurs with a-Te and trigonal Te. The differences in the IR and also in the Raman spectra of the two phases are essentially due to the intermolecular interactions that are specifically related to a parallel alignment of helical chains in the crystalline phase that is not present in a-Te. The comparative studies of vibrational spectra of different phases of selenium in section 2.2.1 consequently simply imply that a-Se is molecular in the sense of α-monoclinic Se where the intermolecular forces are weaker than those of the trigonal phase.

Martin, Lucovsky and Helliwell have moreover shown that isolated rings and chains display essentially the same bond-stretching frequencies (251 cm^{-1}), so any assignment to monomer or polymer units must involve the bond bending vibrations at low frequencies.

Consider the two ways of bonding five selenium atoms, as shown in Fig.2.8, to represent (a) a local atomic arrangement in a Se_8 ring, or (b) in a long helical chain. The bond angles and lengths are nearly the same in both structures

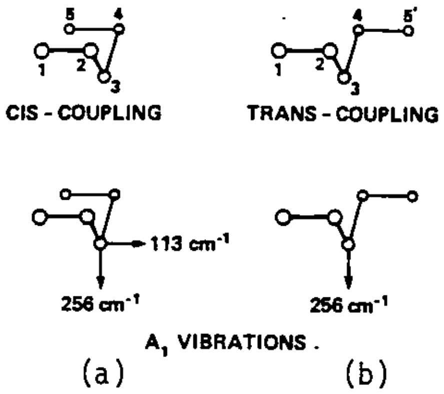

Fig. 2.8(a): Cis-coupling and (b) trans-coupling configurations for molecular bonding in selenium. The difference in the two configurations is in the placement of atoms 5 and 5'. In the cis-coupling the dihedral angles alternate in sign, whilst in the trans-coupling configuration the sign is preserved. Also shown are the atomic displacements of the A_1 symmetry modes. For the cis-coupling there are two modes with displacements in the bonding plane, and perpendicular to this plane. In contrast, the trans-coupling gives only one mode. (Lucovsky 1979, Lucovsky and Galeener 1980).

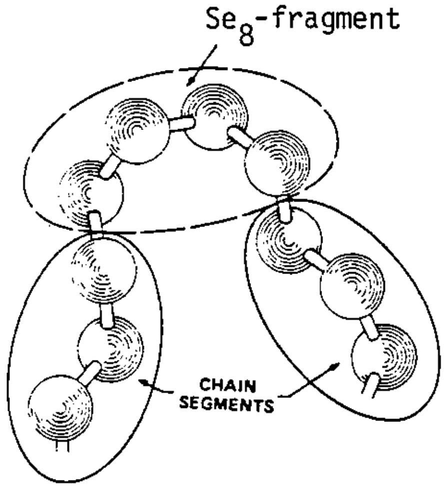

Fig. 2.9: Local molecular order in a selenium chain in which there are segments characterised by repetition of the same dihedral angle, "chain-like" in the sense of trigonal Se, and segments characterised by alternating dihedral angles, "ring-like" in the sense of the Se_8 molecule (Lucovsky 1979).

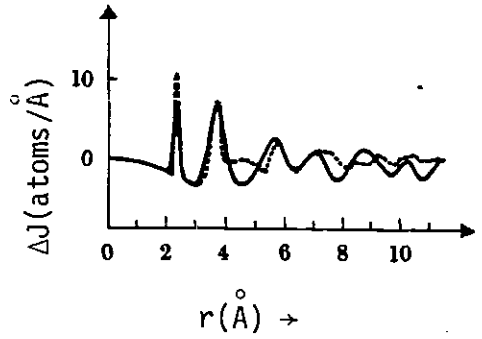

— Long et al model

.... Experimental ΔJ from X-ray work of Kaplow et al 1968.

Fig. 2.10: Gaussian broadened $\Delta J \equiv 4\pi r^2[\rho(r) - \rho_0]$ curve for the Long et al model and the experimental ΔJ for vapour deposited a-Se at 77K. In determining ΔJ, Long et al employed the 363-atom interior sphere from the 539-atom model (see Long et al 1976).

but in (a) the dihedral angle,ϕ, alternates in sign whereas in (b) it remains the same (see section 2.2.1). The first structure is called cis-coupling and the second is termed trans-coupling. The cis-coupling has two A_1 modes of vibrations at approximately 256 cm^{-1} due to bond stretching and another at 113 cm^{-1} due to bond bending (see Fig. 2.8a). The trans-coupling structure on the other hand has only one A_1 mode of vibration which also occurs at 256 cm^{-1} (Fig. 2.8b).

The structural model for a-Se according to Lucovsky 1979, then has all the atoms in two-coordinated chain structures, as shown in Fig. 2.9, but where the dihedral angle, ϕ, is constant in magnitude but varies in sign. This leads to regions which are either ring-like or chain-like, depending on a particular sequence of ϕ. Suppose + or - is used to indicate the relative phase of the dihedral angles between adjacent bonding-planes. Then a sequence +-+- is termed ring-like and a sequence +++ or --- chain-like. The local order shown in Fig. 2.9 may then be characterized as +++-+-+---. This model which assumes only local molecular order within a selenium chain can be used to explain the vibrational spectra. It can be seen that all the atoms contribute to the 256 cm^{-1} mode but only those atoms in local regions where the dihedral angle undergoes a sequence of alternating signs contribute to the lower frequency mode at 113 cm^{-1}. Note that the symmetry of the bond-stretching mode is completely determined by the local environment of three selenium atoms, whereas the bending mode has a complete A_1 symmetry in a closed ring configuration. Nonetheless, Martin et al have shown that five or six atom ring fragments indicate vibrations with approximately the same displacements as the A_1 mode and the frequencies of these modes are nearly the same as that of the A_1 Se_8 ring mode.

Meek 1976 studied the vibrational spectra of a two-fold coordinated isolated chain using bond-stretching and bending forces only. The bond lengths and angles were kept constant but the dihedral angles were allowed to take different distributions (e.g. $\phi = 102°$, $-180 < \phi < +180$, $\phi = 180°$, $|\phi| = 102°$).

He concluded that there was a preferred value for $|\phi|$ (probably ≈102°) along the chain molecular units and that the sign of ϕ is constant or random. Small variations of ±5-10° about the optimal 102° do not affect the vibrational density of states drastically.

Robertson 1976 has argued that the lowest local energy occurs for $|\phi| \approx 102°$ by discussing the interactions between different orbitals. He studied the influence of the dihedral angle on the electronic band structure of the chain-like and ring-like regions and concluded that a-Se consists of two-fold coordinated structural units in which the sign of the dihedral angle either alternates or is random from atom to atom. Alternation of sign in ϕ does not necessarily lead to closed rings.

Another important conclusion from Robertson's work is that because even small changes in ϕ (say ~40°) cause large increases in the local energy, the structural models in which ϕ is greatly different from the optimal value 102° are unlikely. Therefore Richter's model of flat ziz-zag chains ($\phi = 180°$), the models of Joannopoulos et al 1975, and Shevchik 1974, and Richter and Herre 1958, for example, which assume the presence of Se_6 rings($\phi \sim 80°$) are unlikely.

Although RDF studies, discussed in section 2.2.1, have not shown to provide a unique model for a-Se structure, one recent study by the group Alben, Galison, Long and Connell (see Alben et al 1976, Long et al 1976) has been of considerable value. These researchers constructed, by hand, a 539-atom chain model for the structure of a-Se. The chains are linked by flexible plastic tubes which represented weak intermolecular forces. The following points of construction were followed: (1) no large holes were permitted in the structure; (2) no regular patterns on a large scale, e.g. groups of parallel chains, were permitted so as to avoid microcrystal-like arrangements; (3) the distortions of covalent bond lengths and angles were kept as small as possible; (4) the number of nearest neighbours on adjacent chains was kept at four whenever possible to simulate the local order in crystalline form of Se and (5) the chains of covalently bonded units were not allowed to close on themselves or to terminate in the interior of the model. Hence this model contained no rings of atoms. The rules in (2) and (3) meant that some of the inter-chain links were not used.

The coordinates of the atoms were measured approximately to provide a starting point for the computer relaxation by minimizing the local energy with stretching and bending forces and a van der Waals force represented by a Lennard-Jones' potential. The relaxed model had an rms bond length variation of less than 1% and rms bond angle variation of less than 4%. However, the dihedral angle distribution was broad. There was no preferred dihedral angle in contrast to the above conclusions of Meek and Robertson.

The gaussian broadened RDF for this model is shown in Fig. 2.10 with an experimental RDF for a-Se deposited at 77K (from Kaplow et al 1968). There is a better agreement produced with the experimental RDF than by any microcrystalline model for the structure (Kaplow et al 1968), particularly with regard to the feature near 5.7 Å which cannot be produced by any mixture of helical chains and Se_8 rings (Grigorovici 1974). However the model fails to reproduce the plateau between 4 and 5.5 Å and shows shifts in peaks at large r towards lower r relative to the experiment. The authors argue that the reason for the former failure is the deliberate avoidance of any parallel arrangement of chains.

§2.3 GLASS TRANSITION AND CRYSTALLIZATION

2.3.1 Glass Transition

The study of glass transition and crystallization phenomena play an important role in the structural and thermal characterization of amorphous solids, particularly of non-crystalline polymers. It is instructive,firstly, to summarize some aspects of glass transition.

Glass is considered by technologists to be any solid formed by the continuous hardening of a cooled liquid. Turnbull 1969 defines glass as a state of matter characterized by a viscosity η in excess of 10^{15} poise. An alternative description (see Gee 1970) of the glassy state involves the first order extensive thermodynamic properties of matter V, H or S. When the molten state is cooled, a temperature range is reached below which the second order thermodynamic properties, e.g. α, C_p, C_v are typically 'solid-like' and above which they are typically 'liquid-like'. This temperature range is often termed the glass transition or transformation range T_g, in which the second order parameters evince a relatively discontinuous change. The first order parameters do not show any discontinuity in T_g.

Consider the specific volume-temperature, V-T, relationship of selenium in Fig. 2.11. When liquid selenium is cooled infinitely slowly it will crystallize to the solid phase at the temperature T_m following the broken line ABCD. There is a discontinuous volume change at $T_m \approx 220°C$. At some high cooling rate on the other hand the material's V-T relationship follows along the super-cooled liquid line, BE. There is no discontinuity in V. When a certain temperature range, EF, is reached (see the upper inset in Fig. 2.11) there is a change in the rate of dependence of V on T or $\frac{dV}{dT}$. At lower temperatures the V-T relationship follows the glass line FG. The physical properties of the system are more solid (glass)-like than liquid-like. The glass and crystal have nearly the same expansivity, α (see lower inset in Fig. 2.11). The temperature dependence of α marks clearly the glass transition. The intersection of the glass line FG with the super-cooled liquid line BE is commonly referred to as a glass transition temperature T_g. Some texts refer to this as the fictive temperature, T_f. As shown in the diagram, this temperature depends on the rate of cooling. If this is fast, the trajectory may be ABE'F'G' and T_g' is higher. Therefore there is no one unique temperature but a range of temperatures characterizing glass transition.

In calorometric measurements, for example in experiments involving the monitoring of enthalpy vs temperature, a glass transition temperature may similarly be defined by the intersection of the glass and super-cooled liquid lines (see Gee 1970). Note that normally in such measurements the starting point is the lowest temperature. The glass transition temperature so obtained however is not necessarily the same as that observed during the cooling of the specimen from the melt (see Owen 1973).

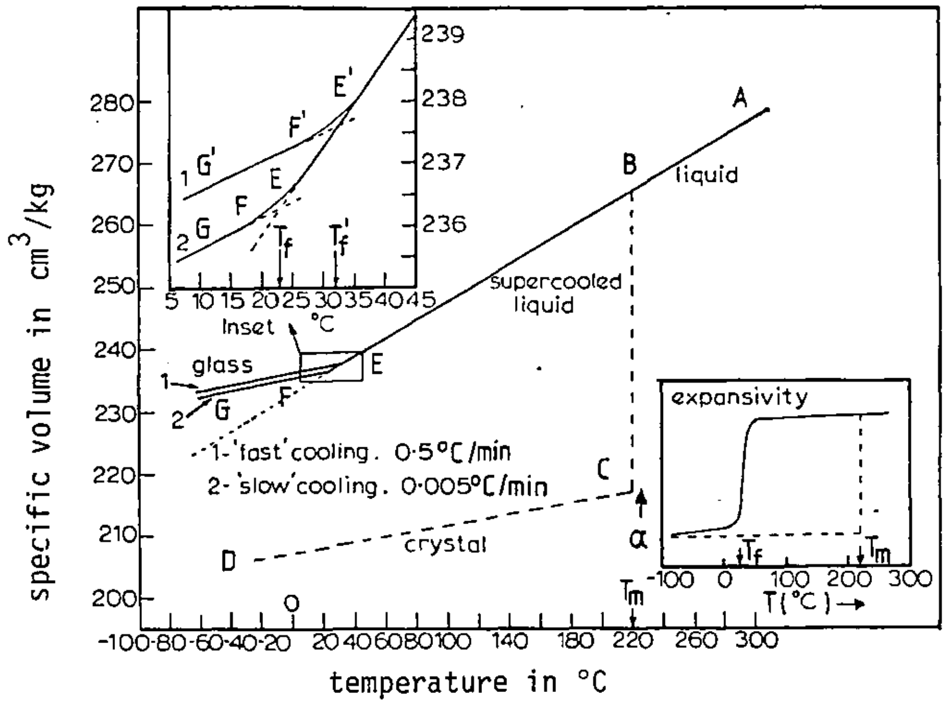

Fig. 2.11: Volume-temperature relationship of selenium at the liquid-crystal and liquid-glass transition. The upper inset shows in more detail the effect of different cooling rates on the glass transition and the lower one illustrates the discontinuity in the expansion coefficient, α, a second-order property. T_m is the melting temperature. Measurements by Dzhalilov and Rzaev 1967 (from Owen 1970).

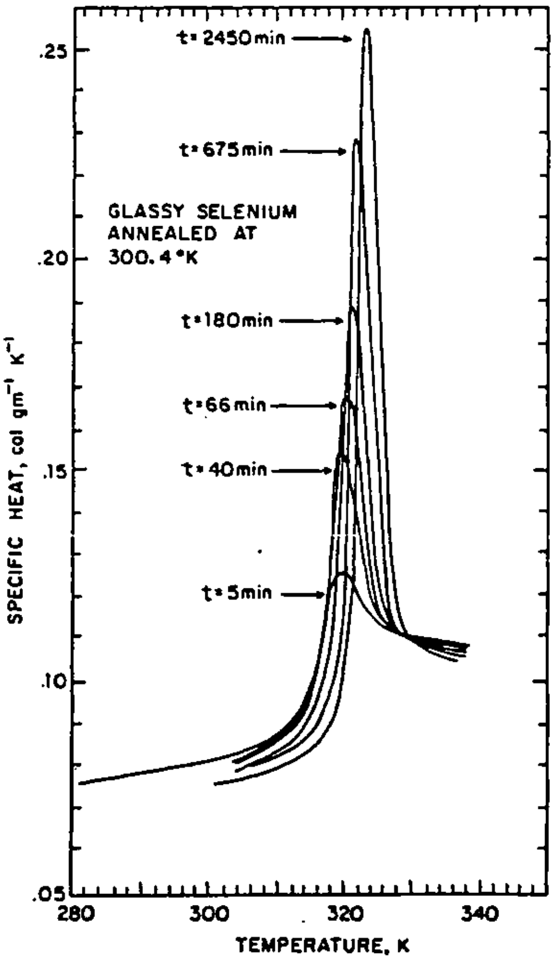

Fig. 2.12: Heat capacity vs temperature for glassy Se in the T_g region after annealing for various times at 300.4K (27.2°C) (Stephens 1976).

In general, T_g depends on the time-temperature history of the glass before and during measurements. It also depends on the nature of the measurement itself. For example, the dilatometric measurements of Dzhalilov and Rzaev 1967 (Fig. 2.11) show clearly that T_g depends on the experimental time base; its value ≈32°C at 0.5°C min^{-1} is lowered to ≈23°C when the cooling rate is two orders of magnitude lower.

In their expansion studies of bulk vitreous selenium specimens, Eisenberg and Tobolsky 1962 were surprised to find that T_g did not seem to depend on the equilibrated liquid temperature before quenching. Since the degree of polymerisation P in the liquid was proposed to depend on the liquid temperature (Eisenberg and Tobolsky 1960), it was inferred that T_g is unaffected even when the ring population is doubled and the degree of polymerization is changed by a factor of 20. In view of the discussions in §2.2 (2.2.2) this if, of course, further evidence against a mixture of monomer and polymer units for the structure of a-Se.

Fig. 2.12 shows the behaviour of a second order parameter the isobaric heat capacity C_p (from differential scanning calorimetry; DSC) around the glass transition region. Notice that the C_p-T curves evince a distinct peak whose nature depends on the annealing time. This behaviour is also shown typically in the DSC thermograms of this work around T_g (see Figs. 4.10 and 4.11 in §4.7). It is attributed to structural relaxation effects and marks the importance of the kinetic theory of glass transition. Several authors (e.g. Das et al 1972, Stephens 1976, 1978, Abkowitz 1979, Larmagnac et al 1981, Grenet et al 1981) have studied the relaxation phenomena in a-Se. Qualitatively, the kinetic interpretation can be understood by examining a typical glass enthalpy vs temperature H-T relationship as in Fig. 2.13 (p.48).

Consider the specimen at some starting temperature, $T_L > T_g$, in thermal equilibrium at C on the H-T curve. Suppose it is cooled to a temperature $T_A < T_g$ and annealed (or held) at that temperature for a time, t_A. On arrival at temperature T_A the sample has not reached thermal equilibrium because the molecular 'mobilities' or structural relaxation rates are too slow below T_g .

As a result at $t_A = 0$, there is an excess enthalpy in the sample which relaxes out during the subsequent annealing of the sample. The thermodynamic state relaxes towards the expected equilibrium state (A) on the extended liquid (equilibrium) H-T curve (A-L).

Suppose we now take the well annealed sample at A through a heating cycle to T_L. The initial path will be AB parallel to the glass curve because below T_g the thermodynamic state cannot follow the equilibrium (liquid) curve AL. But at T_L above T_g it is in equilibrium, so the heat given out during annealing at T_A must be replaced. This corresponds to an endhothermic relaxation peak which is often observed in differential thermal analysis (e.g. Figs. 4.10 and 4.11).

If the heating process had been started at $t_A = 0$, i.e. immediately following the cooling cycle, LDE, then the trajectory would have been along EFL with a smaller endothermic peak in C_p-T thermogram.

It can be seen that the glass transition has been regarded as a kinetic phenomenon and the sharp behaviour of some of the physical parameters in this region has been attributed to the very strong temperature dependence of structural relaxation rates near T_g. The temperature dependence of all mechanical (and some electrical) relaxation times in amorphous polymers and other glass forming liquids has been shown to obey the empirical Williams-Landel-Ferry (WLF) (1955) equation, i.e.

$$\tau(T) = \tau_g \exp[-\frac{C_1(T-T_g)}{C_2+T-T_g}] \qquad (2.1)$$

where C_1 and C_2 are universal constants 17.4 and 51.6K respectively and τ_g is the value of τ at $T = T_g$. Abkowitz, Pochan and Pochan 1980 (see also Abkowitz and Pai 1977) have recently reported dielectric activity in a-Se and a-Se/As alloys in the neighbourhood of their respective glass transition temperatures.

They investigated the dielectric loss (ε'' component) via the a.c. conductance as a function of temperature and frequency. Typical dielectric loss vs temperature curves at various frequencies are shown in Fig. 2.14a. When these authors examined the dependence of the central dielectric relaxation time† $\tau = \omega^{-1}$ on the temperature where the loss is a maximum they found a WLF type of behaviour, Fig. 2.14b, with C_1 = 10.4K, C_2 = 20.5K and a free volume fraction, $f(T_g)$, of 0.042. Note that to obtain the latter quantity they used the equations of Cohen and Turnbull to relate C_1 and C_2 to the free-volume theories (see, e.g. Young 1981, Ch.4). Their τ_g value was 50 sec. Addition of As decreased the fractional free volume to 0.021 due to enhanced cross-linking associated with the As branch point in the selenium chain. Note that Dzhalilov and Rzaev (see Fig. 2.11) using their expansivity data find the fraction of free volume $f(T_g) = 0.030$. In addition they demonstrate that at T_g for a-Se $(\alpha_{\text{liquid}} - \alpha_{\text{glass}})\, T_g \approx 0.115$ which conforms with the Simha-Boyer (1962) empirical relationship found for many polymers.

In polymeric materials the glass transition temperature has been shown (see, e.g. Billmeyer 1971, Ch. 7) to depend on the molecular weight M_n by the equation $T_g = T_g^{\infty} - KM_n^{-1}$, where T_g^{∞} is the glass transition temperature at infinite molecular weight and K is a constant. We have already mentioned that the glass transition temperature observed on bulk vitreous selenium samples is apparently independent of the quench temperature T_q. This suggests that the average molecular weight per polymer unit in the liquid must be independent of temperature.

The glass transition temperature in selenium alloyed with Ge, Sb, As, Te in small quantities has been observed to increase with the alloy composition (see e.g. Tomura et al 1975, Dzhalilov and Rzaev 1967 and Ward 1970). This is expected since Ge, Sb and As will act to link Se chains, thereby reducing the molecular mobility and forming a more 'rigid' structure. Te atom is heavier than the Se atom so the inclusion of Te atoms in Se chains will increase T_g.

In §4.7 we discuss further the glass transition phenomenon in a-Se, a-Se/As and a-Se/Te alloys in connection with the DSC studies of this project.

---

†In general a relaxation process at the glass transition region of an amorphous solid should be described by a distribution of relaxation times rather than a single relaxation time. For a-Se, ε'' vs ω experiments at given temperatures (see Figs. 6 and 7 in Abkowitz, Pochan and Pochan) indicate broad loss peaks and hence imply a distribution of relaxation times. The relaxation rate τ^{-1} in Fig. 2.14b is the inverse of the central relaxation time of this distribution.

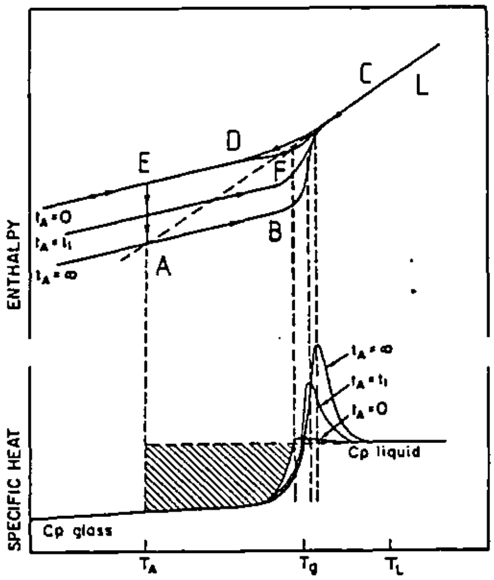

Fig. 2.13: Enthalpy and heat capacity vs temperature cycle of a glass as it is cooled from T_L to T_A, annealed there for time t_A and then warmed back to T_L. The maximum area of the relaxation peak at T_g is given by the shaded area formed by extrapolating the liquid C_p line down to T_A and is equivalent to the maximum enthalpy change at A. (Stephens 1978).

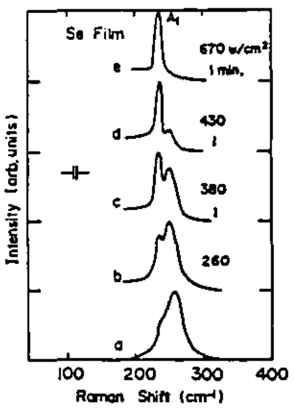

Fig. 2.15: Raman spectra in crystallization of amorphous Se film. Scattering intensities are normalized at peak values. Curve 'a' is the spectrum for the as-evaporated amorphous state and is measured at 90K. Both 'a' and 'b' are spectra measured with the incident laser beam of 260 W/cm^2. For this intensity the spectra do not change their overall shapes. 'c', 'd' and 'e' are measured at 260 W/cm^2 after annealing the sample with the beam of 380, 430 and 670 W/cm^2 for one minute, respectively. The sample is kept at 293K for 'b' through 'e'. (From Yashiro and Nishina 1979).

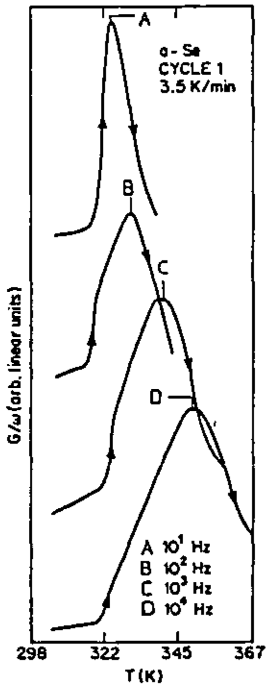

(a)

(a) Dielectric loss (σ/ω) of a-Se measured at various rms bias vs emf of a copper-constantan thermocouple. Equivalent temperatures are shown. Data recorded during first thermal cycle of a well annealed sample.

(b) Central relaxation rate τ^{-1} vs $10^3/T$ for a-Se obtained from measurements in (a). Curve (A) is the WLF equation with C_1 and C_2 as universal constants whereas (B) is the WLF equation from best linear regression fit to data.

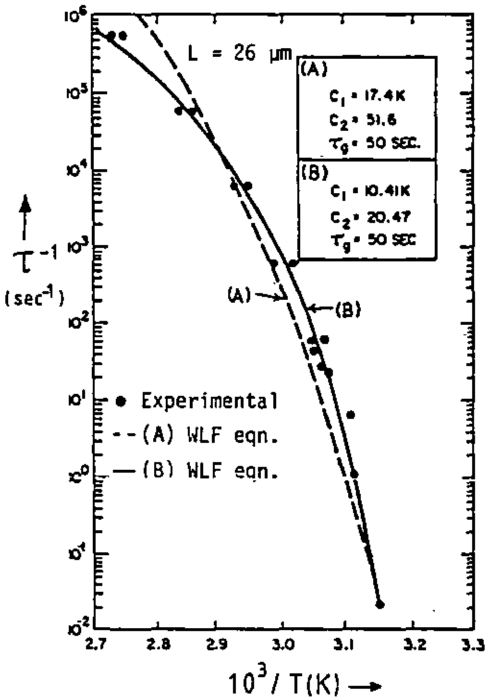

(b)

Fig. 2.14: Dielectric behaviour of a-Se around its glass transition region (From Abkowitz, Pochan and Pochan 1980)

2.3.2 Crystallization

When a-Se is used as a commercial electrophotographic photoreceptor even a fractional crystallization causes it to be unsuitable for the xerographic process. Therefore the crystallization mechanism has attracted much attention and there are numerous papers on this subject[†].

The crystallization of the amorphous phase occurs towards the stable trigonal modification. Consider the recent Raman spectral studies of Yashiro and Nishina 1979 on the crystallization of evaporated a-Se films. Crystallization was induced by 'annealing' with a variable intensity laser beam. Fig. 2.15 shows the Raman spectrum at the various stages of the crystallization process, (a) corresponding to a-Se spectrum (c.f. Fig. 2.4) and (e) to polycrystalline trigonal selenium. It can be seen that there is no marked shift in the dominant peak at 250 cm^{-1} towards the trigonal peak position at 235 cm^{-1}, in contrast to the significant spectral shift observed in amorphous-to-polycrystalline transition in Te. Instead, the 235 cm^{-1} weak shoulder in the a-Se spectrum grows at the expense of the 250 cm^{-1} peak and eventually becomes the prominent feature. From their investigations Yashiro and Nishina infer that the disordered chain model (see 2.2; 2.2.2) may not be applied to a-Se.

Crystallization of a-Se depends[†] on temperature, thermal history, impurities, substrate, light, electron or nuclear irradiation, electric field (Bolotov and Komarova 1975) and the chemical environment. A variety of techniques* have been used to investigate the crystallization of a-Se: X-ray diffraction (Mamedov and Nurieva 1964); electron microscopy (Montrimas and Petretis 1973, 1974, Kim and Turnbull 1973, Clement et al 1974, Gross et al 1976); optical microscopy (Hamada et al 1967, Kim and Turnbull 1973, Brower and Capo 1976, Gross et al 1976, Kawarada and Nishina 1977a); Raman spectroscopy (Yashiro and Nishina 1979); DTA or DSC[#] (Kawarada and Nishina 1975, 1977a,b, Thornburg 1976, Matsuura and Suzuki 1979, Grenet et al 1980); dilatometry (Dzhalilov 1965,

---

[†] See Cooper and Westbury 1974 for a review

*References are examples taken mostly from recent work

[#] Differential Scanning Calorimetry

Janjua et al 1971); electrical conductivity (Champness and Hoffmann 1970, El-Mously et al 1976, El-Mously and El-Zaidia 1978, Fleury et al 1981).

Hamada et al 1967, Kawarada and Nishina 1977a,b and others have shown that the morphology of trigonal selenium growth in a-Se occurs in the form of spherulites. The nucleation may begin in the bulk, on the free surface or at the substrate interface. The growth on the surface or at the interface is inwards and the geometry is hemispherical. The spherulites are believed to consist of thin lamellae radiating from a common centre (see Griffiths and Fitton 1969). The molecular chains are oriented normal to the radius and therefore to the growth direction. The widths of the lamellae are much less than the typical chain lengths expected. The lamellae twist as they grow outwards radially, giving the concentric alternate light and dark rings observed under polarized light. This spherulitic aspect of selenium crystallization reflects its polymeric nature.

Kim and Turnbull 1973 and Gross, Stephens and Turnbull 1976 studied the morphology of crystallization of va pour deposited a-Se films on mica. They, in contrast, showed that crystallization begins with the formation and radial growth of crystalline aggregates with a cylindride morphology at the mica interface. Filamentary crystals stem from the less regular regions of these cylindrites and grow upwards through the film. Upon reaching the vicinity of the free surface some of the filamentary tips develop into cylindrites which grow in and parallel with the free surface plane. These authors therefore attribute the initiation of crystallization to nucleation at the substrate interface alone. Free surface or bulk nucleation may, however, be started by impurities.

The volumetric rate of growth of the crystalline phase out of the amorphous phase has been extensively studied. Most experiments have been generally interpeted by the Avrami (1939) equation:

$$x = 1-e^{K(T)t^{n}} \qquad (2.2)$$

where x is the fraction of crystalline phase, t is time, K(T) is the crystallization rate constant and n is a parameter characteristic of the geometry of growth, and nature of nucleation. In the dilatometric study of Janjua et al 1971, n varied between 3.7-4.7 indicating a heterogeneous nucleation and three-dimensional growth of spherulites for the crystallization mechanism. As the crystallization proceeded n decreased towards a value of 3. Dzhalilov 1965, however, found that $n = 1.6 - 3$ and interpreted this as two-dimensional crystal growth.

The growth rate of the crystalline phase, as determined from a variety of experiments, has been shown to be thermally activated. The activation energy depends on preparation methods (Kawarada and Nishina,1977a,b); substrates (Thornburg 1976); impurities (Hamada et al , Janjua et al); irradiation by light (Dresner and Stringfellow 1967, Clement et al 1974, Gross et al 1976). Its value for pure Se seems to be ≈1eV per atom, although it does vary slightly depending on whether nucleation and crystallization proceed in the bulk,on the free surface or at the substrate interface.

Because the structural model based on monomer Se_8/polymer Se_n mixture has dominated the scientific literature on a-Se, most interpretations of the crystallization mechanisms incorporate breaking of Se_8 rings (energy of ~2eV). For example, according to Coughlin and Wunderlich 1973, the crystallization process involves the crystallization of polymeric chains and the polymerization of Se_8 rings. Further, sites of polymerization are removed in time and space from the sites of crystallization (see §4.7 for discussions).

The addition of arsenic to selenium in small quantities has the very marked effect of retarding the rate of crystallization of selenium. This has been attributed to As atoms cross-linking some of the polymer chains and therefore reducing molecular mobility. Se/As alloys play a very important commercial role in xerographic photoreceptor technology since the useful lifetime of a pure selenium photoreceptor is limited by its eventual crystallization.

The effect of chlorine doping in selenium is more complex but for the quantities used in this project ($\lesssim$ 40 wt. ppm) the crystallization rate seems to be either retarded (Janjua et al) or relatively unaffected (Hamada et al).

§2.4 ELECTRONIC STRUCTURE AND STATES IN THE GAP

The molecular ring or chain units comprising the a-Se structure discussed in §2.2 were built on Se atoms having two-fold coordination. The isolated Se atom has four p-electrons,two of which are already paired and form a lone-pair. The other two electrons are available to form covalent bonds with the p-electrons on two neighbouring atoms. This simple view attributes the interatomic covalent bond to overlapping p-orbitals.

The observed bond angle, ~105°, on the other hand, suggests the participation of hybrid orbitals in covalent bond formation. Since the atomic s-states are well separated from the higher p-states (~10 eV), one may expect the s-p hybridization to be relatively small. However, a mixture with d-states is also possible. According to Joannopoulos et al 1975, the two bonds per atom are essentially formed from p-type orbitals with small admixtures of s and d characters of about (5-10)% and (1-5)% respectively. The nature of hybridization of molecular orbitals in selenium chains and rings is still unclear (see Robertson 1976) and it is often neglected for bonding purposes in the selenium literature.

Fig. 2.16 shows the experimental density of valence states, DOVS, vs energy, E, spectrum for d.c. sputtered a-Se and polycrystalline (trigonal) Se obtained from UPS and XPS measurements (Shevchik et al 1973). The region 0 to ≈-2 eV is the lone-pair band due to the non-bonding p-orbitals whereas the -2 to -8 eV area is the bonding p-like band. The s-band is located in the -8 to -18 eV interval. The overall structure of the trigonal and amorphous spectra remains essentially unaltered. In particular, no broadening with respect to the crystalline phase can be oberved in the amorphous phase. Note, however, that the twin peaks in the p-bonding band of trigonal Se are reversed in intensity in a-Se.

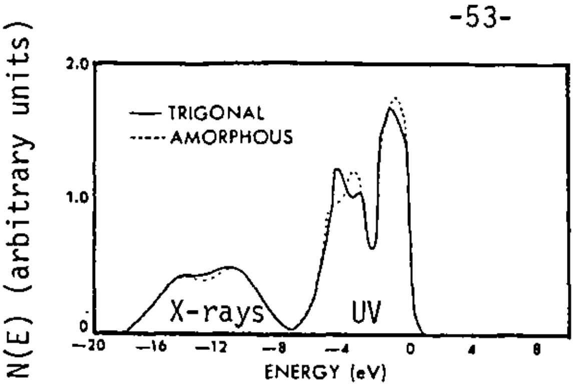

Fig. 2.16: Density of Valence States (DOVS), N(E) vs energy for amorphous and trigonal selenium from XPS and UPS measurements (Shevchik et al 1973).

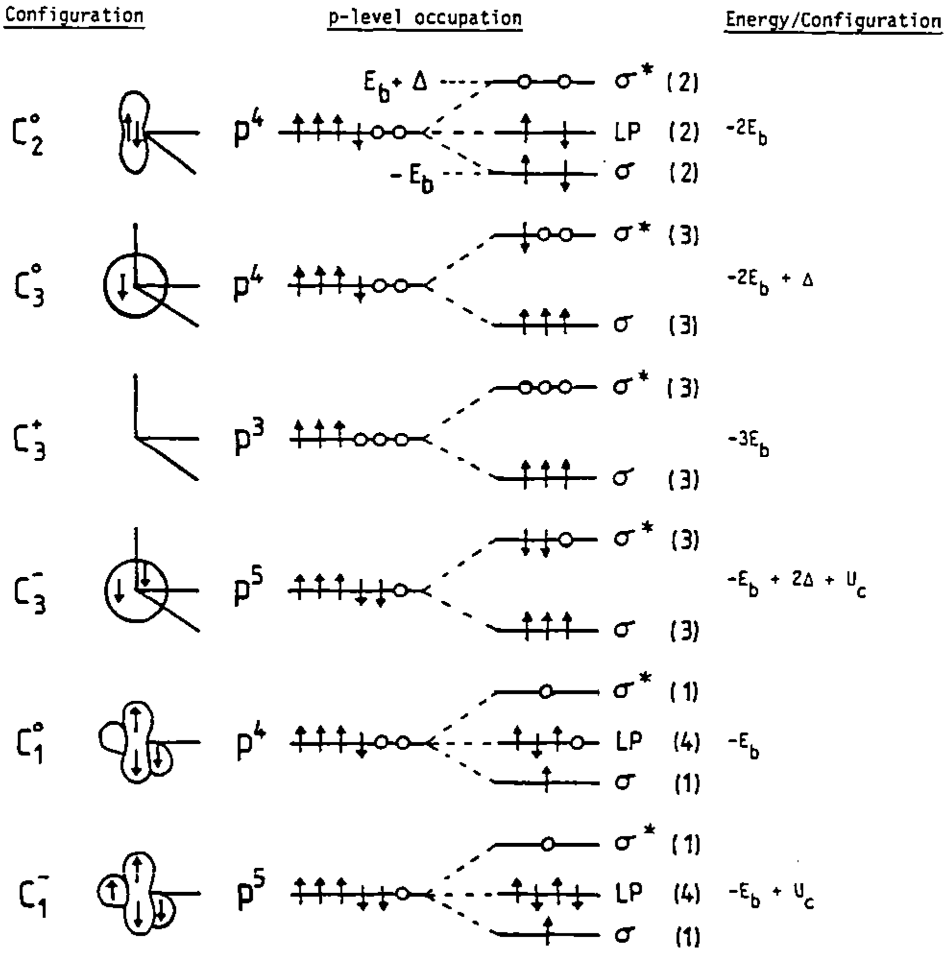

Fig. 2.17: Structure and energy of simple bonding configurations for chalcogen atoms in covalent amorphous semiconductors. Straight lines represent bonding (σ) orbitals, lobes represent the lone-pair (LP) orbitals and large circles represent the antibonding (σ^*) orbitals. Arrows represent electrons with spin, at left on atom (or ion) or at right in bonding configuration. Energies are given using LP energy as zero. (From Kastner et al 1976).

It is also possible for a Se atom to be over and under coordinated giving rise to defect centres in structure. Kastner,Adler and Frizsche 1976, Kastner 1977, 1978 studied the bonding energetics of a chalogen atom, like Se, in different coordination environments. Fig. 2.17 shows their proposed bonding configuration-energy relationships, where σ and σ^* represent the bonding and antibonding states and LP the non-bondong lone-pair states. The energy of the latter states are assigned zero for reference. The σ^* states constitute the conduction band CB of the solid, whereas the LP states comprise the upper valence band VB (Kastner 1972). The energy of an electron on a σ-orbital is $-E_b$, and that on a σ^*-orbital $E_b + \Delta$ where, from classical bonding theory, we expect $\Delta > 0$. U_c represents the 'true' electronic correlation energy which may be defined as the difference between the electron energy of the one-electron and two-electron states at identical distortional configurations. Note that in the notation of Fig. 2.17, C stands for chalcogen, the superscript for the net charge and the subscript for the coordination of the centre.

The lowest energy configuration C_2° is the ordinary neutral two-fold coordinated chalcogen atom with energy of $-2E_b$. According to Kastner et al, the lowest energy neutral defect possible is C_3°. Two C_3° centres, however, can convert to two charged defect centres C_3^+ and C_1^- because the reaction

$$2C_3^\circ \rightarrow C_3^+ + C_1^- \qquad (2.3)$$

is exothermic by an amount : $-\Delta H = -U_c(LP) + 2\Delta + M + W$, where the $-U_c + 2\Delta$ term is apparent from Fig. 2.17, M is the Coulomb attraction energy of the oppositely charged defects and W the energy change resulting from atomic (lattice) relaxations accompanying this reaction. W is polaronic in origin and is believed to be sufficiently negative (Street and Mott 1975; but note that their neutral defect is not C_3° but C_1°) for all defects to be C_3^+ and C_1^- type.When C_3^+ and C_1^- centres are created from ordinary C_2^0 centres, the valency is altered from the normal two to three and one respectively. These centres have, therefore, been called valence alternation pairs (VAP's). If two centres are close in proximity they are called an intimate valence alternation pair (IVAP). Distant pairs, which have M ≅ 0, are called non-intimate valence alternation pairs (NVAP's). Neither C_3^+ nor C_1^- have unpaired spins, whereas the neutral defects C_3° and C_1° are spin-active.

Consider the electronic behaviour of these defects. A C_3^+ can capture an electron from the conduction (σ^*) band and convert to C_3°. The inverse process

$$C_3^\circ \rightarrow C_3^+ + e^- \tag{2.4}$$

needs a certain thermal ionization energy, say W_2. C_1^- centre can capture a hole to convert to the neutral dangling bond C_1° which is a free radical. It most likely lowers its energy by shifting slightly towards a lone-pair orbital of a neighbouring C_2°. The new configuration is practically indistinguishable from $C_3^\circ + C_2^\circ$, as shown in Fig. 2.18 (Fritzsche 1977) thus

$$C_2^\circ + C_1^\circ \rightarrow C_3^\circ + C_2^\circ \tag{2.5}$$

Although energy is gained by the creation of a new bond this is partially compensated by the electron entering a σ^* state. It can be seen that VAP centres can interconvert into each other. Furthermore, the interconversion may involve different neighbours which leads to the possibility of a motion of a centre by bond switching.

C_3° can either release a hole into the valence band with a thermal ionization energy W_1,

$$C_3^\circ \rightarrow C_1^- + h^+ \tag{2.6}$$

or an electron to the conduction band CB via the process (2.4). The amphoteric character of C_3° with the thermal donor level, B, at W_2 and thermal acceptor level, B', at W_1 is shown in the energy level diagram of 2.19. Because of the polaronic nature of the reactions (2.4) and (2.6), B and B' levels refer to thermal transitions of the C_3° centre as distinct from optical transitions which obey the Frank-Condon principle. When C_3° is involved in an optical transition as a result of which C_3° loses an electron, then the process is described by the level C. If C_3° gains an electron through an optical transition,

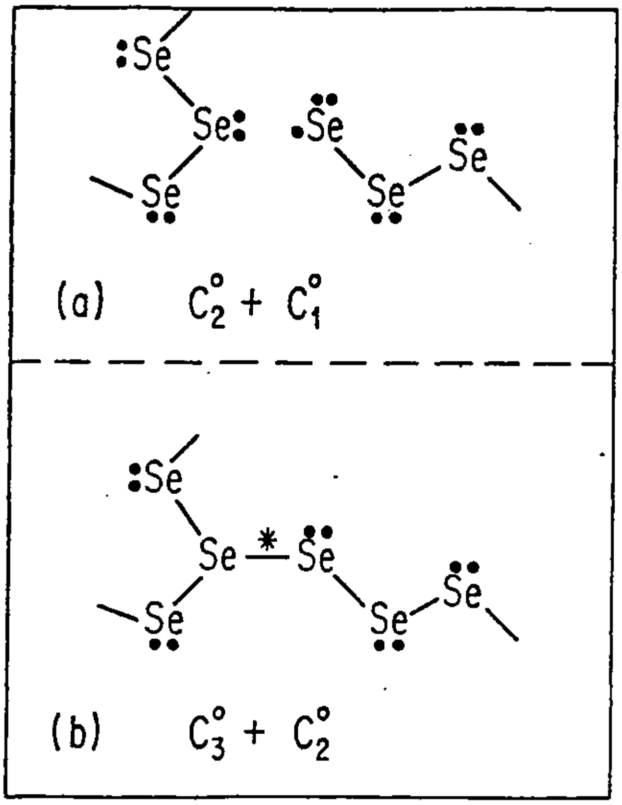

Fig. 2.18: Configuration of (a) a neutral dangling bond C_1^0 next to a two-fold chalcogen (Se) and (b) a neutral three-fold chalcogen bonded to two-fold chalcogens. Line (-) respresents a covalent bond, dot (•) a non-bonding p-electron and (*) an electron in an antibonding state (From Fritzsche 1977).

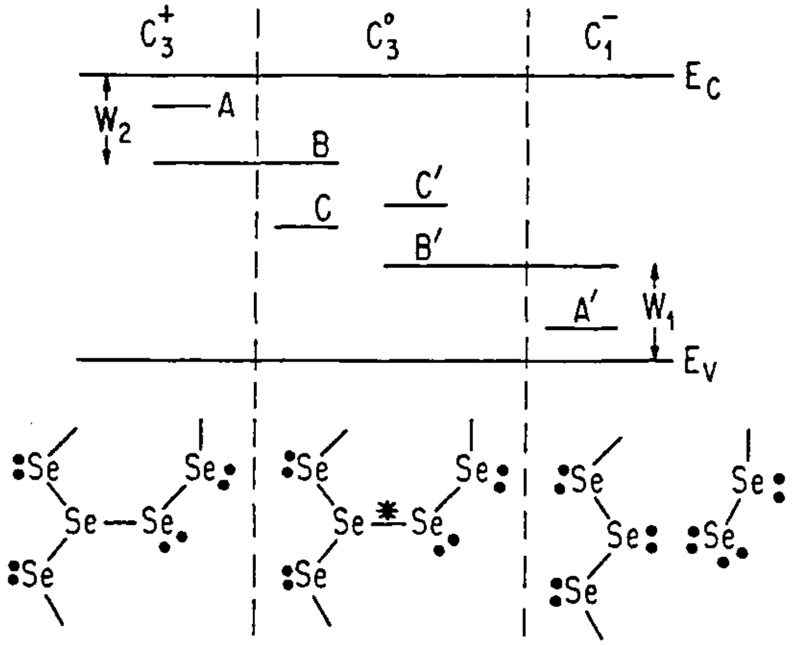

Fig. 2.19: Energy levels associated with the C_3^+, C_3^0 and C_1^- defect centres. Levels A, C, A' and C' correspond to optical transitions at fixed atomic configurations noted at the top. B and B' are the thermal transition levels. (From Fritzsche 1977).

the level C' is of interest which is positioned higher than C since the electron must enter a σ^* state. The latter transition however yields a C_1^- centre.

The energy levels pertaining to the C_3^+ defect and the C_1^- dangling bond are shown as shallow donor and acceptor levels A and A' respectively (Street and Mott 1975) in Fig. 2.19. The level A represents the energy of an optical excitation of an electron from the valence band VB to C_3^+ or of an electron capture by C_3^+ from the CB. Level A' describes an optical transition from C_1^- to the CB or a hole capture by C_1^- from the VB.

It can be seen that, due to lattice distortions accompanying the defect interconventions, it has not been possible to assign a single energy to a localized state. In particular, the energies of thermal and optical transitions differ by a polaron energy.

The VAP density is governed by the mass action law. Thus (Kastner 1978)

$$[C_3^+]\ [C_1^-] \ = \ N_o^2 \exp - \frac{G_{VAP}}{kT_g} \qquad (2.7)$$

where N_o = density of atoms ($\approx 3.3 \times 10^{22}$ cm^{-3} for a-Se); G_{VAP} = Gibbs' free energy required to create a VAP which is either $G_{IVAP} = U_c$ - W-M for IVAP's or $G_{NVAP} = U_c$ - W-M-TΔS for NVAP's. ΔS is the increase in the entropy when NVAP's are formed from IVAP's as a result of diffusion. T_g appears in the formula because this is the temperature region in which the defects are expected to be frozen-in. It is difficult to ascertain whether IVAP or NVAP free energy is lower. Typical VAP densities estimated for Se are $\gtrsim 10^{16}$ cm^{-3}

The VAP centres have been shown to be effective in determining the Fermi energy, E_F, provided the density of states due to these defects is greater than that due to any other kind (Mott, Davis and Street 1975, Adler and Yoffa 1976,1977). Consider the average energy needed to excite electrons into the CB. The first electron ionized from C_1^- costs work $E_g - W_1$ (see Fig. 2.19), i.e.

$$C_1^- \rightarrow C_3^o + e^- \ ; \ E_g - W_1 \qquad (2.8)$$

The second electron is removed from C_3° thus created and so it needs less work, W_2. The process is in (2.4). The total energy $2\varepsilon_n$ for thermally exciting two electrons via $C_1^- \rightarrow C_3^+ + 2e^-$ is therefore $2\varepsilon_n = E_g - W_1 + W_2$. This places the Fermi level

$$E_C - E_F = \frac{1}{2}(E_g - W_1 - W_2) \qquad (2.9)$$

below the mobility edge E_C. E_F is expected to lie near the mid-gap and pinned, i.e. relatively insensitive to impurities etc. Fritzsche 1977 calculates that, to effect a shift of kT in E_F, the number of electrons that must be added is about 75% of the number of VAP centres.

Experimental evidence for these charged defect centres in chalcogenides comes from several different sources. For a-Se we consider some of these.

Agarwal 1973 detected no ESR signal from very pure vitreous Se samples and chalcogenide glasses at room temperature or at 77K. Heat treatment with fast and slow cooling had no effect, although a weak ESR signal was obtainable when impurities (hydrocarbons) were introduced. These results are expected if the defect centres have paired spins, i.e. are C_3^+ and C_1^-.

Bishop Strom and Taylor (henceforth BST) 1975, 1976 showed that although no ESR signal is present in the cold-dark (unirradiated) state, ESR absorption can, however, be induced by optical irradiation corresponding to the Urbach tail ($\alpha \sim 100\ \mathrm{cm}^{-1}$). The identity of the induced paramagnetic metastable states, whether C_3° or C_1° or other, is still unresolved (see BST 1979).

The photoluminescence (PL) spectra of glassy Se and chalcogenide glasses show a considerable Stokes shift. For glassy Se the PL excitation (PLE) peak is located slightly below the band gap energy but the two PL spectra are at energies half the band gap or less (at $\simeq 0.8$ eV and 0.57 eV, BST 1979) and are present at different temperatures (4.2K and 77K). In principle, the observed Stokes shift can be interpreted in terms of the charged defect centres (Street and Mott 1975). The PLE spectrum is due to an exciton absorption near a charged defect, C_3^+ or C_1^-, followed by a photoluminescing electron capture of the resulting 'relaxed' neutral defect (probably C_3°) and thus involving levels C' or C respectively in Fig. 2.19. There are several aspects of PL spectra concerning the fatigue, effect of impurities (oxygen), temperature dependence (two separate peaks at 4.2K and ~77K) which require much work in this field (see BST 1979), Kastner 1978 suggests that IVAP's may play a more central role in luminescence phenomena.

Abkowitz et al (1977, 1980) as mentioned in §2.3, reported considerable dipolar activity in a-Se near T_g. The Debye loss and the dielectric increment observed could be attributed to dipoles arising from IVAP's but their density calculations required $5 \times 10^{18} - 10^{21}$ cm^{-3} IVAP's depending on their separation, effective charge, screening etc. However the dielectric loss could also be interpreted using the dynamic charge model, i.e. phonon induced dipole moments.

Other experiments, e.g. effects of impurities on the d.c. conductivity, drift mobility measurements have also been interpreted using the charged defects model . For example Mott and Davis 1979 propose that addition of $C\ell$ reduces the C_1^- (D^-) centres making selenium n-type (Twaddel et al 1972). Adler and Yoffa 1977, on optical absorption in chalcogenides, suggest that the existence of a large density of positively and negatively charged centres would set up sufficiently strong internal fields to account for the Urbach tail of the absorption coefficient†. It can be seen that the charged defects discussed above play a central role in understanding many of the properties of chalcogenides.

---

†In a number of crystalline solids, e.g. alkali-halides, CdS, and trigonal selenium, and in many a-semiconductors, e.g. Se, Te, As_2Te_3, As_2S_3, the absorption edge has an exponential behaviour with the photon energy. The absorption coefficient α obeys the empirical relationalship (Urbach's rule)

$$\alpha \sim \exp[-\gamma'(E_0-\hbar\omega)/kT]$$

where γ' is a constant. The explanations for this behaviour have, in general, incorporated the presence of electric fields (see reviews by Davis 1973, Mott and Davis 1979, Ch. 6 and references therein).

§2.5 ELECTRICAL PROPERTIES

2.5.1 Crystalline and Liquid Se

It is instructive to summarize the electrical properties[†] of the crystalline and liquid states of selenium for comparative purposes before discussing charge transport in a-Se. Table T2.2 shows some drift mobility data on these phases taken from various types of experiments. Fig. 2.20 shows the temperature dependence of drift mobilities determined in crystalline, amorphous and liquid phases.

(i) Trigonal Se

(1) Thermoelectric power measurements (Plessner 1951) show that trigonal Se is essentially p-type. Moreover, the hole concentration, $p_0 \sim 10^{14}$ cm^{-3}, is relatively independent of temperature down to 100K and unaffected by small amounts of impurities.

(2) The I-V characteristics are ohmic at low voltages up to about 10^3 V cm^{-1}, which depends on temperature. At high fields, I-V characteristics become superohmic, $I \sim \frac{V^2}{L^2}$.

(3) The d.c. conductivity, σ, along the c-axis is larger than $\sigma_\perp$, perpendicular to the c-axis. The ratio $\sigma/\sigma_\perp = 3\text{-}4$ is independent of temperature. The conductivity σ is thermally activated with an activation energy $E_\sigma \approx 0.20$ eV at $T \gtrsim 270$K. At room temperature σ is in the range 10^{-6} to 10^{-4} Ω^{-1} cm^{-1} and relatively insensitive to small quantities of impurities.

(4) The Hall mobility μ_H (≈ 0.14 cm^2 V^{-1} s^{-1} at room temperature) is thermally activated with an activation energy $E_{\mu H} \approx E_\sigma$. Note, however, that μ_H represents the quantity $R_H\sigma$ where R_H is the Hall coefficient.

[†] Taken mainly from Stuke 1974 and others mentioned in the text and T2.2.

Table T2.2: Summary of Drift Mobility Measurements on Crystalline and Liquid Phases of Selenium

Se Phase	μ(at T ≈ 298K)		Temperature dependence	Method	Reference
	holes $[cm^2\ V^{-1}\ s^{-1}]$	electrons $[cm^2\ V^{-1}\ s^{-1}]$			
Trigonal	$\mu \approx 28$	?	$\sim T^{-3/2}; T \gtrsim 200K$	Magnetoconductance	Mell and Stuke 1967
	$\mu_{\perp} \approx 8$	?			
Trigonal	$\mu \approx 26$	?	$\sim T^{-3/2}; T \gtrsim 250K$	Acoustoelectric current	Mort 1967
	$\mu_{\perp} \approx 7$				
Trigonal	$\mu_{\perp} \approx 10$	?	$\sim \exp(-\frac{0.16eV}{kT})$	SCLC	Champness & McLaughlin 1971
Monoclinic		$\mu \approx 2$ $\perp$ to (101)	$\left\{ \begin{array}{l} \sim T^{-3/2};\ T \gtrsim 244K \\ \sim \exp(-\frac{0.25eV}{kT})\ ;\ T \lesssim 244K \end{array} \right.$	TOF	Spear 1961
Monoclinic	$\mu \approx 0.2$ $\perp$ to (101)		$\sim \exp(-\frac{0.23eV}{kT})\ ;\ T \lesssim 320K$	TOF	Caywood & Mead 1970
Liquid	$\sim 7 \times 10^{-3}$	?	$140 \exp(-\frac{0.42eV}{kT})$	TOF	Vengris et al 1972

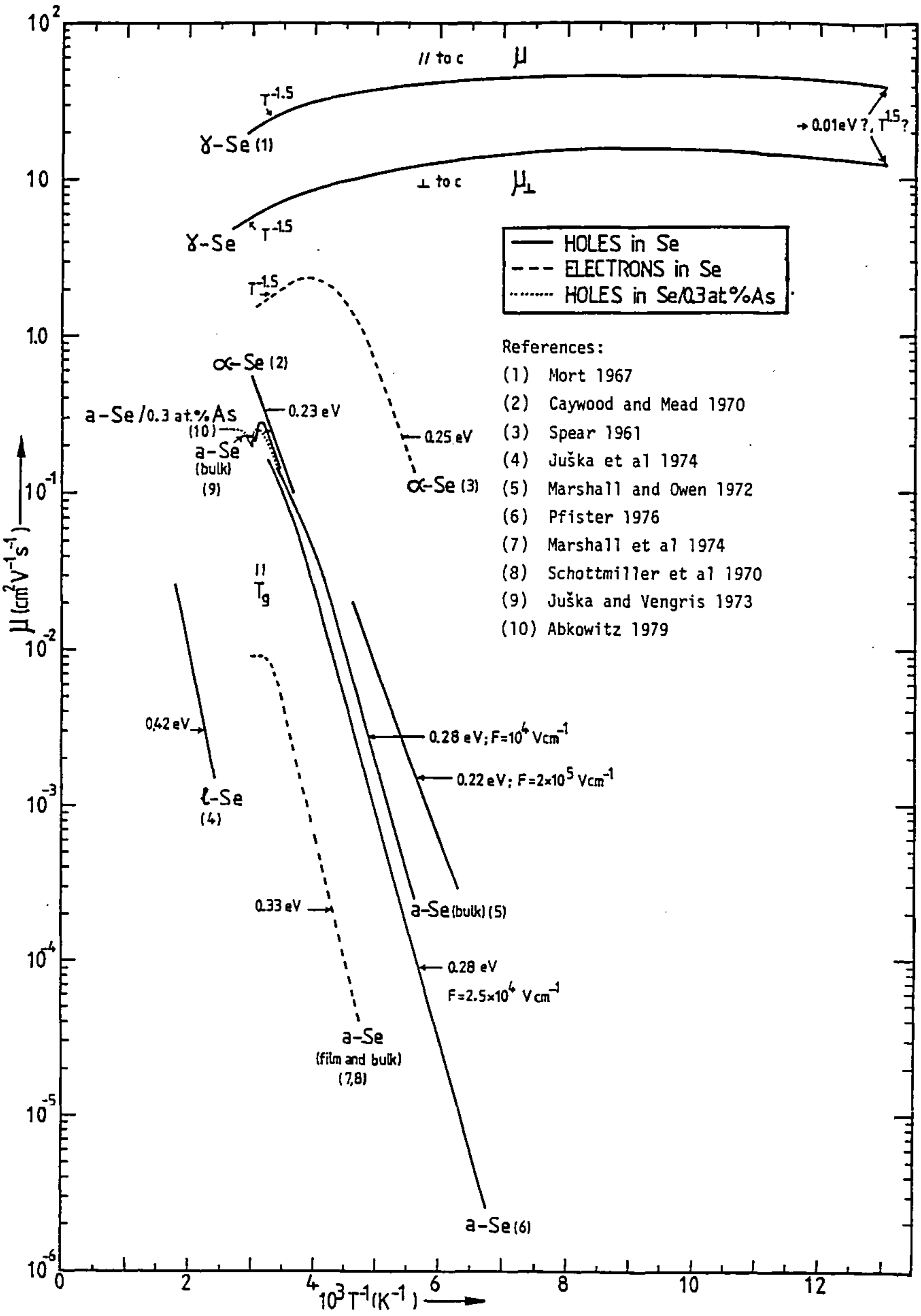

Fig. 2.20: Temperature dependence of drift mobility for holes and electrons in different phases of Se

(5) Magnetoconductance and acoustoelectric current measurements indicate that above $T \gtrsim 250K$, the hole drift mobilities along and perpendicular to the c-axis, μ and $\mu_\perp$ respectively, are limited by lattice scattering, i.e. follow a $T^{-3/2}$ dependence. The ratio $\mu/\mu_\perp \approx 3.5$ is relatively insensitive to temperature. μ has been reported to be independent of pressure up to about 5 kbar (Dolezalek and Spear 1970).

The conduction mechanism is believed to be determined by a distribution of potential barriers in the crystal (Stuke 1969, Lemercier 1971a,b). In this barrier model, the crystal contains a network of thin depeletion layers in which the hole density p is much smaller than p_0 in the 'main' crystal. These depletion regions may arise from local donor-acceptor compensation but their exact nature and origin is still unresolved. To account for the experiments, the model requires the barrier thicknesses to be 0.1-1 μm. They have been correlated with lattice defects (probably dislocations).

(ii) α-Monoclinic Se

(1) Dark conductivity at room temperature is in the range 10^{-10}-10^{-9} Ω^{-1} cm^{-1}.

(2) TOF experiments indicate that at low temperatures ($T \lesssim 273K$) electron drift mobility is thermally activated,probably due to shallow traps of density $\sim 10^{14}$ cm^{-3} at about ≈ 0.25 eV below the conduction band. At high temperatures ($\gtrsim 273K$) the mobility is limited by lattice scattering, $\mu \sim T^{-3/2}$, its room temperature value being ~2 cm^2 V^{-1} s^{-1}.

The hole mobility seems to be thermally activated over the measured range $T \approx 275$ - 323K. Its room temperature value, ≈ 0.2 cm^2 V^{-1} s^{-1}, is nearly two orders of magnitude smaller than that in the trigonal form. If shallow traps are controlling the hole transport then their density is $N_t \approx 10^{16}$ cm^{-3}.

(iii) Liquid Se

(1) Thermopower sign for pure liquid Se is probably positive (Perron 1967, Vengris et al 1972).

(2) Conductivity $\sigma = \sigma_0 \exp(-\frac{E_\sigma}{kT})$ has an activation energy $E_\sigma \approx 1.15$ for $T \lesssim 500$ K, or 1.25 for $T \gtrsim 500$K (Vollmann et al 1973).

(3) TOF experiments show a thermally activated hole drift mobility with an activation energy ≈ 0.42 eV (Juška et al 1974). At the melting point, ≈ 218°C, the mobility is $\sim 7 \times 10^{-3}$ $cm^2\ V^{-1}\ s^{-1}$.

2.5.2 D.C. Conduction

The dark d.c. resistivity of pure a-Se at room temperatures is very high ($\rho \sim 10^{14}\ \Omega$ cm). Therefore conductivity vs. temperature measurements are difficult to extend to low temperatures. The high temperature range is limited by the crystallization temperature (§2.3 and §4.7). There are, however, numerous papers on the steady-state dark I-V measurements at room temperatures and overall the number of articles published seems to be in favour of a space charge limited current (SCLC) regime†. This interpretation although widely used has never been rigorously demonstrated by testing it in the scaling formula (Lampert and Mark, 1970).

$$\frac{J}{L} = F\left(\frac{V}{L^2}\right) \qquad (2.10)$$

which for diffusion free SCLC should give a master plot for different sample thicknesses, L. F is a function specfic to the sample material. Hartke 1962 argued that Au and Te to a-Se make hole injecting contacts (i.e. ohmic) and that the resulting dark I-V characteristics at large V are space charge limited because of a uniform distribution of trapping centres, of density

---

†See for example, Hartke 1962; Lanyon 1963; Viščakas et al 1968; Carles et al 1971, 1972, 1973; Isaev et al 1975, 1976; Vautier et al 1979.

N_t, near the Fermi energy. The SCLC equation in this case[†]

$$J = 2p_0 \, e\mu \, \frac{V}{L} \exp \frac{2\varepsilon_0\varepsilon_r V}{eL^2 N_t kT} \qquad (2.11)$$

was shown to fit the experimental data over a limited range. N_t was found to be 10^{15} cm^{-3} eV^{-1} starting at about 1 eV above E_v and extending towards it.

The French group of researchers, Carles, Vautier and Viger 1972, 1973 extended the range of the applicability of the SCLC theory by modifying eqn. (2.11). They assumed that the occupation density of traps obeys

$$dp_t = \frac{dE}{1 + \frac{1}{2}\exp(E_{Fp}-E)/kT} \qquad (2.12)$$

where E_{Fp} is the quasi-Fermi level. Then applying the normal steps in Rose's simplified theory (Rose 1955) of SCLC's they found

$$J = \frac{1}{2} N_v \exp\left(-\frac{E_2-E_v}{kT}\right) \frac{e\mu V}{L} \; \frac{\exp \frac{9}{8} tV}{\exp \frac{\Delta E}{kT} - \exp \frac{9}{8} tV} \qquad (2.13)$$

where the traps are distributed between E_1 and E_2 $(E_1 > E_2)$, $\Delta E \equiv E_1 - E_2$ and $t \equiv \dfrac{\varepsilon_0\varepsilon_r}{eN_t L^2 kT}$.

Excellent fit obtained with the experimental data over a wider range# gave a trap distribution of $N_t \simeq 5 \times 10^{14}$ cm^{-3} eV^{-1}, with a width $\Delta E = 0.25$ eV starting at about $E_2 - E_v = 0.74$ eV above the valence band. It must be remarked, however, that a wider range of fit would be naturally expected when the number of variable parameters is increased.

The same group (Vautier et al 1979) were also able to interpret the dark I-V characteristics using SCLC's resulting from a Gaussian distribution of traps located at about 0.88 eV, above E_v, where the density was 7×10^{14} cm^{-3} eV^{-1}.

[†] Hartke missed the factor 2 inside and outside the exponential but this makes no difference to the argument.

#of applied voltage

Evidence against the dark currents being space charge limited comes from several sources. Pfister and Lakatos 1972 studied the I-V characteristics obtained when one or both of the electrodes to a-Se were illuminated with an intense and strongly absorbed light ($\lambda = 3990\ \mathring{A}$). They found that the steady-state photogenerated currents obey the SCLC theories, $J \sim V^2/L^3$ (Child's Law) for one carrier and $J \sim V^3/L^5$ for two carrier injection, and scale in accordance with eqn. (2.10). Their magnitude is much higher than the dark currents. At very high voltages, the photocurrents became emission limited. Clearly, to obtain SCLC's, the authors had to generate an ohmic contact which is a prerequisite condition.

Müller and Müller 1970, reported that the dark I-V characteristics of a-Se layers on Cu substrates with Au contacts are probably Schottky emission limited, i.e.

$$I = I_o \exp\left(\frac{\beta_s F^{\frac{1}{2}} - \phi}{kT} \right) \qquad (2.14)$$

with experimental β_s values within 10-20% of the expected values.

The observation of nearly ideal square transient current pulses in TOF measurements on a-Se having Au contacts (or similar, e.g. Pd) is incompatible with the interpretation or assumption of reservoir contacts in steady-state dark I-V characteristics. This paradoxial situation also exists, for example, for a-As_2Se_3. Abkowitz and Scher 1977 showed that although the Au contact to a-As_2Se_3 may give linear steady-state dark I-V properties, it cannot however be interpreted as an 'ohmic' contact. They suggest that the steady-state dark current must ultimately reflect an equilibrium between rates of carrier extraction and resupply in the interfacial region. Because the carrier extraction rate is related to the bulk transport parameters, it is not surprising to find steady-state currents reflect a dependence on these bulk parameters. A similar argument would obviously be applicable to a-Se.

It can be concluded that the reported d.c. conductivity measurements on a-Se systems do not necessarily represent the 'true' or intrinsic bulk conductivity, but probably incorporate contact effects and thus cannot be used directly to deduce bulk transport parameters. Activation energies (E_σ), determined therefore have no simple interpretation, Mehra et al 1977, 1978, 1979, for example, find the measured conductivity of Ag/a-Se/Aℓ structures to be field dependent and thermally activated with a 'zero field' activation energy of 0.84 eV. It is interesting to note that this is equal to the potential barrier ϕ_h of hole photo-emission into a-Se at the Au/a-Se interface as reported by Mort and Lakatos 1970 (Mort 1973b).

Thermoelectric power measurements (Vengris et al 1972, Juška et al 1974) indicate that a-Se exhibits predominantly p-type transport.

2.5.3 Transient Conduction[†]

Small signal TOF experiments on a-Se were first carried out by Spear 1957, 1960 and Hartke 1962 who determined the hole and electron drift mobilities from transient voltage waveforms. The TOF method, details of which will be described in §3.2, enables the motion of injected excess charges in a solid to be monitored via the external current they generate. There have been numerous TOF experiments on a-Se and some of its alloys over the last two decades. Table T2.3 and Fig. 2.20 summarize some of the drift mobility data of different scientists. Their experimental details may be found in Table T4.1 in §4.2. The hole and electron transport will be discussed separately.

Hole Transport

From T2.3 and Fig. 2.20, it can be seen that at low temperatures, $T \lesssim 250K$, the drift mobility is thermally activated with an activation energy $E_{\mu h} = 0.25 - 0.28$ eV. At high temperatures, in the neighbourhood of the glass transition region $T_g \sim 310K$ (§2.3), the mobility seems to saturate (Grunwald and Blakney 1968, Pai 1974). More detailed analysis of the mobility

---

[†] See reviews by Owen and Spear 1976, Enck and Pfister 1976 and Pfister and Scher 1977, Owen and Marshall 1977, Pfister 1979 and references therein. Detailed theory is given in ch. 3.

Table T2.3: a-Se Hole and Electron Drift Mobility Data of Different Researchers

	Holes		Electrons			
Preparation	μ_h (≈298K) $[cm^2 V^{-1} s^{-1}]$	$E_{\mu h}$ [eV]	μ_e (≈298K) $[cm^2 V^{-1} s^{-1}]$	$E_{\mu e}$ [eV]	Ref.	Notes
Evaporated	≈0.14	≈0.16	$(4.7-5.5) \times 10^{-3}$	0.25	1	40 > T > - 30°C
Evaporated	0.13-0.14	0.14			2	50 > T > - 70°C
Evaporated	0.165	0.14	7.8×10^{-3}	0.285	3	25 > T > -50°C
Evaporated	0.12	0.13	6.5×10^{-3}	0.29	4	300 > T > 250K; At top contact
Evaporated	0.11-0.12	0.20-0.247	$(4.5-5.8) \times 10^{-3}$	0.285-0.332	5	$E_{\mu h}$ and $E_{\mu e}$ depend on substrate temperature; μ_h and μ_e both saturate at high T; Lowest T ≈ -65°C
Bulk	≈0.19	0.30			6	T = 330K to 200K; μ_h saturates at high T
Evaporated	0.13-0.17	0.23			7	T = 35 to -130°C; Below -70°C $\mu_h \sim F^n$, and $E_{\mu h}$ is also field dependent
Evaporated	0.16	0.26	5×10^{-3}	0.32	8	T ≈ 330K to 230K. No pressure dependence up to 4.2 kbar
Evaporated	0.14	0.16	6×10^{-3}	0.33	9	Fig. 2.26a
Evaporated	0.14	0.095(a) 0.0093(b)	6×10^{-3}	0.27 (T > 260K)	10	TSCLC† (electron beam excitation) (a) T > 167K, (b) T < 167K
Bulk	≈0.11	0.28	$\approx 6 \times 10^{-3}$	0.33	11	300 > T > 167K; μ_h and $\mu_e \sim \exp[\frac{eaF}{kT}]$
Evaporated			6×10^{-3} (c) $(5.3-8) \times 10^{-3}$(d)		12	TSCLC† (c) from t_T, (d) from maximum current vs voltage (Many and Rakavy 1962)
Evaporated	0.16	0.20-0.28			13	65 > T > -10°C; μ_h-T shows hysteresis, μ_h saturates above T_g
Evaporated	0.16	0.24	$\approx 6 \times 10^{-3}$	0.28(e) 0.45(f)	14	(e) 294 > T > 260K; (f) 260 > T > 208K μ_h and $\mu_e \sim F^n$
Evaporated	0.18	0.27 at $F = 10^5 V cm^{-1}$			15	297 > T > 123K; $E_{\mu h}$ depends on F At low F, $E_{\mu h}$ ≈ 0.28 eV. Below 250K $E_{\mu h}$ is independent of T
Evaporated	0.15	0.10	3×10^{-3}	0.29	16	298 ≥ T ≥ 250K

†Transient Space Charge Limited Current Technique (see Many and Rakavy 1962, Baru and Temnitskii 1972). References [1] Spear 1957; [2] Spear 1960; [3] Hartke 1962; [4] Kolomiets and Lebedev 1966; [5] Grunwald and Blakney 1968; [6] Juška et al 1969; [7] Tabak 1970; [8] Dolezalek and Spear 1970; [9] Schottmiller et al 1970; [10] Rossiter and Warfield 1971; [11] Marshall and Owen 1972 for hole transport; Marshall et al 1974 for electron transport; [12] Kolomiets and Lebedev 1973; [13] Juška et al 1973, 1974; [14] Pai 1974; [15] Pfister 1976; [16] Takahashi 1979.

behaviour with increasing temperature (Juška and Vengris 1973, Abkowitz and Pai 1978 Abkowitz 1979) has shown that the drift mobility undergoes a sharp drop in the T_g region before reaching its saturated value, 0.2 - 0.3 $cm^2\ V^{-1}\ s^{-1}$, above T_g (Fig. 2.20).

Spear, Hartke and others (e.g. Grunwald and Blakney 1968) proposed a shallow trap controlled transport mechanism to explain the thermally activated mobility. The carrier transport essentially occurs in the extended states with frequent interruption by trapping in levels energetically close to the transport state (see §3.3). If N_t is the density of these traps which are all at E_t above the valence band VB then the effective drift mobility would be (Rose 1951, Spear 1969)

$$\mu = \mu_o [1 + \frac{N_t}{N_v} \exp \frac{E_t}{kT}]^{-1} \qquad (2.15)$$

where μ_o is the microscopic mobility and N_v the density of states at the VB edge. This equation at sufficiently low temperatures approximates to

$$\mu \cong \mu_o \frac{N_t}{N_v} \exp(- \frac{E_t}{kT}) \quad ; \quad kT \ll E_t \qquad (2.16)$$

To account for the saturation of the mobility, Grunwald and Blakney 1968 suggested that at high temperatures μ_o is limited by lattice scattering. Using $\mu_o = AT^{-3/2}$ and $N_v = BT^{3/2}$ in eqn. (2.15) they found a good fit between

$$\mu = AT^{-3/2} [1 + N_t B^{-1} T^{-3/2} \exp \frac{E_t}{kT}]^{-1} \qquad (2.17)$$

and the experimental data over the whole temperature range accessed. The best fit values at room temperature were $\mu_{oh} \simeq 0.34\ cm^2\ V^{-1}\ s^{-1}$ and $\frac{N_{th}}{N_v} = 10^{-4} - 7 \times 10^{-4}$. The latter quantity depended on the substrate temperature of the samples during preparation. Using the same equation, (2.17), Abkowitz and Pai 1978 found the room temperature microscopic mobility to be 0.44 $cm^2\ V^{-1}\ s^{-1}$. These estimates for a lattice limited mobility, $\mu_{oh} \approx 0.4\ cm^2\ V^{-1} s^{-1}$, seem to be in good agreement with the dark hole Hall mobility

$\mu_{Hh} \approx 0.37\ cm^2\ V^{-1}\ s^{-1}$ determined by Juška et al 1969. As pointed out by Owen and Spear 1976, however, $\mu_{oh} \sim 0.4\ cm^2\ V^{-2}\ s^{-1}$ is probably too low to be consistent with lattice scattering. In §5.2 various transport mechanisms for μ_o in eqn. (2.14) are investigated.

Another possible conduction mechanism which evinces a thermally activated mobility is hopping transport, described by eqn.(1.12). The pre-exponential factor found in the thermally activated mobility of a-Se is $\gtrsim 10^3\ cm^2\ V^{-1}\ s^{-1}$; several orders of magnitude higher than that typically expected in hopping transport (§1.1.2). Furthermore, Dolezalek and Spear 1970 found that down to temperatures ∿230K, both the hole and electron drift mobility in a-Se were independent of pressure up to 4.2 kbar. Therefore, hopping transport is not expected to contribute to the observed mobility.

Above T ≈ 250K, the transient photocurrents display no apparent dispersion (Pfister 1976, see also Noolandi 1977a). Typical transient currents observed at T = 250K and 188K are shown in Fig. 2.21a and b. At room temperatures the current transients at high fields become nearly ideal square pulses. At low fields, however, when the transit times are long and comparable to any deep trapping time τ then the transient currents have an exponential decay as in Fig. 2.21c. The time constant of the exponential TOF signal is the hole lifetime or deep trapping time τ_h (Tabak and Warter 1968, Tabak and Hillegas 1972, Tabak et al 1973, Herms et al 1974) which in combination with the drift mobility μ determines the xerographically important parameter Schubweg, s, defined by

$$s = \mu\tau F$$

This is the distance a charge carrier travels before being trapped. If s is comparable to or less than the sample thickness L then a considerable number of the injected excess carriers will be trapped. In a xerographic process, this may lead to an unacceptably high residual voltage in the photoreceptor (see Warter 1969). The hole lifetime has been found to depend

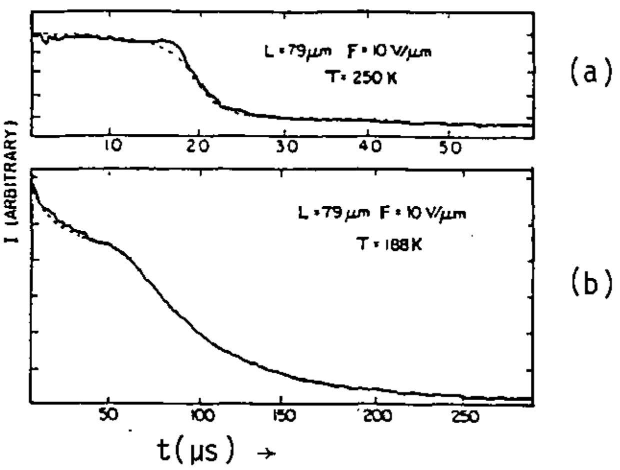

Hole photocurrent transients for a-Se at two different temperatures (a) T = 250K and (b) T = 180K. The dashed line is the multiple trapping model of Noolandi. (From Noolandi 1977a)

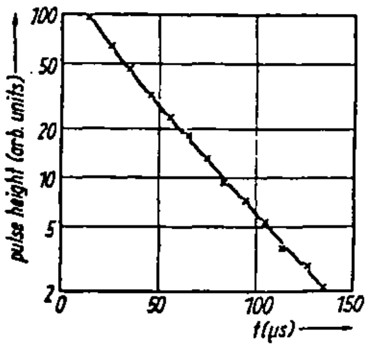

(c) Semilogarithmic representation of a hole transient photocurrent for a-Se at T = 313K. (From Herms et al. 1974).

Fig. 2.21 : Hole photocurrent transients for a-Se from TOF experiments

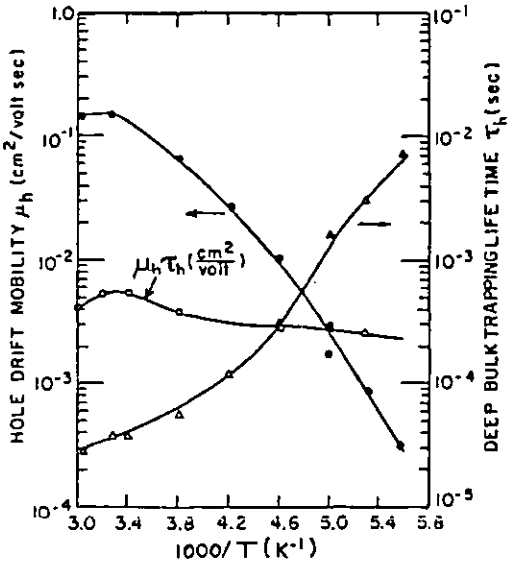

Fig. 2.22: Temperature dependence of the hole drift mobility μ_h, deep trapping time τ_h and range $\mu_h\tau_h$ for a-Se. (From Pai 1974).

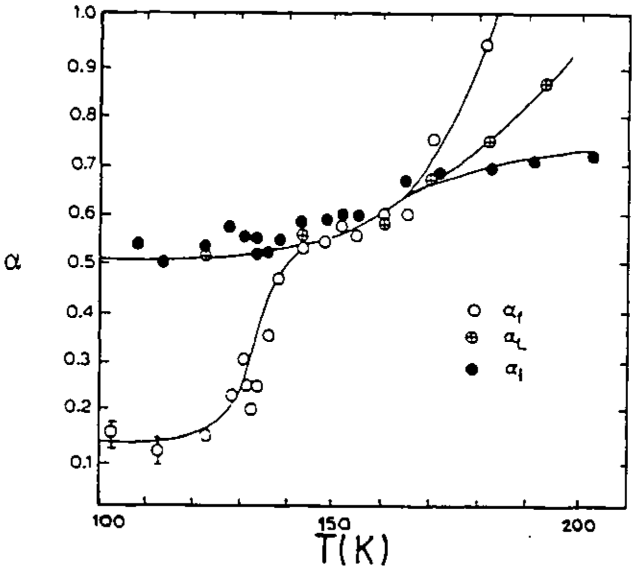

Fig. 2.23: Temperature dependence of parameter α for hole transport in a-Se determined from thickness dependence of transit time, α_L, initial and final part of current trace α_i and α_f respectively. (From Pfister and Scher 1978).

on the preparation conditions, e.g. substrate temperature (Kalade et al 1972) 'origin' of the selenium and impurities (Tabak 1971, Tabak and Hillegas 1972). Table T2.4 summarizes some lifetime data from various sources. It can be seen that there is a considerable variation in the lifetime values (from $\tau < 0.25$ to ~ 50 μs for 99.999% pure Se).

As the temperature is decreased, the lifetime increases in such a manner that the range $r \equiv \mu\tau$ seems to be relatively temperature insensitive (Pai 1974) as shown in Fig. 2.22. This behaviour is naturally expected in diffusion limited trapping process inasmuch as the factor reducing the mobility μ_0 in eqn. (2.15) then enhances the deep trapping time to an effective value[†].

$$\tau = \tau_0 \left[1 + \frac{N_t}{N_v} \exp \frac{E_t}{kT}\right] \tag{2.18}$$

where τ_0 is the lifetime in the absence of shallow traps.

At very low temperatures, below T ∿ 180K, the transient photocurrents (Fig. 2.21b) become dispersive (Pfister 1976) and can be described by the stochastic transport equations (see §3.4).

$$i(t) \sim \begin{cases} t^{-(1-\alpha_i)} & ; \quad t < t_T \quad (2.19a) \\ t^{-(1+\alpha_f)} & ; \quad t > t_T \quad (2.19b) \end{cases}$$

and

$$t_T \sim \left[\frac{L}{\ell(F)}\right]^{\frac{1}{\alpha_L}} \exp \frac{E_h}{kT} \tag{2.20}$$

Here α's are the dispersion parameters, E_h the activation energy and $\ell(F)$ the mean displacement per stochastic event. t_T represents the transit time characteristic of the leading edge of the carrier packet. Fig. 2.23 shows the temperature dependence of the dispersion parameters α_i, α_f and α_L obtained from the logi vs. log t slopes and the thickness dependence of the transit time. It can be seen that in the region 140-170K $\alpha_i \simeq \alpha_f \simeq \alpha_L \sim 0.5$ and therefore the sum of the two slopes before and after t_T in the log i vs. log t

---

[†] See eqn. (5.5), p.164.

Table T2.4: Hole and Electron Deep Trapping Lifetime Data

Material Composition	τ_h(298K) [μs]	τ_e(298K) [μs]	Reference	Sample preparation/Technique/Comment
99.99% pure Se	10-45	40-50	Tabak & Warter 1968	Evaporation onto substrates at $T_{sub} \cong 55°C$/TOF technique/
99.999% pure Se	10-50	50	Schottmiller et al 1970	Flash evaporation onto Aℓ ; T_{sub} = room temp or > T_g/TOF technique
Pure Se		10-70	Rossiter & Warfield 1971	Evaporation, $T_{sub} \cong 60°C$/TSCLC technique/τ_e decreases with F
Pure Se	≈21		Tabak & Scharfe 1970	Evaporation/Transition from Emission-Limited to Space-Charge-Limited Photoconductivity/
99.999%-99.9999% pure Se	$\tau_h < 0.25$ to 14	$\tau_e < 1$ to 44	Tabak & Hillegas 1972	Evaporation onto Aℓ; $T_{sub} \approx 50°C$/TOF/τ_h and τ_e both sensitive to the origin of Se (supplier) and impurities
Pure Se	0.3 - 50		Kalade et al 1972	Evaporation onto Aℓ; $T_{sub} \approx 20-75°C$/XTOF/ τ_h increases with T_{sub}
Pure Se	37		Pai 1974	Evaporation onto Aℓ; $T_{sub} \approx 55°C$/TOF/τ_h increases with falling T
99.995% pure Se	≈44	≈120	Herms et al 1974	Evaporation; $T_{sub} \approx 50°C$/TOF/τ_h and τ_e fall at T_g

plots gives $\approx$-2 as expected from the Scher and Montroll theory. Above $\sim$180K dispersion approaches the Gaussian case; $\alpha_i = \alpha_L = 1$ and $\alpha_f >> 1$. Below 140K, $(1 - \alpha_i) + (1 + \alpha_f)$ is smaller than the theoretical value of 2, probably due to the distortions of the current pulse caused by the space charge effects of trapped charges (see, for example, Scharfe and Tabak 1969).

There are two important conclusions from Pfister's work. (1) The transition from the Gaussian transport at high temperatures to the stochastic transport at low temperatures, $\lesssim$180K, is not accompanied by a change in the activation energy at a given applied field. (2) $\log \frac{i(t)}{i(t_T)}$ vs. $\log \frac{t}{t_T}$ plots assume universality with respect to field at low temperatures. Universality is not, however, obtained with respect to temperature.

In determining the microscopic process for the transport mechanism, the model used must encompass the above two conclusions. Noolandi 1977a showed that a multiple trapping transport model involving three isoenergetic traps, say E_t above the VB, would account for the shapes of the transient photocurrents from room temperature down to -122K. The apparent dispersion with falling temperature arises solely from the temperature dependence of the trap capture events represented by $M_i = \omega_i t_o$, where ω_i = capture rate of trap species i (i = 1,2,3), and $t_o = L/(\mu_o F)$ is the transit time of untrapped carriers. M_i is the number of times a carrier is captured by trap i alone while crossing the sample. The variations in the release rates from the traps are caused by the pre-exponential factor, i.e. attempt to escape frequency, since E_t was constant to satisfy conclusion (1) above.

Marshall 1977, on the other hand, showed that a Gaussian broadening of a discrete energy level at E_t participating in trap controlled transport would also account for the observed dispersion in a-Se transient photocurrents. Marshall finds a broadening of $\approx$0.025 eV from the centre of the distribution at $\approx$0.25 eV. The amount of broadening was associated with the thermal energy at $T_g \sim$ 310K.

Note that below T $\sim$ 250K, the drift mobility in evaporated a-Se samples has an increasingly strong field dependence, apparently, of the form $\mu \sim F^n$ (Rossiter and Warfield 1971, Tabak 1970, Pai 1974). The index n is very small at room temperatures, $n \lesssim 0.05$, (Pai 1974) and increases with decreasing temperature. For example, at $T \approx 193K$, $\mu \sim F^{0.8}$. This field dependence, however, cannot be accounted for by the stochastic nature of the transport mechanism alone†. The activation energies quoted above and in T2.3 are the 'low field' values.

Fig. 2.24 shows a semi-logarithmic plot of the hole drift mobility against applied field in bulk vitreous Se samples obtained by Marshall and Owen 1972, at various temperatures. Note the exponential dependence of μ_h on F.

Electron Transport

The electron drift mobility μ_e (T2.3 and Fig. 2.20) is also thermally activated with $E_{\mu e} \approx 0.33$ eV and abruptly saturates above T_g. There is, however, no sharp fall in μ_e in the T_g region as displayed by μ_h (Abkowitz and Pai 1978). The pre-exponential factor in the thermally activated mobility expression is $\sim 2 \times 10^3$ cm^2 V^{-1} s^{-1}. Mobilities measured in the range 238-330K are unaffected by the application of pressures up to 4.2 kbar (Dolezalek and Spear 1970). Therefore the electron transport mechanism may also be shallow trap controlled and described by eqns. (2.15) and (2.16). Grunwald and Blakney 1968, assuming $\mu_{oe} \approx 0.32$ cm^2 V^{-1} s^{-1} from photo Hall effect measurements (Dresner 1964), found $\frac{N_t}{N_c} = (1.4 - 6.4) \times 10^{-4}$ which depended on the substrate temperature T_{sub} during evaporation of a-Se. Note that both N_{th} and N_{te} depend on T_{sub} in the same fashion (T2.3) and $\frac{N_{th}}{N_v} \approx \frac{N_{te}}{N_c}$.

In the earlier experiments (e.g. Spear 1957, Hartke 1962, Grunwald and Blakney 1968) no field dependence of the electron drift mobility was

---

† For discussion excluding dispersion effects see Marshall and Miller 1973, Hill 1974 and Fox and Locklar Jr. 1972, Tabak et al 1971.

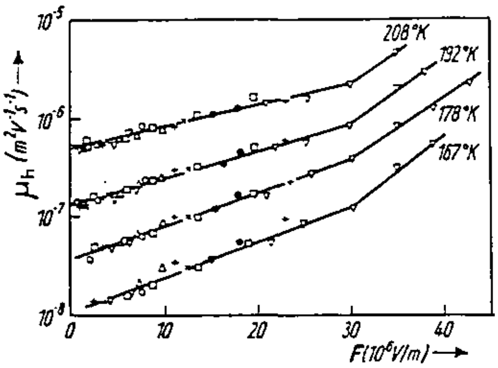

Fig. 2.24: Log μ_h vs F for bulk a-Se (Marshall and Owen 1972).

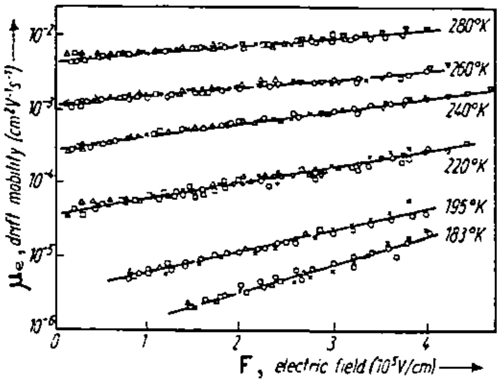

Fig. 2.25: Log μ_e vs F for bulk a-Se (Marshall et al 1974).

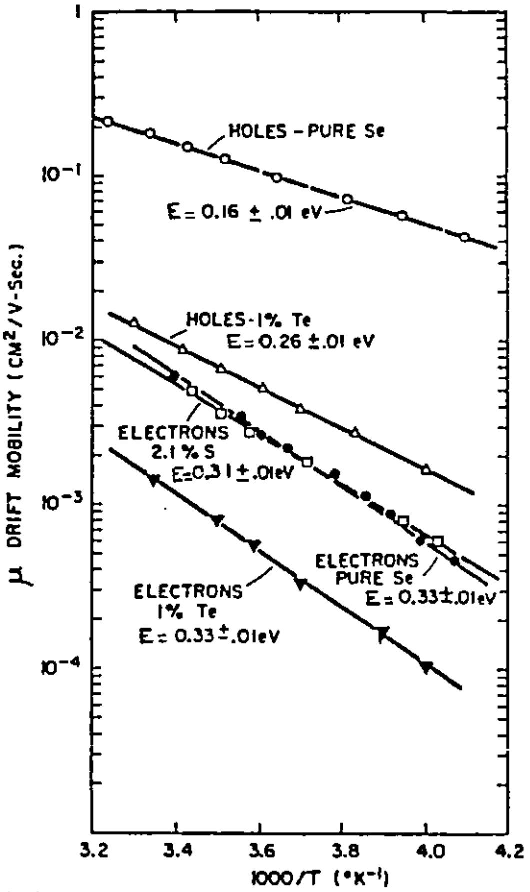

(a) Temperature dependence of drift mobility in Se, Se-Te and Se-S alloys (Schottmiller et al 1970).

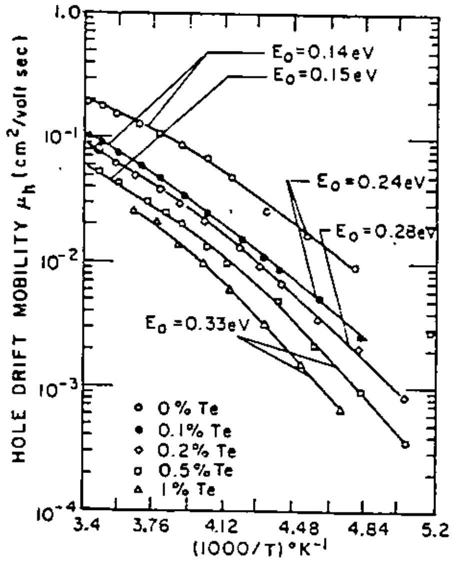

(b) Temperature dependence of hole drift mobility in Se and Se-Te alloys. Applied field F - 8 x 10^4 V cm^{-1} (Pai 1974).

Fig. 2.26: Effects of alloying Se on the temperature dependence of the drift mobility

reported. More recent experiments on evaporated films show an algebraic power dependence, $\mu_e \sim F^n$, with the exponent n increasing from ≈ 0.2 at room temperature to ≈ 0.8 at 221K (Pai 1974). At high fields, e.g. $F \gtrsim 2 \times 10^5$ V cm^{-1} at 300K, μ_e has been observed to increase rapidly with the applied field (Juška et al 1978).

Marshall et al 1974, on the other hand, have found the electron drift mobility in bulk vitreous Se, down to $\sim$183K, to obey the empirical relationship (Marshall and Miller 1973).

$$\mu_e(F) = \mu_e(0) \exp [ea(T) \frac{F}{kT}] \qquad (2.21)$$

with a(T) monotonically increasing with fall in temperature. Note that they were also able to describe the field dependence of hole drift mobility by this formula with approximately the same a(T) values (Fig. 2.24).

The shapes of the transient photocurrents have been examined only at room temperatures or $T \gtrsim 250$K (Blakney and Grunwald 1967, Tabak and Warter 1968). Blakney and Grunwald reported that the transient currents have two exponential components; fast and slow. Tabak and Warter, Scharfe and Tabak 1969, on the other hand, find single exponential signals, similar to those for hole transport at room temperatures, only for well rested samples. Apparently the fast component is generated in fatigued samples (not well rested samples) and is due to the presence of trapped holes. Note that Blakney and Grunwald did not use the 'single shot' mode of operation (see §4.2, §4.3) required to eliminate any space charge build-up. Table T2.4 shows electron lifetimes τ_e reported by various researchers.

Juška et al 1978 used the 'transient current interruption method' to determine the electron lifetime. In this technique the bias voltage present across the sample in the usual TOF experiment is switched off when the drifting packet of carriers arrives approximately at the middle of the sample, i.e. $t \approx \frac{1}{2} t_T$. After a delay time t_D the electric field is switched on again and the decrease of the current $i_2/i_1 = i(\frac{1}{2} t_T + t_D)/i(\frac{1}{2}t_T)$ is measured as a function of t_D. The slope of $\ell n(i_2/i_1)$ vs t_D then gives τ_e^{-1}. The lifetime was found to increase in an Arrhenius fashion with falling temperature down to ~263K, with an activation energy equal to that of the drift mobility.

2.5.4 Effects of Impurities

The effects of the various impurities upon the charge transport properties are conveniently grouped according to the valence of the impurity (Schottmiller et al 1970). These are (i) univalent additives (Cℓ,Tℓ), (ii) additives isoelectronic with Se (S,Te) and (iii) additives capable of introducing chain branching (P, As, Bi, Ge). Figs. 2.26 and 2.27 show the effects of some of these impurities on hole and electron transport in a-Se, taken from TOF experiments. Only those dopants used in this project will be discussed.

(i) Univalent additives (e.g. Cℓ)

The addition of small quantities (~20 ppm) of Cℓ completely annihilates the TOF electron response. Either the electron lifetime $\tau_e \lesssim 0.2$ μs or the Scubweg at 10^5 V cm^{-1} is < 1 μm. Hole transport, however, is largely unaffected (Tabak and Hillegas 1972, Schottmiller et al 1970). Some improvement in the hole range has also been reported (Tabak 1971).

(ii) Isoelectronic additives (e.g. Te)

The effect of isolectronic additives is not as drastic as that of univalent elements and relatively large concentrations, e.g. ~0.1 at.% Te or ~2.5 at.% S, are necessary to influence the transport properties in a noticeable way.

For the Se-Te alloy system (see Schottmiller 1970, Pai 1974, Tomura and Maekawa 1977, Takahashi 1979) the hole and electron drift mobilities decrease significantly with Te composition. There is no significant effect on the hole lifetime whereas the electron lifetime probably becomes very short for $\gtrsim$ 3 at.% Te. The hole mobility activation energy increases with the Te composition to a final value of 0.33 eV at about 0.5 at.%Te (Pai 1974). The electron mobility activation energy seems to be relatively unchanged up to ~2.7 at.%Te (Takahashi 1979).

(iii) Branching additives (e.g. As)

For small concentrations of As, $\lesssim 2$ at.%, the hole mobility is unaffected but the hole lifetime falls sharply with As concentration. The hole mobility activation energy remains unchanged.

The electron mobility is reduced and the electron lifetime is enhanced with As composition (up to ~9 at.%As). The electron mobility activation energy seems to increase with As concentration both in bulk (Marshall et al 1974) and evaporated (Pai 1974) samples.

Interpretations of these impurity effects are given in Ch.5 to incorporate the findings of this work as well.

§2.6 CONCLUSIONS

The structure of a-Se, whether prepared by evaporation or quenching the melt, seems to be composed almost entirely of chains which contain ring fragments. The latter sections occur where along a few of the atoms in a chain the dihedral angle alternates in sign (Fig. 2.9). Ring fragments essentially cause chain bending.

Glass transition and crystallization behaviour of a-Se portray its polymeric nature.

D.C. conduction mechanism and metal/a-Se contact behaviour is unresolved.

Transport of excess holes and electrons, as observed in a typical TOF experiment, above 200K is probably shallow trap controlled.

Motion of excess holes below ~200K may be described by stochastic transport equations. There is, however, no observable change in the drift mobility thermal activation energy in the transition from the Gaussian to the non-Gaussian transport.

Both hole and electron transport are sensitive to preparation conditions and impurities.

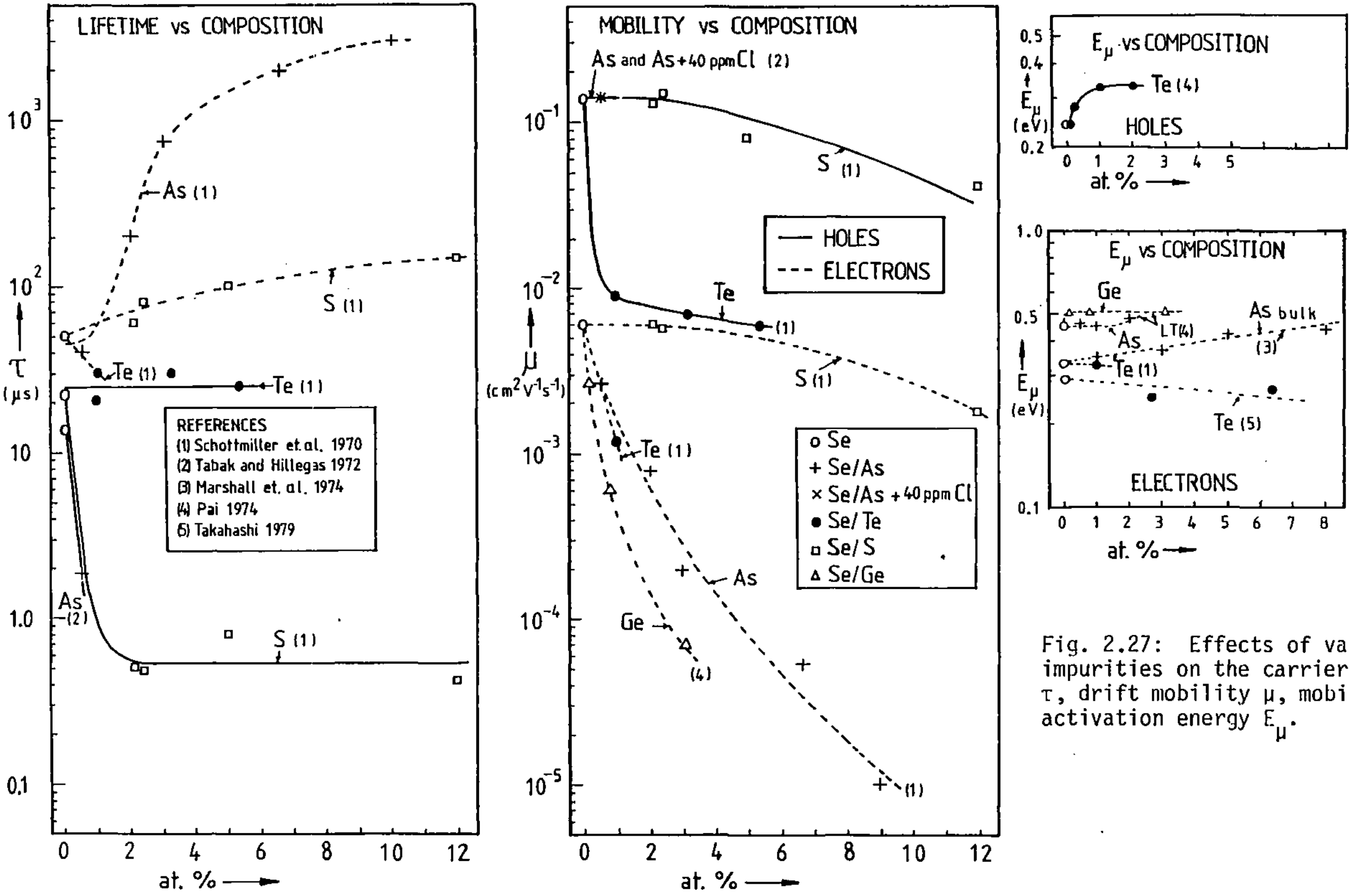

Fig. 2.27: Effects of various impurities on the carrier lifetime, τ, drift mobility μ, mobility activation energy E_μ.

CHAPTER 3

THEORY

§3.1 INTRODUCTION

In Chapter 1 the physical models and charge transport mechanisms used in studying crystalline and amorphous solids were discussed. In this chapter, the principles and theories involved in investigating and interpreting transient conduction in solids will be reviewed. D.C. experiments necessarily represent steady-state measurements whereas time of flight (TOF) and transient space charge limited current (TSCLC) techniques involve time resolving the motion of charges that are generated instantaneously or by step excitation. This transient current displays features which are a characteristic of the transport mechanism.

'Time of Flight' terminology is now widely used to describe what is essentially a drift mobility experiment. Synonymous names which also appear in scientific literature are 'Transient Charge Technique' (TCT) and 'Transient Photoconductivity'. In the next section a short background needed to understand the principles behind the TOF technique will be given. In the subsequent sections the effects of different transport mechanisms on the transient current waveforms will be discussed.

It must be remembered that strictly,the transport process which the injected excess charge in the solid undergoes may not necessarily be identical to that executed under steady-state measurements. The latter involves thermal equilibrium and thus Gaussian concepts. The transport process of the excess charge on the other hand is limited to that which occurs within the time scale of observation, i.e. $0(t_T)$, generated by the 'fastest' moving carriers. In this time range, thermal equilibrium may not have been established.

§3.2 GENERAL PRINCIPLES OF THE TOF TECHNIQUE

Fig. 3.1 shows a simplified TOF experiment to demonstrate the principles involved. An insulator or a high resistivity sample is sandwiched

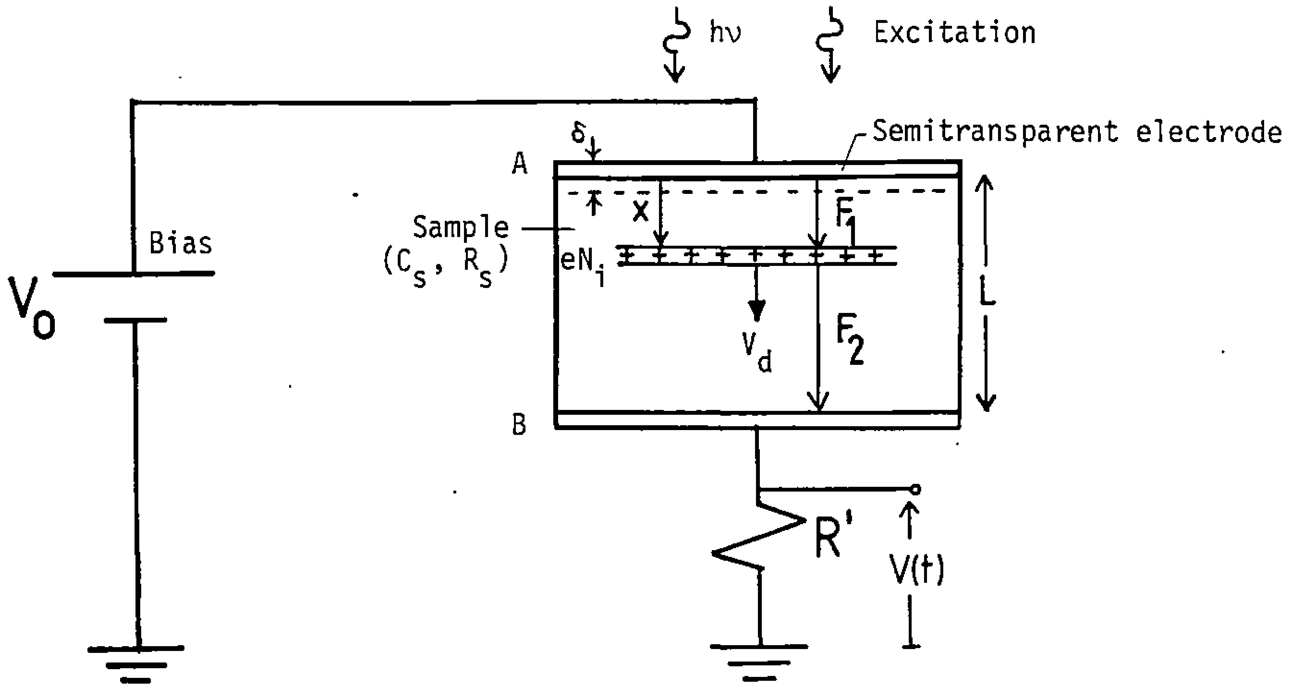

Fig. 3.1: Illustration of the principle of the TOF technique

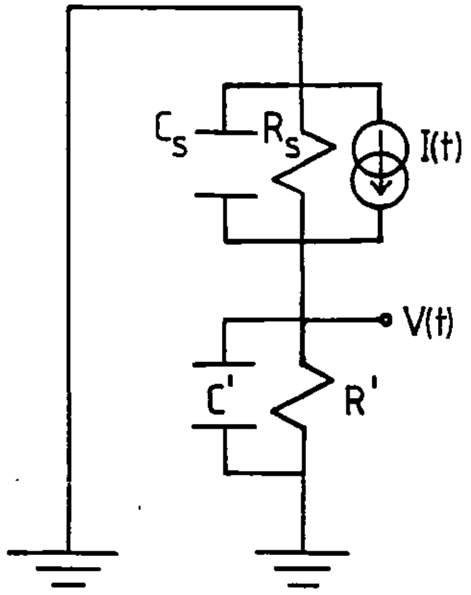

Fig. 3.2: The equivalent electric circuit

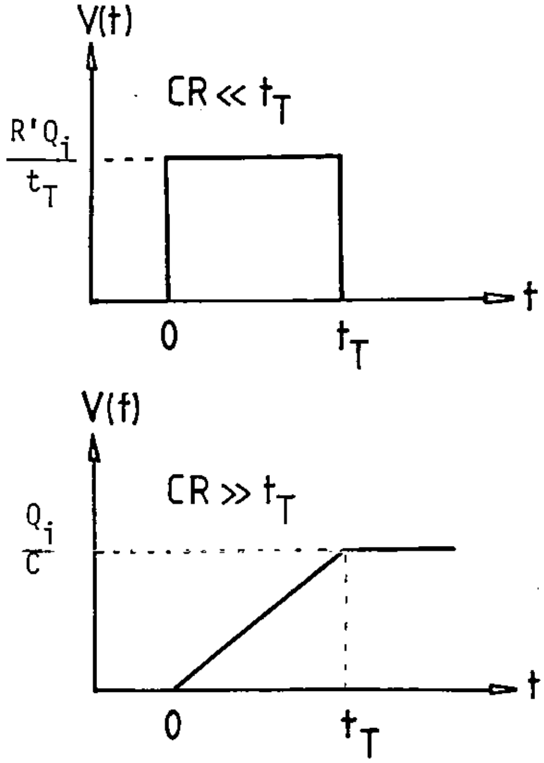

Fig. 3.3: Detected TOF signals across R'. Upper: I-mode signal. Lower: V-mode signal.

between two electrodes A and B, the former being semitransparent. At least one of the contacts is blocking so that the d.c. conduction is zero. The external resistance R' is normally much smaller than the sample resistance, R_s. Therefore, electrode B may be considered earthed whereas A is at bias V_o of the supply.

A short pulse of strongly absorbed radiation through A is used to generate a thin sheet of electron hole pairs near the surface of the sample. The wavelength of irradiation is chosen so that the absorption depth $\delta << L$, the thickness of the sample. Electrons are neutralized almost immediately by reaching the top electrode whereas holes have to traverse the thickness, L.

Let N_i be the number of carriers injected in a surface area A between $x = 0$ to $x = \delta$.

The drifting sheet of charge at position x will modify the applied field $F_o \equiv \frac{V_o}{L}$.

The fields behind and in front of the charge 'cloud' are (Spear 1969):

$$F_1(x) = F_o - \frac{eN_i}{\varepsilon_o \varepsilon_r AL}(L-x) \qquad (3.1)$$

and

$$F_2(x) = F_o + \frac{eN_i}{\varepsilon_o \varepsilon_r AL}x \qquad (3.2)$$

These equations show that the drifting carriers perturb the field within the sample. If N_i is kept sufficiently small to allow the self-field term, $\frac{eN_i}{\varepsilon_o \varepsilon_r A}$, to be negligible in comparison with F_o, i.e. $eN_i << C_s V_o$, then the internal field can be considered to be equal to the applied field $\frac{V_o}{L}$. This condition is called the 'small signal operation' and it is a widely assumed case in theoretical work on transient photocurrent analysis.

The hole charge sheet or 'cloud' moves under the action of the field F_o with a constant drift velocity $v_d = \mu_d F_o$, where μ_d is the drift mobility. The time taken for charge sheet to reach the back electrode, where it is neutralised, is called the transit time, t_T;

$$t_T = \frac{L^2}{\mu_d V_o} \tag{3.3}$$

The drifting hole 'cloud' ($t < t_T$) is equivalent to a transient current I(t) which can be considered to be generated by the charge density $eN_i/(AL)$ moving at a velocity v_d;

$$I(t) = \frac{eN_i}{L} v_d \tag{3.4}$$

i.e.

$$I(t) = \frac{Q_i}{t_T} \quad ; \quad t < t_T \tag{3.5}$$

For times $t > t_T$, this current is zero since the carrier packet would have reached the back electrode.

The current I(t) can be detected via the voltage it induces in the external circuit. The equivalent electrical circuit of the TOF experiment under small signal conditions is shown in Fig. 3.2. This circuit is applicable to signal variations only. R_s and C_s are sample resistance and capacitance and C' is any stray or additional capacitance. The Laplace transform of the voltage detected across R' is therefore

$$\tilde{V}(s) = \frac{R}{SRC+1} \tilde{I}(s) \tag{3.6}$$

where $R = R_s // R' \cong R'$ and $C = C_s + C'$.

Since I(t) = 0 for $t > t_T$, the time domain of interest lies in $0 \leq t \leq t_T$ and eqn. (3.6) has two convenient asymptotic solutions arising from (i) $CR \ll t_T$ and (ii) $CR \gg t_T$. The former condition corresponds to an I-mode mode of operation because the detected signal is proportional to I(t);

$$V(t) = RI(t) \quad ; \quad RC \ll t_T \tag{3.7}$$

The second condition, $CR \gg t_T$, corresponds to the detected signal being proportional to the integral of current;

$$V(t) = \frac{1}{C}\int_0^t I(t)\,dt \; ; \quad RC \gg t_T \tag{3.8}$$

This method of detection is called the V-mode of operation because $\frac{1}{C}\int_0^t I(t)\,dt$ is the transient voltage induced across the sample. V(t) given by eqn. (3.8) is commonly termed the transient voltage response whereas I(t) given by eqn. (3.4) is called the transient current response.

An alternative derivation of I(t) is to consider the charge induced $\Delta q(t)$ on electrode B as a result of the change ΔF in the electric field F_2 due to the motion of the charge sheet (see, for example, Spear 1969). In this case $\Delta q(t) = \frac{eN_i x}{L}$, which leads to eqn. (3.4).

It can be seen that there are essentially two ways in which the transit time of carriers across the sample can be determined. In the I-mode of operation the detected signal is proportional to a square current pulse of width t_T whereas in the V-mode of operation it is a ramp of rise time t_T. The two signals are shown in Fig. 3.3 (p.82).

In considering the motion of the charge sheet it was tacitly assumed that no carriers were lost from the sheet due to trapping. As the number of carriers N(t) in the carrier packet diminishes by trapping, the current I(t) decreases with time. Suppose that there is an isoenergetic set of deep traps which have a mean capture time, τ. The latter quantity is also called the mean free time, life time or trapping time and can usually be expressed as (e.g. Martini et al 1972);

$$\tau = \frac{1}{N_t S_t \bar{v}} \tag{3.9}$$

where N_t is the density of the traps, S_t is the capture cross-section and $\bar{v}$ is the average velocity of the carrier. Since $\frac{1}{\tau}$ represents the average probability of trapping per unit time, the number of carriers in the charge sheet is then,

$$N(t) = N_i \exp(-\frac{t}{\tau}) \tag{3.10}$$

Consequently the transient current is (Brown 1955, see also Mayer et al 1970)

$$I(t) = \frac{eN_i}{t_T} e^{-t/\tau} \quad ; \quad t < t_T \qquad (3.11)$$
$$= 0 \quad ; \quad t > 0$$

The carrier lifetime can therefore be determined from the exponential decay of the transient current.

Transient voltage waveform with deep trapping of carriers is therefore

$$V(t) = \frac{Q_i}{C} [1 - \exp(-\frac{t}{\tau})] \quad ; \quad t < t_T \qquad (3.12)$$
$$= \frac{Q_i}{C} [1 - \exp(-\frac{t_T}{\tau})] \quad ; \quad t > t_T$$

This is called the Hecht relationship (Hecht 1932). Note that the shape and also the final height of the waveform depends on the deep trapping time, τ.

The motion and shape of the injected carrier packet, which is ideally a δ-function at time $t = 0^+$,is influenced by a variety of factors. For example, 'deep' trapping, trapping and detrapping from shallow traps, diffusion are some factors intrinsic to the sample material. In general, the shape of the transient current depends on the behaviour of the density function of injected carriers. If $n_c(x,t)$ is the density of mobile carriers, i.e. carriers in the conduction state in the sample then the transient current, neglecting diffusion, is given by

$$I(t) = \frac{e\mu_0 F}{L} \int_0^L n_c(x,t)dx \qquad (3.13)$$

where μ_0 is the microscopic mobility of the carriers in the conduction states. Eqn. (3.13) essentially applies to band transport. $n_c(x,t)$ has to be determined by solving the transport equations, applicable to the solid under consideration, with the appropriate boundary conditions.

It should be apparent from the concepts used above that the following four conditions are required:

(1) Absorption depth $\delta \ll L$

(2) Duration of excitation $t_{ex} \ll t_T$

(3) Dielectric relaxation time $\tau_{rel} \gg t_T$

(4) Injected charge $Q_i \ll C_s V_o$, i.e. small signal condition.

In addition a further condition, either $CR \ll t_T$ or $CR \gg t_T$, is needed for I- or V-modes of operation respectively if more easily interpretable TOF signals are preferred.

§3.3 TRANSIENT TRANSPORT THEORY

3.3.1 Transport in the Presence of Monoenergetic Traps

The transient current and voltage waveforms obtainable from a solid with a monoenergetic set of traps have been studied by several authors (e.g. Tefft 1967, Blakney and Grunwald 1968, Zanio et al 1968, Rudenko 1976, Rudenko and Arkhipov 1978). The conduction problem may be solved by employing the equations of charge conservation which govern the free and trapped carrier densities $n_c(x,t)$ and $n_t(x,t)$ respectively for a single trap model. For planar geometry,

$$\frac{dn_c(x,t)}{dt} = \mu_o F \frac{\partial n_c(x,t)}{\partial x} - \frac{n_c(x,t)}{\tau_c} + \frac{n_t(x,t)}{\tau_r} \qquad (3.14)$$

$$\frac{dn_t(x,t)}{dt} = \frac{n_c(x,t)}{\tau_c} - \frac{n_t(x,t)}{\tau_r} \qquad (3.15)$$

where τ_c is the capture time and τ_r, the release or detrapping time.

In writing these equations, diffusion and recombination, which introduce additional terms of the form $D \frac{\partial^2 n(x,t)}{\partial x^2}$ and $\frac{n_c(x,t)}{\tau_{Recombination}}$ into eqn. (3.14), and free and trapped thermal carrier densities, n_{co} and n_{to}, have been neglected.

The initial conditions for the system are

$$n_c(x,0) = N_i \delta(x) \qquad (3.16)$$

$$n_t(x,0) = 0 \qquad \text{for } x > 0 \qquad (3.17)$$

The boundary conditions are

$$n_c(x,t) = 0 \; ; \; x > L \qquad (3.18)$$

$$n_t(x,t) = 0 \; ; \; x > L \qquad (3.19)$$

Eqns. (3.14) and (3.15) with the conditions in eqns. (3.16) to (3.19) may be solved by Laplace transforms for $n_c(x,t)$ and $n_t(x,t)$ (Zanio et al 1968, Akutagawa and Zanio 1968). For example, the free carrier density is

$$n_c(x,t) = \left[\frac{N_i}{\mu_o F}\right] \delta(t-t') \exp(-\frac{t'}{\tau_c}) +$$

$$\left[\frac{N_i}{\mu_o F}\right] U(t-t') \; [\frac{\xi B_1(\xi)}{2(t-t')}] \exp[-\frac{(t-t')}{\tau_r}] \exp(-\frac{t'}{\tau_c}) \qquad (3.20)$$

where $$t' \equiv \frac{x}{\mu_o F} \qquad (3.21)$$

$$\xi \equiv 2[\frac{t'(t-t')}{\tau_c \tau_r}]^{\frac{1}{2}} \qquad (3.22)$$

and $B_1(\xi)$ is the first order hyperbolic Bessel function and $U(t)$ is the unitary step function.

Eqn. (3.20) shows the free charge carrier density $n_c(x,t)$ to be the sum of two components. The first term which contains the $\delta(t-t')$ function is, in fact, the Hecht term and represents the charge remaining in the injected carrier packet as it drifts. The number of carriers in this packet decreases as $\exp(-\frac{t}{\tau_c})$ until the transit time t_T is reached. The second term is attributed to the multiple trapping and detrapping of the carriers and represents those carriers which have been removed from the spike and at time t are back in the conduction band. Since these carriers have suffered at least one trapping event, they lag behind the advancing spike and will continue to contribute to the current after the transit time.

The transient current response may be found by integrating $n_c(x,t)$ over the sample length. The resulting transient current for times $t \leq \frac{L}{\mu_o F}$

has the form (e.g. Rudenko 1978)

$$I(t) = \frac{Q_i}{t_{To}} \frac{\tau_c}{\tau_c+\tau_r} + \frac{Q_i}{t_{To}} \frac{\tau_r}{\tau_c+\tau_r} \exp[-\frac{(\tau_r+\tau_c)t}{\tau_r\tau_c}] \qquad (3.23)$$

$$t \leqq t_{To}$$

where $t_{To} \equiv \frac{L}{\mu_o F}$ is the transit time of the untrapped carriers, or the transit time in the 'equivalent trap-free solid'. The transient current for $t > t_{To}$ has a complicated functional form (Rudenko 1976, Rudenko and Arkhipov 1978) but it can still be evaluated numerically. Figs. 3.4 and 3.5 show some current transients under various conditions. The parameter θ in Fig. 3.4 is defined as τ_c/τ_r. Note that if there is no detrapping, i.e. the traps are deep and thus $\tau_r = \infty$, then eqn. (3.23) simplifies to eqn. (3.11) derived in the previous section from simple arguments.

It is instructive to study the transient current for two cases of interest; heavy trapping with detrapping, $\tau_c \ll t_{To}$, $\tau_r \gtrsim \tau_c$ and light trapping with detrapping, $\tau_c \gtrsim t_{To}$.

Heavy trapping with detrapping ($\tau_c \ll \frac{L}{\mu_o F}$, $\tau_r \gtrsim \tau_c$):

In this case the carriers are trapped and detrapped many times before reaching the back electrode and as a result the effective transit time and the transient current amplitude are trap controlled. With the $\tau_c \ll t_{To}$ condition imposed on eqns. (3.14) and (3.15) the total number of free carriers is[†] (Zanio et al 1968)

$$N(t) = \int_o^L n_c(x,t)dx = N_i \frac{\tau_c}{\tau_c+\tau_r} \qquad (3.24)$$

$$\text{for } \tau_c < t \leqq t_T$$

and therefore the transient waveforms are

$$I(t) = \frac{Q_i}{t_T} \quad ; \tau_c < t_T \leqq t_T \qquad (3.25)$$

$$\cong 0 \quad ; t_T < t$$

[†] For simplicity the surface area A is taken as unity

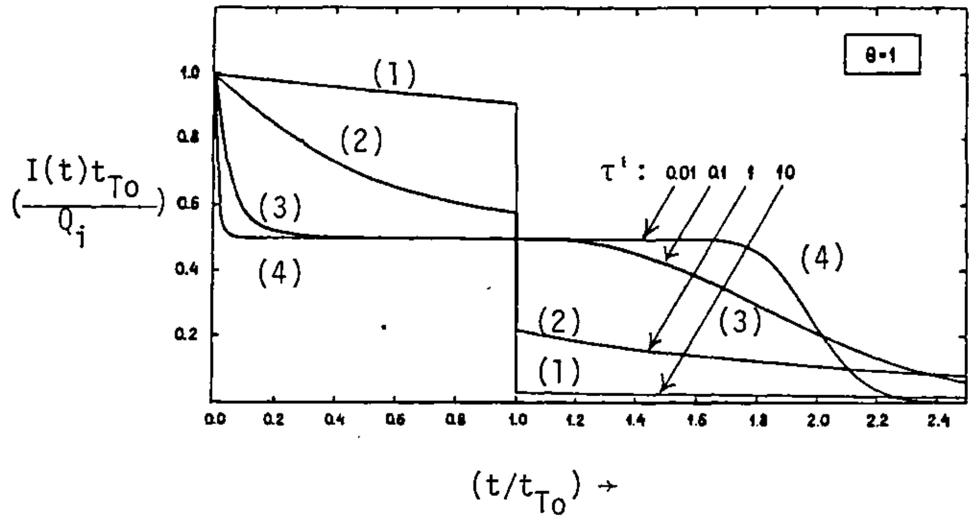

Fig. 3.4: Transient current waveforms in the presence of a mono-energetic set of traps. $\tau' \equiv \tau_c/t_{To}$ and $\theta \equiv \tau_c/\tau_r$. (From Rudenko 1976, Rudenko and Arkhipov 1978).

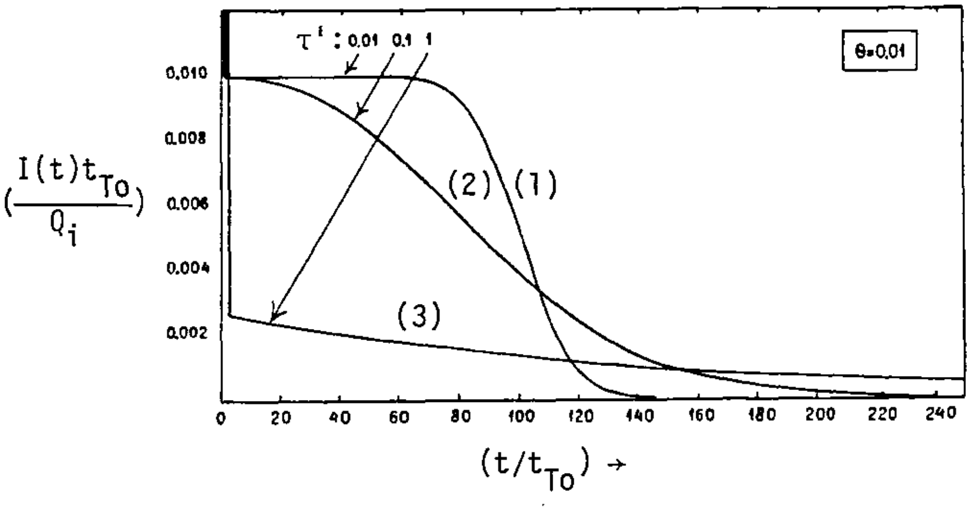

Fig. 3.5: Transient current waveforms in the presence of a mono-energetic set of traps. $\tau' \equiv \tau_c/t_{To}$ and $\theta \equiv \tau_c/\tau_r$.

(From Rudenko 1976, Rudenko and Arkhipov 1978).

$$V(t) = \frac{Q_i}{C} \frac{t}{t_T} \quad ; \quad \tau_c < t \leqq t_T \tag{3.26}$$

$$\cong \frac{Q_i}{C} \quad ; \quad t_T < t$$

where

$$t_T = t_{To} \left(\frac{\tau_c+\tau_r}{\tau_c}\right) \tag{3.27}$$

is the extended transit time which incorporates the effect of the traps on the time taken to traverse the sample. The current transients corresponding to $\frac{\tau_c}{t_{To}} << 1$ are the waveforms (4) and (1) in Fig. 3.4 and 3.5 respectively. It can be seen that these transients resemble the trap-free case but now there is a current tail for $t > t_T$ and also t_T is not as sharp; c.f. curve (1) in Fig. 3.4 for which $\tau_c = 10\ t_{To}$.

The effective drift mobility μ_d is given by

$$\mu_d = \frac{L}{t_T F} \tag{3.28}$$

i.e.

$$\mu_d = \mu_o \frac{\tau_c}{\tau_c+\tau_r} \tag{3.29}$$

Thus the extended transit time t_T may be attributed to a reduced mobility $\mu_o \frac{\tau_c}{\tau_c+\tau_r}$. Because $\tau_c << t_T$, the free and trapped carriers may be assumed to reach thermal equilibrium in a time much shorter than t_T, so $\frac{\tau_c}{\tau_r}$ from eqn. (3.15) is

$$\frac{\tau_c}{\tau_r} = \frac{n_c}{n_t} = \frac{N_c}{N_t} \exp\left(-\frac{E_t}{kT}\right) \tag{3.30}$$

where N_c is the density of states at conduction band edge, N_t the trap density and E_t the activation energy of the traps (with respect to the conduction band). Using eqn. (3.30) the drift mobility is

$$\mu_d = \mu_o \left[1 + \frac{N_t}{N_c} \exp\frac{E_t}{kT}\right]^{-1} \tag{3.31a}$$

or

$$\mu_d \cong \mu_o \frac{N_c}{N_t} \exp(-\frac{E_t}{kT}) \quad ; \quad E_t \gg kT \tag{3.31b}$$

Light trapping with detrapping ($\tau_c \gtrsim \frac{L}{\mu_o F}$):

Eqn. (3.23) for the current transient shows an exponential decay for times $t < t_{To}$ with a time constant $\tau_c\tau_r/(\tau_c+\tau_r)$. It is apparent from the light and intermediate trapping waveforms, (1) and (2) in Fig. 3.4, that there is a discontinuity in I(t) at the transit time. There is a 'long' tail after t_T which for $\tau_c > t_{To}$ is given by (Akutugawa and Zanio 1968)

$$I(t) = \frac{1}{2} Q_i \frac{t_T}{\tau_r\tau_c} \exp(-\frac{t}{\tau_r}) \quad ; \quad t > t_T \tag{3.32}$$

It can be seen that (Fig. 3.4) with light trapping the transient waveforms I(t) and V(t) have two components corresponding to $t < t_{To}$ and $t > t_{To}$.

3.3.2 General Extended State Transport Theory

The concepts used in the previous section to study the transient response in the presence of a monoenergetic set of traps can be extended to formulate a general multiple trapping band transport theory. The multiple trapping model for unipolar conduction is defined by the continuity equations[†] (see, for example, Rudenko 1976, Schmidlin 1977, Noolandi 1977a, Lakin et al 1977, Fleming 1979)

$$\frac{\partial p_c(x,t)}{\partial t} = g(x,t) - \mu_o F \frac{\partial p_c}{\partial x} - \sum_i \frac{\partial p_{ti}(x,t)}{\partial x} \tag{3.33}$$

$$\frac{\partial p_{ti}(x,t)}{\partial t} = p_c(x,t)\,\omega_i - p_{ti}(x,t)\,r_i \tag{3.34}$$

where $p_c(x,t)$ is the density of carriers in transport states (conduction band); $p_{ti}(x,t)$ is the density of carriers captured by traps of type i;

[†] Note change to p(x,t) notation from n(x,t). Diffusion, recombination, and thermal equilibrium free and trapped carrier densities have been neglected.

$g(x,t)$ is the local photogeneration rate; ω_i and r_i are the capture and release rates respectively from trap i. For band transport ω_i and r_i are defined by

$$\omega_i = \frac{1}{\tau_{ci}} = N_{ti}S_i\bar{v} \tag{3.35}$$

and

$$r_i = \frac{1}{\tau_{ri}} = \nu_i \exp(-\frac{E_{ti}}{kT}) \tag{3.36}$$

where τ_{ci} and τ_{ri} are the capture and release times with respect to trap i; N_{ti} is the density of type i traps; S_i is their capture cross-section; $\bar{v}$ is the average speed of a mobile carrier; ν_i is an attempt to escape frequency, and E_{ti} is the activation energy for release.

In the steady state,

$$\frac{\partial p_c(x,t)}{\partial t} = \frac{\partial p_{ti}(x,t)}{\partial t} = 0 \tag{3.37}$$

which via eqn. (3.34) leads to

$$\frac{\omega_i}{r_i} = \frac{p_{ti}}{p_c} = \frac{N_{ti}}{N_v} \exp \frac{E'_{ti}}{kT} \tag{3.38}$$

where $E'_{ti} = E'_{ti}$ (F,T) is the effective difference between trap i and transport eigenenergies.

For a monoenergetic set of traps, i = 1 and setting,

$$g(x,t) = N\delta(x)\,\delta(t) \tag{3.39}$$

reduces eqns. (3.33) and (3.34) to (3.14) and (3.15) as expected.

The solution of the general eqns. (3.33) and (3.34) with $g(x,t) = N\delta(x)\delta(t)$ gives (Noolandi 1977a, Lakin et al 1977)

$$\tilde{p}_c(x,s) = \frac{N}{\mu_o F} \exp [- \frac{a(s)t_{To}x}{L}] \tag{3.40}$$

where the parameter a(s) is defined by

$$a(s) = s \left[1 + \frac{1}{t_{To}} \sum_i \frac{M_i}{s + r_i} \right] \tag{3.41}$$

where

$$M_i \equiv \omega_i t_{To} = \frac{t_{To}}{\tau_{ci}} \tag{3.42}$$

The parameter M_i represents the number of times a carrier is captured by trap i alone while crossing the sample.

For i = 1, eqns. (3.40), (3.41), (3.42), (3.35) and (3.36) give

$$\tilde{p}_c(x,s) = \frac{N}{\mu_o F} \quad \exp\left\{- \frac{sx}{\mu_o F}\left[1 + \frac{1}{s\tau_c + \tau_c/\tau_r}\right]\right\} \tag{3.43}$$

which, as expected, is equivalent to the transform of $n_c(x,t)$ given in eqn. (3.20) (Zanio et al 1968).

The transform of the current from eqn. (3.13) is

$$\tilde{I}(s) = \frac{e\mu_o F}{L} \int_o^L \tilde{p}_c(x,s)dx \tag{3.44}$$

Thus,

$$\tilde{I}(s) = \frac{eN}{t_{To}} \quad \frac{1}{a(s)} \left\{ 1 - \exp\left[- t_{To}\ a(s)\right] \right\} \tag{3.45}$$

This is the basic expression for the transform of the transient current in a multiple trapping model.

While the free carriers are drifting in the transport band their motion may be interrupted by trapping in a distribution of localized states in energy. Rudenko and Arkhipov (Rudenko and Arkhipov 1978, 1982a,b, Arkhipov and Rudenko 1977, 1982) considered this transport problem in a general context by incorporating an arbitrary distribution of traps, $\eta(E)$, in energy into the theoretical framework of the multiple trapping model.

The appropriate equations in integral form for planar geometry are

$$\frac{\partial p(x,t)}{\partial t} + \mu_o F \ \frac{\partial p_c(x,t)}{\partial x} - D_o \ \frac{\partial^2 p_c(x,t)}{\partial x^2} = 0 \tag{3.46}$$

$$\frac{\partial \rho(x,t,E)}{\partial t} = c(E)\, \eta(E)\ p_c(x,t) - c(E)\ N_c \exp(- \frac{E}{kT})\ \rho(x,t,E) \tag{3.47}$$

$$p(x,t) = p_c(x,t) + p_t(x,t) \tag{3.48}$$

$$p_t(x,t) = \int_o^\infty \rho(x,t,E)dE \tag{3.49}$$

where p(x,t) is the total density of carriers, $\rho(x,t,E)dE$ is the density of carriers captured by traps between E and E + dE, $\eta(E)dE$ is the density of traps between E and E + dE, c(E) determines the transition probability between the mobile and localized states, μ_0 is the microscopic mobility in the conduction state and D_0 is the diffusion coefficient in the conduction state. The latter two quantities are related by the Einstein relationship $D_0 = \frac{kT}{e}\ \mu_0$.

The total density of traps N_T is

$$N_T = \int_0^\infty \eta(E)dE \tag{3.50}$$

The lifetime of mobile carriers is now defined by

$$\tau_0 = [\int_0^\infty c(E)\ \eta(E)dE\ ]^{-1} \tag{3.51}$$

Eqn. (3.47) may be rearranged as

$$\rho(x,t,E) = p_c\ \frac{\eta(E)}{N_c}\ \exp(\frac{E}{kT}) - \frac{1}{c(E)N_c}\ \exp(\frac{E}{kT})\ \frac{\partial\rho(x,t,E)}{\partial t} \tag{3.52}$$

Assuming the free and trapped carriers to reach thermal equilibrium almost instantaneously we can take $\frac{\partial\rho}{\partial t} \cong 0$, so

$$\rho(x,t,E) = \frac{\eta(E)}{N_c}\ \exp(\frac{E}{kT})\ p_c(x,t) \tag{3.53}$$

Integrating this with respect to E and using eqn. (3.48) a relationship between p_c and p may be obtained as

$$p_c(x,t) = \frac{\theta_e}{1+\theta_e}\, p(x,t) \tag{3.54}$$

where θ_e is defined by

$$\frac{1}{\theta_e(T)} = \int_0^\infty \frac{\eta(E)}{N_c} \cdot \exp\frac{E}{kT}\ dE \tag{3.55}$$

In many problems $\theta_e << 1$.

Using eqn. (3.54) in eqn. (3.46) gives the equilibrium transport equation,

$$\frac{\partial p(x,t)}{\partial t} + \mu_{eq} F \frac{\partial p(x,t)}{\partial x} - D_{eq} \frac{\partial^2 p(x,t)}{\partial x^2} = 0 \qquad (3.56)$$

where μ_{eq} and D_{eq} are the mobility and diffusion kinetic coefficients defined by

$$\mu_{eq}(T) = \frac{\theta_e(T)}{1+\theta_e(T)} \mu_o \cong \theta_e(T)\,\mu_o \qquad (3.57)$$

$$D_{eq}(T) = \frac{\theta_e(T)}{1+\theta_e(T)} D_o \cong \theta_e(T)\,D_o \qquad (3.58)$$

It can be seen that under equilibrium conditions the transport of charge carriers in the presence of a distribution of traps may be described by effective mobility and effective diffusion coefficients μ_{eq} and D_{eq} respectively. The effect of multiple trapping thus leads to a considerable reduction of mobility and diffusion coefficient from the trap-free values μ_o and D_o. Furthermore, μ_{eq} and D_{eq} have an additional temperature dependence.

Consider, for example, a monoenergetic set of traps with the energy E_t. With

$$\eta(E) = N_t \delta(E-E_t)$$

in eqn. (3.55) we obtain by (3.57) and (3.58)

$$\mu_{eq} = \mu_o[1 + \frac{N_t}{N_c} \exp \frac{E_t}{kT}]^{-1} \qquad (3.59)$$

$$D_{eq} = D_o[1 + \frac{N_t}{N_c} \exp \frac{E_t}{kT}]^{-1} \qquad (3.60)$$

The assumption of instantaneous establishment of thermal equilibrium may be slightly relaxed by introducing an approximation for the $\frac{\partial \rho}{\partial t}$ term in eqn. (3.52) by using the differential of eqn. (3.53) with respect to time (see Rudenko and Arkhipov 1982a). Transport under these conditions is called quasi-equilibrium regime and the relationship between $p_c(x,t)$ and $p(x,t)$ is

$$p_c(x,t) = \frac{\theta_e}{1+\theta_e}\ p(x,t) - \frac{1}{(1+\theta_e)^2}\ \frac{\mu_{eq}F}{\omega}\ \frac{\partial p(x,t)}{\partial x} + \frac{1}{(1+\theta_e)^2}\ \frac{D_{eq}}{\omega}\ \frac{\partial^2 p(x,t)}{\partial x^2} \qquad (3.61)$$

where ω is a temperature dependent parameter defined by

$$\frac{1}{\omega(T)} = \frac{1}{\theta_e^2} \int_0^\infty \frac{\eta(E)}{N_c c(E)}\ \exp \frac{2E}{kT}\, dE \qquad (3.62)$$

Using eqn. (3.61) in eqn. (3.46) leads to the quasi-equilibrium transport equation;

$$\frac{\partial p(x,t)}{\partial t} + \mu_{eq}F\ \frac{\partial p(x,t)}{\partial x} - D_{eq}\ \frac{\partial^2 p(x,t)}{\partial x^2} - D_F\ \frac{\partial^2 p(x,t)}{\partial x^2} + 2\left[\frac{1}{\theta_e(1+\theta_e)}\right]^{\frac{1}{2}} \frac{D_{eq}D_F^{\frac{1}{2}}}{\omega^{\frac{1}{2}}}\ \frac{\partial^3 p}{\partial x^3} - \frac{1}{\theta_e(1+\theta_e)}\ \frac{D_{eq}^2}{\omega}\ \frac{\partial^4 p}{\partial x^4} = 0 \qquad (3.63)$$

where D_F is called the 'field diffusion' coefficient defined by

$$D_F(T) = \frac{1+\theta_e(T)}{\theta_e(T)}\ \frac{[\mu_{eq}(T)F]^2}{\omega(T)} \qquad (3.64a)$$

$$D_F(T) \cong \frac{(\mu_{eq}D)^2}{\theta_e\omega} = \theta_e\ \frac{(\mu_o F)^2}{\omega} \qquad (3.64b)$$

An important feature of the transport equation (3.63) is the appearance of the field diffusion term $D_F \frac{\partial^2 p}{\partial x^2}$. The importance of this term becomes especially apparent under the conditions which allow the neglect of the effect of conventional diffusion. For example, the transport eqns. (3.14) and (3.33) neglect the conventional diffusion term since they were written under the 'drift approximation'.

Eqn. (3.63) can be approximated to a convenient form by neglecting the higher order differential terms in $\frac{\partial^3 p}{\partial x^3}$ and $\frac{\partial^4 p}{\partial x^4}$. The resulting quasi-equilibrium transport equation is

$$\frac{\partial p(x,t)}{\partial t} + \mu_{eq}F \frac{\partial p(x,t)}{\partial x} - (D_{eq} + D_F) \frac{\partial^2 p(x,t)}{\partial x^2} = 0 \qquad (3.65)$$

This transport equation may be applied to the TOF case with $p(x,0) = N\,\delta(x)$. The solution represents a Gaussian carrier packet

$$p(x,t) = \frac{N}{[4\pi D_t t]^{\frac{1}{2}}} \exp\left\{- \frac{(x-\mu_{eq}Ft)^2}{4D_t t}\right\} \qquad (3.66)$$

where $D_t \equiv D_{eq} + D_F$ is called the total diffusion coefficient.

The mean of the packet moves with a constant velocity $\frac{d\bar{x}}{dt} = \mu_{eq}F$ since from eqn. (3.66)

$$\bar{x}(t) = \mu_{eq}Ft \qquad (3.67)$$

The spreading of the packet is characterised by the dispersion σ defined as

$$\sigma \equiv [\overline{(\Delta x)^2}]^{\frac{1}{2}} \qquad (3.68)$$

Thus

$$\sigma = 2(D_{eq} + D_F)^{\frac{1}{2}}\, t^{\frac{1}{2}} \qquad (3.69)$$

Therefore for a Gaussian carrier packet $\sigma/\bar{x} \sim t^{-\frac{1}{2}}$.

It should be remarked that even if conventional diffusion is negligible, the carrier packet still suffers dispersion due essentially to the presence of a distribution of traps which leads to finite values for $\theta_e(T)$, $\omega(T)$ and hence D_F. In the case of a trap free solid, however, $D_F = 0$ and within the drift approximation the carrier packet exhibits no spreading.

When the peak of the carrier packet in eqn. (3.66) reaches the back electrode the transient current will start to fall sharply because the majority of the carriers would have been removed from the solid. If t_T is the time taken for the peak of the Gaussian packet to reach the back electrode then at time t_T, $I(t)$ will show a sharp change. It is, therefore, natural to call t_T the transit time for TOF purposes although it represents an average quantity rather than a single unique parameter (see §3.2).

The drift mobility μ_d determined from t_T is

$$\mu_d = \frac{L}{t_T F} \tag{3.70}$$

Substituting for t_T from eqn. (3.67)

$$\mu_d = \mu_{eq} = \frac{\theta_e(T)}{1+\theta_e(T)} \mu_o \cong \theta_e(T)\, \mu_o \tag{3.71}$$

Clearly the measured drift mobility from the 'break' in I(t) is the same quantity as the effective mobility μ_{eq} which determines the transport of the carriers in the presence of traps. This conclusion is valid under equilibrium or quasi-equilibrium transport conditions since it is based on the Gaussian carrier packet equation (3.66).

A quantitative verification of the above arguments involves the examination of the current transient I(t) arising from the Gaussian carrier packet (see Rudenko and Arkhipov 1982b). Eqn. (3.13) for I(t) involving $p_c(x,t)$ is equivalent to

$$I(t) = \frac{e}{L} \frac{\partial}{\partial t} \int_0^\infty (L-x)\, p(x,t)dx \tag{3.72}$$

which involves p(x,t). Therefore substituting for p(x,t) from eqn. (3.66) would lead to a general current expression under quasi-equilibrium transport conditions;

$$I(t) \cong \frac{eN}{\left(\frac{L}{\mu_{eq}F}\right)} \pi^{-\frac{1}{2}} \operatorname{erfc} \left\{ \frac{\left[\frac{\mu_{eq}Ft}{L} - 1\right]}{2\left[\frac{\mu_{eq}Ft}{L}\right]^{\frac{1}{2}} \left[\frac{\mu_o F}{\omega L}\right]^{\frac{1}{2}}} \right\} \tag{3.73}$$

Rudenko and Arkhipov (1982b) discuss the form of I(t) in eqn. (3.73) with the same conclusions as presented above.

§3.4 TIME-DEPENDENT TRANSPORT

There are a number of TOF experiments in which the observed transient currents do not obey the general transport equations based on a Gaussian carrier packet. For example, in a-As_2Se_3 the transient hole current typically displays an initial peak, then a plateau region which is followed by an 'unusually' long tail as shown in Fig. 3.6a. If the shoulder in this transient dividing the plateau from the tail is associated with the 'transit time' of a fraction of the injected carriers then the TOF drift mobility determined from $\frac{L}{t_T F}$ for this fraction of carriers shows a thickness dependence[†] (Scharfe 1970, 1973, Pai and Scharfe 1972, Pfister and Scher 1977a). When the current transients are plotted as log I(t) vs. log t, two lines are obtained whose slopes add to -2. The intersection of the two lines at t_T, which probably represents a 'transit time' (to be clarified later) leads to a thickness dependent drift mobility $\mu_{d(TOF)}$ whose value decreases with the thickness. The latter observation is tantamount to the deduction that the average velocity of the injected carrier packet is a decreasing function of time.

Clearly, $\mu_{d(TOF)}$ in this case cannot represent the quasi-equilibrium mobility coefficient, $\mu_{eq} = \theta_e \mu_o$, which is an intrinsic property of the material. In addition, the transient currents I(t) - t evince a universality (Fig. 3.6b) when plotted as log $\frac{I(t)}{I(t_T)}$ vs log $\frac{t}{t_T}$, i.e. the plots superimpose for different thicknesses, fields and temperatures (e.g. Pfister and Scher 1977a,b). This universality property of I(t) can be accounted for by $\sigma/\bar{x}$ being independent of time.

The anomalous thickness dependence of $\mu_{d(TOF)}$ and the shapes of the transient currents have been associated with the injected carrier packet propagating in a non-Gaussian manner, i.e. eqn. (3.66) is not obeyed. This anomalous carrier pulse propagation (often abbreviated to ACPP in TOF literature) has been the centre of considerable recent theoretical work. The transient response resulting from the non-Gaussian dispersion of the carrier packet is often termed 'dispersive tranport'.

Scher and Montroll 1975 were able to explain the anomalous features of the TOF signals obtained on a-As_2Se_3 by considering the motion of the

---

[†] Other materials showing a similar behaviour are, for example, a-SiO_2, PVK:TNF and some molecularly doped organic polymers (see reviews by Pfister and Scher 1977b, 1978, Pfister 1976b, Mort 1977).

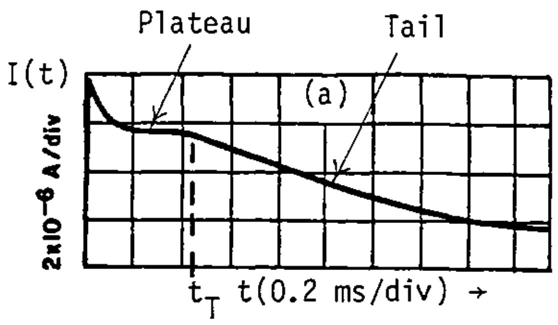

(a) Highly dispersive transient hole photocurrent obtained from a-As_2Se_3 by Scharfe (1970).

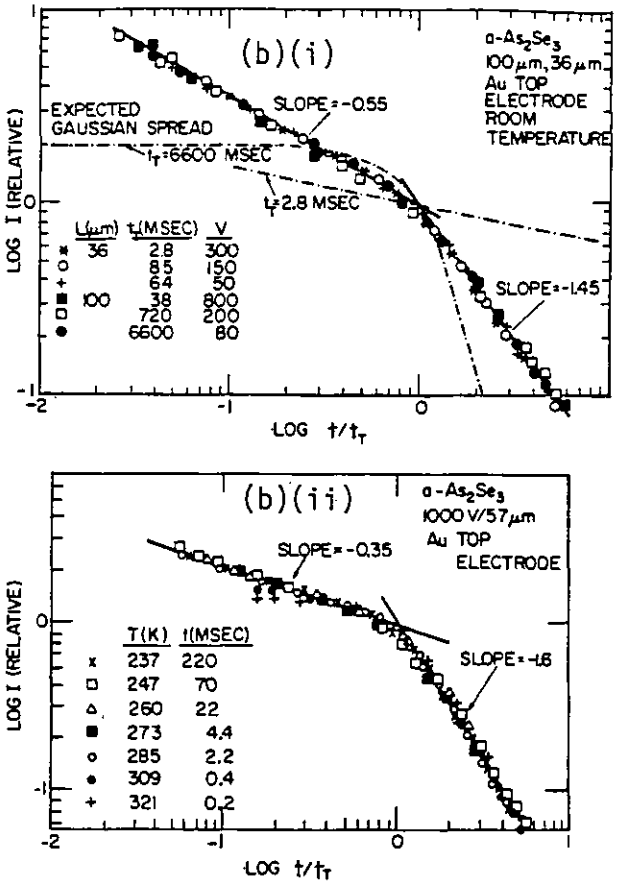

(b) Universality plots of log I(t) vs log (t/t_T) for hole transients in a-As_2Se_3. The plots were obtained by parallel shifting of the current traces along the time and current axes. (i) Variation of applied field and sample thickness at room temperature. Expected Gaussian dispersion is schematically indicated. (ii) Fixed applied field and sample thickness, variation of temperature. (From Pfister and Scher 1977a).

Fig. 3.6: Dispersive hole transport in a-As_2Se_3

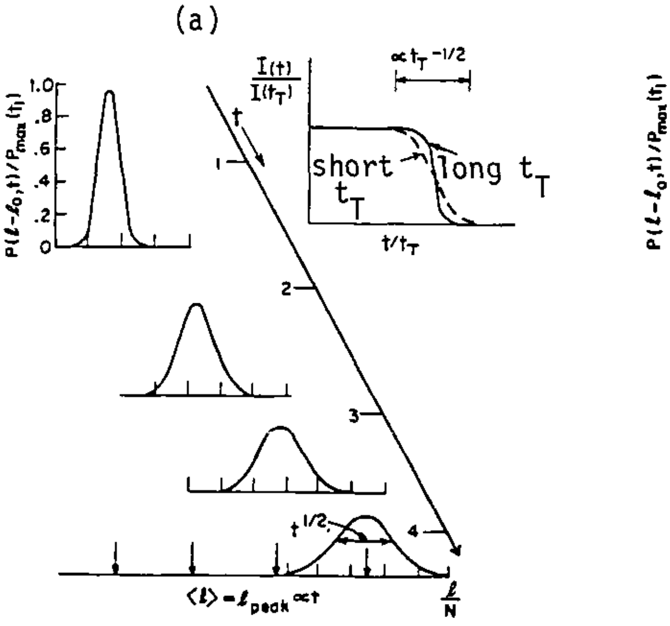

(a) Spatial distribution of a carrier packet at various subintervals of the transit time for $\psi(t) = W \exp(-Wt)$. The inset shows the effect of Gaussian spreading of the carrier packet on I(t) vs (t/t_T).

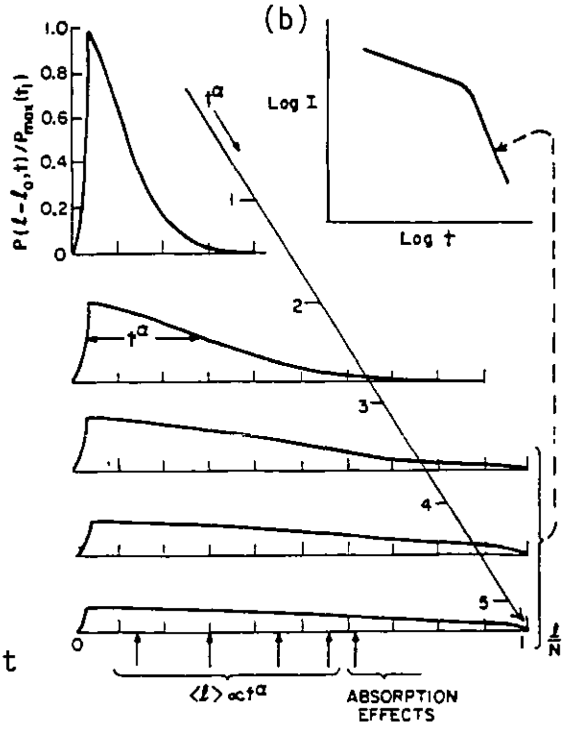

(b) Spatial distribution of a carrier packet at various subintervals of $t_T^{\frac{1}{2}}$ for $\psi(t) \sim t^{(1+\alpha)}$. The inset shows ~~the~~ corresponding log I vs log t.

Fig. 3.7: Propagation of a Gaussian and a non-Gaussian carrier packet (from Pfister and Scher 1977a)

injected carriers as a stochastic transport process. The motion of a carrier in the Scher and Montroll (SM) model is subject to a broad distribution of event times. These event times can be hopping times, trap release times or both so that the general framework of the stochastic theory of dispersive transport does not depend on any specific microscopic transport mechanism . SM consider essentially a carrier hopping from one site to another through a random distribution of hopping sites. The transition rate $W(\vec{r})$ between sites in a disordered structure is expected to show a highly fluctuating behaviour, since it is a sensitive function of the intersite variables $\vec{r}$ and ΔE_{hop};

$$W(\vec{r}) = W_o \exp\left(- \frac{r}{r_o} \right) \exp\left(- \frac{\Delta E_{hop}}{kT}\right) \tag{3.74}$$

where $\vec{r}$ and ΔE_{hop} are the differences in position and energy levels of the sites respectively, and r_o the radius of the local charge distribution (see §1.1). The sensitivity of $W(\vec{r})$ to small changes in $\vec{r}$ and ΔE_{hop} means that the site to site hopping time in such a disordered system will have a broad distribution. The fluctuation in hopping times as the carrier moves along some path through the random array of sites can be described by using a function $\psi(t)$ defined as follows: $\psi(t)dt$ is the probability that a carrier appears on a site during the time interval, t to t + dt if it arrived at t = 0 on a neighbouring site. $\psi(t)$ is called the waiting time distribution function since it describes the waiting time of a carrier on a lattice site before it jumps to a neighbouring site under the influence of an electric field. Positional disorder present in the real material is therefore incorporated into $\psi(t)$.

In an ordered system of sites, there is one unique transition rate W and $\psi(t)$ is therefore

$$\psi(t) \sim W \exp(-Wt) \tag{3.75}$$

This shows that the carrier has a probability close to unity to hop before a characteristic time W^{-1}. SM propose that a good approximation (over the time interval of observation) for $\psi(t)$ in their hopping model is

$$\psi(t) \sim t^{-(1+\alpha)} \quad , \quad 0 < \alpha < 1 \tag{3.76}$$

where α is called a dispersion parameter and in the hopping model depends on the hop distance, the hop energy and the spatial extent of the localised wavefunction. Such algebraic time dependence for $\psi(t)$ can also describe extended state transport with multiple trapping. For example, for transport with trapping in an exponential distribution of localized states of the form[†]

$$\eta(E) \;=\; N_0 \exp(-\frac{E}{kT_c}) \tag{3.77}$$

$\psi(t)$ represents the spectrum of release times from traps with (e.g. Scher 1977, Tiedje and Rose 1980)

$$\alpha = \frac{T}{T_c} \tag{3.78}$$

SM using this broad $\psi(t)$ in the formalism of continuous time random walk (CTRW) on a biased periodic cubic lattice with the non-Markoffian transport equation calculated the distribution of the carriers in the sample. This distribution of carriers is represented by a propagator function $P(\ell,t)$ defined as the probability that a carrier is found at a position ℓ at time t if at time $t = 0$ it was at the origin $\ell = 0$. $P(\ell,t)$ completely specifies the dynamics of the carrier packet. For quasi-equilibrium extended state transport as shown in §3.3, $P(\ell,t)$ has a Gaussian form; eqn. (3.66). Fig. 3.7a and b show $P(\ell,t)$ for (a) a Gaussian packet and (b) for $\psi(t) \sim t^{-(1+\alpha)}$. It can be seen that in (b) the peak of the propagator P_{max} stays close to the point of initial carrier injection but the mean position moves with a velocity which decreases with time. In fact, SM show that, for $P(\ell,t)$ resulting from $\psi(t) \sim t^{-(1+\alpha)}$,

$$\langle\ell\rangle\,(t) \;\equiv\; \Sigma\ell P(\ell,t) \tag{3.79}$$

$$\sim\; \bar{\ell}(F)\, t^{\alpha} \;\; ; \quad 0 < \alpha < 1 \tag{3.80}$$

[†] T_c is a constant which has the dimension of temperature

and

$$\frac{<\ell>}{\sigma} \sim \text{const} \tag{3.81}$$

where $\bar{\ell}$ is the mean displacement for a single hop and is a function of the electric field, F. Because $<\ell>$ is not linear in time, the current before any of the carriers reach the back electrode is

$$I(t) \sim \frac{d<\ell>}{dt} \tag{3.82}$$

i.e.

$$I(t) \sim t^{-(1-\alpha)} \tag{3.83}$$

When the forward tail of the carrier packet starts to get absorbed (Fig. 3.7b) the current decays more rapidly. A transit time t_T may be defined approximately as the time when the mean position approaches the thickness of the sample. The transient current I(t) is given by

$$I(t) \sim \begin{cases} t^{-(1-\alpha)} & ; \quad t < t_T \\ t^{-(1+\alpha)} & ; \quad t > t_T \end{cases} \tag{3.84}$$

Therefore the current transient on a log-log plot has two asymptotes whose slopes add to -2. A more exact criterion for t_T is the time corresponding to the intersection of the two slopes on the log I-log t plot (Fig. 3.6b). t_T is given by

$$t_T \sim \left[\frac{L}{\bar{\ell}(F)}\right]^{\frac{1}{\alpha}} \exp \frac{\Delta E_{hop}}{kT} \tag{3.85}$$

It can be seen that the drift mobility determined from t_T will have a thickness and field dependence. For low fields $\bar{\ell}(F) \sim F$ and

$$\mu_{d(TOF)} \sim \left(\frac{F}{L}\right)^{\frac{1-\alpha}{\alpha}} \exp\left(-\frac{\Delta E_{hop}}{kT}\right) \tag{3.86}$$

At higher fields $\mu_{d(TOF)}$ increases more steeply than $F^{\left(\frac{1-\alpha}{\alpha}\right)}$ (Pfister 1977).

The dispersive transient currents described by eqn. (3.84) can also be generated from the multiple trapping model embedded in eqns. (3.33) and (3.34) as shown by Noolandi 1977a. In this connection it was pointed out in § 2.5.3 that three discrete species of isoenergetic traps would account for the dispersive photocurrents observed in a-Se at low temperatures. Noolandi 1977b in fact has shown that the model of multiple trapping from a band of states is formally equivalent to the CTRW model.

It is interesting to note that departure from quasi-equilibrium conditions discussed in §3.3 can readily lead to such time dependent transport (Tiedje and Rose 1980, Arkhipov and Rudenko 1982, Rudenko and Arkhipov 1982b). If the injected carriers have not had sufficient time to thermalize then the mobility and diffusion coefficients describing the transport cannot be considered to be independent of time. Tiedje and Rose 1980 for example considered band transport with trapping in an exponential distribution of localized states extending from E_c and described by eqn. (3.77). Retaining the general definition of drift mobility as (Rose 1951)

$$\mu_d = \frac{n_c}{n} \mu_0 \tag{3.87}$$

these authors find that

$$\mu_d(t) \cong \mu_0 \, \alpha(1-\alpha) \, (\nu t)^{\alpha-1} \tag{3.88}$$

where $\alpha = \frac{T}{T_c}$ and ν is an attempt to escape frequency for a trapped carrier.

Arkhipov and Rudenko 1982 from the general band transport equations (3.46) to (3.51) derived a non-equilibrium transport equation in the presence of a distribution of traps. If at time t = 0 an initial carrier distribution p(x,0) is created and all the injected carriers are in extended states, i.e.

$$p_c(x,0) = p(x,0) \text{ and } \rho(x,0,E) = 0 \text{ at } t = 0$$

then at time t there exists a time dependent critical energy $E^*(t)$ which divides the traps into two groups. Those localized states which have energies less than $E^*(t)$ act as shallow traps since there has been sufficient time to establish thermal equilibrium with respect to these traps. Those localized states with energies greater than $E^*(t)$ act as deep traps from which there is no detrapping in time t. Concentration of carriers in the latter localized states changes only due to trapping and thus the release term $c(E)\ N_c \exp(-\frac{E}{kT})$ in eqn. (3.47) may be neglected in describing the population in deep traps.

Since the probability of detrapping per unit time is

$$\tau_r(E)^{-1} = c(E)\ N_c \exp(-\frac{E}{kT}) \tag{3.89}$$

the boundary energy $E^*(t)$ is determined by the condition

$$tc(E^*)\ N_c \exp(-\frac{E^*}{kT}) = 1 \tag{3.90}$$

Thus

$$E^*(t) = kT\ \ell n\ t\nu\ ;\quad t \geqq \nu^{-1} \tag{3.91}$$

where $c(E) = c_o$ was assumed to be independent of E and $\nu \equiv c_o N_c$ is the attempt to escape frequency used above.

With these conditions imposed on eqns. (3.46) to (3.51) the general transport equation is of the form

$$\frac{\partial p(x,t)}{\partial t} + \mu(t)F\ \frac{\partial p(x,t)}{\partial x} - D(t)\ \frac{\partial^2 p(x,t)}{\partial x^2} = -\lambda(t)\ [p(x,t) - p(x,0)] \tag{3.92}$$

where

$$\mu(t) = \frac{\theta(t,T)}{1+\theta(t,T)}\mu_o \tag{3.93}$$

$$D(t) = \frac{\theta(t,T)}{1+\theta(t,T)}\ D_o \tag{3.94}$$

$$\lambda(t) = \frac{\theta(t,T)}{1+\theta(t,T)}\ \frac{1}{\tau(t)} \tag{3.95}$$

$$\frac{1}{\theta(t,T)} = \int_o^{E^*(t)} \frac{n(E)}{N_c}\ \exp\frac{E}{kT}\ dE \tag{3.96}$$

and

$$\frac{1}{\tau(t)} = \int_{E(t)}^{\infty} c(E)\,\eta(E)\,dE \tag{3.97}$$

Note that θ is now calculated only for those traps which have achieved thermal equilibrium and τ for those traps which are deep [c.f. eqns. (3.55) and (3.51)].

It can be seen that the non-equilibrium transport equation (3.92) [c.f. eqn. (3.56)] has 'mobility-like' and 'diffusion-like' time dependent coefficients $\mu(t)$ and $D(t)$ and, in addition, a correction term on the right-hand side which depends on $\lambda(t)$ in eqn. (3.95). As $t \to \infty$ $\mu(t) \to \mu_{eq}$, $D(t) \to D_{eq}$ and $\lambda(t) \to 0$.

Consider, for example, a rectangular uniform trap energy distribution extending from E_c downwards to E_o, i.e.

$$\begin{aligned} \eta(E) &= \frac{N_t}{E_o} \quad ; \quad 0 \leqq E \leqq E_o \\ &= 0 \quad ; \quad E > E_o \end{aligned} \tag{3.98}$$

The time dependent coefficient $\mu(t)$ is

$$\mu(t) = \mu_o \quad ; \quad 0 \leqq t \leqq t_1 \tag{3.99a}$$

$$= \mu_o \frac{E_o}{kT} \frac{\tau_o}{t} \quad ; \quad t_1 < t < t_e \tag{3.99b}$$

$$= \mu_{eq} = \mu_o \frac{N_c}{N_t} \exp(-\frac{E_o}{kT}) \; ; \; t_e < t \tag{3.99c}$$

where $t_1 \equiv \frac{E_o}{kT}\tau_o$ and t_e is the time taken to achieve equilibrium which in this case is determined by $E^*(t_e) = E_o$, i.e.

$$t_e = \frac{1}{c_o N_c} \exp \frac{E_o}{kT} \tag{3.100}$$

It can be seen that non-equilibrium transport concepts lead to time dependent transport coefficients. Transient currents under non-equilibrium conditions are distinctly and anomalously different from those under quasi-equilibrium conditions described in § 3.3.

§3.5 CONCLUSIONS

TOF experiments enable the transient current I(t) generated by the transport of the injected carrier packet to be studied. There are, however, several stringent conditions required for the TOF technique to be applicable (p.87).

Under quasi-equilibrium conditions the injected carrier packet has a Gaussian form [eqn. (3.66)]. I(t) displays a well defined transit time, t_T, corresponding to the exit of the majority of the injected carriers from the sample. The drift mobility, μ_d, hence determined represents the intrinsic effective mobility, μ_{eq} of the carriers. Quasi-equilibrium effective mobility, μ_{eq} depends on the distribution of traps $\eta(E)$ via the parameter $\theta_e(T)$ defined in eqn. (3.55).

If the transport of injected carriers across the sample is subject to a broad spectrum of event times which may be hopping times or detrapping times or both, then the injected carrier packet shows non-Gaussian features. The drift mobility extracted from the dispersive current transients shows a thickness and field dependence. The behaviour of the dispersion parameter, α, is expected to be an important diagnostic in determining the nature of the microscopic process.

CHAPTER 4

EXPERIMENTAL DETAILS AND PROCEDURE

§4.1 INTRODUCTION

In this chapter we will describe the details of the experimental procedure used as well as presenting experimental data in support of material and sample characterization. The first part is devoted to TOF measurements and the following sections to sample preparation and characterization. Differential Scanning Calorimetry (DSC) analysis which has become of considerable importance in studying the structure-thermal behaviour of amorphous solids is included in a separate section, although it forms an integral part of sample characterization.

§4.2 EXPERIMENTAL BACKGROUND ON TOF MEASUREMENTS

It is interesting to note that the drift mobility experiments have become popular during the last two decades due mainly to the pioneering works of Brown 1955, Spear 1957, Le Blanc 1959, 1960 and Kepler 1960 who have successfully applied the technique to solids in the fifties. There are several different TOF experimental arrangements used but the principles remain the same as discussed in Chapter 3. The experimental differences usually mean different types of excitation pulse source or differences in the way the field is applied to the sample. For example, Kepler employed a short light pulse from a xenon flash tube for charge generation whereas Spear's system used an electron beam excitation as shown in Fig. 4.1a. The electron beam excitation according to Spear has the following main advantages over the optical excitation; (i) the intensity of the beam is high and its duration can be made sufficiently short for the generation of sufficient

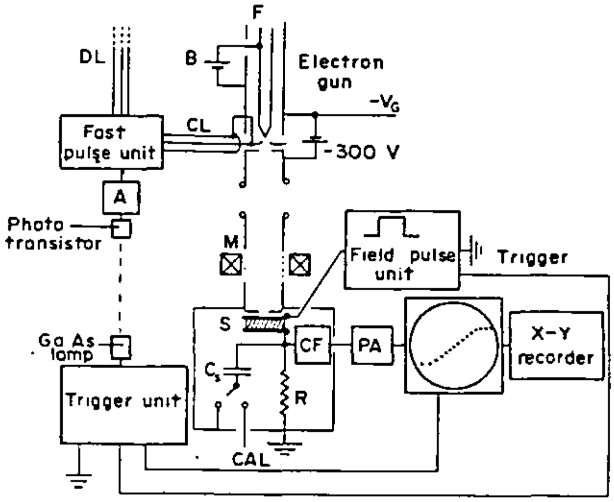

(a) Basic experimental TOF arrangement for drift mobility experiments using an electron beam excitation. F = hairpin filament, DL = delay line, CL = connecting line, M = magnetic lens, S = specimen, CF = cathode follower, PA = pre-amplifier (After Spear 1969).

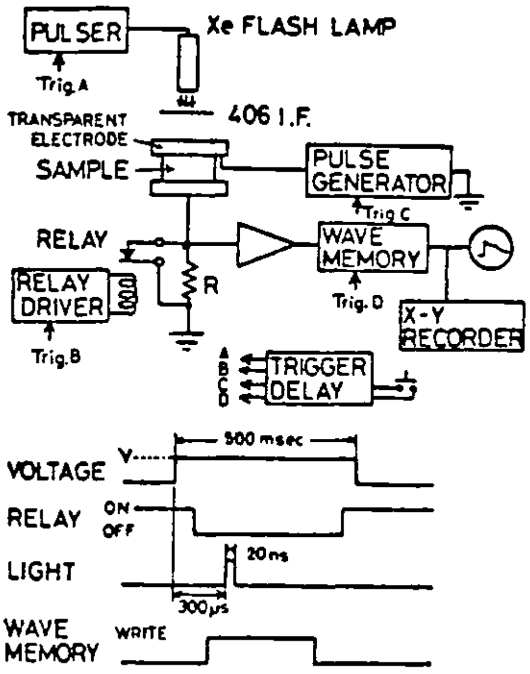

(b) A TOF system using a xenon light flash excitation and a 'single shot' pulsed bias (After Okamoto and Nakamura 1979).

Fig. 4.1: Two TOF systems

carriers, (ii) the depth of the generation region below the top surface can be varied within wide limits by means of the accelerating potential, V_G applied to the gun, (iii) it does not involve the absorption in the electrode and, (iv) in wide gap materials for which the optical excitation is not feasible, electron beam or α-particle excitation is the only means for generating electron-hole pairs. Note that Spear's system shown can provide a single short excitation pulse or a series of pulses at repetition rates of 50 or 100 pulses per sec. Similarly, it can also provide a pulsed applied field (as well as a d.c. field) to the specimen. When the system is run using a single pulse for the applied field and the excitation, then it is said to be operating in the "single shot" mode. This mode of operation is particularly important in drift mobility experiments on a-Se because it enables the sample to be 'rested' between the single shot measurements and hence avoid space charge accumulation and 'fatiguing' of the sample (see, for example, Scharfe and Tabak 1969, and also §4.4).

A TOF set-up using a xenon flash modulated by a Kerr cell to obtain 5 nsec light pulses for excitation was employed by the Xerox scientists Tabak and co-workers (see, e.g. Tabak 1967, 1969) in their drift mobility experiments on a-Se and some of its alloys. A more recent TOF experimental arrangement used by the Japanese scientists Okamoto and Nakamura 1979 is shown in Fig. 4.1b. This set-up which has a pulsed applied field and xenon light pulse excitation is experimentally very similar to that used in this project.

A generally reported requirement in drift mobility experiments is that at least one of the contacts must be blocking. In experimental terms this means that when a bias voltage V is applied, the d.c. conduction level must be low enough to prevent the introduction of an intolerable amount of noise. Ideally, of course, the device should have a zero d.c. conduction, but this situation can be approximated by using low injecting (but non-ohmic) contacts. Although artificial blocking electrodes have been used, they normally tend also to impede the extraction of the oppositely charged carriers. This may give rise to polarization effects and neutralization techniques described by Spear 1969 are then essential. If blocking contacts are made to the sample by placing a thin insulator layer between the metal electrode and the sample (forming a metal insulator, MI, contact) then a pulsed bias must be applied. The field in the sample in the MI contact structure at time = ∞ is zero so the use of d.c. bias must be precluded. Most of the reported drift mobility work on a-Se has employed direct metallic electrodes to the sample to make a sandwich structure. The semitransparent electrode has generally been Au whereas the other electrode, which is normally the substrate, has varied between different researchers.

In Table T4.1 we summarize the experimental details of some of the different TOF work carried out on a-Se. Note that the different drift mobility articles published by the same group of researchers or institution have tended to use the same experimental set-up so only one entry into the table has been taken. This table is obviously useful when comparing the drift mobility results by the different researchers (see Table T2.3 in §2.5).

TOF experiments have been widely used in studying charge transport in high resistivity or low mobility solids. Its principles as well as its experimental details and requirements have been extensively reviewed by several authors, namely by Spear 1969, Martini et al 1972, Dolezalek 1976, Reggiani 1980, and Kao and Hwang (Ch.5).

§4.3 DESCRIPTION OF THE TOF SYSTEM

4.3.1 Room Temperature System

Fig. 4.2 shows the basic experimental set-up used for the TOF measurements. It should be apparent that the bias voltage V_S is applied to the sample S through a 'control box' CC. A push-button PB_1 on CC provided

Table T4.1: Experimental Details of the TOF Systems Used on a-Se by Some Different Authors

Authors	Excitation Source	Bias	Electrode A	Electrode B	Comments
Spear 1960	electron gun	pulsed/single shot	Au	Aℓ	$t_d \sim 2$ ms
Hartke 1962	air spark gap (pulsed)	dc[a]	NESA glass	MI	Neutralization techniques used against space-charge build-up $t_{ex} \sim 0.01$ µs
Blakney & Grunwald 1967	air spark gap	dc[a]	MI (Tinoxide-Pyrex-Se)	MI (as A)	$t_{ex} \sim 0.01$ µs Se films clamped between A and B Repetitive operation
Tabak & Warter 1968	xenon flash + Kerr cell shutter	pulsed[b]	MI (Au-Formvar-Se)	(as A)	Essentially 'single shot' mode $t_{ex} \sim 5$ ns. Probably pulsed field.
Tabak 1970	xenon flash + Kerr cell shutter	pulsed[b]	Au	Au	No MI contact. Kerr cell used for short transit times (< 2µs)
Rossiter & Warfield 1971	eletron gun	dc	Au	Au	IMPORTANT: Transient SCLC mode used, i.e. $t_{ex} > t_T$ ($t_{ex} \lesssim 900$ µs) 'Single shot' or repetitive operation at 60 Hz
Marshall & Owen 1972	electron gun	pulsed	Aℓ	Aℓ	Repetitive operation with a low duty cycle to prevent space charge accumulation
Juška, Vengris & Viscakas 1973, 1974	light pulse	dc[a]			
Herms et al 1974	xenon flash	dc[a]	Au	Au	Space charge nuetralization technique used Sample recovery time ~5 mins
Pfister 1976	Laser (3371Å)	pulsed	MI (Au-I-Se)	Aℓ	I = Lexan polycarbonate $t_{ex} \approx 5$ ns $t_d \sim 0.5$'s
Takahashi 1979	light flash	dc	SnO_2	Au	$t_{ex} \sim 0.01$ µs
Okamoto & Nakamura 1979	xenon	pulsed	Au	Au	Se and Se/Te alloys and multi-layers

MI = metal insulator contact

a = dc bias inferred (bias applied by switching but not pulsed)

b = pulsed bias inferred but t_d unknown

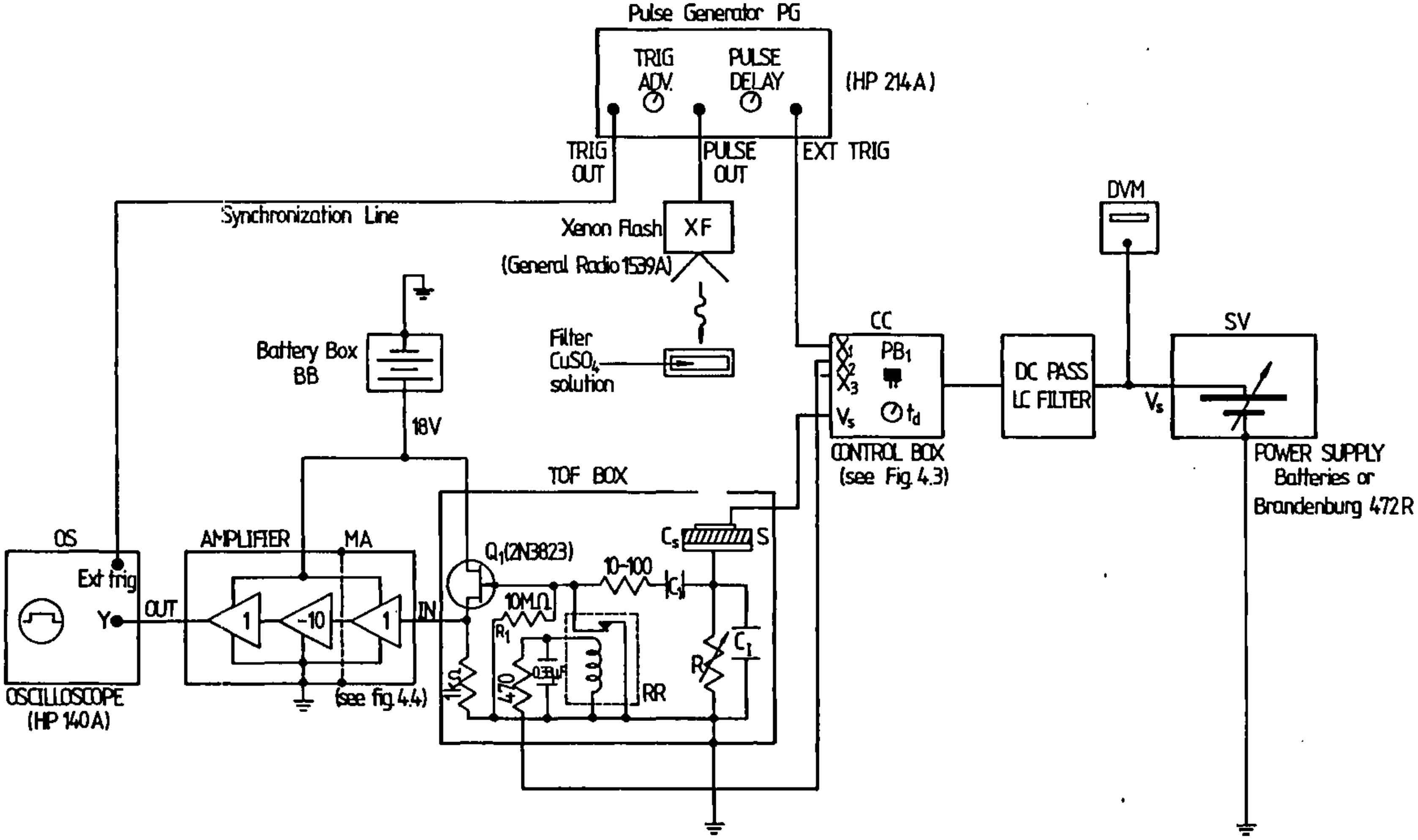

Fig. 4.2: Schematic Diagram of the TOF System

a step bias voltage V_s to the sample and a trigger pulse X_1 to the pulse generator, PG. The pulse generator was used to drive the xenon flash unit XF.

The circuitry of the TOF box in which the sample S was mounted is also shown. The value of the current measuring resistor R was selected between 33 Ω to 10 MΩ by a 12-way rotary switch. Each selection increased R by approximately a factor of three. A three-way switch was used to select the value of the integrating capacitor C_I; 0, 180 or 360 pF. So, the time constant CR determining I- or V-mode operation is $(C_S + C_I)R$ where C_S is the sample capacitance, $\lesssim$100 pF. A source follower employing a 'fast' n-channel FET was used to follow the signal across R. A capacitor C_1 was used to couple the voltage follower to R. C_1R_1 value was chosen to be much greater than any signal time parameter that may have to be measured[#]. A switch selected $C_1 = 110$ pF or $C_1 = 5000$ pF giving a maximum input time constant of $\tau_{in} \approx 500$ ms. A reed relay RR[†], normally closed type, was connected across the input of Q_1 so as to protect the input gate of the FET against the initial high voltage surge appearing across R when the step bias V_s is applied. The 'opening time' of this reed relay was adjusted to be about ≈0.2 msec. by connecting a capacitor (≈ 0.33 μF) in parallel and a resistor (≈ 470 Ω) in series with its actuating coil. Note that this actuation time for RR is shorter than the CR time constants that may be used in V-mode measurements. In such cases RR was actuated by the trigger voltage X_3 which itself has a considerable delay with respect to V_s. This is discussed later.

The control box CC provided not only the step bias voltage V_s but also three trigger signals X_1, X_2 and X_3. Its basic circuitry is shown in Fig. 4.3a. The output voltage waveforms from CC are shown in Fig. 4.3b. X_1 was delayed by an adjustable amount $t_d = R_dC_d$. R_d was a linear 100 kΩ

[†] Reed relay obtained from R.S. Components Ltd. (Stock No. 349-355).

[#] R_1 is the 10 MΩ biasing resitor between the gate of Q_1 and ground (Fig. 4.2).

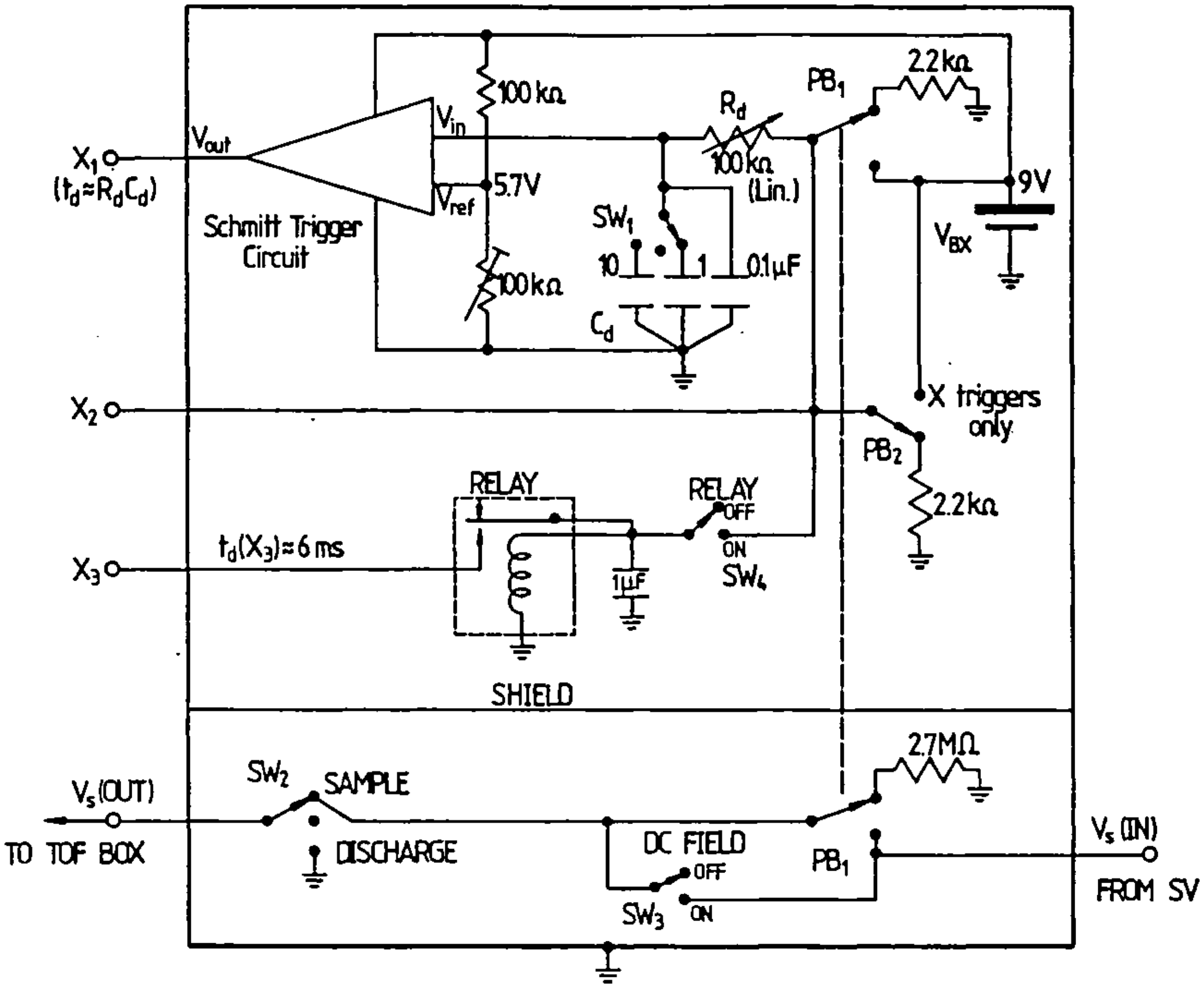

(a) Basic circuitry of the control box CC

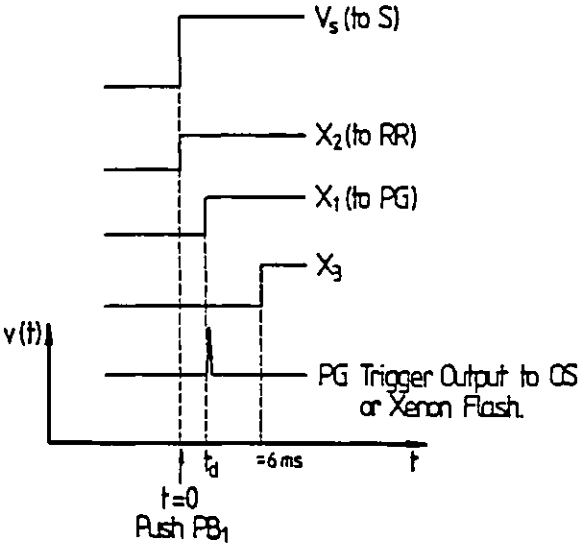

(b) Bias voltage V_s and X-trigger waveforms from CC

Fig. 4.3: The control box CC and its output waveforms

(<< R_{in} of the Schmitt trigger) potentiometer and C_d could be selected by a switch between 0.1, 1 and 10 μF values. Therefore a maximum delay of 1 sec was achievable. The delay t_d obtained was linear with the R_d potentiometer scale because the Schmitt trigger voltage was adjusted to 63% of 9V. A double pole double throw fast signal switch[†], PB_1, was employed to switch on V_s and the trigger pulses. PB_1 used quick make-and-break silver contacts. Its switch on time, including 'bounce', was measured to be about 0.1 msec on the 'slower pole'. Since there was some time lag between the two poles of PB_1, the pole with the quicker switch on time was used for the delay network. The slower pole switched on V_s. The X_1, delayed output, was connected to the PG to flash the xenon after a delay of $t_d + t_{XF}$ following the application of V_s. t_{XF} is the inherent time delay in the xenon flash unit, which was about a few microseconds. X_2 was connected to the reed relay RR to 'switch on' the input of the amplifier. In V-modes when RC was large, X_3 was used for RR. X_3 is a step voltage delayed by a fixed amount t_R through a relay, so the delay on X_3 depended on this relay's voltage V_{BX}. For V_{BX} = 9V, $t_d(X_3)$ was ≈6 msecs which is larger than the maximum CR of ≈4.6 msec available for V-mode measurements. If V_{BX} is doubled, $t_d(X_3)$ falls to 2.5 msec. A sample discharge switch was also incorporated into CC. A separate push button was available to trigger the xenon flash line alone so that if required the samples could be short circuited and pulse illuminated for discharge purposes (§4.4).

The output from the voltage follower was amplified by a -10X MOSFET amplifier, MA in Fig. 4.2, the circuitry of which is shown in Fig. 4.4. There are two main reasons for incorporating a signal amplification: (i) the $\frac{C_s R}{t_T}$ ratio may be reduced further by a factor equal to the amplifier gain, (ii) the signal content of the I-mode waveform is inversely proportional

---

[†] Japanese make push button signal switch marketed by R.S. Components Ltd. as Stock No. 339-235.

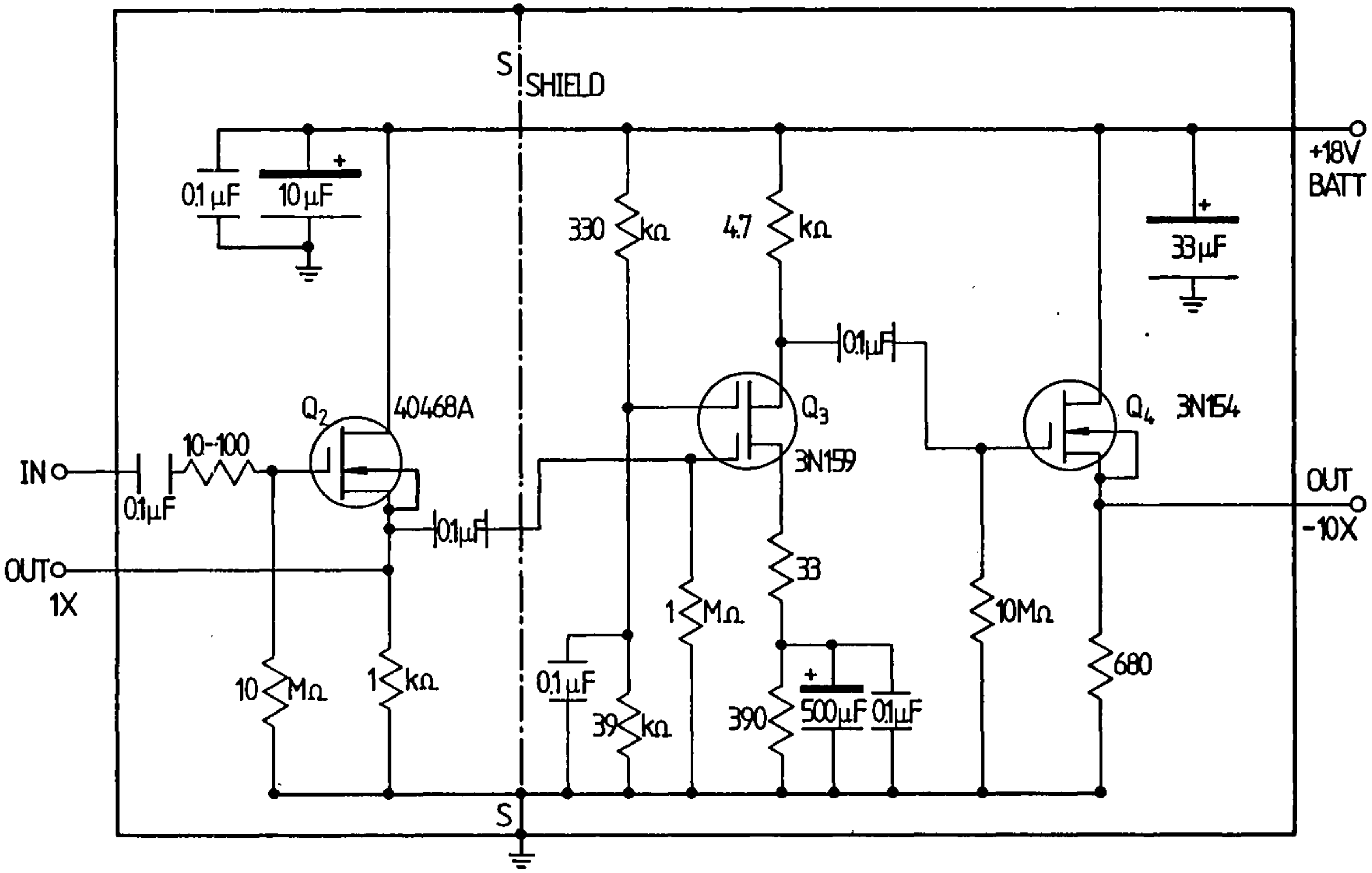

Fig. 4.4: Circuitry of the mosfet amplifier MA.

to the transit time and directly proportional to the injected charge Q_i. For a given $\frac{C_sR}{t_T}$ and $\frac{Q_i}{C_sV}$ ratios, the signal is weaker at low fields and therefore needs amplification. We can demonstrate this quantitatively by noting that, neglecting trapping effects, the I-mode signal can be shown to be

$$V_i = \alpha\beta V \tag{4.1}$$

where V is the applied voltage, and α and β are ratios defined as

$$\alpha = \frac{C_sR}{t_T} \tag{4.2}$$

and

$$\beta = \frac{Q_i}{Q_o} = \frac{Q_i}{C_sV} \tag{4.3}$$

For I-mode waveforms $\alpha \ll 1$, and for small signal or space charge free (SCF) conditions $\beta \ll 1$. The effect of α on the shape of the transient space charge limited current has been investigated by Silver et al, 1962, and the effect of β on the transient current waveform has been studied by Papadakis 1967. Taking $\alpha \approx \beta \lesssim 1/100$, we have $V_i \lesssim 10^{-4}V$. This means that the maximum distortionless, SCF I-mode signal at 10V applied is about 1 mV which, without the amplifier, cannot be resolved clearly on the oscilloscope.

The MOSFET amplifier MA was designed to have a large bandwidth and a low noise figure. A dual gate MOSFET which has a relatively high forward transconductance, $y_{fs} \approx 12{,}000$ mS, very low drain-gate feedback capacitance, $C_{rss} \approx 0.025$ pF and a low noise figure, 3.5 dB, was found to be excellent for use as an amplifier. The input and output of the dual gate MOSFET amplifier were buffered by single gate MOSFET source followers. The rise and fall times of MA were measured to be better than 15 ns. Note that the low frequency time constant of MA was 500 μF x 390 Ω, i.e. 200 ms, so only signals with durations much shorter than this could be amplified without distortion. The maximum sensitivity on the oscilloscope with the use of the amplifier was increased to 0.5 mV per cm. The noise level on the signal was about ~0.02 mV pk-pk, mainly due to the Q_1 and Q_2 stages. Note that for a 1 kΩ source resistance in Q_1 or Q_2, $\bar{v}_n$ (rms) = $[4kTRB]^{\frac{1}{2}} \approx 0.02$ mV for $B \approx 30$ MHz, the bandwidth of the oscilloscope. The shield SS which separates Q_2 from Q_3 and Q_4, is absolutely essential inasmuch as a three-pole transfer function can readily become unstable.

An LC filter using a series of LC arrangements was used to reduce further the power supply ripple and also filter out any r.f. pickup that occurred at the d.v.m. terminals. For temperature measurement it was not possible to insert a mercury thermometer into the TOF box without obliterating the TOF signal. The mercury thermometer acted as an aerial for the radiation from the xenon flash. An alcohol thermometer was used instead.

The excitation pulses were obtained from a xenon flash gun (General Radio Stroboslave 1539A) which was triggered from the PG. Its original xenon tube was replaced by an EGG tube type FX6A which gave a xenon flash of duration ≃0.5 μs between half intensity (not power) points. This was measured using a fast pin photodiode (Motorola MRD510). A typical intensity vs wavelength data for a xenon flash (see, for example, Henderson and Marsden, 1972) shows a general peak around 4000 Å (in the blue region) and a long tail far into the red region with several minor peaks at various wavelengths in the red and infrared region. Wavelengths longer than about 6500 Å give absorption depths δ (Hartke and Regensburger,1965) comparable with the thickness of the sample L, and therefore to satisfy the condition $\delta \ll L$ the red tail in the spectrum must be filtered out. This was achieved using a $CuSO_4$ solution which filters the wavelengths $\lambda \gtrsim 6000$ Å. Its transmission spectrum was measured on an absorption spectrometer. Note that the Au electrode on the sample strongly reflects the red and infrared wavelengths (Davey and Pankey, 1965).

With excitation wavelengths $\lambda \leq$ 6000 Å, the absorption depths are $\delta \lesssim$ 1 μm. The peak radiation at 4000 Å gives $\delta \approx$ 0.05 μm. It must be remembered that at long wavelengths, $\lambda \gtrsim$ 4500 Å, there is a considerable amount of absorption in a-Se without any free carrier pair generation. The quantum efficiency $\eta_{h\nu}$ for free carrier photogeneration becomes unity only for photon energies $h\nu \gtrsim$ 3 eV, or wavelengths $\lambda \approx$ 4100 Å. For smaller photon energies, $\eta_{h\nu}$ falls sharply with λ. At $\lambda \approx$ 6000 Å, $\eta_{h\nu} \approx 10^{-2}$. It can be seen that most of the free carrier generation occurs in a region of a few tenths of a micron from the surface.

4.3.2 TOF Cryostat System

To carry out transport measurements at different temperatures it was necessary to incorporate the TOF circuitry in a cryostat system. A stainless steel, well shielded cryostat was used to obtain low temperatures. Fig. 4.5 shows a basic diagram of the cryostat system used. It also shows how the TOF circuitry was completed in this case. A special shielded junction box, J, on the cryostat provided the connections to the sample S, heater H and the thermocouples, T_1 and T_2. The sample was mounted onto the copper base of the stainless steel 'cold finger' by using 'liquid solder'. Therefore the Aℓ substrate of the device was earthed. Hence the basic TOF circuitry in this case had the sample and the resistor R interchanged. The resistor R was actually outside the cryostat in a metal box M which also contained the voltage follower Q_1. The value of R was selected by a 12-way rotary switch as before. It should be apparent from Fig. 4.5 that Q_1 follows the signal across S which has the opposite polarity to that across R. The box M was plugged onto a b.n.c. terminal on the junction box, J, so that the main contribution to stray capacitance came from the single insulated wire W which travelled from the junction box, J, to the top electrode of S via a nylon pillar terminal N standing next to the sample. W was in fact connected at this support point, N, to a thin wire w which was stuck onto

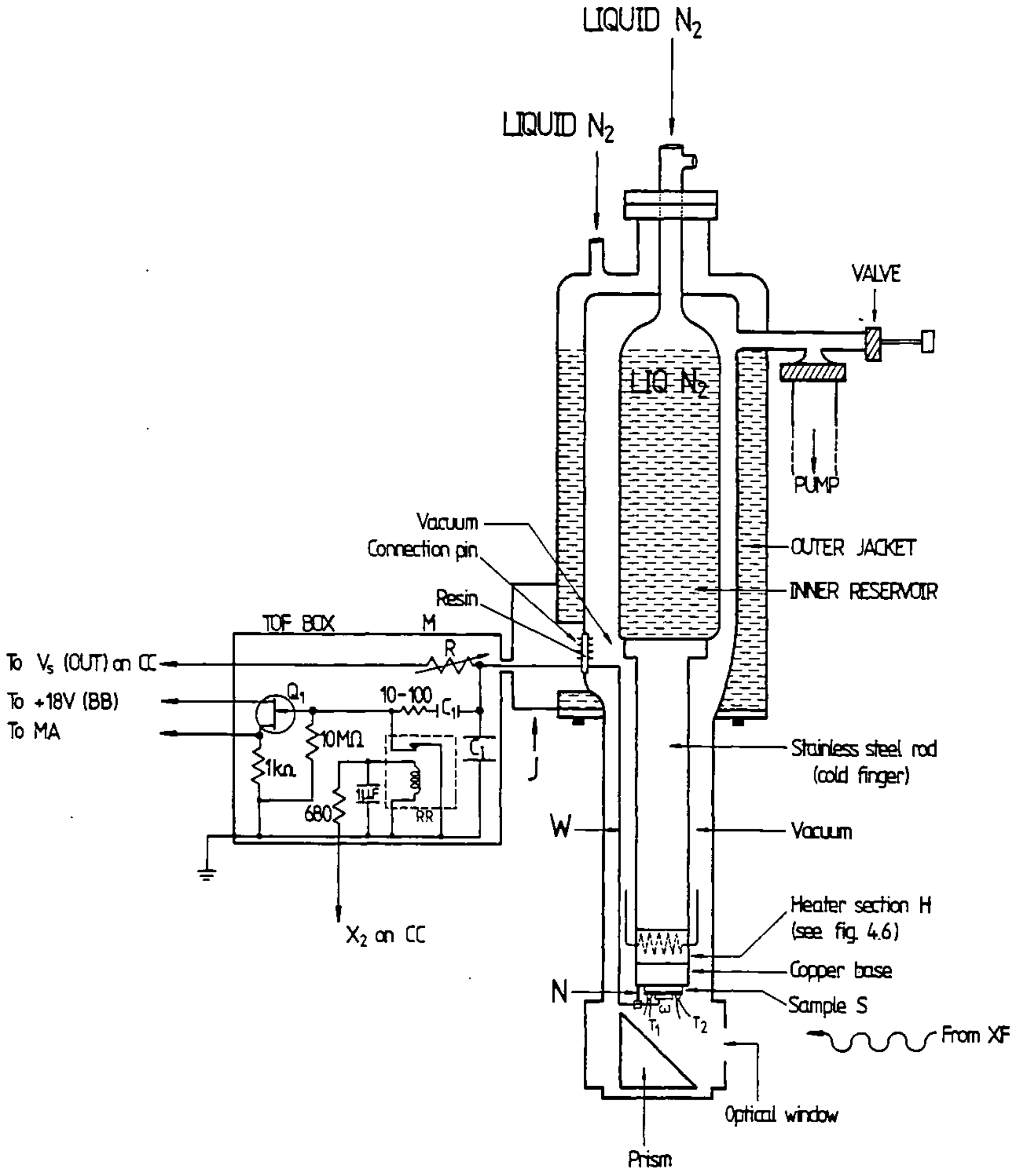

Fig. 4.5: The cryostat and the TOF circuitry

the top electrode of S by electrodag as before.

The main advantage of this arrangement is that the thermocouples can be directly attached to the surface of the selenium. Two chromel-alumel thermocouples stuck onto the selenium surface by electrodag, as shown in Fig. 4.6, were used to monitor the temperature of the selenium films. It must be remarked that it is absolutely necessary to shield the parts of the thermocouples outside the cryostat against radiation 'pick-up'. This is because the thermocouple points are directly attached to the Se films and any pick-up would be just coupled to the measuring top electrode and obliterate the TOF signal. Well shielded wires connected the thermocouples from the junction box, J, to a thermocouple junction box, TJ, which contained series RC-RC filtering networks as shown in Fig. 4.6. This filter network had a time constant higher than 20 ms but shorter than any of the cooling rates used. Note that the reference junction or the 0°C junction thermocouples were also well shielded.

The cryostat was pumped by a conventional vacuum system down to pressures better than 10^{-3} torr. Two coaxial cables carried the heater currents from a well shielded variac to the junction box, J. The maximum allowable current through the tungsten heater H was limited to 5A. It was, therefore, possible to have a reasonable manual control over the cooling rate (see next section §4.4).

§4.4 PROCEDURE FOR TRANSPORT MEASUREMENTS

Most TOF measurements were carried out in the 'single shot' mode of operation. I-mode traces were normally used because of their easier interpretation. The traces were photographed by a polaroid camera (Shackman Instruments Ltd., Type B20) attached to the screen of the oscilloscope. This later enabled detailed analysis of the waveforms. After a single shot measurement, the sample was short circuited and pulse illuminated until

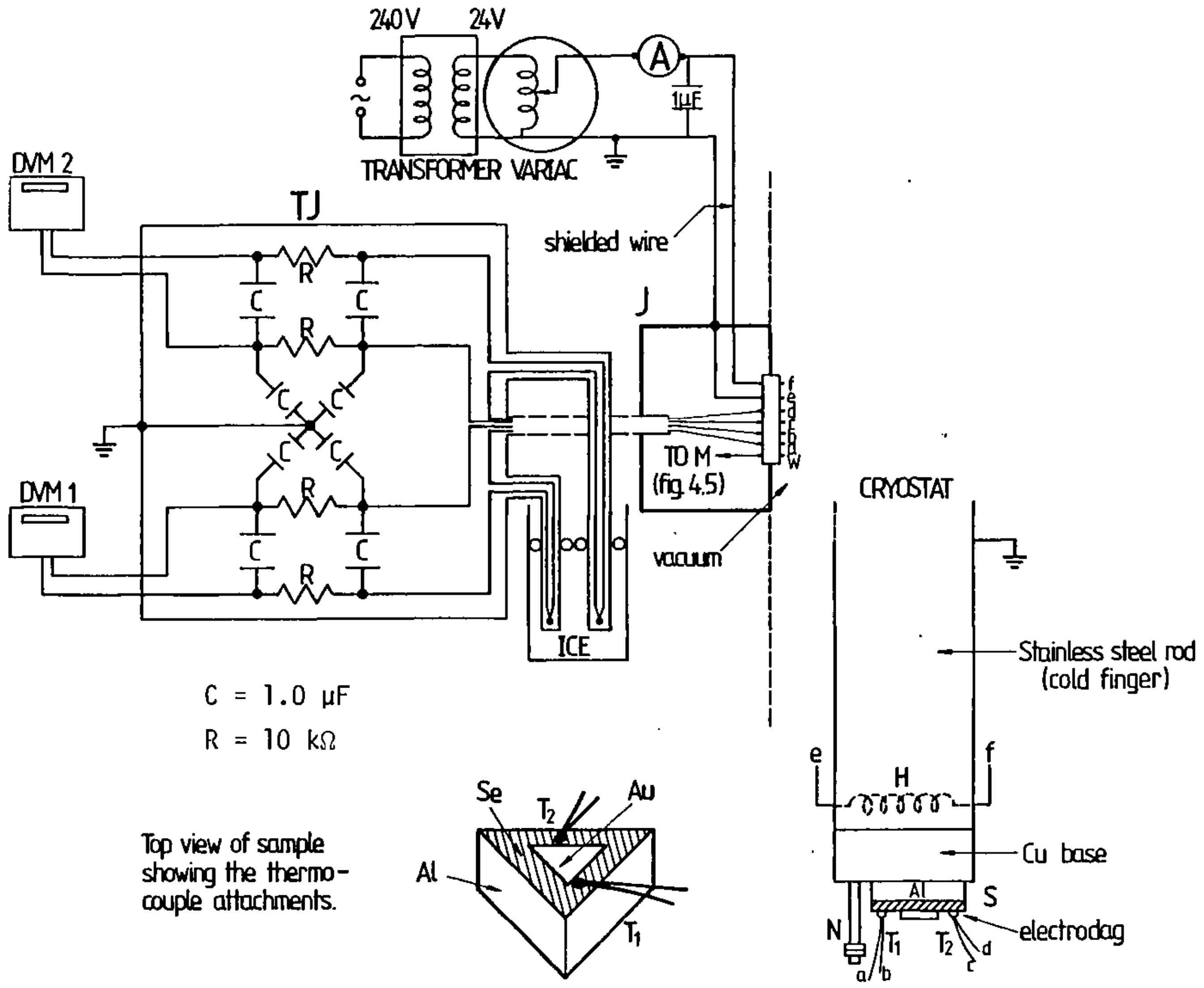

Fig. 4.6 : Heater and thermocouple circuits of the TOF cryostat. Also shown is an illustration of a typical sample. (Note that normally the exposed Se outside the Au contact is masked with black tape.)

no 'residual' TOF signal could be observed. Following this neutralization technique the device was rested (in dark) for several minutes. For TOF measurements at room temperature this rest time was about 10-15 minutes, longer than the typical dielectric relaxation times τ_{rel}. This is the time required to 'relax' any excess charge and restore charge neutrality. For pure a-Se, for example, with $\rho \approx 10^{13}\ \Omega$ cm, $\varepsilon_r \approx 6$; $\tau_{rel} \approx 9$ mins. For $Se_{1-x}Te_x$ alloy and Se + y ppm Cℓ samples the resistivity is lower so that τ_{rel} becomes shorter. In the case of mobility-temperature measurements this rest time was only a few minutes owing to a finite cooling rate.

The xenon light flash intensity was kept as low as possible to give signals of the order of a few millivolts. This was necessary to maintain small signal conditions during the measurements. Thin Au films deposited on glass slides were used when a reduction in the xenon flash intensity was required. High excitation intensity was found to give current waveforms which had similar appearance to those observed by Gibbons and Papadakis, 1968 on sulphur crystals. These waveforms show a progressive rise in the current and a sharp break at a time $t_T' \lesssim \frac{L^2}{\mu V}$, due to the space charge of the injected carriers (Papadakis, 1967). The transit time t_T was obtained from the break point of the current transient waveform. The mobility was calculated using $\mu = \frac{L^2}{t_T V}$. The trapping time τ was normally obtained from the analysis of the waveforms. For pure a-Se and a-Se with low level 'doping' the decay in the current at room temperatures was of the form $\sim e^{-t/\tau}$ as reported by many other researchers (see §2.5).

Before carrying out temperature measurements several dummy runs on the cryostat system using a dummy sample enabled a manual control procedure to be established on the cooling rate. Fig. 4.7 shows two typical temperature-time curves obtained by using different heating currents for the same amount of liquid nitrogen. These show that initially the rate of cooling is slow and non-linear (A → B) but later when the temperature has fallen by

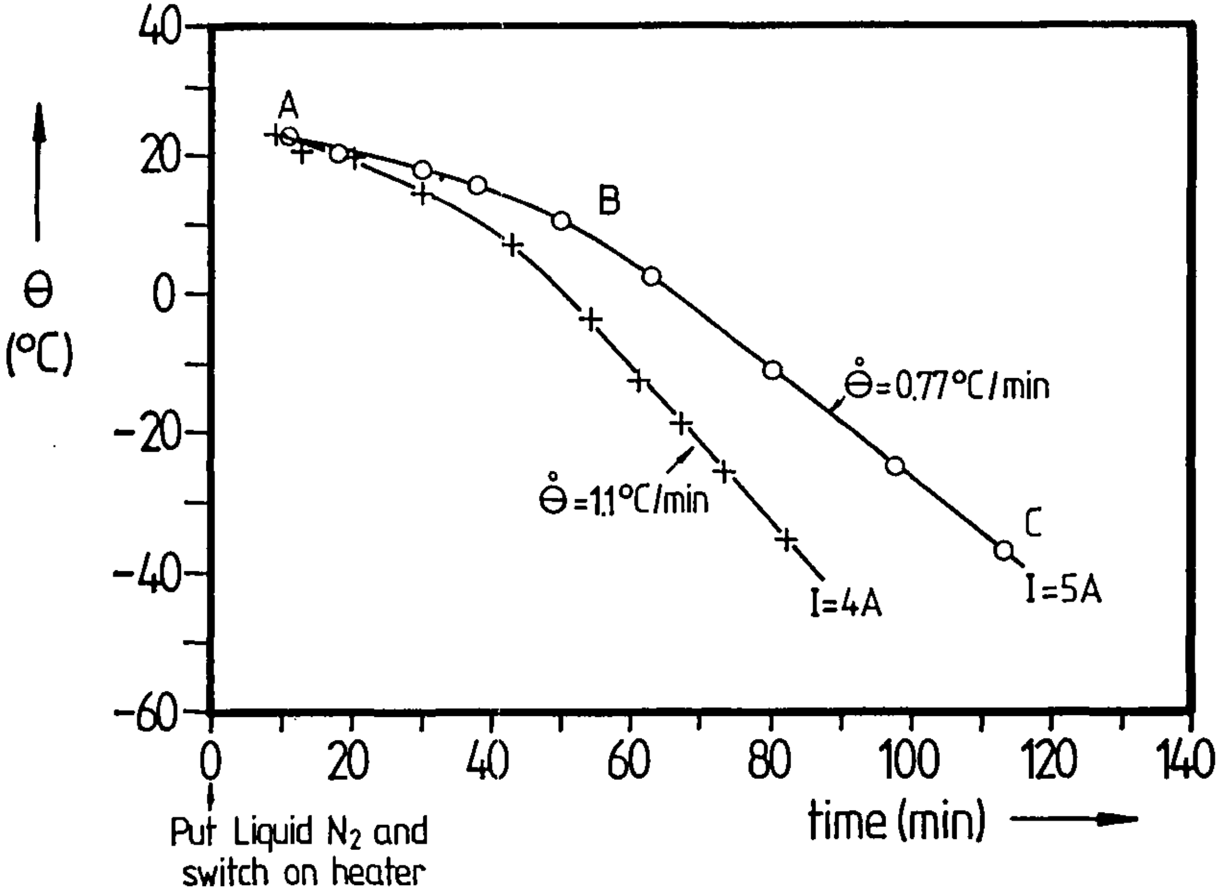

Fig. 4.7: Sample temperature-time relationship for two typical temperature runs. I is the heater current.

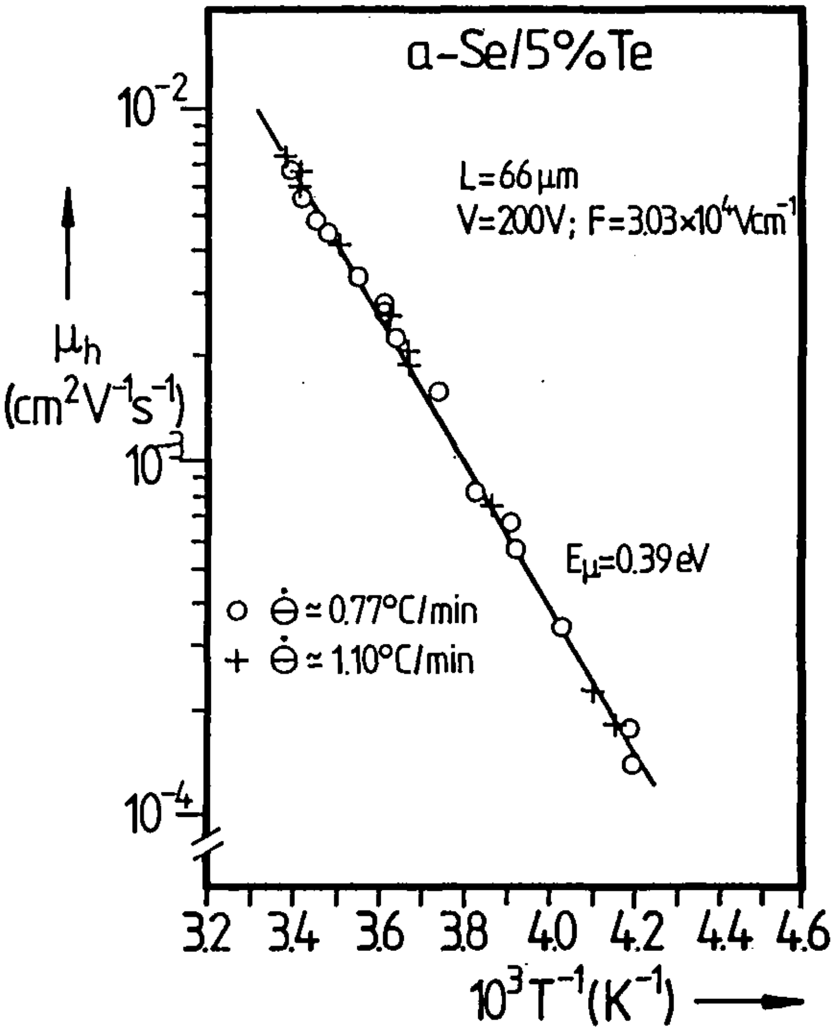

Fig. 4.8: Hole drift mobility-temperature measurements for a-Se/5%Te + 60 ppm Cℓ under two different sample cooling rates, $\dot{\theta}$.

~ 15°C the cooling rate becomes linear (B → C). TOF transport measurements carried out at these two cooling rates on an a-Se/Te film are shown in Fig. 4.8. It is clear from this graph that the cooling rate does not seem to affect the results. The mobility is thermally activated with an activation energy that is independent of the cooling rate. Therefore there is a good reproducibility of data at these cooling rates.

If, on the other hand, fast cooling rates are used, $\dot{\theta} \gtrsim 1°\mathrm{C}\ \mathrm{min}^{-1}$, it is found that the transport measurements show a dependence on $\dot{\theta}$. The results indicate that with fast cooling rates the $\log \mu$ vs T^{-1} curve 'lags' behind the 'true' $\log \mu$ vs T^{-1} curve. Although its low temperature activation energy is the same as the 'true' value its high temperature activation energy is lower. Such $\dot{\theta}$ dependent transport data cannot obviously be interpreted in terms of the usual transport arguments which are based on thermal equilibrium concepts.

It was noted that in the linear cooling range (B → C in Fig. 4.7) both the thermocouples on the sample gave identical readings. So, there was a uniform temperature across the surface of the film. In the non-linear range however it was recorded that there could be a difference of ~1°C across the surface. This implies of course a non-uniform temperature distribution in the sample.

In most temperature TOF measurements, typical cooling rates (B → C) were 0.5 - 0.7°C min^{-1}. Once the sample temperature dropped down to ≈-60°C, it was found that the films on the Aℓ substrates cracked. This was due to the mismatch of the thermal expansion coefficients of Se and Aℓ.

TOF measurements above the room temperature were carried out in two ways: (a) using the cryostat system and heating the sample from the heater H, or (b) using the room temperature TOF system but employing a hot air gun to heat up the whole TOF box. The latter was preferable inasmuch as the large heat capacity of the TOF box meant that the temperature could be controlled more easily and the temperature variations with time were small. Two thermocouples connected to two opposite faces of the box showed a temperature difference of ≃0.5 °C. So essentially, the sample was in a uniform temperature environment.

One serious difficulty experienced in measuring very long transit times (~20 ms) at low temperatures, particularly with Se/Te alloys in which the mobility is considerably lower than pure Se, was that the transient waveform was superimposed on an a.c. mains ripple of a few millivolts. Even the use of the highest excitation intensity could not provide sufficient transient current magnitude to eliminate this effect. There are two causes for the decrease in the signal strength with falling temperature. Firstly, the transient current amplitude is inversely proportional to the transit time, t_T, and secondly, the photogeneration efficiency falls with decreasing temperature (see, for example, Pai and Ing, 1968). Owing to the exponential dependence of t_T on T, the signal magnitude falls sharply with the drop in temperature.

It must be remarked on TOF measurements that the signal contents of I- and V-mode waveforms for a given bias voltage V depend on the acceptable limits on the ratios $\alpha = \frac{CR}{t_T}$ and $\beta = \frac{Q_i}{Q_o}$. Detectable signal strengths, excluding trapping effects, can be written as

$$V_i = \alpha\,\beta LF \qquad (\alpha \ll 1) \quad \text{I-mode signal} \qquad (4.4)$$

and

$$V_{vmax} = \beta LF \qquad (\alpha \gg 1) \quad \text{V-mode signal} \qquad (4.5)$$

where for SCF transients $\beta \ll 1$. Since we are normally interested in the field dependence of transport parameters, the TOF signals may be enhanced by using thicker samples. However, range limitations of the charge carriers, due to trapping, preclude the use of thicker samples. When the sample thickness is larger than $\mu\tau F$, where F is the field of interest, the transport becomes essentially trap-limited. The signal decays rapidly showing no transit time.

§4.5 SAMPLE PREPARATION

The selenium used in the preparation of the samples was obtained as small vitreous pellets, each typically 50 mgm in weight, from three different commercial manufacturers. From each manufacturer several different batches were obtained. The nominal purity of the selenium was 99.999%. This purity is the xerographic grade used in selenium based commercial xerographic photoreceptors. The required alloys of Se/Te were normally achieved by mixing the correct amounts by weight of pure selenium with portions of the prealloyed master batches. The Se/0.5 wt% As alloy was obtained as vitreous pellets from the manufacturers. The chlorine doping in the required content was achieved by mixing a pure selenium batch with a portion of a master chlorine doped selenium batch in correct amounts. Fractionation effects in the evaporated films due to the differences in vapour pressures of the elements comprising the alloy will be discussed later.

The samples used in this work were prepared industrially by vacuum evaporation on either Aℓ drums or Aℓ sheets. The Aℓ drums used as substrates were those typically employed in selenium drum based photocopying machines. The substrates were chemically cleaned before any evaporation. The evaporation plant was a conventional stainless steel vacuum system[†] pumped by a silicone diffusion pump to obtain a pressure of 10^{-5}-10^{-6} torr. Vitreous selenium pellets were evaporated from a stainless steel open boat. The boat temperature during deposition was about 310°C with a variation in the range 295-320°C. The Aℓ drums were rotated at a constant speed during the evaporation to ensure a uniform coating around the drum. The drum or substrate temperatures were normally held at 79-81°C. Note that this temperature is higher than the glass transition temperatures of any of the

---

[†] For example, as described by Yarwood, 1967 (Chs. 1 and 3).

alloys used (see §4.7). In a typical preparation procedure, for example, 40 gms of selenium pellets were evaporated onto an Aℓ drum in about 80 minutes giving a selenium film of thickness ≈50 µm. In the preparation of Se/Te alloy layers, the Te concentration across the layer thickness depends on the coating rate. The coating rates used were chosen to give a relatively uniform Te composition across the sample thickness. Generally it was found that the surface Te concentration could be reduced to be comparable to the bulk value by using slow evaporation rates (Rollason 1978, 1979).

After the evaporation of the selenium or selenium alloy, the coated drums were left to cool in the vacuum plant over an hour. Following this the coated drums were allowed to age or to 'anneal' over several weeks at room temperatures for bulk and surface relaxation. In this process some diffusion of Te, for example, occurs from the surface region, where initially there is a high Te composition to the bulk. It is expected that most physical properties would have been stabilized following this procedure (see, for example, Das, Bever and Uhlmann 1972, and Stephens 1976). Schotmiller 1975 has discussed the improvement in the xerographic performance of Se/As alloys arising from the ageing phenomenon.

The samples were cut out from these coated drums. To obtain uniform thickness devices, it was necessary to cut out the samples as far away from the drum edges as possible. This was important because the TOF signal in a non-uniform thickness device becomes distorted. The film thicknesses were measured on a comparator gauge (by Baty, London) after they had been stripped off their Aℓ substrates with liquid nitrogen. An a.c. bridge (Wayne Kerr Universal Bridge B224) was used to measure the sample capacitance from which the dielectric constant was determined. A typical device geometry was a triangle of sides ≈2.5 cm.

A semitransparent Au contact was deposited on part of the top surface by vacuum evaporation from a tungsten filament in a conventional vacuum plant*, under a pressure of ~10^{-6} torr. The thickness of the Au electrode was chosen to be a few hundred Ångstroms(≈300 Å was typical) to be semitransparent. A nomograph provided by Bond 1954 was found to be excellent in determining the weight of Au needed for a certain electrode thickness, given the evaporant-sample distance. It was found important to keep the selenium samples as far away from the filament as possible to avoid any surface crystallization during deposition. Distances $\gtrsim$12 cm were found to be adequate. The surface area outside the gold was masked with a black tape to stop light entering the sample from outside the electrode during transport measurements.

A typical Au electrode area was 0.5-1 cm^2. High conductivity paint (electrodag 915) was used to make the wire connections to the Au electrode and Aℓ substrate.

Note that for a few of the devices, Pd was used as the top electrode. The nomograph by Bond was again used to determine the weight of Pd evaporant needed for the required electrode thickness.

The sample compositions will normally be quoted in wt% for the alloys and will be written as A/x%B. The impurity contents will also be quoted by wt, i.e. p.p.m. will imply wt p.p.m. The conversion factor to at.% for small concentrations ($\lesssim$10%) is approximately given by the ratio of the atomic weight of Se to the atomic weight of solute. When an alloy formula is written in the form $A_{1-x}B_x$, however, x is in at fraction or at.% unless wt.fraction or wt.% is specified.

---

*Constructed by the author, 1976-1977, for metal evaporation

§4.6 MATERIAL AND SAMPLE CHARACTERIZATION

To determine the impurity contents of the samples in the p.p.m. range some typical specimens were sent for spark source mass spectrometer (S.S.M.S.) analysis at this college* as well as to Nottingham University†. For pure Se samples, the typical impurities detected are shown in Table T4.2 for two different manufacturers, A and B. Note the higher level of impurities in pure Se type A.

The Cℓ contents of the Se + y ppm Cℓ samples are not shown here, because any Cℓ amount mentioned in Chapter 5 would have been taken from such mass spectrometer work.

Bulk Te, or the 'average' Te, concentration in some of the samples was obtained using atomic absorption spectroscopy with a Te lamp, employing a standard solution†. These values agreed very well with the manufacturers specifications on the starting batches. The Te or As concentration distribution across the thickness of an alloy sample was obtained using a scanning electron microprobe (S.E.M.)*†#. This was also used to obtain the top surface Te or As concentration. The results in general indicated the following conclusions:

(1) In Se/Te alloys, the top surface region, $\lesssim 2\mu m$ of a 50 μm thick sample, has a Te concentration which depends on the coating rate. For fast coated samples it has been found that this concentration may be considerably greater than the bulk value. For slow coated specimens, the top surface Te composition becomes comparable to that of the bulk. The bottom surface region, $\lesssim 6$ μm, on the other hand, has a lower Te concentration than the bulk, by 40-50%.

---

*Analytical Laboratories of Imperial College, London

†Wolfson Institute, Nottingham University

#Principles of the S.E.M. technique and analysis are discussed by Campbell 1978

Table T4.2: Spark Source Mass Spectrometer Analysis for type A and B Selenium

Element	ppm content Type A	 Type B
Ag	< 0.8	0.3
Cu	0.06 - 0.1	-
Fe	0.5	0.3
Hg	< 0.8	-
Ni	0.3	-
O	1.5	-
Si	< 0.5	-
Te	1-2	-

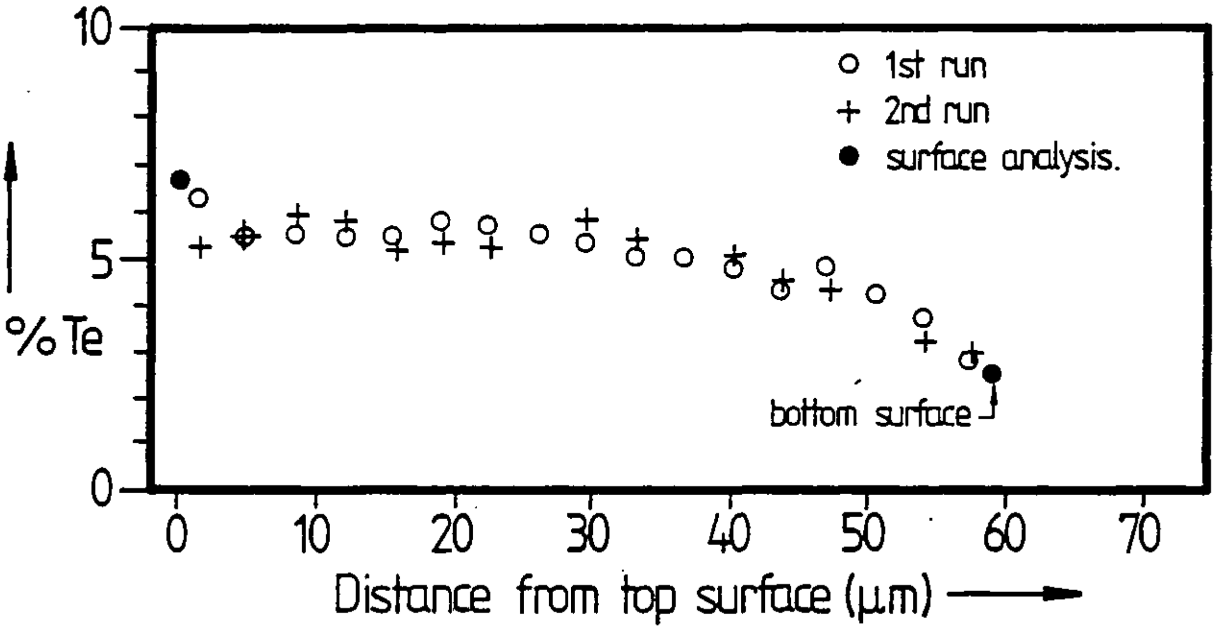

Fig. 4.9: Te density profile in a typical a-Se/5%Te sample

Fig. 4.9 shows a typical S.E.M. analysis on a Se/Te alloy.

The composition of the condensed material at any time during deposition would depend on the partial pressures of Se and Te in the vapour. Deviations from Raoult's Law would result in condensed layers having different compositions, i.e. fractionation effects. We can show that the partial vapour pressure of Te over the Se/Te alloy is lower than its Raoult's partial pressure because the latter occurs in an ideal solution in which all the bonds, Se-Se, Te-Te, Se-Te, are assumed to be alike (Moore 1976 Ch.7). These bond energies are given as (Pauling 1960) $E_{Se-Se} = 1.91$ eV, $E_{Te-Te} = 1.43$ eV and $E_{Se-Te} \approx 1.8$ eV. In fact, we calculated the latter by using the Pauling electronegativity equation, $\chi_{Se} - \chi_{Te} = [E_{Se-Te} - (E_{Se-Se}E_{Te-Te})^{\frac{1}{2}}]^{\frac{1}{2}}$. It can be seen that the Te atoms in the Se/Te solution are more tightly bound than those in the parent (pure Te) material. Consequently their escape tendency is reduced and the Te partial vapour pressure is lower than the Raoult value.

(2) In Se/0.5% As alloys, fractionation leads to the top surface ($\lesssim 2$ μm) having a richer As concentration by 50-100% over the bulk value.

The compositional profile of the chlorine was not known due to the difficulties of the analysis. In this connection note that using the TOF waveform itself as an indirect probe to determine the Cℓ profile has been suggested (Pai 1981, private communication).

To determine whether the method of preparation described above (§4.5) gives amorphous structures, X-ray diffraction studies were carried out on some typical films from pure Se, Se/0.5% As and Se/7% Te coated drums. In this study, an x-ray cylindrical texture camera was used. Full details of this camera and the principles behind its operation have been discussed by Wallace and Ward, 1975. The diffraction patterns of polycrystalline films in this technique are 'textured' horizontal lines, bound within a cone, at $y = R \cot 2\theta$ where R is the radius of the camera and θ the Bragg angle. Since the radiation wavelength (CuK_α wavelength) is accurately known, the interplanar distances can readily be determined. The diffraction photographs showed no evidence of any crystalline structure. Therefore it was assumed that the preparation method described in §4.5 gave essentially amorphous films. Note that the cylindrical texture camera method is not a quantitatively useful technique for studying disordered structures.

§4.7 THERMAL ANALYSIS

4.7.1 Introduction

Differential Thermal Analysis (DTA) and Differential Scanning Calorimetry (DSC) are techniques for studying the thermal behaviour of materials as they undergo physical and chemical changes during heating. There are many detailed review articles and books on DTA and DSC techniques which discuss the principles, instrumentation and analysis of data (see for example, Wendlandt 1964,Ch5, Ke 1964 Ch. 9, Daniels 1973 Ch.4, Jespersen 1978 and for review of DTA on polymeric materials, see Murphy 1970 and references therein).

4.7.2 Experimental Details

DSC studies were carried out on a Dupont Differential Thermal Analyser, type 990, equipped with the DSC cell attachment (e.g. as described by Mackenzie and Mitchell 1970). The specimens were either in the form of crimpled films stripped off their substrates by mechanical means or they were vitreous pellets. The samples were placed in small $A\ell$ pans and then sealed. An empty pan was used as the reference. Most temperature readings from the thermograms required a small calibration correction. The ordinate calibration was normally to within 10-15%. The tests were carried out from room temperature upwards.

4.7.3 Experimental Results and Discussion

Some typical DSC thermograms obtained are shown in Figs. 4.10 and 4.11 for pure a-Se and a-Se alloy pellets and films. These traces show three phenomena of interest, (i) the melting endotherm with melting point T_m, (ii) the crystallization exotherm, with maximum rate occurring at temperature T_c and (iii) the glass transition, at temperature T_g. 'Significant' crystallisation begins at T_x.

The enthalpy ΔH of the transition associated with a DSC peak may be found by evaluating the area A enclosed by the peak. The relationship which gives ΔH as heat evolved per mole is

$$\Delta H = \left(\frac{M}{m}\right) \left(\frac{1}{r}\right) A \qquad (4.6)$$

where M is the atomic (or molecular)weight of the material, m is the weight of the specimen used in grams and r is the heating rate $\dot{\theta}$ or $\dot{T}$ (in °Cs^{-1} or Ks^{-1}). This formula assumes that r is a constant independent of the temperature and A is found by integration of the peak bound between T_1 and T_2 using

$$A = \int_{T_1}^{T_2} C(T) \left(\frac{\partial \Delta H}{\partial t}\right) dT \qquad (4.7)$$

where C(T) is a calibration factor for the ordinate $\left(\frac{\partial \Delta H}{\partial t}\right)$. When the instrument is properly calibrated C(T) should, ideally, be unity. Besides the temperature T, C(T) will also depend on m, r, 'time and usage', etc.

<u>Melting:</u> The melting endotherm for pure Se was a sharp peak with a fusion temperature $T_m \approx 219$°C which was independent of the heating rate. T_m was the same for pellets and films and increased approximately linearly with the Te composition. Addition of 0.5% As was found to broaden to endotherm and reduce

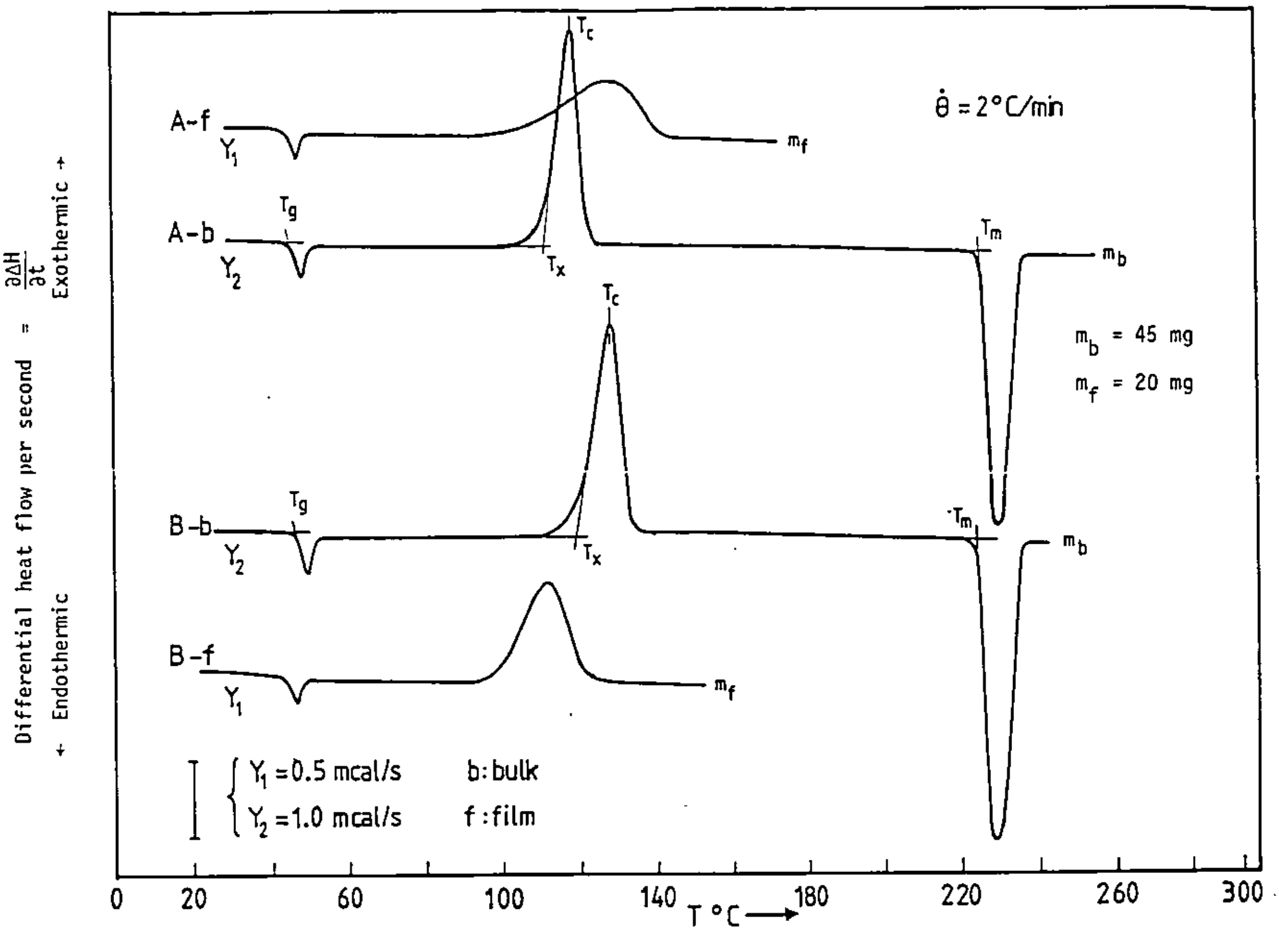

Fig. 4.10: DSC thermograms for A and B type a-Se

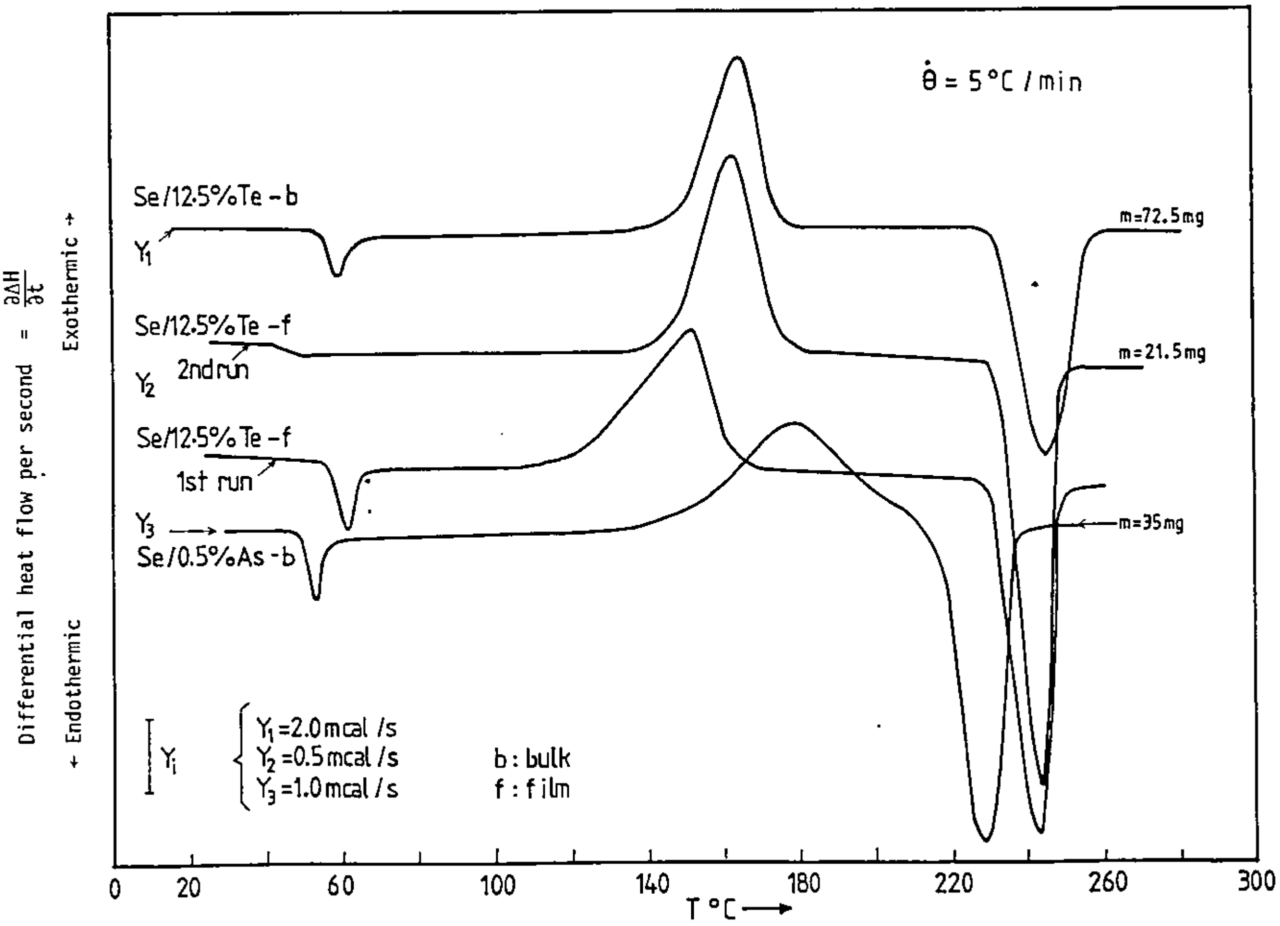

Fig. 4.11: DSC thermograms for Se/Te and Se/As alloys

T_m to ≈ 215°C. Note that in the latter T_m was less well defined. The upper parts of Fig. 4.12(a) and (b) show the effects of alloying selenium with Te and As on T_m and ΔH_f, the fusion enthalpy.

Before melting the samples would have gone through crystallization. Thus the melting endotherms represent the reaction:

$$\text{trigonal (poly)crystalline-Se} \rightarrow \text{liquid Se} \quad ; \quad \Delta H_f \qquad (4.8)$$

i.e. $$\gamma\text{-Se} \rightarrow \ell\text{-Se} \quad ; \quad \Delta H_f$$

The fusion enthalpies (latent heats of fusion) calculated for pure Se, by the numerical integration of the endotherms, have been in the range 1.20 - 1.56 kcal mole^{-1} with an average value 1.4 kcal mole^{-1}. This is within the range of values quoted in literature, e.g. 1.35 kcal mole^{-1} (Tomura et al 1975), 1.49 kcal mole^{-1} (Moynihan and Schnaus 1970), both from DSC measurements. The variations in ΔH_f values calculated are probably due to the difficulty in evaluating A from sharp and narrow peaks, instrumental and calibration errors mentioned above.

The melting enthalpy ΔH_f seems to decrease with Te concentration (Fig. 4.12(a)) indicating a reduction either in intramolecular and/or intermolecular forces in Se/Te alloys. The bond enthalpy for the Se-Te bond is smaller than that for the Se-Se bond as mentioned previously in §4.6, so that the reduction in ΔH_f in part may be attributed to weaker intrachain bonding in Se/Te. For Se/0.5% As, ΔH_f is relatively unchanged (Fig. 4.12(b)).

Crystallization: The shapes and positions of the exothermic peaks of crystallization have been found to depend on the heating rate, sample preparation, thermal history, and material composition (see Figs. 4.10, 4.11 and Table T4.3).

(i) Pure Se: The crystallization onset temperature T_x and the maximum rate temperature T_c are different for bulk and film samples. For the selenium from a given manufacturer there are also differences between batches. Within a given batch however the bulk and film thermograms, although different, are

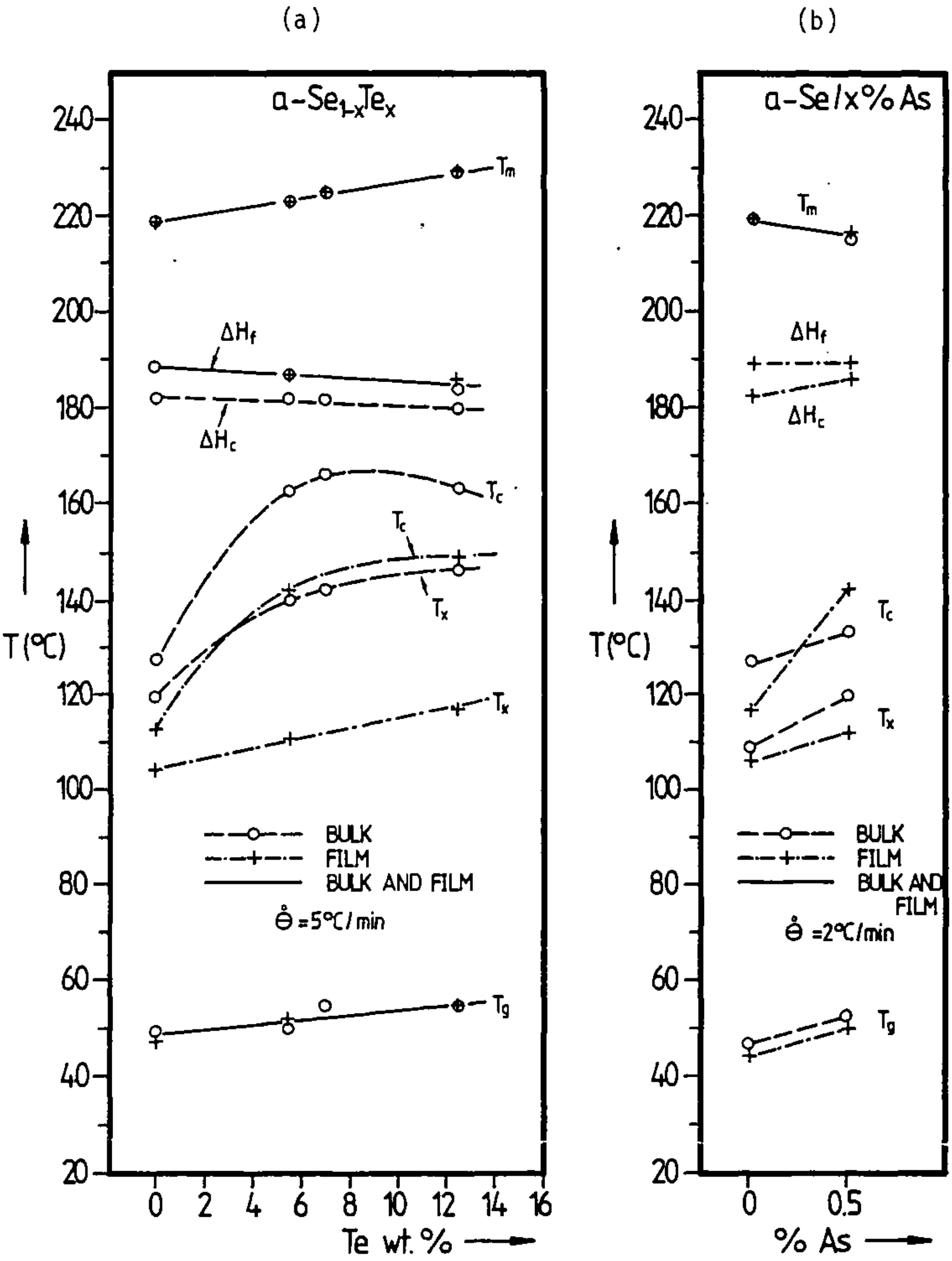

Fig. 4.12: Melting temperature T_m, maximum crystallization temperature T_c, crystallization onset temperature T_x, glass transition temperature T_g, fusion and crystallization enthalpies, ΔH_f and ΔH_c, vs composition in the systems (a) a-$Se_{1-x}Te_x$ and (b) a-Se/x%As.

reproducible to within about 2°C. Since for a given batch the Se pellets are prepared nearly identically (probably at the same time from the same source of Se) the reproducibility is not unexpected. For film samples from the same drum, reproducibility is also observed. Table T4.3 shows a summary of DSC data on two different sources (manufacturers) of selenium. It can be seen that, type B bulk samples have higher T_x and T_c temperatures than type A bulk samples. More rapid crystallization in batch A samples may be due to their higher amount of impurity content as noted previously in T4.2 (§4.6). Impurities in small amounts, in general, encourage crystallization via heterogeneous nucleation. On the other hand the differences may be due to the varied preparation techniques (e.g. quenching temperatures, methods, etc.) of the manufacturers. Little information is available on the details of production.

It can also be seen from T4.3 that the films tend to crystallize more rapidly, i.e. have lower T_x and T_c than their bulk parents. This conclusion, however, is limited to the particular a-Se pellets used and films prepared as described in §4.5.

The enthalpy of crystallization, ΔH_c, corresponds to the heat evolved in the reaction

$$\text{a-Se} \rightarrow \gamma\text{-Se} \quad ; \quad \Delta H_c \tag{4.9}$$

and it seems to depend on the batch rather than the sample being in bulk or film form. For example, for A-batches, whether bulk or film, $\Delta H_c \approx 1.1$ kcal mole^{-1} and for B-batches $\Delta H_c \approx 1.3$ kcal mole^{-1}. It must be remarked, however, that 15-20% difference in ΔH_c may still be due, if not in full then in part, to the instrumentation and calibration errors. For example, ideally the specimens (and also the standard) should be of the same weight since the $(\frac{\partial \Delta H}{\partial t})$-axis is not necessarily linear in m (Daniels 1973 Ch. 4).

The activation energy for the crystallization may be found using Kissinger's (1957) equation, i.e.

$$\frac{d[\ln(rT_c^{-2})]}{d(T_c^{-1})} = -\frac{\Delta h}{R} \tag{4.10}$$

Table T4.3: Summary of Pure Se DSC Data

Batch	$\dot{\theta}$ (°C/min)	T_g (°C)	T_x (°C)	T_c (°C)	T_m (°C)	ΔH_c (kcal/mole)	ΔH_f (kcal/mole)
A Bulk (A3)	1	44.5	101.0	108.5	-	0.99	-
	2	47.5	109.0	111.5	-	0.92	-
	5	50.5	118.5	127.5	-	1.14	-
	5	50.0	118.0	126.0	219.0	1.03	1.21
	10	53.0	128.5	138.5	-	1.12	-
A Bulk (A3X)	2	46.0	109.0	116.0	221.0	1.01	1.32
	5	49.0	120.0	129.0	-	0.99	-
A Bulk (A28387)	2	45.5	121.0	135.0	220.0	1.30	1.40
A Film (A3)	2	44.0	106.0	124.0	-	1.00	-
	2	44.0	106.0	127.0	-	0.97	-
B Bulk	2	47.5	117.0	126.0	221.0	-	-
	5	51.0	130.5	141.0	219.0	1.20	1.56
	5	51.0	131.0	141.0	-	1.30	-
B Film	0.5	41.0	84.0	94.5	-	1.35	-
	1.0	42.5	87.0	96.0	-	1.41	-
	2.0	44.5	97.5	106.5	-	1.50	-
	5.0	48.0	104.5	113.0	-	1.33	-
	10.0	51.0	112.5	127.0	-	-	-
	20.0	53.0	124.0	139.5	-	-	-

<u>NOTES:</u> ΔH_f(average) ≈ 1.37 kcal/mole. ΔH_c(average) for A type Se ≈ 1.00 kcal/mole and for B type Se ΔH_c(average) ≈ 1.35 kcal/mole

where Δh is the activation energy of the reaction (crystallization) and R, the gas constant. This equation can readily be derived (see, e.g. Thornburg and Johnson 1975) by writing the reaction rate as

$$\frac{dx}{dt} = c(T)\ (1-x) \tag{4.11}$$

where x is the fraction of crystallized material and c(T) is the rate constant given by

$$c(T) = c_o \exp(-\frac{\Delta h}{kT}) \tag{4.12}$$

in which c_o is a constant in $[s^{-1}]$ independent of T. Location of the maximum in the crystallization exotherm is then found by $\frac{d^2x}{dt^2} = 0$ (see Appendix A1).

Fig. 4.13 shows plots of $\ell n[r/T_c^2]$ vs. $1/T_c$ for batch A bulk and batch B bulk and film samples. It can be seen that the plots confirm a thermally activated behaviour with the rate equation of the first order, eqn. (4.11). Fig. 4.13 also shows the activation energy Δh and the pre-exponential c_o values. These values are comparable with those obtained on other a-Se samples by similar DTA/DSC analysis† (Grenet et al 1980, Thornburg 1976). For example for a-Se deposited on Aℓ (but not stripped off it) Grenet et al find $\Delta h = 0.91 - 0.98$ eV and $c_o = (1.6 - 32) \times 10^9\ s^{-1}$ depending on the ageing duration. For bulk a-Se, Thornburg reports $\Delta h = 1.14$ eV and $c_o = 1.4 \times 10^{13}\ s^{-1}$ but for a-Se previously deposited on Aℓ coated polymide he finds $\Delta h = 1.02$ eV and $c_o = 1.9 \times 10^{11}\ s^{-1}$.

It is apparent from Fig. 4.13 that although $\Delta h \approx 0.94$ eV seems to be approximately the same, within experimental errors, for bulk and film and for different bulk samples, the pre-exponential constant c_o varies considerably. Higher c_o would correspond to more rapid crystallization and hence lower T_x and T_c.

It is important to distinguish between ΔH_c, the crystallization enthalpy and Δh the crystallization activation energy. The former corresponds

---

† Motsuura and Suzuki 1979 report slightly lower activation enthalpies, e.g. $\Delta h \simeq 0.89$ eV for film and bulk (quenched from 700°C) a-Se. The bulk thermograms however were broad and/or had shoulders below T_c.

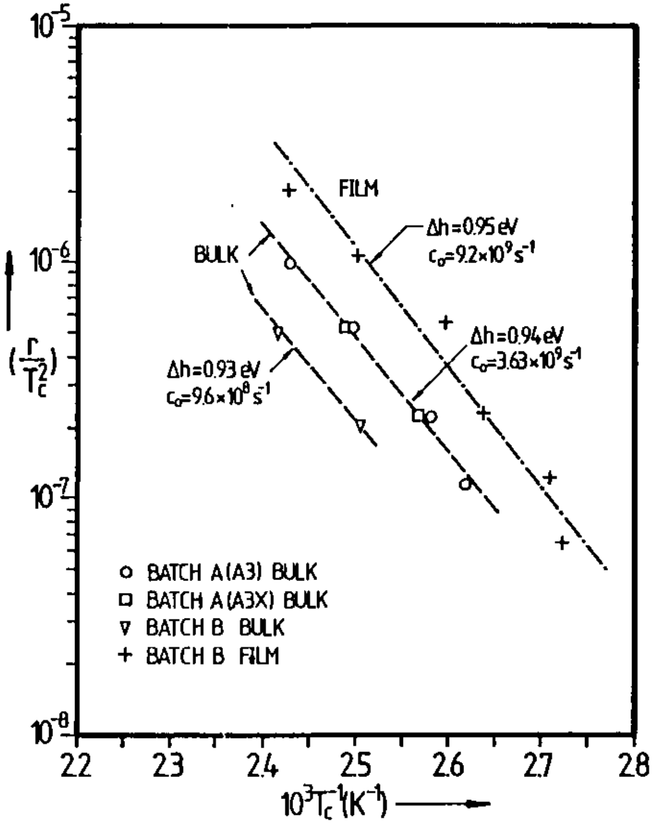

Fig. 4.13: Log (r/T_c^2) vs T_c^{-1} for different types of a-Se. Here r is the heating rate and T_c the maximum crystallization temperature.

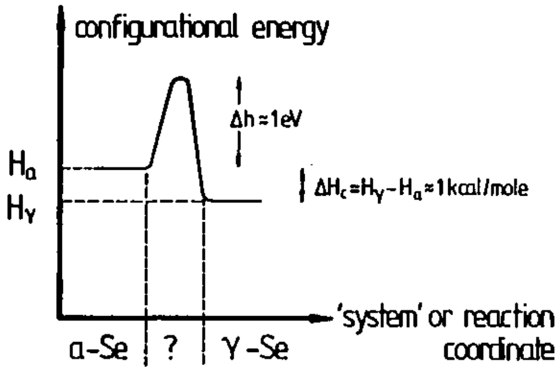

Fig. 4.14a: Thermally activated reaction

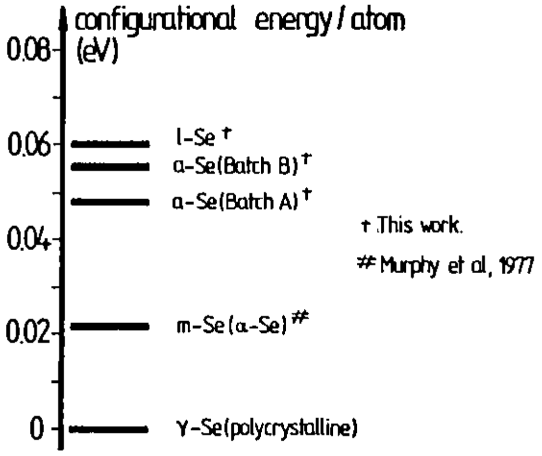

Fig. 4.14b: Relative energy per atom in different phases of Se. †DSC data of this work. #From DSC measurements of Murphy et al 1977.

to the enthalpy[†] or energy difference between the final (γ-Se) and initial (a-Se) states of a reaction whereas the latter corresponds to the height of a potential barrier, of one exists, which must be overcome in the process. Fig. 4.14a shows an energy-'configuration' diagram for a thermally activated reaction (e.g. Atkins 1978 Ch. 27, p. 906). The nature of the crystallization mechanism, as pointed out in §2.3, is not resolved (what happens in the '?' region in Fig. 4.14(a)?) Although the activation energy, ≈0.94 eV, is smaller than the Se-Se bond energy[#] (~1.9 eV, see also §4.6) it cannot be used as an argument to rule out the existence of Se_8 rings (or other rings, e.g. Se_6) in the amorphous phase and their polymerization during crystallization. This can be seen from the consideration of the phase transformation of monoclinic Se (m-Se) to the stable trigonal Se (γ-Se). The former consists of Se_8 rings whereas the latter of Se_8 chains (§2.2.1). The activation energy of this transformation is about ~1.1 eV/atom (Murphy et al 1977).

It is also possible for the activation energy Δh measured to represent the energy required to rotate or 'change' the dihedral angle ϕ by ~180°. It was pointed out in §2.2 that the signs of the dihedral angles along a 'chain' (or molecule) in a-Se may be random whereas in γ-Se they have the same sign. The magnitudes, on the other hand, were thought to be about the same ~102°. Thus 0.94 eV may be the potential barrier against this angle change.

[†] For solids and liquids, at normal pressures, reaction enthalpy $\Delta H \approx \Delta U$, change in the internal energy (e.g. Atkins 1978 Ch. 4).

[#] Pauling (1960) quotes (and others requote) the bond enthalpy for Se-Se as 44 kcal/mole (1.9 eV/atom). Alternatively, consider the dissociation enthalpy for $Se_2(g) \rightarrow 2\,Se(g)$ which is 72.96 kcal/mole or 3.16 eV/Se_2-molecule (Chandler et al 1966). Since this involves breaking two bonds, average energy per bond is 1.58 eV. Note, however, that the two bonds in Se_2 are not identical; one is a σ- and the other a π-bond.

Fig. 4.14 b shows a relative energy diagram for an arbitrary atom in different phases of Se. Note that the energy released ~0.05 eV per atom due to crystallization of a-Se is nearly twice that evolved (≈0.022 eV/atom) in the transformation of α-Se (α-monoclinic Se) to γ-Se.

The use of the DSC data in eqn. (4.10) to obtain Δh and c_o (as in Fig. 4.13 and in Thornburg 1976, Grenet et al 1980) accepts a first order rate equation (eqn. (4.11)) for the crystallization reaction. If the transformation rate $\dot{x}$ is written as an nth order equation,

$$\dot{x} = c(T)\ (1-x)^n \tag{4.13}$$

then the positions of the maxima in the crystallization peaks obey (Appendix A1, eqn. (a.5))

$$\ln \left[\frac{r}{T_c^2\, Y_c^{\frac{n-1}{n}}} \right] = \ln \left[\frac{n c_o k}{\Delta h\, \gamma^{\frac{n-1}{n}}} \right] - \left(\frac{\Delta h}{nR}\right) \frac{1}{T_c} \tag{4.14}$$

where $Y(T)$ represents the ordinate in a DSC thermogram so that $Y_c = Y(T_c)$ and $\gamma \equiv \frac{m}{M} \Delta H_c$.

When the DSC crystallization data, r, T_c, Y_c for, say, batch B film are used as input into eqn. (4.14) to calculate the correlation coefficient C_n for $n = 1$ and 2, we find $C_1 = 0.9787$ and $C_2 = 0.9760$. This justifies the employment of eqn. (4.11). Note that the activation energy for the second order reaction was ≈0.79 eV. Notice also that the slight asymmetry of the crystallization peaks in Fig. 4.10 indicates that the order of reaction is (Kissinger 1957)

$$n \approx 1.26\ (x/y)^{\frac{1}{2}} \approx 1 \tag{4.15}$$

which further supports the use of eqn. (4.11).

(ii) Se/Te alloys: The crystallization exotherm moves to higher temperatures with Te concentration both for bulk and film samples. Fig. 4.12(a) shows the effects of Te composition on T_x, T_c and ΔH_c. It can be seen that alloying Se with Te seems to inhibit crystallization. One explanation is the reduction in molecular mobility by the inclusion of heavier Te atoms in the molecular units. The enthalpy of crystallization ΔH_c, within experimental errors, remains relatively unchanged or indicates a slight decrease with Te content.

It is noticeable in Fig. 4.12(a) that for Te concentrations in excess of 5-6 wt.%, the crystallization exotherm at T_c seems to show little sensitivity to the Te composition. It can also be seen from the figure that the bulk alloys show slower rates of crystallization than their films following the similar behaviour noted above for a-Se.

(iii) Se/0.5% As alloys: The crystallization exotherms are broader and occur at higher temperatures in comparison with those for pure a-Se. Addition of 0.5% As thus inhibits crystallization. This is not unexpected since the trivalent nature of As implies that As atoms in these Se alloys can branch chains, i.e. form primary interchain bonds, and thus strongly hinder relative chain motion. Note that the crystallization peaks (at $r = 2°C\ min^{-1}$) for bulk a-Se and a-As_2Se_3 occur at $T_c \approx 126°C$ and $T_c \approx 310°C$ (Thornburg and Johnson 1975) respectively. The crystallization enthalpy seems to increase with the As addition. This may be attributed to the presence of strong Se-As 'branching bonds' which have an energy ~1 eV (e.g. Pelevin 1966) in comparison with the 'intermolecular' or interchain bond energies $\lesssim 0.1$ eV (Stuke 1974) in pure Se.

Glass Transition: An interesting feature of the glass transitions observed in the thermograms (see Figs. 4.10 and 4.11) is that in addition to the change in the base line they also show an endothermic peak. One may expect the glass transition to be evinced only as a change in the base line corresponding to ΔC_p. This is indeed observed in thermograms on samples during second thermal cycling carried out immediately after cooling from the first cycle so that there was insufficient time for annealing (see Fig. 4.11).

As discussed in §2.3.1, during the isothermal annealing of a sample which has just been cooled through its T_g, the structure relaxes towards the equilibrium state corresponding to the extended liquid state at the same temperature (see Fig.2.13 p.48), losing some of its surplus enthalpy. In the subsequent heating cycle this heat lost has to be replenished; hence the endotherm.

Similar glass transition endotherms are also observed in various polymers (see review by Murphy 1970). In fact, to facilitate the identification of an endothermic peak in DTA as a glass transition phenomenon certain empirical rules have been proposed by Strella (1963); (1) the shape of the peak should be sigmoidal, (2) the maximum in the endotherm should increase linearly with the heating rate, and (3) the inflection point or 'T_g' should increase with the heating rate. These rules are best considered as useful guides rather than necessary or sufficient conditions. As applied to present work on DSC thermograms on a-Se, rule (1) is vague, rule (3) is true and rule (2) is obeyed for small heating rates though its general implication is valid, as shown in Fig. 4.15. This figure also shows the dependence of the glass transition enthalpy ΔH_g, on the heating rate, r. ΔH_g, representing the heat absorbed in the transition, initially increases with r and then at fast heating rates it seems to saturate. Such rate dependent transition enthalpy behaviour should be contrasted with a well defined transition enthalpy of a first order phase change; $\Delta H_f \approx 1.4$ kcal mole^{-1} found above showed no dependence on r.

(i) Pure Se: Table T4.3 also shows T_g values for various types of pure a-Se. It can be seen that at a given heating rate the bulk samples from different batches have approximately (to within 1°C) the same glass transition temperatures. This is surprising since the vitreous pellets come from different manufacturers and have different crystallization behaviour as noted above. The films seem to possess lower glass transition temperatures than their

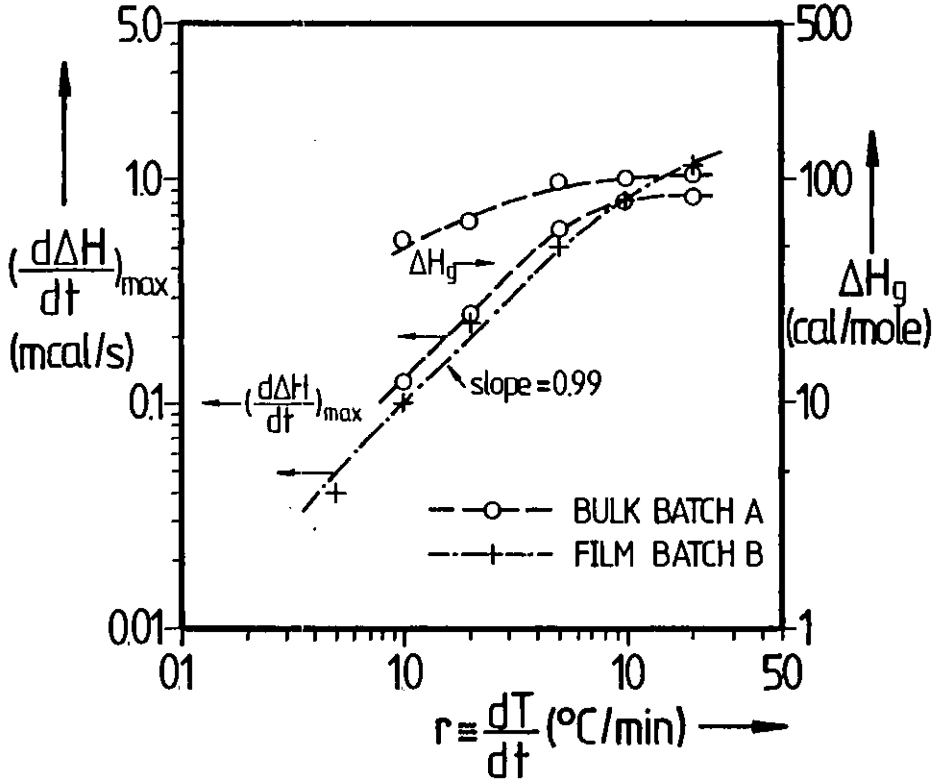

Fig. 4.15: Maximum differential heat flow per second, $(\frac{d\Delta H}{dt})_{max}$, and heat evolved, ΔH_g vs heating rate r in the glass transition region of a-Se.

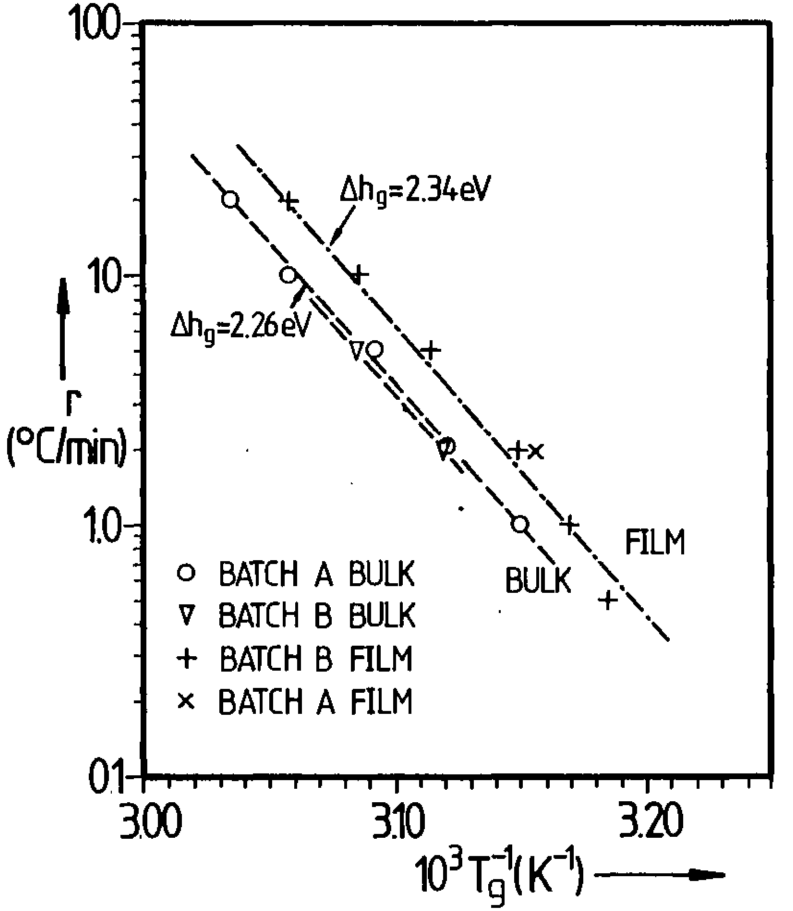

Fig. 4.16: Log (heating rate) vs T_g^{-1} for various a-Se batches.

parent bulks but notice that at a given r, T_g for different batch films are the same.

The cooling rate dependence of T_g obtained from the volumetric studies by Dzhalilov and Rzaev 1967 indicated that T_g and the cooling rate $q = |r|$ obey the empirical relationship (Bartenev and Lukianov 1955).

$$\frac{1}{T_g} = C_1 - C_2 \ \ell nq \tag{4.16}$$

with an activation energy ~2.1 eV/atom. This type of behaviour between the glass transition temperature T_g and q was predicted by Ritland 1954 (see also Moynihan 1974) from the kinetic or relaxational interpretation of the glass transition phenomenon (see §2.3.1) and Tool's (1948) fictive temperature concept[†].

Suppose the enthalpy H(T) of the system under consideration (Fig. 2.13, p.48), after some process, relaxes towards its equilibrium value $H_e(T)$ through a relaxation equation of the form

$$\frac{\partial H(T)}{\partial t} = - \frac{H(T) - H_e(T)}{\tau} \tag{4.17}$$

Then it can be shown that (Moynihan et al 1974, 1976, Larmagnac et al 1981)

$$\frac{d\ell n|r|}{d(T_g^{-1})} \approx - \frac{\Delta h_g}{R} \tag{4.18}$$

where Δh_g is the 'activation energy' for the relaxation time $\tau(T)$. It must be

---

[†] The fictive temperature T_f may be defined quantitatively by

$$[H(T) - H_e(T)]/(T_f - T) = C_{pe} - C_{pg}$$

where H(T) and $H_e(T)$ are respectively, the enthalpy of the glass at temperature T and the enthalpy of the 'equivalent' super-cooled liquid-equilibrium system at the same temperature. C_{pg} and C_{pe} are their heat capacities. T_g may be defined as the limiting value of T_f, i.e. $\lim_{T>T_g} T_f = T$ and $\lim_{T<T_g} T_f = T_g$. (See §2.3.1, pp. 42-46 for a qualitative discussion on T_g).

remarked however that this equation has a number of assumptions and approximations. For example, it is assumed that $\tau(T)$ can be expressed as

$$\tau(T) = a \exp(-bT) \exp(-cT_f) \tag{4.19}$$

where a,b,c are constants related to the material properties. T_g is obtained from heat capacity cooling curves started well above the transition region or heat capacity heating curves representing the heating of the glass from a temperature well below the transition region after it has been previously cooled through the transition region at a rate q equal to the heating rate. Further, in a small temperature range around some T_r in the transition region,

$$b \approx \frac{\Delta h_g}{RT_r^2} \tag{4.20}$$

Fig. 4.16 (p.48) shows log r vs T_g^{-1} plots for batch B bulk and film and for batch A bulk samples. The lines give a 'relaxation activation energy' $\Delta h_g \simeq 2.3$ eV/atom comparable with $\Delta h_g \simeq 2.58$ eV found by Larmagnac et al 1981 for a-Se films on Aℓ and $\Delta h_g \simeq 2.47$ eV found by Matsuura and Suzuki 1979 for bulk (quenched from $\gtrsim 450°C$) and evaporated a-Se. Since $\Delta h_g \simeq 2.3$ eV is larger than the Se-Se bond energy, bond breaking and chain reformation during the structural relaxation cannot be ruled out.

It is important to point out that Δh_g may not necessarily be as well defined as it appears, but may be some 'smeared' average energy parameter. This is because the enthalpy relaxation, (eqn. (4.17)), may be a sum of n processes, i.e.

$$\left[\frac{\partial H}{\partial t}\right]_T = \sum_{i=1}^{n} \left(\frac{\partial H_i}{\partial t}\right)_T = \sum_{i=1}^{n} \frac{H_i(T) - H_{ei}(T)}{\tau_i} \tag{4.21}$$

with each process i having its own relaxation time τ_i.

It may be of interest to rearrange the empirical relationship in eqn. (4.16) into the form (see, e.g. review by Owen 1973)

$$r = r_o \exp\left\{-\frac{\Delta h_g}{R}\left(\frac{1}{T_g} - \frac{1}{T_m}\right)\right\} \tag{4.22}$$

Then from Fig. 4.16 we find $r_o \sim 10^{11}$ K s^{-1}. The latter is the heating rate at which $T_g = T_m$.

Notice that the T_g values measured yield

$$\frac{T_g}{T_m} = 0.64 \rightarrow 0.67 \approx \frac{2}{3} \tag{4.23}$$

i.e. obeying approximately Kauzmann's (1948) two-thirds rule (see, e.g. review by Sakka and Mackenzie 1971).

(ii) Se/Te alloys: Fig. 4.12(a) shows the effect of alloying Se with Te on the glass transition temperature, T_g. Both for bulk and film samples, T_g increases nearly linearly with the Te composition. Since Te atoms are heavier and larger their substitution for Se atoms would be expected to decrease molecular mobility. One may view the amorphous Se/Te copolymer structure pictorially as a 'soup' or an entanglement of thousands of strings each having many random knots in it; knots representing the Te atoms. Motion of any string is then hindered by the knots and thus 'string mobility' is considerably reduced in comparison to an entanglement of strings without knots (pure a-Se). This, however, is only a useful pictorial analogue and a more rigorous explanation may be put forward by noting that the inclusion of Te atoms in the a-Se structure would increase the average molar mass $\bar{M}_n$ and thus also increase T_g via the equation (Fox and Loshaek 1955, or see Young 1981, Ch.4).

$$T_g = T_g^{\infty} + K\bar{M}_n^{-1} \tag{4.24}$$

where K is constant and T_g^{∞} is the glass transition temperature at infinite $\bar{M}_n$.

Notice that, the rise in T_g with the Te concentration seems to be concomitant with that of T_m as shown in Fig. 4.12(a).

The increase in the softening temperature, i.e. T_g, with the addition of Te would also account for the slow crystallization rates observed in Se/Te alloys.

(iii) Se/0.5% As: The glass transition temperature as shown in Fig. 4.12(b) is increased by the addition of 0.5% As. Myers and Felty 1967 find that T_g in the Se-As system, as determined from DTA, increases with As content until the compound As_2Se_3 formation. Note that in bulk a-As_2Se_3 $T_g \simeq 175°C$ at $r = 2°C\ min^{-1}$ (Thornburg and Johnson 1975) is considerably larger than that in pure a-Se and thus the noticeable increase in T_g with 0.5%As is not unexpected. The rise in T_g, as pointed out in 2.3.1, is due essentially to the cross-linking of Se chains by the As atoms. Cross-linking bonds are now primary bonds (of energy ~1 eV) which means that relative chain motion and molecular mobility is diminished. The Se/As structure is more 'rigid' due to As containing regions having a three-dimensional covalent character.

4.7.4 Conclusions

Crystallization of a-Se is sensitive to temperature, heating rate, preparation methods, e.g. bulk or film, 'origin' of Se, i.e. batch, and impurities. The activation energy of crystallization, ~0.94 eV, however does not seem to depend on the origin and preparation of a-Se. The existence of Se_8 monomer units in a-Se structure cannot be ruled out from the energies involved in crystallization.

Addition of small amounts of Te and As inhibits crystallization. An increase in the crystallization onset temperature is accompanied by an increase in the softening temperature.

a-Se/Te alloys exhibit copolymer character in their crystallization and glass transition behaviour.

The glass transition temperature for a given form of a-Se, bulk or film, does not depend on the origin of Se. The relaxational (or kinetic) view of the glass transition phenomenon seems to provide a reasonable interpretation to the heating rate dependent data. Activation energy for the structural relaxation time is ~2.3 eV (for bulk and film a-Se) which probably implies structural relaxation involving bond breaking.

CHAPTER 5

RESULTS AND DISCUSSION

§5.1 INTRODUCTION

The previous chapter established the experimental procedure used for transport measurements. In this chapter the results of the TOF measurements and their interpretation and discussion are presented. The earlier chapters, with their different contents, were necessary not only to provide a meaningful and an essential background but also to serve as useful guides to data analyses, interpretations, discussions of this chapter and the conclusion hence drawn in the next chapter.

It may be helpful to view this chapter as a direct continuum to the DSC analysis of the last section, even though different properties are now under examination.

The analysis of experimental data involving curve fitting a function with two or three variable 'constants' (parameters) was carried out using the least squares method or the best (highest) correlation coefficient as described elsewhere (e.g. Heading 1970, Ch. 24).

§5.2 a-Se

5.2.1 Results and Discussion

(A) Hole Transport:

The shapes of the TOF transient current and voltage waveforms for hole transport at different applied fields are shown in Figs. 5.1(a) to (d). The arrows on the waveforms define operationally the transit times (t_T) which may be used to determine the corresponding drift mobilities via eqn. (3.3),

$$\mu = \frac{L^2}{t_T V} \qquad (5.1)$$

Fig. 5.2 shows a series of log t_T vs logV plots from I-mode measurements on different thickness but identical a-Se samples (e.g. batch A868). The current mode of operation is preferred over the voltage mode because the current

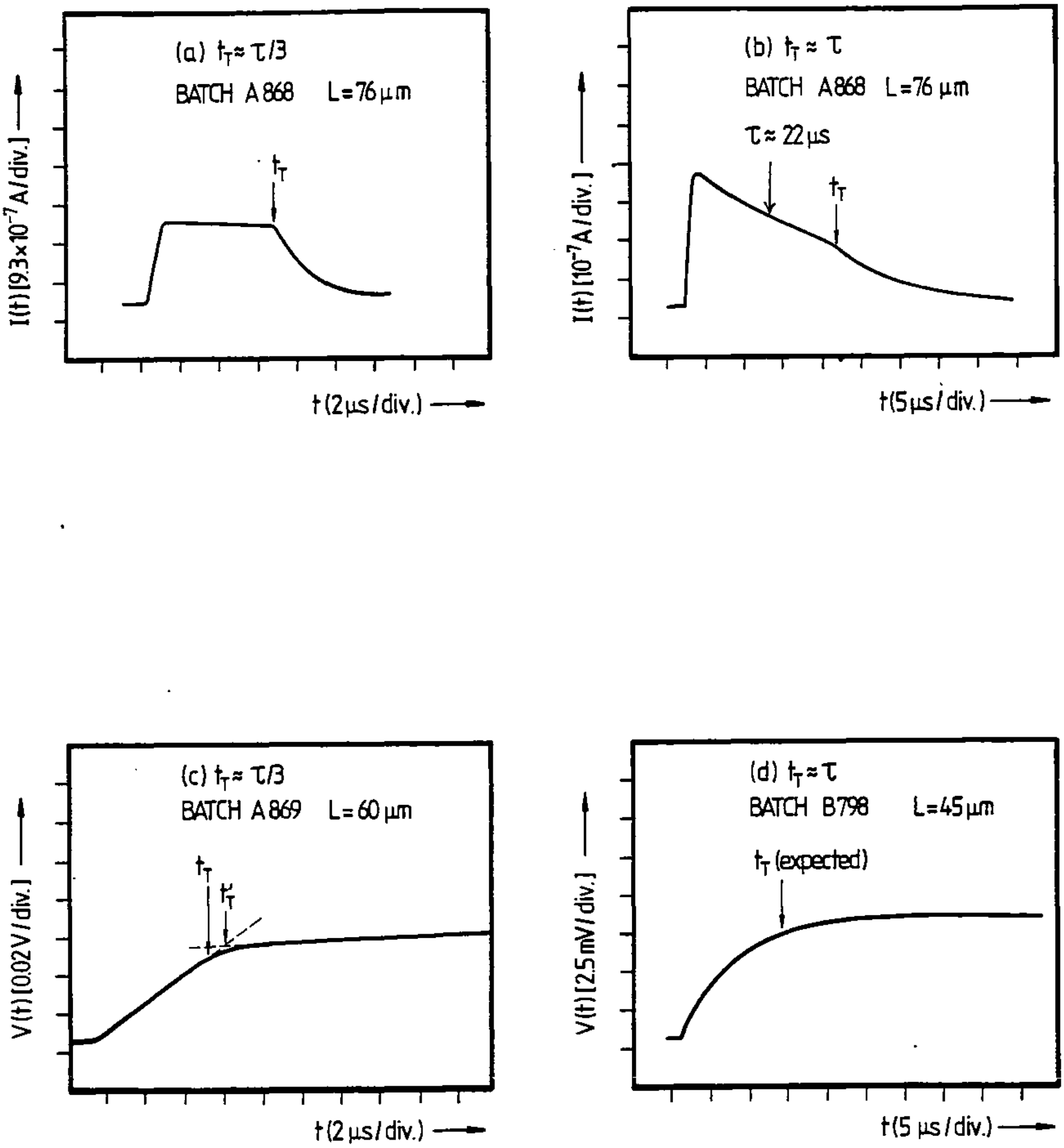

Fig. 5.1: Typical TOF waveforms for hole transport in a-Se. Transit times are indicated by t_T. Deep trapping time is τ. (a) and (b) are I-mode signals whereas (c) and (d) are V-mode.

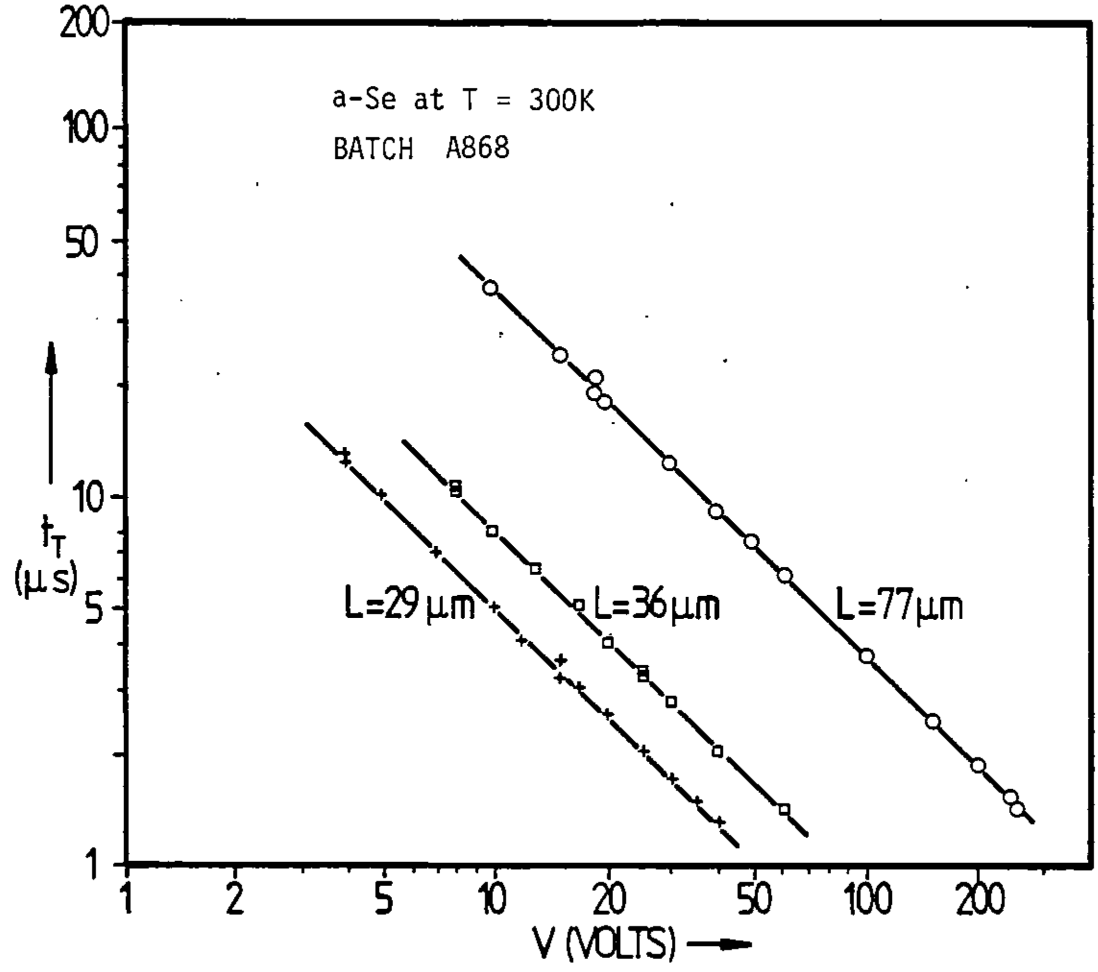

Fig. 5.2: Log-log plots of transit time t_T vs applied voltage V for a-Se samples of different thickness.

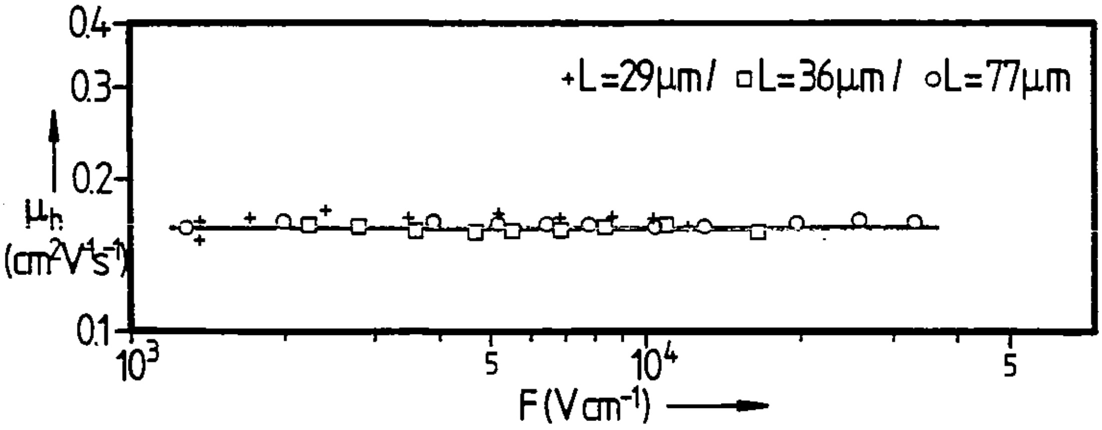

Fig. 5.3: Log-log plot of hole drift mobility μ_h vs applied field F. (Data from Fig. 5.2).

transient has the advantage that the transit time t_T is evinced by a clearer 'break' in the waveform as pointed out in §4.4.

The straight lines with slopes $s \cong 1.00$ in Fig. 5.2 indicate a field independent (constant) hole drift mobility, μ_h, which is confirmed by the log μ_h vs log F plots in Fig. 5.3. The latter plots at different thicknesses superimpose and thus also confirm that μ_h determined by eqn. (5.1) is a meaningful intrinsic property of the sample material.

It is apparent that the I-mode transient trace (a) in Fig. 5.1 is nearly an ideal square pulse displaying a clearly well defined transit time t_T and practically no trapping, i.e. obeying eqn. (3.5) or (3.25). The corresponding V-mode transient waveform in Fig. 5.1(c) as expected is nearly an ideal ramp. Both waveforms show slight rounding around t_T probably due to multiple trapping effects (see §3.3.1, waveforms (4) and (1) in Figs. 3.4 and 3.5). Trace (b) shows that at relatively low fields I(t) decays with time and shows a transit time which is not as sharply marked as in (a) but still observable. At the 'lowest' fields (corresponding to $t_T > \tau$) however no transit time could be discerned due to most of the injected carriers being deeply trapped before transit. Fig. 5.1(d) shows a V-mode transient for which $t_T \approx \tau$.

Fig. 5.4 shows some typical log I(t) vs t and log $[V_\infty - V(t)]$ vs t plots obtained from I-mode and V-mode transient waveforms respectively for various a-Se samples. The straight lines in the time domain $t \leqq t_T$ verify that the hole transient current decays exponentially until the transit time t_T. The time constant τ of the decay in I(t), or the rise in V(t), may be assigned to a deep trapping time or a lifetime following eqn. (3.11),

$$I(t) = \frac{Q_i}{t_T} \exp(-\frac{t}{\tau}) \quad ; \quad t \leqq t_T \tag{5.2}$$

as, for example, demonstrated previously by Tabak and Warter 1968 and others (see §2.5.3 and Fig. 2.21(c)).

To verify the assignment of the time constant τ_h of the TOF signal to a hole lifetime, τ_h values were checked against the sample thickness L, the applied field F, and the excitation light intensity J. The results of the

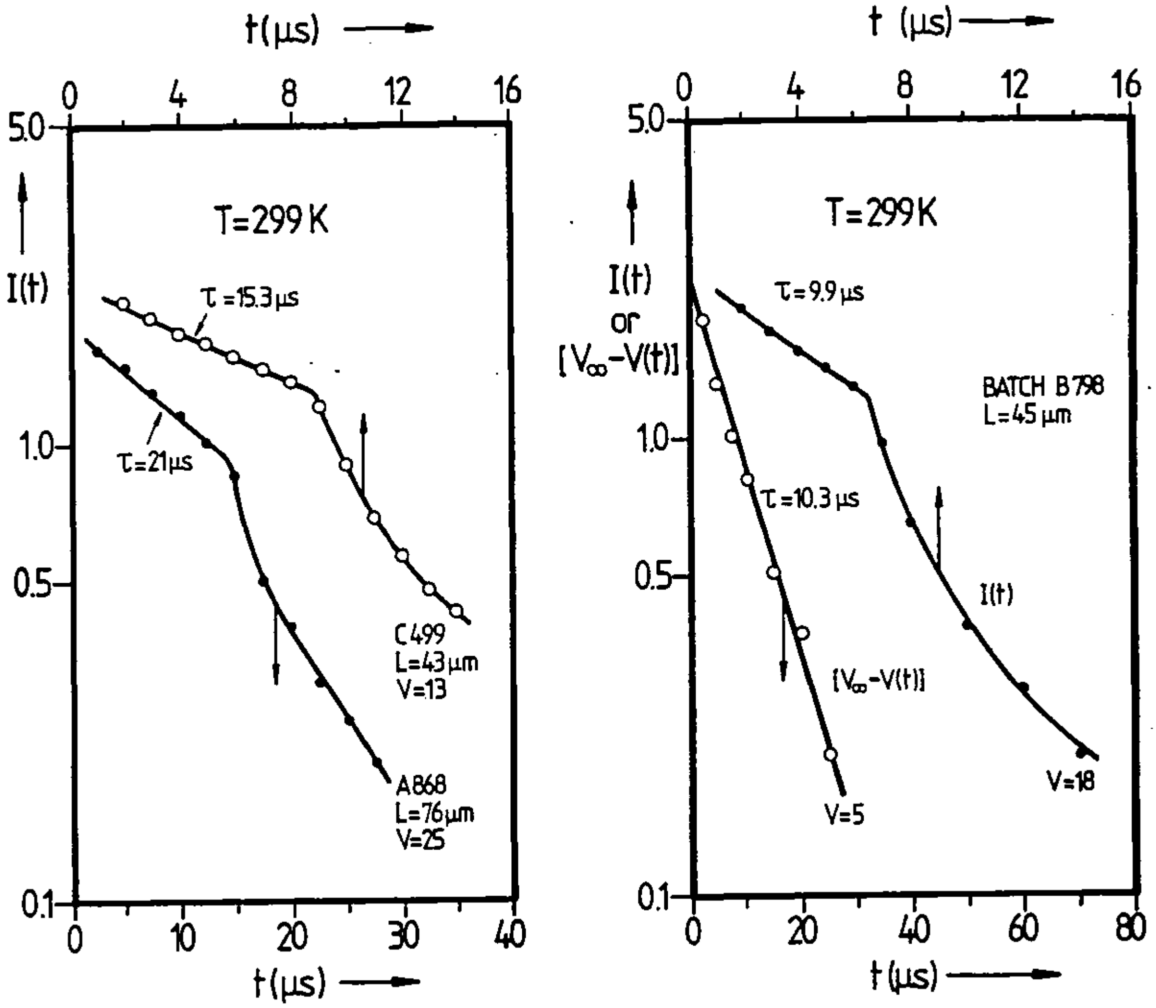

Fig. 5.4: Semilogarithmic representation of hole current and voltage transients for a-Se at room temperature.

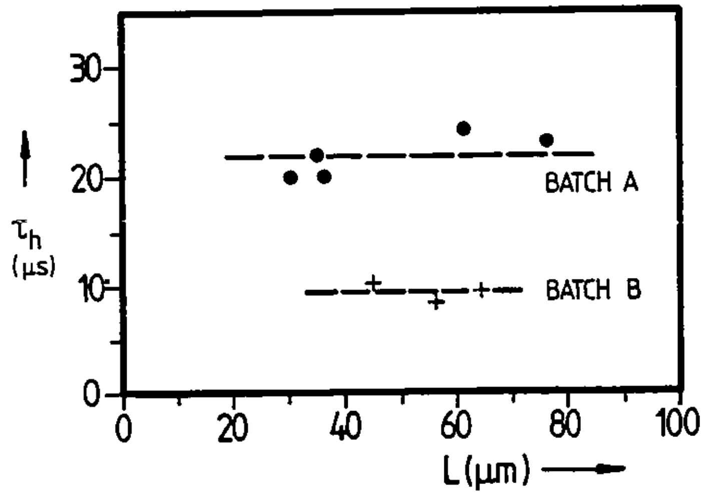

Fig. 5.5: Dependence of hole lifetime τ_h on thickness L, for two batches of a-Se.

thickness, field and light intensity tests on τ_h are shown in Figs. 5.5, 5.6 and 5.7 respectively. It can be seen that for a given batch, τ_h is independent of L, F and J, thus confirming its employment as a hole lifetime. When Pd was used as a semitransparent top electrode, instead of the usual Au, the transient waveforms, and t_T and τ_h hence obtained, remained unaffected. This provided further support in interpreting the current decay as arising from intrinsic bulk properties.

It can also be seen from Figs. 5.5 and 5.6 that τ_h is sensitive to the Se batch or to the 'origin' of Se.

The hole lifetime was found to depend on the substrate temperature, T_{sub}, during deposition of the films as shown in Fig. 5.8. Notice that τ_h tends to shorten with fall in T_{sub} (as also reported by Kalade et al 1972; see T2.4) although at high substrate temperatures for batch A it seems to be relatively constant.

Table T5.1 summarizes drift mobility μ_h, lifetime τ_h, and range $r_h = \mu_h\tau_h$ data for various different batches of pure Se. The hole Schubweg s_p at an applied field F can readily be calculated from $s_p = r_hF = \mu_h\tau_hF$. Those Se batches which give longer ranges are obviously more favourable for xerographic purposes from transport considerations alone as discussed in §1.2. It can be seen that although μ_h (≈ 0.16 cm^{2}V^{-1}s^{-1}) is insensitive to the 'origin' of Se, τ_h varies between batch to batch. Both μ_h and τ_h compare well with other earlier research as summarized in T2.3 and T2.4. Notice, however, that the largest lifetime value recorded in this work is about ≈35 μs on an A-type a-Se, in comparison to ≈50 μs by Schottmiller et al (1970) and ≈44 μs by Herms et al (1974) even though these authors have used lower substrate temperatures (see T2.4).

The temperature dependence of the drift mobility and lifetime below and above the room temperature have also been investigated as described in §4.4. Fig. 5.9 shows some typical log I(t) vs t plots for current transients at four different temperatures; (a) $T \cong 23$°C, (b) $T = 7$°C, (c) $T = -9$°C

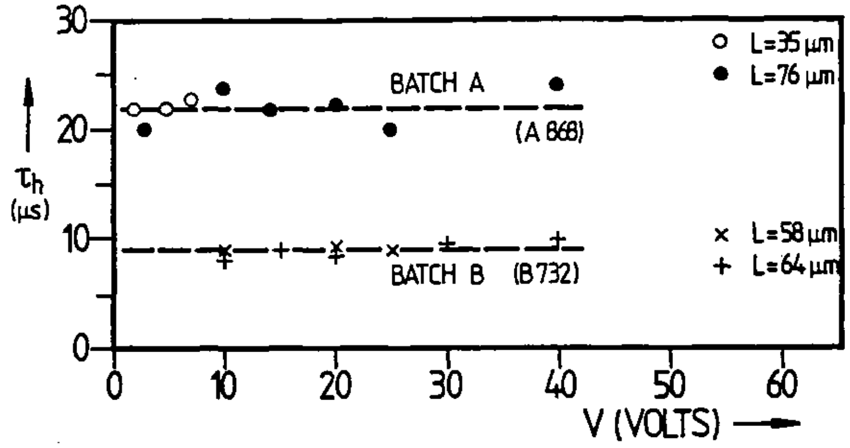

Fig. 5.6: Dependence of hole lifetime τ_h on applied voltage V for various thickness and different batch a-Se samples.

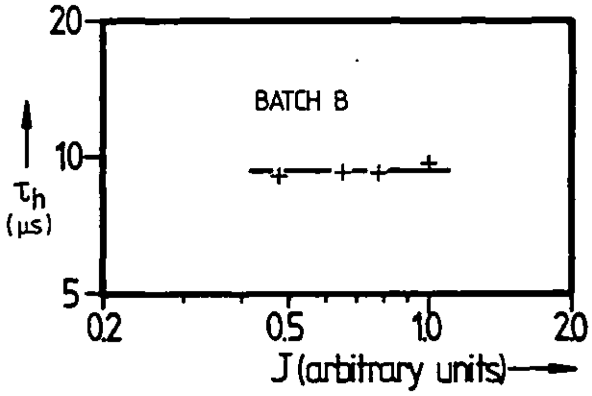

Fig. 5.7: Dependence of hole lifetime τ_h on the light intensity J.

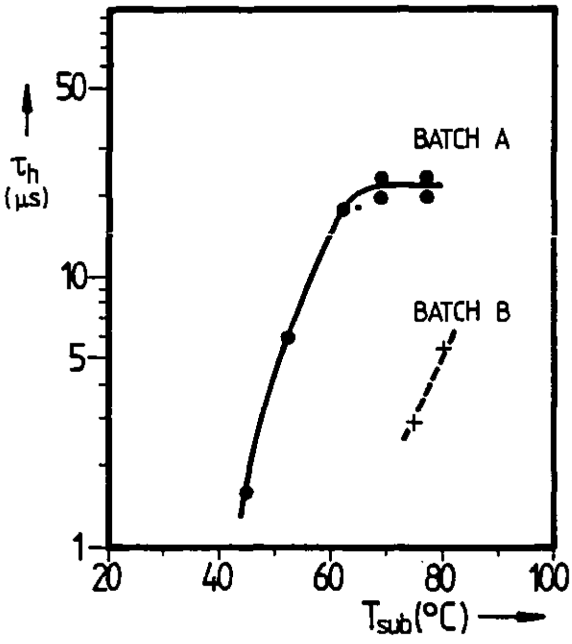

Fig. 5.8: The effect of substrate temperature T_{sub} on hole lifetime τ_h in a-Se.

Table T5.1: Typical Charge Drift Parameters in Various Batches of Pure a-Se at 300K (Nominal purity 99.999%)

BATCH/ SAMPLE	HOLE TRANSPORT			ELECTRON TRANSPORT		
	μ_h $[cm^2V^{-1}s^{-1}]$	τ_h $[\mu s]$	$r_h = \mu_h\tau_h$ $[\mu m/(Vcm^{-1})]$	μ_e $[cm^2V^{-1}s^{-1}]$	τ_e^o $[\mu s]$	$r_e^* \equiv \mu_e\tau_e^o$ $[\mu m/(Vcm^{-1})]$
A868	0.16	22	3.5×10^{-2}	TL	$\lesssim 4$	TL
A869	0.15	16	2.4×10^{-2}	TL	$\lesssim 4$	TL
A900X	0.16	18	2.9×10^{-2}	6.6×10^{-3}	200	1.3×10^{-2}
A2300	0.17	35	6.0×10^{-2}	TL	$\lesssim 8$	TL
B732	0.16	9	1.4×10^{-2}	7.2×10^{-3}	500	3.6×10^{-2}
B798	0.16	10	1.6×10^{-2}	8.2×10^{-3}	900	7.4×10^{-2}
B2100	0.16	11	1.8×10^{-2}	7.6×10^{-3}	1600	1.2×10^{-1}
C499	0.17	15	2.6×10^{-2}	4.0×10^{-3}	330	1.32×10^{-2}

NOTES: TL means trap-limited

The parameter r_e^* is defined by the product $\mu_e\tau_e^o$ and represents the 'zero field electron range', $r_e^o \equiv \mu_e^o\tau_e^o$ when $\mu_e \simeq$ constant.

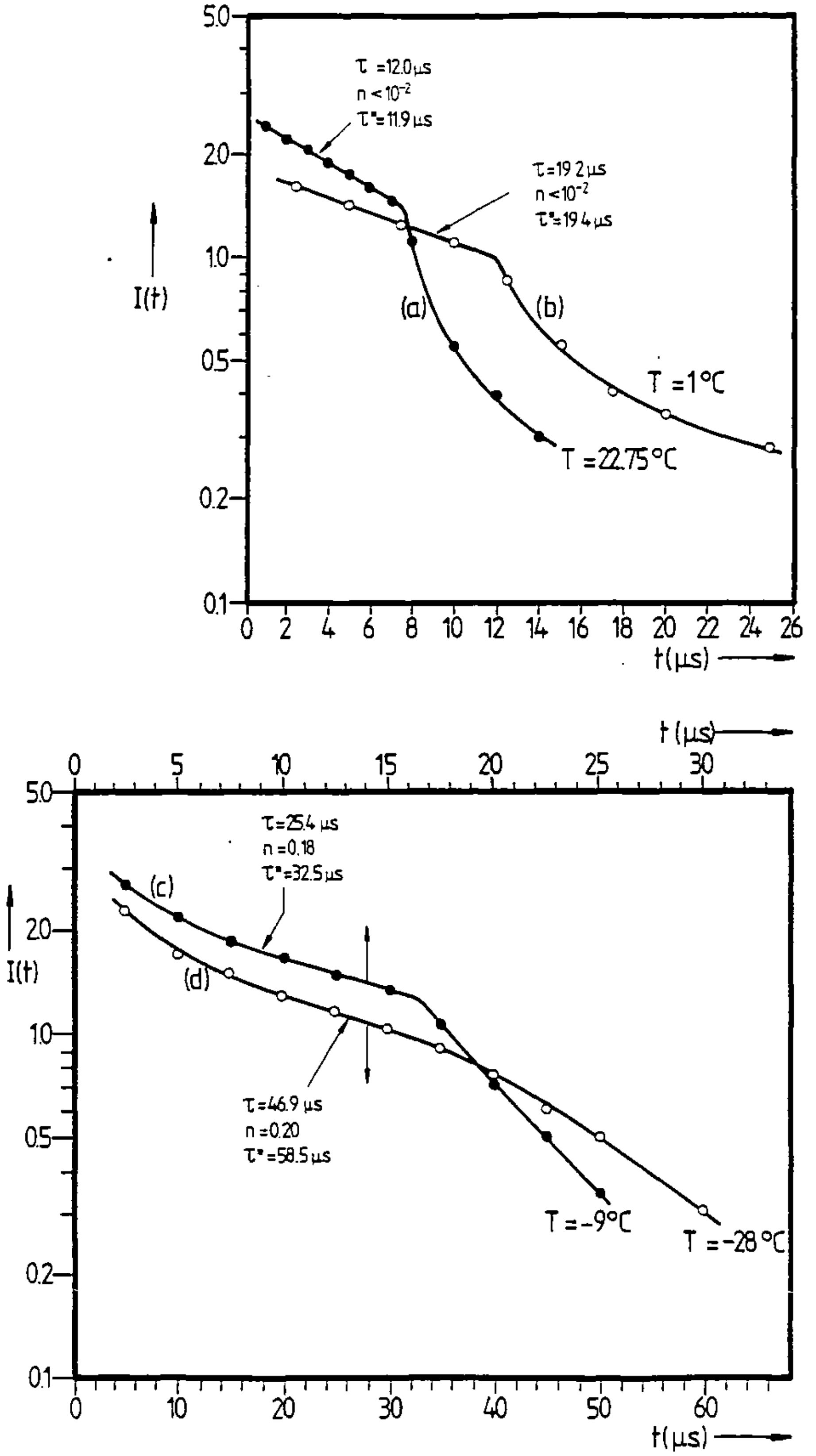

Fig. 5.9: Semilogarithmic representation of transient hole currents in a-Se at various temperatures; (a) T = 22.75°C, (b) T = 1°C, (c) T = -9°C, (d) T = -28°C. τ is obtained from the inverse of the slope of the region before the transit time and n and τ^* are obtained by curve fitting with eqn. (5.4).

and (d) $T \cong -28°C$. It is apparent that below ∿1°C the transient photocurrent decay starts to deviate from its simple single exponential behaviour in eqn. (5.2). It can be seen that as the temperature falls (below ∿1°C) an initial fast component develops in the current transient. This is not unexpected inasmuch as the hole photocurrent at low temperatures tends to become dispersive as discussed in §2.5.3. The photocurrent is then described by eqn. (2.19 a) ;

$$I(t) = At^{-n} \quad ; \quad t < t_T \qquad (5.3)$$

where $n \equiv 1 - \alpha$. This type of behaviour would readily account for the initial fast decay for small t.

The log I(t) vs t plots in (c) and (d) of Fig. 5.9 still, however, show a straight line region, thus implying that some exponential type of decay still exists for times not too short. If we continue to assign a deep trapping time τ_h to the time constant associated with the linear region after the initial fast decay in the log I vs t plots then lifetime vs temperature data may be extended down to temperatures -28°C, below which photocurrents essentially become like eqn. (5.3).

This procedure is in fact approximately equivalent do describing the transient photocurrent by an equation based on the product of the expressions in eqns. (5.2) and (5.3), i.e.

$$I(t) = Kt^{-n} \exp(-\frac{t}{\tau}) \quad ; \quad t < t_T \qquad (5.4)$$

where K is a constant independent of time. The use of eqn. (5.4), which has no formal proof, is discussed in §5.2.2. Fig. 5.9 also shows α and τ values obtained by curve fitting eqn. (5.4) onto the hole photocurrent. Notice that above ~1°C $\alpha \cong 1.00$ indicating no dispersion effects on I(t).

Fig. 5.10 shows the temperature dependence of μ_h and τ_h in the temperature range 58°C to -28°C. The data above the room temperature were obtained by continuous heating (see §4.4) and monitoring of the hole photocurrent. T_g at the heating rate used (obtained from Fig. 4.16) is marked by ||. It can be seen that both μ_h and τ_h saturate as the temperature is raised. The

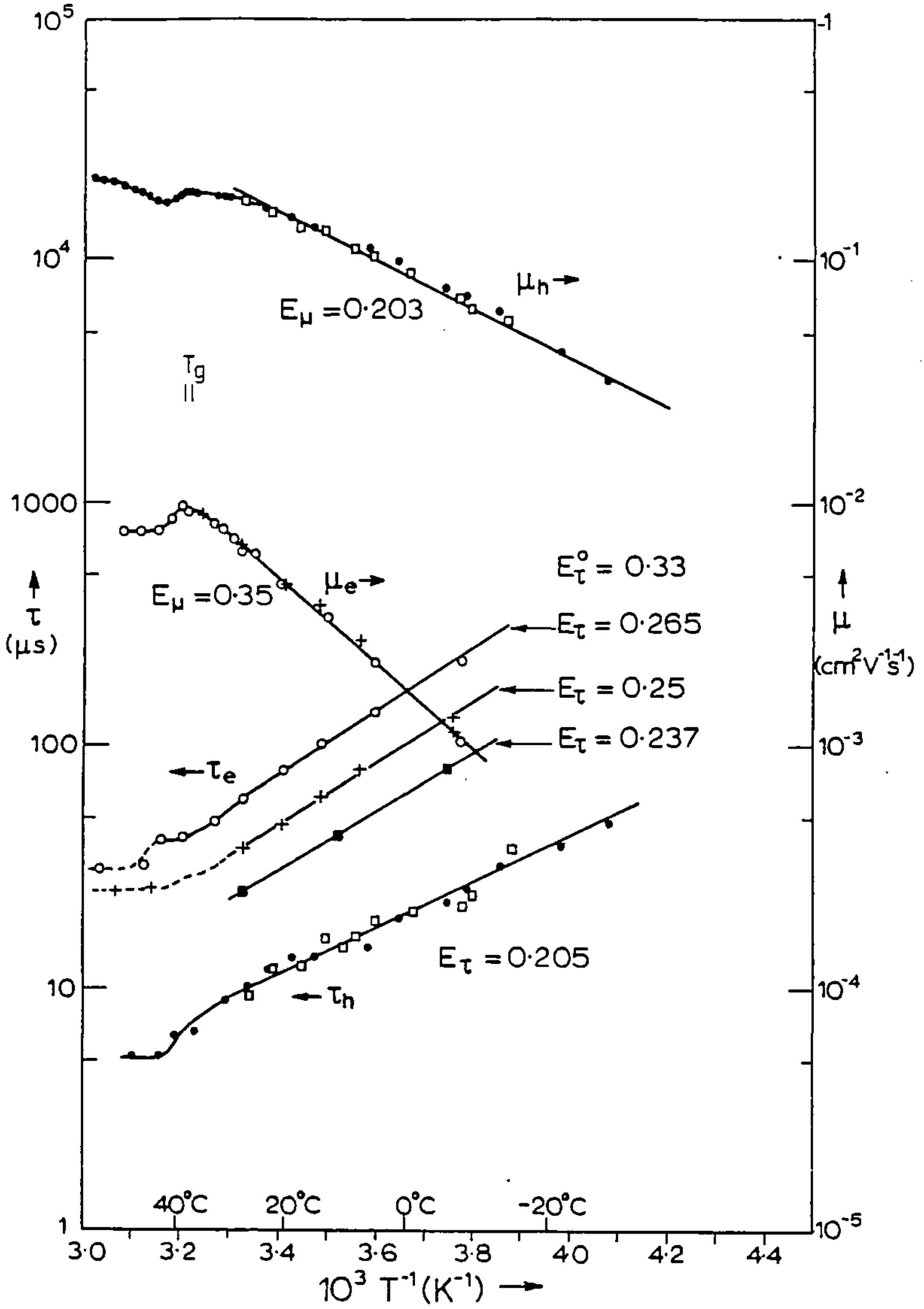

Fig. 5.10: Temperature dependence of the drift mobility μ and lifetime τ for holes and electrons in undoped a-Se. The activation energies E_μ and E_τ are in eV's. Applied field values are (V cm^{-1}): (□) 3 x 10^3; (●) 4 x 10^3; (○) 3.13 x 10^4; (+) 4.69 x 10^4; (■) 6.25 x 10^4.

saturation in $\mu_h(T)$ follows after an anomalous behaviour in the glass transition region where the mobility shows an abrupt 'dip'. A similar behaviour in $\mu_h(T)$ in theT_g region in the first thermal cycling has also been reported by Abkowitz and Pai 1978 and Abkowitz 1979 (see Fig. 2.20).

Below room temperature, both $\mu_h(T)$ and $\tau_h(T)$ seem to indicate a thermally activated behaviour with approximately equal activation energies, $E_\mu \approx E_\tau \approx$ 0.20 eV in the temperature range $T \gtrsim 245$K. In other words, the hole range, $\mu_h\tau_h$, is insensitive to temperature. This fact can be used as evidence for diffusion controlled trapping (see reviews by Kao and Hwang 1981, Ch. 5 and Mort 1981) inasmuch as the capture time τ of a carrier by a coulombic centre is then given by the Langevin (1903) equation;

$$\tau = \frac{\varepsilon_o\varepsilon_r}{N_d e\mu} \qquad (5.5)$$

where N_d is the density of deep traps and μ is the drift mobility. This equation assumes that the mean free path $\bar{\ell}$ of the carrier is smaller than the capture radius r_c $(\sim\frac{e^2}{4\pi\varepsilon_o\varepsilon_r kT})$ of the centre. Clearly if μ is thermally activated then the deep trapping time τ will also be thermally activated with the same activation energy.

The thermally activated behaviour of $\mu(T)$ and $\tau(T)$ in Fig. 5.10 can readily arise from the presence of a monoenergetic set of shallow traps. The drift mobility (see 3.3.1, eqn. (3.31)) and the lifetime (eqn. (5.5)) are then given by

$$\mu = \mu_o \left[\frac{\tau_c}{\tau_c+\tau_r}\right] \cong \mu_o \frac{\tau_c}{\tau_r} = \mu_o \frac{N_c}{N_t} \exp\left(-\frac{E_t}{kT}\right) \qquad (5.6)$$

and

$$\tau = \tau_o \left[\frac{\tau_c+\tau_r}{\tau_c}\right] \cong \tau_o \frac{\tau_r}{\tau_c} = \tau_o \frac{N_t}{N_c} \exp\left(\frac{E_t}{kT}\right) \qquad (5.7)$$

where τ_o is the deep trapping time or lifetime in the absence of the shallow traps, μ_o is the microscopic mobility, and the other parameters are as defined in 3.3.1. The interpretation of the drift parameters in terms of these equations are discussed in detail in the next section (§2.2.2).

Pai 1974 has also found the hole lifetime to increase with decreasing temperature in such a way that the range, $\mu_h\tau_h$, is relatively insensitive to temperature (see Fig. 2.22).

The temperature dependence of the hole drift mobility $\mu_h(T)$ over a wider range of temperature, down to ∿189K, at various applied fields is shown in Fig. 5.11. Clearly at low temperatures, below ∿250K (25°C), the mobility activation energy E_μ has a field dependence as shown in the inset of Fig. 5.11. The decrease in E_μ with the applied field at low temperature is also noticeable, for example in the works of Marshall and Owen 1972 or Pfister 1976.

An important feature in Fig. 5.11 is that although below 250K there is a well defined activation energy at a given field, above ∿250K, the log μ_h vs T^{-1} plot shows a curvature. Any line drawn in this region (Fig. 5.10) corresponds to an activation energy which is lower than that at low temperatures. Smaller hole mobility activation energies reported by the early researchers (see T2.3) are probably due, in part, to the limited temperature range accessed. Also, little experimental information is available to determine whether the reported values were influenced by cooling rates and/or measurement procedures. Fast cooling rates, for example, may give rise to non-uniform temperature gradients which in turn may considerably 'distort' the mobility-temperature relationship (see §4.4).

The 'high' temperature ($\gtrsim$ 250K) departure in the log μ_h vs T^{-1} plots from well defined thermally activated behaviour at 'low' temperatures ($\lesssim$250K) has been attributed by Grunwald and Blakney 1968 to a decreasing release time τ_r with temperature. This causes the drift mobility given by eqn. (3.29) to saturate towards μ_o (see §2.5.3, p. 69). This argument is re-examined in the next section.

As evident from the E_μ vs $V^{\frac{1}{2}}$ in the inset of Fig. 5.11 the field dependence of the mobility activation energy is of 'Poole-Frenkel' type, i.e.

$$E_\mu = E_\mu^o - \beta F^{\frac{1}{2}} \qquad (5.8)$$

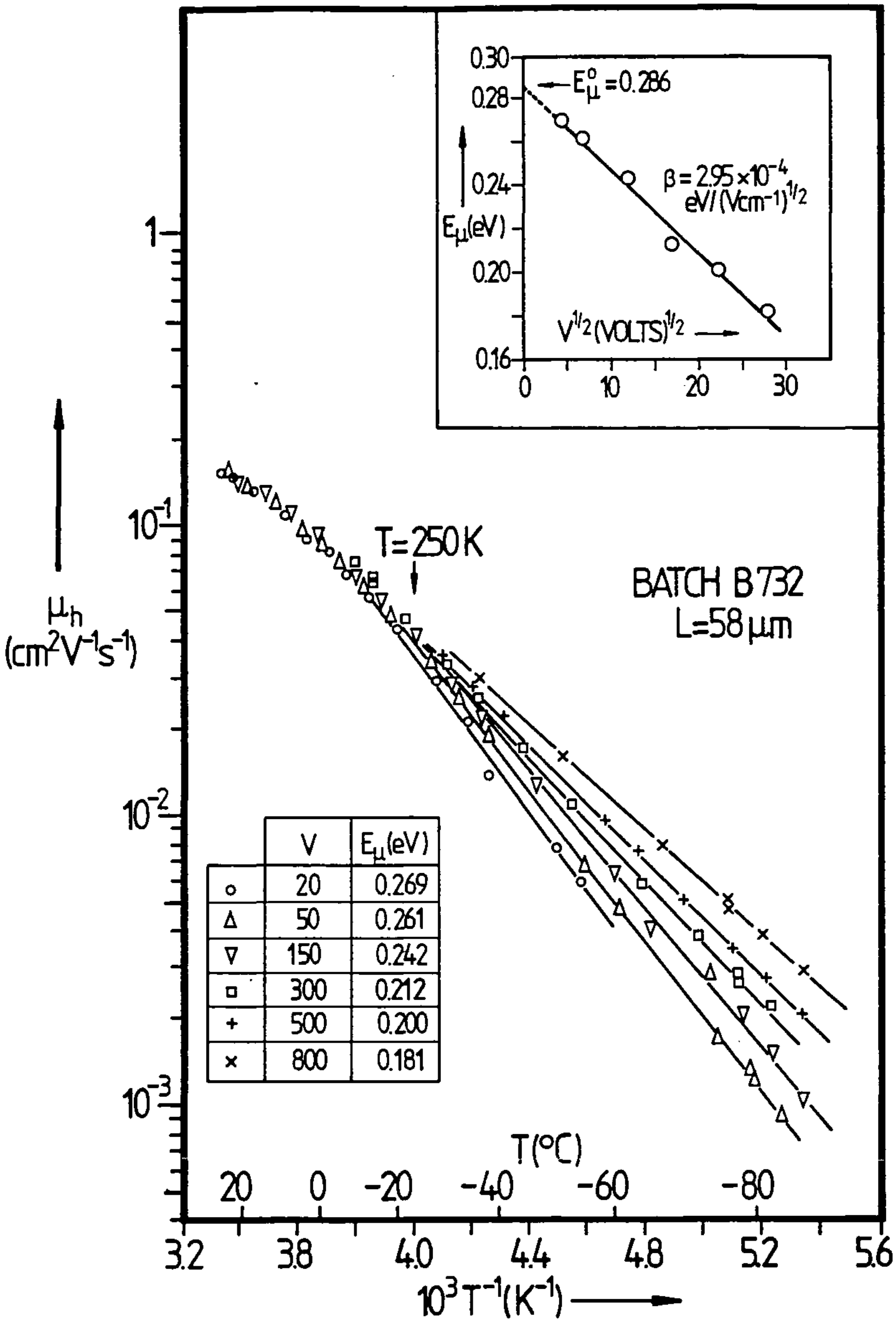

	V	E_μ(eV)
○	20	0.269
△	50	0.261
▽	150	0.242
□	300	0.212
+	500	0.200
×	800	0.181

Fig. 5.11: Temperature dependence of hole drift mobility in a-Se at various applied fields. Data represented as log μ_h vs 10^3T^{-1}. The inset shows the voltage dependence of the low temperature activation energy as E_μ vs $V^{\frac{1}{2}}$.

The Poole-Frenkel coefficient found experimentally (β_{exp}) on this sample was 2.95 x 10^{-4} eV (V cm^{-1})$^{-\frac{1}{2}}$ which is in good agreement, to within 4%, with that calculated from (Frenkel 1938);

$$\beta_{PF} = [\frac{e^3}{\pi\varepsilon_0\varepsilon_r}]^{\frac{1}{2}} = \frac{1.2\text{x}10^{-22}}{\varepsilon_r^{\frac{1}{2}}} \quad (\text{CV}^{\frac{1}{2}}\ \text{cm}^{\frac{1}{2}}) \qquad (5.9\text{a})$$

i.e.

$$\beta_{PF} \cong 4.54 \times 10^{-23}\ \text{CV}^{\frac{1}{2}}\ \text{cm}^{\frac{1}{2}} \text{ or } 2.84 \times 10^{-4}\ \text{eV}/(\text{Vcm}^{-1})^{\frac{1}{2}} \qquad (5.9\text{b})$$

using ε_r ≅7.0 from capacitance measurements (see §4.5). On a different B-type batch[†], β_{exp} was 3.03 x 10^{-4} eV/(Vcm^{-1})$^{\frac{1}{2}}$, i.e. to within 6% with respect to β_{PF}. Clearly the experimental β coefficients suggest a lowering of the activation energy E_μ by a Poole-Frenkel type of effect (see Frenkel 1938 or e.g. Hartke 1968, Hill 1971b). In the shallow-trapped controlled transport mechanism this behaviour is readily understood by noting the field dependence of the release time τ_r. The probability of release per unit time from a coulombing trapping centre of trapping energy depth E_t is given by

$$\frac{1}{\tau_r} = \nu \exp [- \frac{(E_t-\beta F^{\frac{1}{2}})}{kT}] \qquad (5.10)$$

which increases as the field lowers the potential barrier. ν is an attempt to escape frequency.

The lowering of E_μ in a $\beta F^{\frac{1}{2}}$ fashion may be taken to infer that the hole drift mobility may be of the form

$$\mu(F) = \mu^0 \exp \frac{\beta F^{\frac{1}{2}}}{kT} \qquad (5.11)$$

where μ^0 is the zero field mobility and β is probably equal to eqn. (5.9). Fig. 5.12 shows the field dependence of the drift mobility represented as (a) log μ_h vs $V^{\frac{1}{2}}$, (b) log μ_h vs log V and (c) log μ_h vs V at various temperatures. The mobility-field points in Fig. 5.12 were obtained from the log μ_h vs T^{-1} plots in Fig. 5.11. It can be seen that, except at the lowest field used, the field dependence of the drift mobility seems to follow eqn. (5.11) but with experimental β values at least a factor of four or more smaller

---

[†] B798

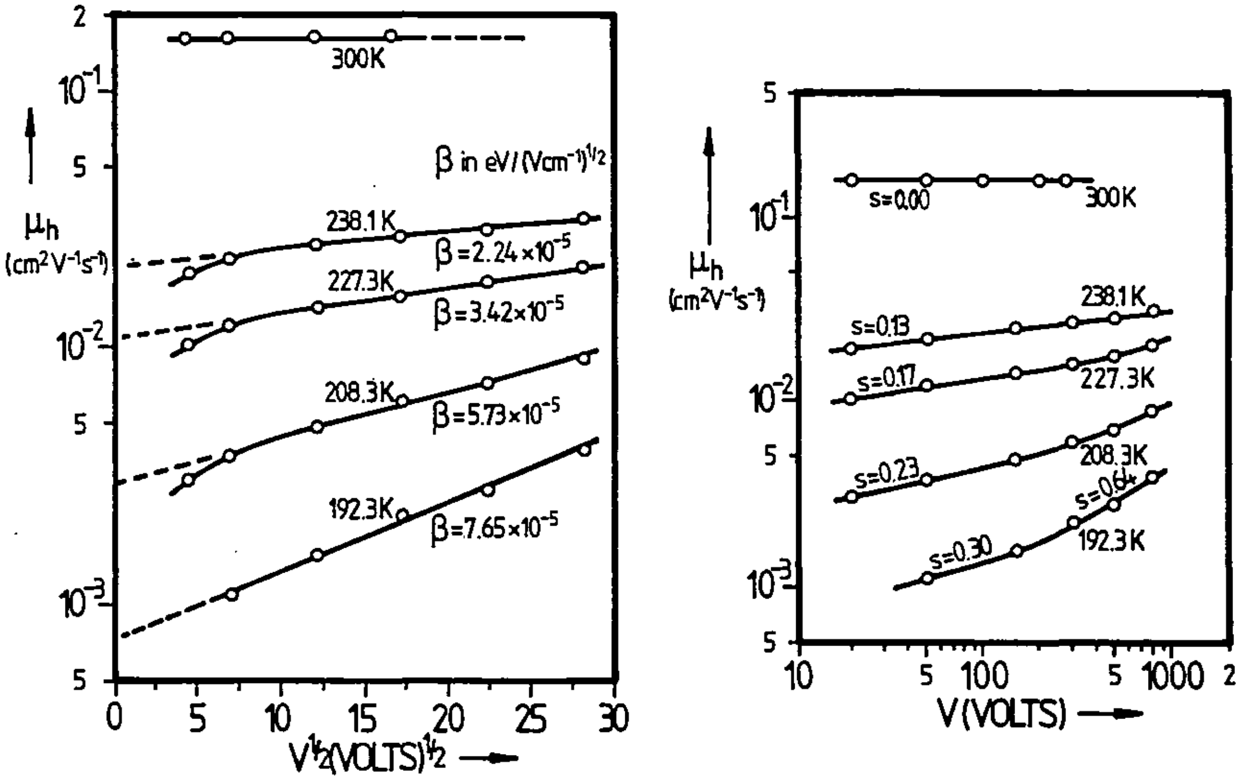

(a) Log μ_h vs $V^{\frac{1}{2}}$

(b) Log μ_h vs Log V

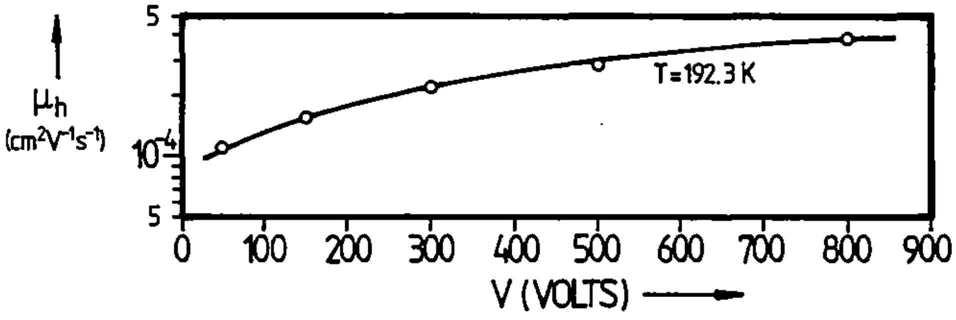

(c) Log μ_h vs V

Fig. 5.12: Electric field dependence of hole drift mobility in a-Se at various temperatures.

than eqn. (5.9b). Moreover the observed β coefficient decreases with temperature.

Over a limited field range, but including the lowest field employed, the drift mobility may, however, be represented by an algebraic field dependence of the form

$$\mu_h \sim F^s \tag{5.12}$$

As apparent from Fig. 5.12(b), although eqn. (5.12) can account for $\mu_h(F)$ behaviour up to the highest field ($\approx 1.4 \times 10^5$ Vcm^{-1}) accessed at T ≅ 238K, as the temperature decreases eqn. (5.12) holds only over restricted field ranges; unless the index s is allowed to increase with the field. Note that an algebraic field dependence of the drift mobility has also been reported by Tabak 1970 and Pai 1974. Tabak, for example, found a $\mu_h \sim F^s$ behaviour down to T ≈ -115°C (158K) and over the whole range of field used ($F \lesssim 10^5$ Vcm^{-1}). The index s increased monotically with the fall in temperature; s was unity at -115°C (i.e. $\mu_h \sim F$).

From the log μ_h vs V plot in Fig. 5.12(c), we cannot infer an exponential field dependence in the drift mobility behaviour as observed by Marshall and Owen 1972 (Fig. 2.24) on bulk quenched a-Se.

(B) Electron Transport

The electron TOF current transients were essentially very similar to the hole photocurrents (Fig. 5.1) described above. Fig. 5.13 shows some typical electron current transients represented as log I vs t. The waveforms in (a), (b) and (c) correspond to three different biases and that in (d) to an electron photocurrent at -8°C. Notice that the transit time t_T is well defined and that the photocurrents decay with time at both 'low' and 'high' fields in contrast to the hole current transients which evince a decay due to trapping at 'low' fields only.

It can be seen from the log I(t) vs t plots in Fig. 5.13 that the decay in I(t) up to t_T seems to be described by a single exponential

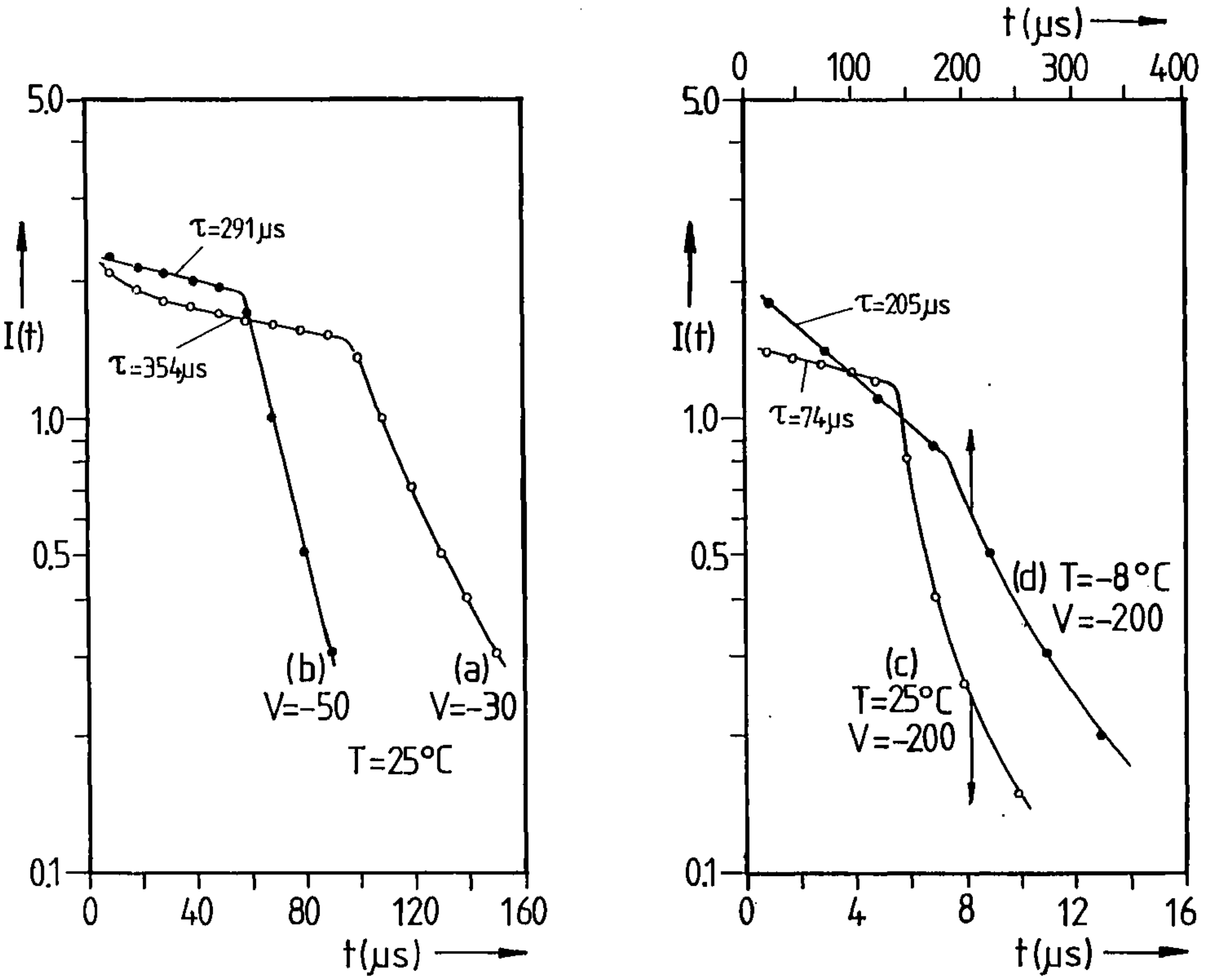

Fig. 5.13: Semilogarithmic representation of electron current transients in a-Se at various applied fields and temperatures. I(t) is in arbitrary units.

(eqn. (5.2)) with a time constant which decreases with the field. Notice, however, that at the 'lowest' fields used, as shown by (a) in Fig. 5.13 there is an initial slight deviation from the simple single exponential behaviour. The large part of the waveform, however, still conforms to eqn. (5.2) for times not too short.

The initial fast decay in Fig. 5.13(a) only appears at the lowest fields. It may be part of an initial 'spike' which is probably 'obscured' for times close to 'zero' due to a finite t_T/CR ratio or it constitutes a fast exponential component in I(t) as observed by Blakney and Grunwald 1967. On the other hand, it may be the beginnings of a dispersion effect since eqn. (5.3) would readily account for an initial fast decay via eqn. (5.4).A more plausible explanation is believed to be the initial disappearance of some of the injected electrons by diffusion and recombination. In the case of holes this surface recombination effect occurs at $F \lesssim 10^3$ Vcm^{-1} (Enck 1974).

At temperatures below 265K, the waveforms were no longer of simple exponential type but showed an initial fast component. The exact functional form of the low temperature ($\lesssim$265K) shapes of the photocurrent were not examined.

If we assume that the exponential decay in the electron photocurrent arises because of the deep trapping of some of the injected electrons during their transit then the time constant τ_e of the current decay may be assigned to an electron lifetime.* Alternatively, τ_e will have to be viewed as 'decay time constant' and not associated with any bulk property. The employment of τ_e as an electron lifetime is supported by the following tests.

Firstly, τ_e seems to be insensitive to the xenon flash intensity, provided the latter is not too large. Secondly, it is independent of the type of top contact, Au or Pd. Recently Vaezi-Nejad† obtained similar waveforms using xerographic time-of-flight technique# (XTOF) which requires no physical

---

* This interpretation is re-examined in section 5.2.2(B)

† Dept. of Elec. Eng., Imperial College London.

\# See, e.g. Pai and Enck 1975

top contact. Further, it seems to depend on the source of Se and impurities. For example for those samples in which τ_e was very short, e.g. most A-type Se samples of this project, no transit time was discernible and the current I(t) just decayed rapidly. This type of TOF electron response has been called trap-limited (e.g. Tabak and Hillegas 1972).

Thus in most A-type a-Se samples used in this work the electron transport was found to be trap-limited.

Fig. 5.14 shows the dependence of τ_e on the field F for different thickness but same batch (B732) a-Se samples. Although the overlap of $\tau_e(F)$ data for L =58μm and L =64μm indicates τ_e may be considered an 'intrinsic material property', the two thicknesses were only 6μm different and this could not allow a definite conclusion. An interesting feature in Fig. 5.14 is that as the field is reduced τ_e seems to tend to a finite value, say τ_e^o.

Fig. 5.15 shows typical log τ_e vs $V^{\frac{1}{2}}$ plots for two different batches of a-Se. It can be seen that over a considerable range of fields the electron lifetime is of the form

$$\tau_e = \tau_e^o \exp(-BF^{\frac{1}{2}}) \qquad (5.13)$$

This represents a Poole-Frenkel type of behaviour in which $B = \frac{\beta}{kT}$. Table T.5.2 summarizes τ_e^o and β_{exp} (experimental β) data for various types of pure a-Se samples. Notice that some of the β_{exp} values are different than β_{PF} in eqn. (5.9).

The high field behaviour of the 'electron lifetime' τ_e in Fig. 5.14 is clearly not described by eqn. (5.13). At these large biases τ_e has either saturated or shows a slight increase with the field.

The electron drift mobilities calculated from eqn. (5.1) at room temperature are represented in Fig. 5.16 as log μ_e vs log F. It is apparent that although for some of the batches μ_e is constant, independent of the field F, in agreement with the early drift mobility experiments (e.g. Spear 1957, Hartke 1962, Grunwald and Blakney 1968), for other batches it appears to have a slight field dependence as reported by Pai 1974, for example. The

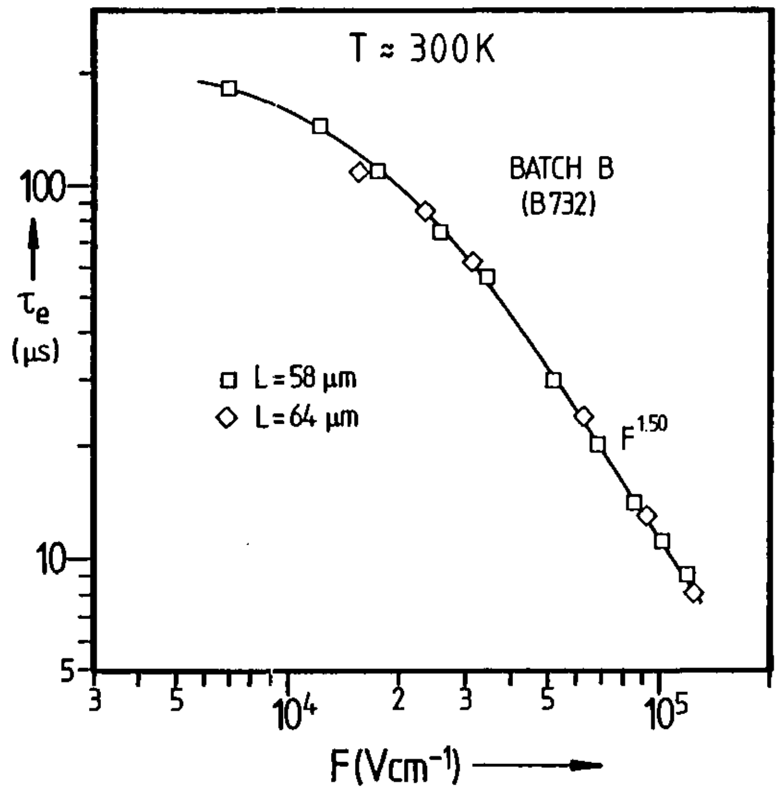

Fig. 5.14: Log-log plot of electron lifetime τ_e vs applied electric field F for B-type a-Se.

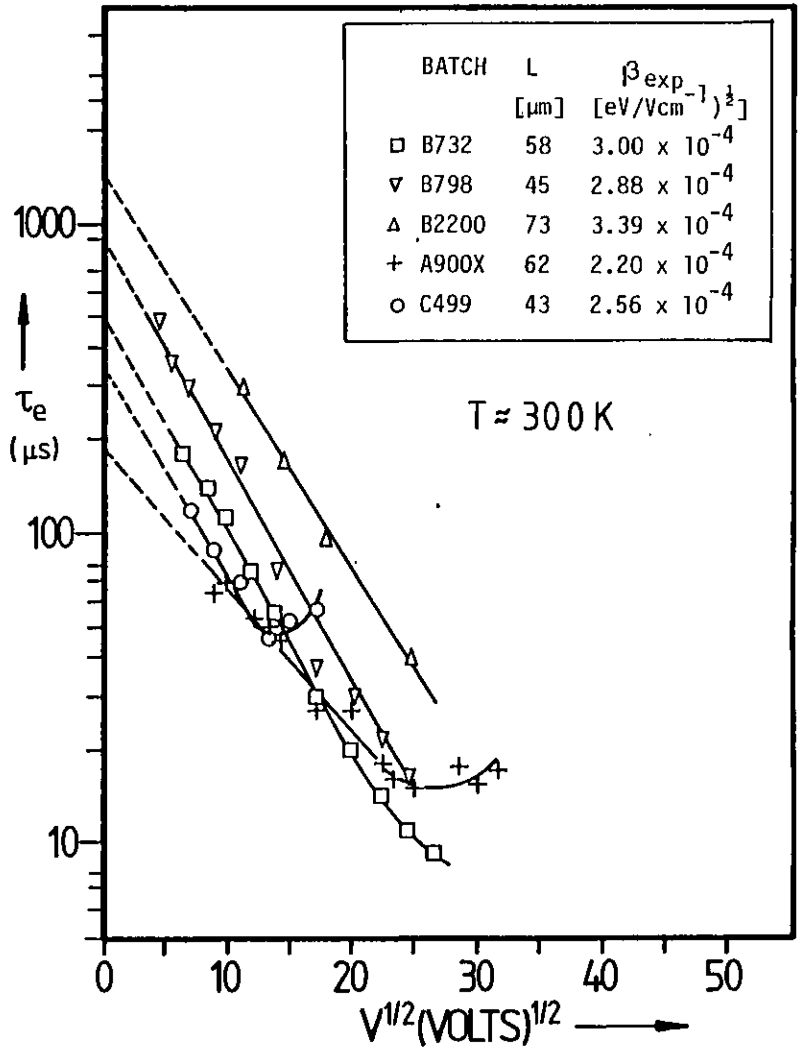

	BATCH	L [μm]	β_{exp} [eV/Vcm^{-1})$^{\frac{1}{2}}$]
□	B732	58	3.00×10^{-4}
▽	B798	45	2.88×10^{-4}
△	B2200	73	3.39×10^{-4}
+	A900X	62	2.20×10^{-4}
○	C499	43	2.56×10^{-4}

Fig. 5.15: Log (electron lifetime) vs $\sqrt{}$(applied voltage) for various batches of a-Se.

Table T5.2: Electron Lifetime Data for Pure a-Se, a-Se/0.5%As and a-Se/0.5%As + Cℓ

Batch/ Sample	τ_e^o [μs]	β_{exp} [eV/(Vcm^{-1})$^{\frac{1}{2}}$]	Comment
	Pure Se		
A868	$\lesssim 4$	?	Trap limited
A900X	200	2.2×10^{-4}	τ_e saturates at high F
B732	500	3.00×10^{-4}	$\tau_e \sim F^{-1.5}$; $F \gtrsim 4 \times 10^4$, also possible
B798	900	2.88×10^{-4}	
B2200	1500	3.39×10^{-4}	$\tau \sim F^{-1.27}$ also possible
C499	330	2.56×10^{-4}	
Commercial grade	300	2.06×10^{-4}	Fig. 8 in Rossiter and Warfield 1971. Evaporated a-Se; $T_{sub} \approx 60°C$
	Se/0.5%As		
A734	600	2.2×10^{-4}	Pd and Au tried
A871	94	3.86×10^{-4}	
A441	340	2.64×10^{-4}	0.3%As content
	Se/0.5%As + 30 ppm Cℓ		
A864	185	1.75×10^{-4}	
A865	200	1.75×10^{-4}	

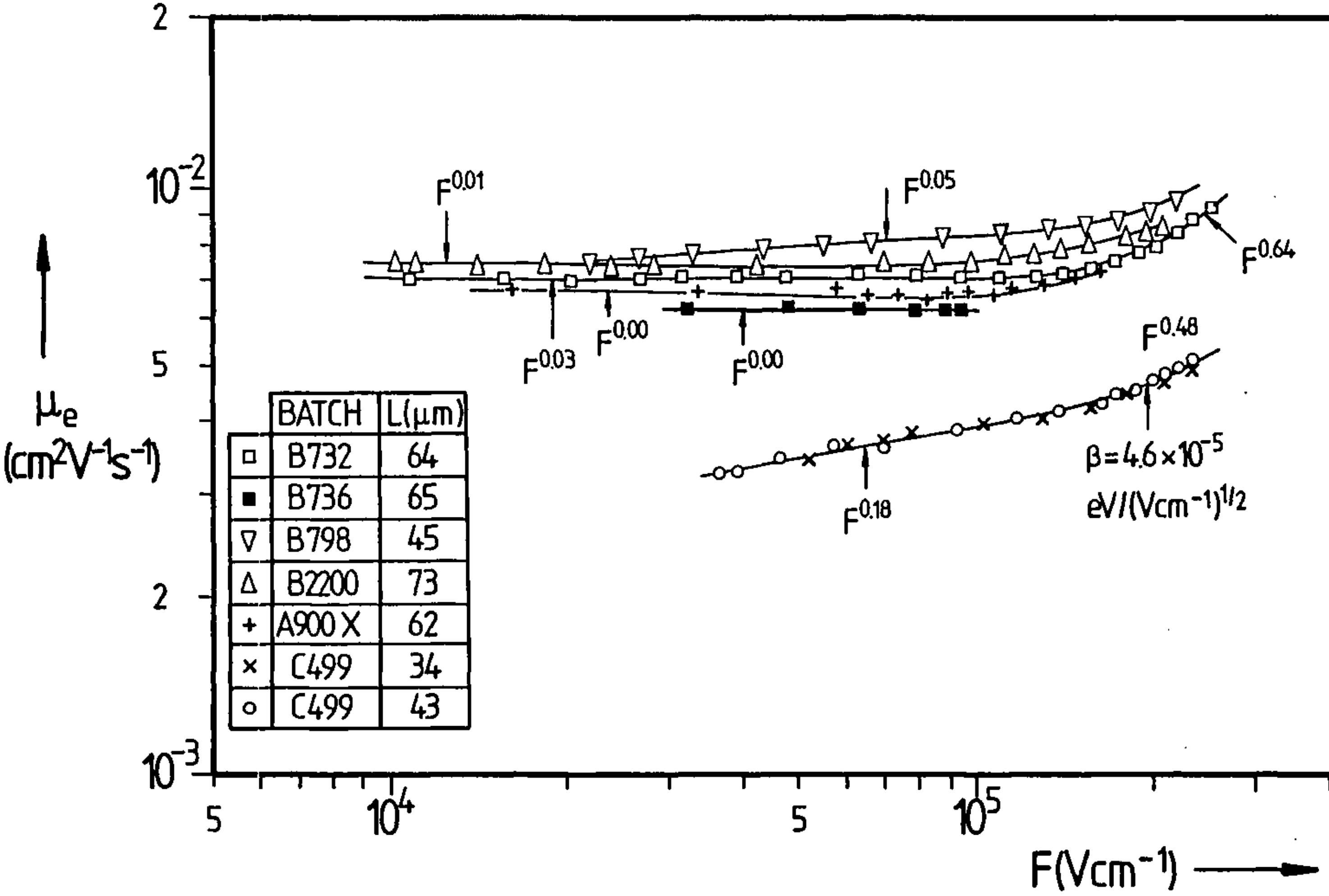

Fig. 5.16: Log-log plots of electron drift mobility μ_e vs applied electric field F for various a-Se batches. Data taken at room temperature; T ≈ 299K.

relationship between μ_e and F seems to be of the form (eqn. (5.12))

$$\mu_e \sim F^n \tag{5.14}$$

with n = 0 to 0.18 depending on the batch. Also apparent is that at high fields, in excess of $\sim 1.6 \times 10^5$ V cm^{-1}, the electron drift mobility shows a strong field dependence. For some of the batches, e.g. B798 , C499, the field dependence was more pronounced whereas for others, e.g. B736, B2200, the mobility was constant. Notice that C-type a-Se has a distinctly different electron drift mobility behaviour than B-type a-Se, in that μ_e for the former is not only considerably lower than that for the latter, but also has a stronger field dependence with n = 0.18 for $F \lesssim 1.6 \times 10^5$ V cm^{-1} and $n \cong 0.48$ for $F \gtrsim 1.6 \times 10^5$ V cm^{-1}.

Electron drift mobility measurements on most A-type a-Se samples have been trap-limited.

Table T5.1 also summarizes some μ_e and τ_e^o data at room temperature on various a-Se batches. For samples in which μ_e showed a field dependence, μ_e values correspond to $F = 1 \times 10^5$ V cm^{-1} (typical of fields in the xerographic process). The parameter r_e^* in T5.1 is defined as the product $\mu_e \tau_e^o$ where μ_e is the drift mobility at $F = 1 \times 10^5$ V cm^{-1}. For those batches in which μ_e is field independent, r_e^* corresponds to the zero field range. r_e^* is useful for comparative purposes between batches.

Fig. 5.10 shows the temperature dependence of μ_e and τ_e over a restricted temperature range down to ∿265K (∿ - 8°C). The drift mobility is thermally activated as expected with $E_\mu \approx 0.35$ eV. The electron lifetime τ_e also seems to be thermally activated with an activation energies E_τ which depends on the applied field. With only three values for E_τ it is not difficult to fit the E_τ points onto a

$$E_\tau = E_\tau^o - \beta F^{\frac{1}{2}} \tag{5.15}$$

type of dependence as in Fig. 5.17. The 'zero field' lifetime activation energy $E_\tau^o \cong 0.33$ eV is very close to E_μ within experimental errors. The

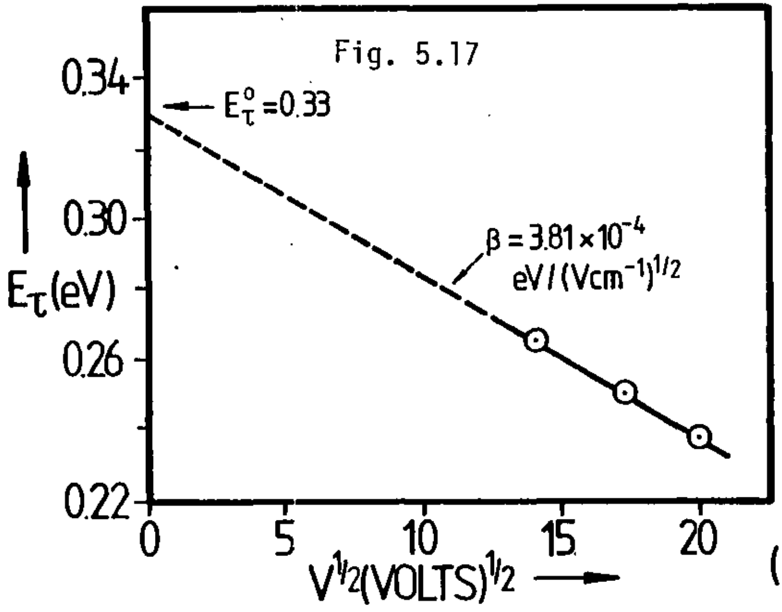

Fig. 5.17: Electron lifetime activation energy E_τ vs $V^{\frac{1}{2}}$ for a-Se. Data obtained from Fig. 5.10.

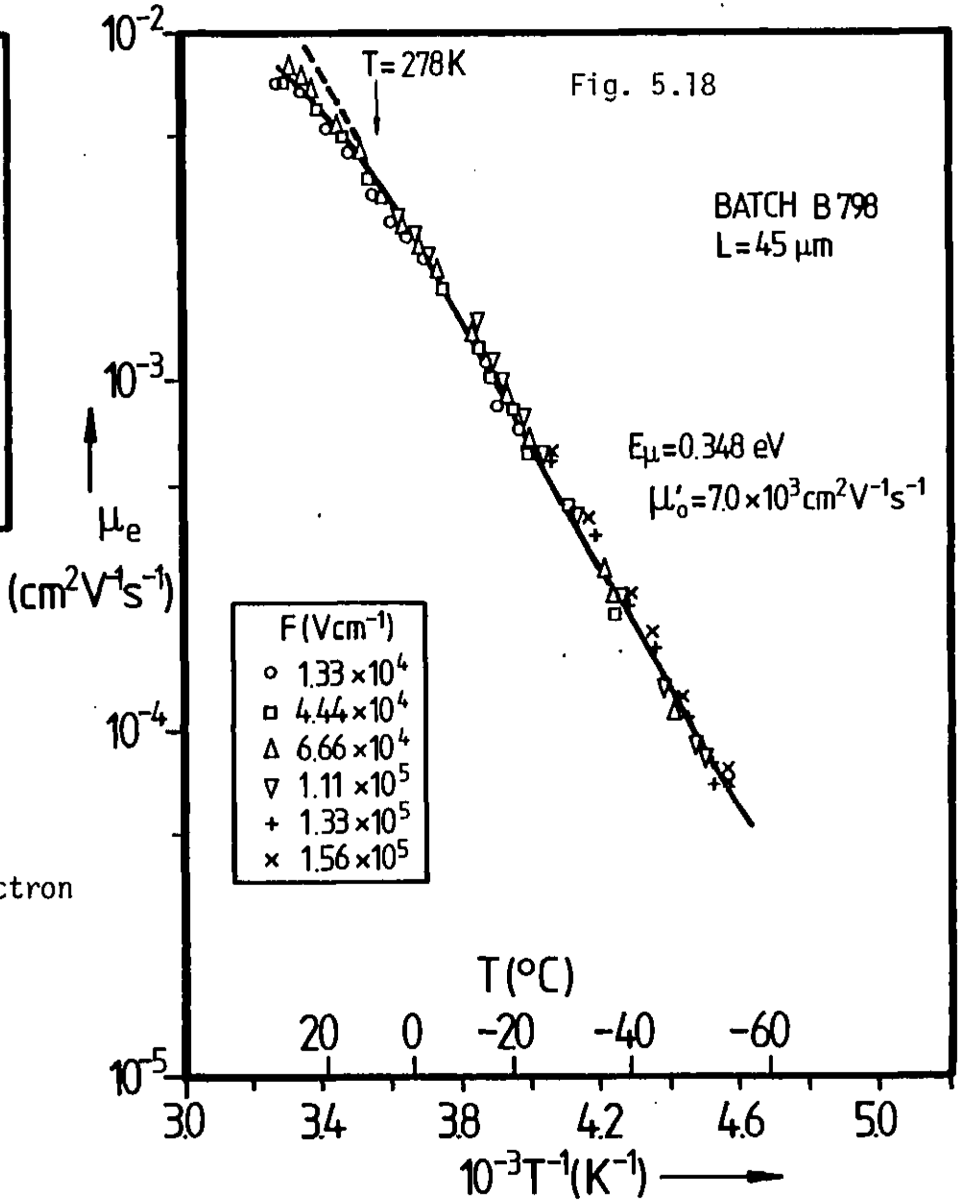

Fig. 5.18: Temperature dependence of the electron drift mobility in a-Se at various values of applied electric field.

experimental β value, 3.8×10^{-4} eV/(Vcm^{-1})$^{\frac{1}{2}}$, is about 30% larger than eqn. (5.9 b) . With only three points it is not possible to infer the exact nature of the field dependence of E_τ, but note that β from the E_τ vs $V^{\frac{1}{2}}$ plot is not drastically different from β obtained from the log τ_e vs $V^{\frac{1}{2}}$ plot (see T.5.2).

It is also evident from Fig. 5.10 that as the temperature is raised, eventually μ_e and τ_e saturate after passing through the glass transition region.

Fig. 5.18 shows the temperature dependence of the electron drift mobility over a wider temperature range, i.e. down to $\sim$219K, for a B-type Se batch in which the room temperature mobility was relatively field independent. Below 278K, μ_e displays a thermally activated behaviour with a well defined mobility activation energy, $E_\mu \cong 0.35$ eV. Above 278K however, the log μ_e vs T^{-1} plot starts to deviate from the $E_\mu = 0.35$ eV line and tends to saturate with temperature as noted above. An important feature of the various log μ_e vs T^{-1} plots corresponding to different fields is that the drift mobility, within experimental errors, remains relatively field independent down to the lowest temperature accessed (219K). This finding should be contrasted with the electron drift mobility data of Marshall, Fisher and Owen 1974 on bulk a-Se in which $\mu_e(T)$ had an exponential dependence on F as in eqn. (2.21), and the $\mu_e(T)$ data of Pai 1974 which followed eqn. (5.14) where n increases with the fall in temperature (see p. 75). On the other hand, the early research on the electron drift mobility by Spear 1957, Hartke 1962, Grunwald and Blakney 1968, covering $T \lesssim 240$K, did not indicate any field dependence. The activation energies were, however, slightly lower than the more recent values of ≈ 0.33 eV (see T.2.3).

The fields employed in the $\mu_e(T)$ measurements in Fig. 5.18 were in the range $F \lesssim 1.5 \times 10^5$ V cm^{-1},i.e. fell into the range of fields which do not affect the mobility in a pronounced manner (Fig. 5.16). The TOF cryostat system operation was such that it did not allow very large biases to be used.

5.2.2 Detailed Discussion and Interpretation

(A) Hole transport

General Interpretation

It was pointed out in §2.5.3 that the hole drift parameters in a-Se have been generally interpreted in terms of a shallow-trap controlled extended state transport mechanism. The curvature in the log μ_h vs T^{-1} plots above ~250K and particularly the saturation of $\mu_h(T)$ at high temperatures were attributed to τ_r becoming shorter with temperature by virtue of eqn. (5.10). Grunwald and Blakney 1968 analysed their mobility data (see p.69) by assuming that the microscopic mobility in eqn. (3.31) is limited by lattice scattering, i.e.

$$\mu_o \sim T^{-3/2} \tag{5.16}$$

Writing, for generality,

$$\mu_o = MT^{-n} \tag{5.17}$$

and

$$\frac{N_t}{N_v} = BT^{-3/2} \tag{5.18}$$

we have eqn. (3.31) as

$$\mu = MT^{-n} [1 + BT^{-3/2} \exp \frac{E_t}{kT}]^{-1} \tag{5.19}$$

Rearranging,

$$\frac{x^n}{y} = \frac{B}{M} x^{3/2} \exp ax + \frac{1}{M} \tag{5.20}$$

i.e.

$$Y(x,y,n) = mX(x,a) + c \tag{5.21}$$

where

$$y \equiv \mu, \quad x = T^{-1}, \; Y(x,y,n) \equiv \frac{x^n}{y}, \; X(x,a) \equiv x^{3/2} \exp ax,$$
$$a \equiv \frac{E_t}{k}, \quad m \equiv \frac{B}{M} \text{ and } c \equiv \frac{1}{M}$$

The reason for expressing eqn. (5.19) in the form in eqns. (5.20) or (5.21) is that we can carry out two or three parameter curve fitting by finding the best line fit to the mobility data from the family of lines eqn. (5.21) represents. For two parameter curve fitting we can set $n = 1.5$ (or 1) to represent lattice scattering (or diffusive motion) and E_t to the well defined low temperature mobility activation energy E_μ. Fitting data onto eqn. (5.21) by the least square deviations method[†] then gives the best m and c and hence M and B.

In three-parameter curve fitting we can either find the best n or E_t. This is achieved by starting with an initial guess ξ_i for the third parameter (n or E_t), then finding the highest correlation coefficient $C(\xi)$ by searching, in increments, for the corresponding ξ. Note, however, that although with two variable curve fitting M and B are unique with three parameter curve fitting the best ξ may not be unique.

Since, E_μ is well defined at low temperatures we can set $a \equiv \frac{E_t}{k}$ and find the best M and B, and if required the best n (as described above) which would account for the curvature in the log μ_h vs T^{-1} plots. This method should be contrasted with that of Grunwald and Blakney who set $n = 1.5$ and found E_t, M and B. Both methods are used in this work. It must be remarked, however, that the sharp 'dip' in $\mu_h(T)$ around T_g cannot be generated by eqn. (5.20).

Table T5.3 provides a summary of the essential features of two and three parameter curve fitting results based on eqn. (5.19), employing $\mu_h(T)$ data on two B-type and one A-type a-Se. We note the following deductions.

The correlation coefficient C, which represents the 'goodness' of the fit, is particularly sensitive in the fourth and following decimal places to the number of data points, temperature range accessed, and the constants in eqn. (5.19), i.e. E_t or n. Therefore C is only useful when comparisons involve the first three decimal places. To demonstrate this fact compare the first and last entry for B732. The last entry is based on employing an unusual value of 3 for n which leads to a 'worse' fit as determined from

---

[†] Usually called Linear Regression Analysis

Table T5.3: Hole Transport in a-Se: Curve Fitting with Eqn. (5.19)

Sample	No. of Data Points	Temperature range of fit (K)	n	E_t (eV)	M	B	μ_o $(cm^2V^{-1}s^{-1})$	N_t/N_v	C	Type of Analysis
B732	13	235 - 300	1.0	0.247	$9.00x10^{1}$	$3.33x10^{-1}$	0.298	$6.40x10^{-5}$	0.99901	Fixed n, fixed E_t
	12	241 - 300	1.0	0.247	$8.31x10^{1}$	$3.01x10^{-1}$	0.277	$5.79x10^{-5}$	0.99830	Fixed n, fixed E_t
	13	235 - 300	1.5	0.247	$1.90x10^{3}$	$4.66x10^{-1}$	0.366	$8.98x10^{-5}$	0.99894	Fixed n, fixed E_t
	12	241 - 300	1.5	0.247	$1.67x10^{3}$	$3.95x10^{-1}$	0.321	$7.59x10^{-5}$	0.99857	Fixed n, fixed E_t
	13	235 - 300	1.0	0.254	$7.97x10^{1}$	$2.04x10^{-1}$	0.266	$3.93x10^{-5}$	0.99905	Fixed n, best E_t
	12	241 - 300	1.0	0.228	$1.12x10^{2}$	1.03	0.374	$1.98x10^{-4}$	0.99852	Fixed n, best E_t
	13	235 - 300	1.5	0.264	$1.39x10^{3}$	$1.49x10^{-1}$	0.268	$2.87x10^{-5}$	0.99911	Fixed n, best E_t
	12	241 - 300	1.5	0.236	$2.07x10^{3}$	$8.45x10^{-1}$	0.398	$1.63x10^{-4}$	0.99864	Fixed n, best E_t
	13	235 - 300	0.92	0.247	$5.52x10^{1}$	$3.17x10^{-1}$	0.291	$6.11x10^{-5}$	0.99901	Best n, fixed E_t
	11	235 - 300	1.06	0.247	$1.26x10^{2}$	$3.43x10^{-1}$	0.303	$6.60x10^{-5}$	0.99898	Best n, fixed E_t
	13	235 - 300	3.00	0.247	$2.71x10^{8}$	$1.88x10^{1}$	10.3	$3.62x10^{-3}$	0.99813	Fixed n, fixed E_t
B798	8	244 - 298	1.0	0.255	$1.04x10^{2}$	$3.16x10^{-1}$	0.345	$6.07x10^{-5}$	0.99960	Fixed n, fixed E_t
	8	244 - 298	1.0	0.265	$8.90x10^{1}$	$1.65x10^{-1}$	0.297	$3.17x10^{-5}$	0.99965	Fixed n, best E_t
	8	244 - 298	1.5	0.255	$2.22x10^{3}$	$4.39x10^{-1}$	0.426	$8.44x10^{-5}$	0.99953	Fixed n, fixed E_t
	8	244 - 298	1.5	0.274	$1.59x10^{3}$	$1.30x10^{-1}$	0.306	$2.51x10^{-5}$	0.99969	Fixed n, best E_t
	8	244 - 298	0.723	0.255	$1.95x10^{3}$	$2.70x10^{-1}$	0.242	$5.19x10^{-5}$	0.99961	Best n, fixed E_t
A868	11	236 - 306	1.0	0.240	$8.76x10^{1}$	$4.49x10^{-1}$	0.292	$8.64x10^{-4}$	0.99955	Fixed n, best E_t
	11	236 - 306	1.5	0.249	$1.56x10^{3}$	$3.45x10^{-1}$	0.300	$6.64x10^{-5}$	0.99957	Fixed n, best E_t
	11	236 - 306	0.65	0.231	$1.26x10^{1}$	$6.76x10^{-1}$	0.309	$1.30x10^{-4}$	0.99949	Best n, fixed E_t (E_t estimated)
	11	236 - 306	1.90	0.252	$1.68x10^{4}$	$3.65x10^{-1}$	0.330	$7.02x10^{-5}$	0.99963	Best n, fixed E_t
	9	236 - 306	1.61	0.252	$3.22x10^{3}$	$3.15x10^{-1}$	0.312	$6.07x10^{-5}$	0.99982	Best n, fixed E_t

Table T5.4: Electron Transport in a-Se: Curve Fitting with Eqn. (5.19)

Sample	No. of Data Points	Temperature Range of Fit (K)	n	E_t (eV)	M	B	μ_o $(cm^2V^{-1}s^{-1})$	N_t/N_c	C	Type of Analysis
B732	12	266 - 312	1.0	0.35	$3.67x10^{1}$	$1.213x10^{-1}$	0.122	$2.33x10^{-5}$	0.99874	Fixed n, fixed E_t
	10	266 - 312	1.0	0.35	$3.84x10^{1}$	$1.267x10^{-1}$	0.128	$2.44x10^{-5}$	0.99871	Fixed n, fixed E_t
	12	266 - 312	1.5	0.35	$-2.46x10^{3}$	-0.503	?	?	0.99841	Fixed n, fixed E_t
	10	266 - 312	1.5	0.35	$-2.10x10^{3}$	-0.430	?	?	0.99837	Fixed n, fixed E_t
	12	266 - 312	1.0	0.415	5.90	$1.09x10^{-3}$	0.020	$2.1x10^{-7}$	0.99993	Fixed n, best E_t

the third decimal place in C.

In three parameter curve fitting, n seems to depend strongly on the value of E_t used. It also shows some dependence on the number of data points. Best n values have fallen in the range 0.7 to 1.9 encompassing diffusive motion[†] and also lattice scattering.

It can be seen that no definite conclusion can be drawn on the exact nature of the microscopic mobility, $\mu_o(T)$, either by treating n as a third variable parameter or by comparing correlation coefficients for different n in two parameter analysis.

In three parameter best E_t type of curve fitting, the best E_t values obtained with n = 1.5 are larger than not only the best E_t values with n = 1.0 but also larger than the actual measured low temperature E_μ values. This finding favours n = 1 for $\mu_o(T)$, i.e. diffusive motion.[†] Note, however, that consistently higher C values obtained with n = 1.5 may be used to favour lattice scattering.

The room temperature (≈300K) value for μ_o seems to be typically ~0.3 $cm^2 V^{-1} s^{-1}$ and tends not to change by more than ∿50% for different types of analysis. As pointed out in Chapter 2 dark Hall mobility measurements of Juška et al 1969 have yielded $\mu_H \simeq 0.37$ $cm^2 V^{-1}s^{-1}$ which supports the results here. The order of magnitude of the microscopic mobility $\mu_o \sim$ 0.3 $cm^2 V^{-1}s^{-1}$ would indicate a diffusive type of motion rather than conventional band transport with lattice scattering. A lower limit for the latter transport has been estimated to be about ∿20 $cm^2 V^{-1}s^{-1}$ (see, e.g. Emin 1976).

N_t/N_v values however are sensitive to the type of analysis. The values are within 2×10^{-5} to 2×10^{-4}. N_t seems to be larger for n = 1.5 than for n = 1.0. In other words, if the microscopic transport is by diffusive motion rather than transport limited by lattice scattering then a fewer number of traps are required to reduce the microscopic mobility.

[†] See notes p.275 for the definition of diffusive motion in the context used in this thesis.

From Fig. 5.11, it is clear that the hole mobility activation energy E_μ shows a field dependence in a Poole-Frenkel fashion (eqn. (5.8)) with β_{exp} values close to eqn. (5.9b). We may consequently expect the shallow traps to be charged centres. These traps may, therefore, be ionized impurities or charged structural defects.

The exact origin of the shallow traps controlling the drift mobility is, however, difficult to ascertain. All the three batches in T5.3 have comparable density of shallow traps for a given type of transport analysis. For example, for $\mu_0 \sim T^{-1}$, $(N_t/N_v) \approx (6 \to 7) \times 10^{-5}$ and assuming $N_v \approx 5 \times 10^{19}$ cm^{-3} at room temperature, $N_t \approx 3 \times 10^{15}$ cm^{-3}, (i.e. 0.1 ppm). This suggests that the shallow traps may be an intrinsic property of a-Se rather than arising from impurities. They may be the C_1^- states near the VB mobility edge, as speculated by Mott and Davis for example (Mott and Davis 1979, Ch.10). The activation energy E_t would then represent the energy associated with eqn. (2.6) in §2.4. The densities of these shallow traps,as quoted in T5.3. are well within the concentration estimates for VAP defects from eqn. (2.7) in §2.4. Further discussions on the origins of the shallow traps are given later. Note that impurities in the 0.1 ppm range normally escape detection by SSMS analysis.

The field dependence of the drift mobility μ_h in Fig. 5.12(b) seems to be typical of a-Se prepared by evaporation (cf. mobility data of Tabak 1970 and Pai 1974) but contrasts sharply with the exponential dependence on the field as observed in bulk a-Se samples by Marshall and Owen 1972 (Fig. 2.24). Several authors attempted to explain the observed field dependence, $\mu_h(F)$. Tabak et al 1971 showed that $\mu_h(F)$ was inconsistent with the Bagley expression (Bagley 1970) for the mobility;

$$\mu = \frac{\lambda}{F} \; 2\nu \; \exp(-\frac{\Delta G}{kT}) \sinh \frac{\lambda eF}{kT} \qquad (5.22)$$

where ΔG is the activation energy (i.e. E_μ) of the transport process, λ is the average separation in space of transport sites and ν is the attempt to escape frequency.

Fox and Locklar 1972 suggested the existence of a distribution of traps above the VB mobility edge. They argued[†] that only traps to a certain depth E_t above E_v acted as shallow traps depending on the 'transit time'. In fact they represented the trap-controlled mobility μ_{eff} via

$$\frac{\mu_o}{\mu_{eff}} \cong 1 + \sum_i \frac{N_i(E)}{N_v} \exp \frac{E_i}{kT} \qquad (5.23)$$

where N_i is the density of traps at the energy E_i above E_v. As the voltage increased, i.e. observation time decreased, there were less number of terms in the summation in eqn. (5.23) and thus μ_{eff} increased with the bias. When the authors fitted their theory to Tabak's data (Tabak 1970) they found an exponential trap distribution from E_v of the form

$$N(E) = (1.6 \rightarrow 4.2) \times 10^4 \exp\left[\frac{-E}{k(158K)}\right] \ (\mathrm{cm}^{-3}\ \mathrm{eV}^{-1}) \qquad (5.24)$$

This type of trap distribution according to Marshall 1977 however does not generate the required hole photocurrent shapes for a-Se. In any case, it would not be expected to lead to a finite mobility if only this distribution of traps control the mobility.

Hill's (1974) explanation for the increase in the mobility with the applie field at low temperatures was based on the field dependence of the release time τ_r in eqn. (5.6). In this model, the release of a trapped carrier to the extended states can occur either by simple direct thermionic emission or by emission to a distribution of localized (tail) states near E_v from where the carrier can hop or tunnel under the influence of the field. In the former case, assuming the traps are coulombic, τ_r is approximately, either of the form in eqn. (5.10) or for a high density of traps it follows* (e.g. Vollmann 1974)

$$\tau_r \sim \exp\left[\frac{E_t - aeF}{kT}\right] \qquad (5.25)$$

[†] This is, in principle, the multiple trapping model of dispersive transport described in §3.4.

[*] The general expressions for the probability of release, τ_r^{-1}, are rather complicated and depend on a variety of factors. See, for example, review by Kao and Hwang 1981 (Ch.5) and section 5.4.2 of this chapter.

where 2a is the separation of the ionized centres. In the case where emission is to the localized band tail states followed by escape into the extended states via hopping, Hill proposes

$$\tau_r \sim \exp\frac{E_t}{kT} \exp\left\{\frac{2}{kT}\,\frac{n}{n+1}\left[\frac{eF}{(n+1)\,2.17\,AkT}\right]^{1/n}\right\} \tag{5.26}$$

where it is assumed that the localization parameter α is given by $\alpha = A(E-E_v)^n$; $n \sim 0.6$ for E not far from E_v.

In the trap-controlled transport mechanism the field dependence of the drift mobility incorporates the field dependence of each of the parameters in eqn. (5.6), i.e. $\mu_o(F)$, $\tau_c(F)$ and $\tau_r(F)$. The latter parameter has several forms depending on the release process. τ_r in eqn. (5.10) is the simplest Poole-Frenkel expression which is derived by assuming one-dimensional thermionic emission in the direction of the field (Frenkel 1938). More elaborate models for carrier detrapping involving, for example three-dimensional analysis (e.g. Hartke 1968, Idea et al 1971, Adamec and Calderwood 1975) or high density of traps (Hill 1971b,Vollmann 1974) lead to rather complicated field expressions, none of which can satisfactorily account for $\mu_h(T)$ over the whole field range. It is useful to note that in comparison with the three-dimensional analysis of thermal detrapping by Ieda et al and the Onsager theory† of ionization (see Pai 1975 and Pai and Enck 1975 the simple one-dimensional Poole-Frenkel effect grossly overestimates the escape probability of the trapped carrier (see Fig. 5.18 in Kao and Hwang 1981 Ch.5). Further discussions on the Poole-Frenkel effect (including the Onsager theory) will be given in section 5.4.2(A) following more experimental results.

Possible field dependence for τ_c and μ_o have been discussed by Marshall and Owen 1972 in an attempt to explain their data (Fig. 2.24). Although τ_c in high mobility solids where $\bar{\ell} > r_c$ may be expected to increase

---

†Onsager 1934. See section 5.4.2(A).

with F via the capture cross-section $S_t(F)$ in eqn. (3.9) (Dussel and Bube 1966 and Dussel and Böer 1970), in amorphous semiconductors $\bar{\ell}$ is usually small ($<<r_c$) and τ_c is then diffusion limited and of the form in eqn. (5.5). The field dependence of μ_o for transport near or at E_v is the most difficult to identify (see Marshall and Miller 1973 and Mott and Davis 1979, Ch.2). The observed algebraic field dependence of the drift mobility (below ~250K) down to the lowest fields employed probably arises from the behaviour of $\mu_o(F)$ since $\tau_c(F)$ and $\tau_r(F)$ are expected to be in their so-called 'ohmic regions', i.e. field independent regions. This important inference on $\mu_o(F)$ obviously needs further work.

None of the proposed models have been able to account for the field dependence of the drift mobility and also provide an explanation for the difference in $\mu_h(F)$ for evaporated and quenched samples. For example, the interpretation of Marshall and Owen's mobility data by the use of eqn. (5.25) leads to unreasonably large values of N_t (10^{21} cm^{-3}) and hence inordinately high values of μ_o. There is no doubt, however, that a considerable part of the field dependence of $\mu_h(T)$ at low temperatures arises from dispersion effects. This is clearly demonstrated by noting that at T ∿ 192K the index s in eqn. (5.12) from Fig. 5.12(b) is about 0.30. From the thickness dependence of the mobility (Fig. 2.23) (Pfister 1976), $s \approx 0.15$. Consequently the low temperature field dependence of the drift mobility is in part due to the non-Gaussian dispersion of the carrier packet*; eqns. (3.85) and (3.86)

From the above discussions it should be apparent that trap-controlled transport mechanism provides a reasonable interpretation for the hole drift mobility data. Transport by hopping or by small polaron motion which would also exhibit a thermally activated behaviour (see, e.g. review by Spear 1974) is considered to be unlikely in view of the discussions in §2.5.3. Transport by polaron hopping is ruled out because the data would imply field dependent

---

*The thickness dependence of the TOF 'drift mobility' for a-Se at low temperatures is clearly shown in Fig. 17 of Pfister 1979.

polaron energies of $W_p \lesssim 0.58$ eV.

It is possible however that the hole transport occurs by trap controlled hopping. This novel concept has been shown to explain charge transport in a number of solids, e.g. a-As_2Se_3 (Pfister and Scher 1977, 1978), PVK, PVK:TNF (Hirsch 1979, Tahmasbi et al. 1979) and some disordered organic solids (Mort 1977). The transport process occurs essentially by hopping among a distribution of hopping sites with occasional or frequent interruption by trapping into a distribution of traps. While the charge is in a trap it is immobile until it is released again into hopping sites (which in this model act as transport sites).

Suppose that hopping occurs among the localized tail states above E_v and that there is a monoenergetic set of traps of density N_t at an energy E_t above E_v. Then the effective drift mobility at low fields may be expected to be of the form[†]

$$\mu_{hop} \cong \mu_o \left(\frac{nkT}{\Delta E}\right)^n \frac{N_c}{N_t} e^{-n} \exp\left[-\frac{(E_t + W_1 - \Delta E)}{kT}\right] \qquad (5.27)$$

Here, following the description in §1.1.2, $\mu_o = \nu_{ph} \frac{eR^2}{kT} \exp(-2\alpha R)$ as in eqn. (1.12), W_1 is the hop energy given by eqn. (1.17), $\left(\frac{nkT}{\Delta E}\right)^n N_c$ is the density of the hopping sites, N_m, where transport is most likely to occur, i.e. eqn. (1.15), and e^{-n} occurs because of eqn. (1.14). As a result of the presence of $\frac{N_c}{N_t}$, the pre-exponential factor would be larger than $\mu_o (\sim 10^{-2})$ and thus dispose the usual objection against hopping in a-Se based on a large pre-exponential factor in $\mu_h(T)$. In this transport regime we may expect the drift mobility to show a pressure dependence by virtue of $\mu_o(R)$. The lack of such a dependence up to ∼5 kbar (§2.5.3) is probably the only evidence against any type of hopping. It should be pointed out that in trap controlled hopping mechanism we may expect a transition at low temperatures to hopping among the trap states and hence a change in the mobility activation energy E_μ from

---

[†] Developed from Grant and Davis 1974, Marshall et al 1974.

$E_t + W_1 - E$ to W_2, where W_2 is the hop energy among the traps. No such transition has been observed in TOF experiments even at the lowest temperatures accessed, ∿124K (Pfister 1976). In fact, E_μ below ∿250K, remains, within experimental errors, completely independent of temperature.

Another possible trap controlled hopping process would be to assume a wide distribution of hopping sites in energy, i.e. transport sites are not necessarily limited to the band tail. Hirsch 1979, for example, analysed this situation with a large number of localized states (hopping sites) and a smaller number of coulombic centres (traps). Hirsch assumed that the dielectric constant, above some temperature T_1, increases with temperature so that β vanishes at high temperatures when $T = T_0 > T_1$. Although the model predicts a diminishing field dependence with increasing temperature and a possible eventual transition to $E_\mu = W$ from $E_\mu = W + E_t$, its applicability to a-Se is probably unjustified due to ε_r being temperature independent in the range 77-320K for $\omega = 10^2 - 3 \times 10^{10}$ Hz (Lakatos and Abkowitz 1971). The model also predicts a decrease in E_μ^o at $T \sim T_1$ with lowering of temperature because ε_r becomes temperature insensitive. This is not observed in Figs.5.11 and 5.18.

It may be of interest to notice that for most amorphous semiconductors and organic solids in which charge transport is believed to be by hopping or trap controlled hopping, e.g. a-As_2Se_3, a-As_2S_3, PVK, TNF, PVK:TNF, the measured drift mobilities not only have been at least two orders of magnitude lower than in a-Se, but also have shown stronger field dependence than apparent in Fig. 5.12.

It can be seen that the most probable interpretation of transport data in a-Se is that of trap-controlled diffusive motion in extended states near E_v.

It may be useful to point out that the hole transport in α-monoclinic Se (α-Se), a molecular crystal, as apparent in Fig.2.20 and T2.2 (§2.5.1(ii)). also shows a thermally activated behaviour (see also Dalrymple and Spear 1972) with measured drift mobility values not very much different than those for a-Se.

In fact, E_μ for α-Se is about 0.23 eV and within experimental errors equal to that for a-Se in the same temperature range 250K → 300K. The density, N_t, of the mobility controlling traps are also comparable in both forms of Se; for example for α-Se $N_t \sim 10^{16}$ cm^{-3} and for a-Se $N_t \sim 3 \times 10^{15}$ cm^{-3}. In fact the similarity of transport in both phases of Se lead some authors (e.g. Juška et al 1973, 1974) to speculate that a-Se contains Se_8 rings and hole transport involves motion through the ring molecules. Juška and co-workers argued that the hole drift mobility in a-Se as measured in TOF experiments corresponds to the microscopic (or conductivity) mobility because the difference in activation energy of the conductivity σ and the thermopower S in their experiments is approximately equal to the mobility activation energy, i.e. $E_\sigma - E_S \approx 0.9 - 0.65 = 0.25$ eV $\approx E_\mu$. It must be remembered that both $\sigma(T)$ and $S(T)$ for a-Se are difficult to measure and their interpretations are open to question (see §2.5.2).

In view of the charged defect discussions of §2.4 we may thus conjecture that in both α-Se and a-Se a similar type of defect, e.g. D^- (C_1^-), is probably responsible for the trap controlled mobility.

Photocurrent Waveform

Although at room temperatures the transient hole photocurrent waveform obeyed the equations expected under extended state transport (e.g. eqns. (3.5) and (3.11)), at low temperatures, $T \lesssim 245$K, the photocurrent became dispersive as in eqn. (3.84). It was postulated in the previous section that in the intermediate temperature range the transient photocurrent may be represented by eqn. (5.4).

This postulate may be justified as follows. Firstly, curve fitting eqn. (5.4) onto the hole photocurrents at temperatures $T \gtrsim 1$°C produces lifetimes which are the same as those found by simple exponential fit from eqn. (3.11) as required. The n values are, however, very small (e.g. $\lesssim 10^{-3}$), indicating $\alpha = 1$. At very low temperatures where the lifetimes are large, eqn.(5.4 reduces to the dispersive transport, (eqn. (2.19a)), which describes the low temperature transport in a-Se. In the intermediate temperature range it generates τ values approximately equal to the 'time constants' of the straight line regions in the plots (c) and (d) of Fig. 5.9 (p.161).

Secondly, eqn. (5.4) is qualitatively reasonable because it is the simplest way to represent the transient current decay as due to dispersion arising from the spreading of the carrier packet, and trapping into a set of deep traps. The two processes are assumed independent to enable a simple product to be taken.

It is interesting to note that the change in the shape of the photocurrent occurs around ∿245K where there is also a change in the temperature and field dependence of the drift mobility (Fig. 5.10). This seems to suggest that there may well be a transition from one transport regime to another. For example, transition from trap controlled band transport above T ∿ 250K to trap controlled hopping at low temperatures. Another possibility would be transport controlled by two species of shallow traps at energies E_1 and E_2 above E_v, in which case the effective drift mobility is given by eqn. (5.23) with i = 1 and 2.

Deep Traps

Consider now the deep trapping lifetime τ_h measured for the drifting holes. If the trapping process is diffusion limited then we can use eqn. (5.5) to calculate the density of the deep coulombic traps.

Taking a typical value of, say, $\tau_h \approx 10\ \mu s$ for B-type a-Se and $u_n \approx 0.16\ cm^2\ V^{-1}\ s^{-1}$ we can estimate the concentration of deep coulombic traps responsible for the decay in the hole photocurrent. Using $\varepsilon_r \cong 7$ gives $N_d^- \approx 2.2 \times 10^{12}\ cm^{-3}$ (i.e. 10^{-4} ppm).

If on the other hand we use eqn. (3.9) then we need to assign reasonable values to $\bar{v}$ the average speed and S_d, the deep trap capture cross section. In many crystalline (and semicrystalline) solids experimentally determined capture cross sections have been typically $S_d^o \sim 10^{-16} cm^2$ and $S_d^- \sim 10^{15}$ cm^2(e.g. Lax 1960, Bonch-Bruevich and Landsberg 1968) representing respectively a neutral and an oppositely charged impurity trap. With $\bar{v} = v_{thermal} \sim 10^7$ cms^{-1} the corresponding rap densities are $N_d^o \sim 1 \times 10^{14}$ cm^{-3} (i.e. 5 x 10^{-3} ppm) and $N_d^- \sim$ x 10^{13} cm^{-3} (i.e. 5 x 10^{-4} ppm). Note that the use of $\bar{v} = v_{thermal}$ is necessary inasmuch as S_d values are normally determined from capture coefficients, $\langle Sv \rangle$, by assuming $\langle Sv \rangle = S\langle v \rangle = Sv_{thermal}$.

The source of these traps are unlikely to be foreign impurities since the deep trapping lifetime τ_h was found to depend on the substrate temperature[†] T_{sub} (Fig. 5.8). They are, therefore, probably due to structural defects, or microcrystalline inclusions as suggested by Montrimas and Petretis 1974 for example. In this connection it must be pointed out that typical values for S_d used above are associated with impurity type of traps rather than traps resulting from structural defects. The estimates for N_d^- and N_d^o must, therefore, be taken with caution.

The well defined exponential decays in the hole photocurrents (e.g. Fig. 5.4) indicate that during the transit of the carriers there is no release from the deep traps and the deep trap energy E_d (above E_v) must, therefore, be larger than 0.29 eV, the shallow trap energy, E_t. The location in energy of these deep traps may be determined by the measurement of the deep trap release time τ_{dr}. The release time τ_{dr} may be expected to be large, in the seconds range, since a relatively long ($\sim$ 15 min.) rest time was required to obtain reproducible hole photocurrents at low fields (see Scharfe and Tabak 1969).

It was pointed out in Ch. 1 that deeply trapped excess carriers give rise to a residual voltage V_{res} (e.g. eqn. (1.21)). The decay of the

---

[†] Unless, of course, the substrate temperature drastically affects the distribution of foreign impurities during condensation.

residual voltage depends on the release times τ_{dri} from each type of deep trap i. Abkowitz and Enck 1981, 1982, by studying the temperature dependence of the decay of the saturated residual voltage, have found a distribution of localized states below and above the Fermi energy, E_F. According to these authors' results, the hole deep traps lie between 0.9-1.0 eV above E_v and their density is relatively uniform, of the order of 10^{14} cm^{-3}, comparable to the neutral trap density estimates deduced from this work by the use of eqn. (3.9).

One possible structural candidate for a neutral hole trap is a C_3^o defect centre (§2.4, p. 54). The trapping process is then the conversion of C_3^o to C_3^+. The C_3^o defect would have a deep energy state and thus may not re-emit the hole within the observation time, $O(t_T)$. It must be remarked, however, that Agarwal 1973, as mentioned in §2.4, reports *no* EPR signal from a-Se and estimates $[C_3^o]$ or other spin densities to be less than 10^{14} cm^{-3}.

The increase in N_d with the fall in the substrate temperature, the dependence of N_d on the batch of a-Se, and particularly the absence of detailed information on the structure-preparation relationships make the identification of these deep traps difficult.

(B) Electron Transport

General Interpretation

Most of the discussions and interpretations for hole transport in a-Se can also be applied to electron transport. Although the measured drift mobilities have been a factor of ∿20 less than the hole mobility it has not been difficult to justify extended state or band transport as stated in §2.5.3 by assuming a trap-controlled transport mechanism. Writing the electron mobility at low temperatures ($T \leq 278K$) as

$$\mu = \mu_o' \exp(-\frac{E_\mu}{kT}) \qquad (5.28)$$

it is obvious from Fig. 5.17 that μ_o' is large, $\approx 7 \times 10^3$ cm^2 V^{-1} s^{-1}, indicative of trap controlled transport (see eqn. (5.32), p.204)

If the microscopic mobility is of hopping type in the band tail then eqn. (5.27) with $(\frac{nkT}{\Delta E})\ e^{-n} \sim 1$, $\mu_0 \approx 10^{-2}$ gives a trap density of $N_t \approx 1.4 \times 10^{-6}\ N_c$, i.e. $N_t \approx 7 \times 10^{13}\ \text{cm}^{-3}$ (2×10^{-3} at. ppm).

On the other hand,assuming band transport and taking the microscopic mobility $\mu_0 \approx 0.32\ \text{cm}^2\ \text{V}^{-1}\ \text{s}^{-1}$ from the photo Hall measurements of Dresner (1964) gives $N_t \approx 4.6 \times 10^{-5}\ N_c$, i.e. $2.3 \times 10^{15}\ \text{cm}^{-3}$ (0.07 at.ppm). Clearly, the concentrations of traps required to control the transport are not unreasonable.

Another possible transport mechanism which can exhibit the characteristics in Fig. 5.18 is small polaron transport via non-adiabatic hopping (Holstein 1959). Inasmuch as small polaron motion has been usually observed in narrow band molecular solids in which the observed mobility values have been smaller than those measured in a-Se (see, e.g. Spear 1974), and that the $\mu_e(T)$ data in Fig. 5.18 imply a 'small' polaron energy of $W_p = 2E_\mu \approx 0.70$ eV should be sufficient argument against this mode of transport. In any case, the fact that $\mu_e(T)$ is pressure independent up to $\sim$5kbar is probably good evidence against any type of hopping since the latter would involve a term J^2 where J is the overlap integral and inversely proportional to exponential of the distance between hopping sites (molecules). In orthonombic S, for example, the electron mobility at 5kbar is five times its value at 1kbar (Dolezalek and Spear 1970).

An important aspect of electron transport in a-Se is that the magnitude of the drift mobility and its field dependence (Fig. 5.16, Table T5.1) are sensitive to the origin of the Se, i.e. batch. For batch A a-Se, for example, where there were more impurities (Table T4.2), in type and density, the electron transport was trap limited. Unless there were fundamental differences in structure between the different batches, which we will assume unlikely (§2.2), it seems that electron transport is indeed controlled by traps. The lack of field dependence in the mobility activation energy E_μ up to $F \sim 1.5 \times 10^5\ \text{V cm}^{-1}$ suggests that these traps may be neutral impurities (or defects), positioned in energy at ~ 0.35 eV below E_c.

Table T5.4 shows a summary of the essential results of $\mu_e(T)$ data (Fig. 5.18) analysis using eqns. (5.17) - (5.21) based on trap-controlled transport. It is clear that the deviation in the log μ vs T^{-1} plot at $T \gtrsim 278K$ from the well behaved thermally activated transport at low temperatures can be accounted by the saturation of the drift mobility towards the microscopic value $\mu_0(T)$ as predicted by eqn. (5.6) when $\tau_c/(\tau_c + \tau_r) \rightarrow 1$. $\mu_0(T)$ seems to be diffusion limited, i.e. $\mu_0 = MT^{-1}$, with a room temperature value $\mu_{oe} \sim 0.13$ cm^2 V^{-1} s^{-1}, about half the microscopic hole mobility μ_{oh}. This should not be unexpected as μ_{oh} previously was also found to be of diffusive nature.

There are a number of other trap controlled transport mechanisms which also lead to a thermally activated drift mobility. For example, for electron transport above E_c in the extended states with periodic interruptions by trapping and detrapping from the localized tail states below E_c, the observed drift (i.e. effective) mobility may also be thermally activated. The possibility of this mode of trap controlled electron transport involving a distribution of localized states is examined in section 5.4.2(B) following further electron drift mobility data on the system Se/0.5% As + y ppm Cℓ.

The weak or no field dependence observed in the electron mobility up to $F \sim 1.5 \times 10^5$ Vcm^{-1} should be contrasted with the exponential field dependence, as in eqn. (2.21), found by Marshall et al 1974 for bulk a-Se. The observed field dependence of $\mu_e(F)$ of the form in eqn. (5.14) with no apparent low field saturation to a constant mobility is very similar to the behaviour of $\mu_h(F)$ and may be due to the field modifying transport near or at E_c (Marshall and Miller 1973).

At high fields, the mobility increases sharply with the field, apparently still in the fashion of eqn.(5.14) but with a higher n value Attempts to explain $\mu_e(F)$ in this region by a Poole-Frenkel effect (eqn. (5.11)) have generated experimental β values nearly an order of magnitude lower than eqn. (5.9b) (e.g. see Fig. 5.16). The sharp increase in the mobility with the field at high fields may be due to a transition from multiple trapping transport to that with a few or no trapping events. Consider the capture time τ_c in eqn. (5.6). Taking $N_t \sim 2 \times 10^{-5} N_c \sim 10^{15}$ cm^{-3}, the capture cross section $S_t^o \sim 10^{-16}\ \mathrm{cm}^2$, $\bar{v} \sim 10^7\ \mathrm{cm\ s}^{-1}$ in eqn. (3.9) gives $\tau_c \sim 1$ µs. At high fields when the transit time t_T becomes comparable to τ_c, there are only a few or no trapping events and thus the drift mobility is no longer of reduced form as in eqn. (5.6). This argument however is not supported if τ_c is determined via eqn. (5.5) with $\mu_o \sim 0.13\ \mathrm{cm}^2\ \mathrm{V}^{-1}\ \mathrm{s}^{-1}$. In this case eqn. (5.5) gives $\tau_c \sim 0.03$ µs which is much smaller than the minimum t_T values observed ($\gtrsim 1$ µs). To have τ_c values comparable with $t_T \sim 1$ µs we need to take $\mu_o \lesssim 10^{-2}\ \mathrm{cm}^2\ \mathrm{V}^{-1}\ \mathrm{s}^{-1}$ which would imply hopping transport.

Comparison of Fig. 5.18 for a-Se with the electron mobility data for α-Se (Fig. 2.20 and Table T2.2) shows that at low temperatures both exhibit thermally activated behaviour. Notice, however, that for α-Se the absolute values of μ_e are some two orders of magnitude higher and that at higher temperatures $\mu_e(T)$ is limited by lattice scattering in accord with wide band semiconductor theory. It may be useful here to conjecture that if the low temperature thermally activated behaviour in both forms of Se is due to a common type of trap centre then the $\sim$0.1 eV larger E_μ in a-Se may be due to the extent of the localized tails, i.e. $\Delta E = E_c - E_A \simeq 0.1$ eV.

Deep Traps

The deep trapping time τ_e obtained from the shape of the transient photocurrent was found to be strongly field dependent following eqn. (5.13) for low and moderate fields and then saturating and perhaps increasing with the field as shown in Fig. 5.15. Rossiter and Warfield 1971 also found a similar behaviour for τ_e in their TSCLC[†] measurements on a-Se. Analysis of their τ_e data using eqn. (5.13), shown in Table T5.2, gives a

---

[†] Transient Space Charge Limited Current

β_{exp} values comparable with those found in this work. Although the $\tau_e(F)$ data are sufficiently flexible to allow interpretation in terms of a $\exp \frac{\beta F^{\frac{1}{2}}}{kT}$ type of dependence it is doubtful that a simple Poole-Frenkel type of effect can account for the observed field dependent behaviour. For example, the data in Fig. 5.14 may be viewed $\tau_e \approx$ constant at low fields but $\tau_e \sim F^{-n}$, $n \approx 1.5$ at higher fields. The field dependence exhibited by τ_e in Fig. 5.15 showing a decrease, saturation and slight increase with the field is not unique to a-Se. For example, the field behaviour of the electron lifetime in ZnSe crystals as measured by the TOF technique is qualitatively similar to Fig. 5.15 (Heaton et al 1972).

Note that the decrease in τ_e with F in Fig. 5.15 cannot be explained by diffusion limited ($\bar{\ell} \ll r_c$) trapping inherent in eqn. (5.5) because $\mu_e(F)$ is only slightly field dependend (Fig. 5.16) over the fields employed for τ_e determination. Moreover for $\bar{\ell} \gg r_c$, eqn. (3.9) predicts an increase in τ_e with F via the reduction in the capture cross section $S_d(F)$ (p.186).

It is important here to remark that an exponential decay in the TOF current transient can also arise from a uniform distribution of unneutralized bulk space charge of opposite polarity to injected charge (Scharfe and Tabak 1969). The time constant of decay in I(t) is then given by

$$\tau = \frac{\varepsilon_0 \varepsilon_r}{\mu \rho} \qquad (5.29)$$

where μ is the drift mobility and ρ is the bulk space charge density. For electron transport eqn. (5.29) requires the knowledge of the electron drift mobility μ_e and the trapped hole density in the bulk.

Eqn. (5.29) can account for the behaviour of τ_e with temperature and applied field via the temperature and field dependences of μ_e and ρ. The thermally activated behaviour of $\tau_e(T)$ in Fig. 5.10 is thus attributed to $\mu_e(T)$ whereas the field dependence of $\tau_e(F)$ in Fig. 5.15 is attributed to $\rho(F)$. We may expect the latter to increase with the bias due to field enhanced injection of holes through the substrate contract.

If we take the time constant τ_e of the electron photocurrent to represent the deep trapping lifetime then using eqn. (3.9) we can estimate the minimum deep trap densities required to give τ_e^o varying from ~1 to ~10^3 μs. With $S_d^o \sim 10^{-16}$ cm^2 and $S_d^+ \sim 10^{-15}$ cm^2 as before and $\bar{v} = V_{thermal} \sim 10^7$ cm s^{-1}, the charged and neutral trap densities are

$$N_d^+ = 5 \times 10^{10} \text{ to } 5 \times 10^{13} \text{ cm}^{-3} \quad (\text{i.e. } 1.4 \times 10^{-6} \text{ to } 1.4 \times 10^{-3} \text{ ppm})$$

$$N_d^o = 5 \times 10^{11} \text{ to } 5 \times 10^{14} \text{ cm}^{-3} \quad (\text{i.e. } 1.4 \times 10^{-5} \text{ to } 1.4 \times 10^{-2} \text{ ppm})$$

where the largest N_d correspond to the smallest τ_e values observed.

Since small τ_e^o or large N_d values apply to A-type a-Se (Table T5.2) in which SSMS analysis have shown considerable impurity content of $\gtrsim 1$ ppm (Table T4.2) it seems reasonable to associate deep trapping effects with impurity inclusions. Possible impurities from Table T4.2 which may be acting as deep traps are O or Cu because Fe is common to both types of Se whereas τ_e at 1-2 ppm level leaves electron transport relatively unaffected (§5.5). Oxygen has already been suggested as an electron trap in liquid Se (Gobrecht et al 1971). Its high electronegativity and effect on increasing $\sigma_{dc} \cong pe\,\mu_h(dc)$ (La Course et al 1970) suggests that O rather than Cu is the deep electron trap.

(C) Transport near T_g

Both the hole and electron transport above T_g (Fig. 5.10) seem to show a saturation in the drift mobility and lifetime. In the trap controlled transport mechanism this saturation, i.e. $\mu(T) \to \mu_0$ and $\tau(T) \to \tau_0$, occurs naturally as τ_r becomes short.

As the temperature is raised through T_g, the hole drift mobility shows a 'dip' which does not reappear in the second thermal cycling if the latter starts immediately after cooling (Abkowitz and Pai 1978). Clearly this behaviour is similar to that of $C_p(T)$ or the glass transition peak in the DSC thermogram for first and second thermal runs as discussed in §4.7.3 (see Fig. 4.11). Therefore the dip in $\mu_h(T)$ at T_g is probably due to structural relaxation effects associated with the glass transition phenomenon.

The behaviour of the electron mobility $\mu_e(T)$ through T_g is similar to that of the hole mobility. $\mu_e(T)$ shows a sharp fall at T_g and then remains constant.

Detailed discussion of transport near T_g would require further experimental work.

§5.3 a-Se + y ppm Cℓ

5.3.1 Results and Discussion

(A) Hole Transport

The TOF hole signals observed for a-Se + y wt. ppm Cℓ with y = 30 and 40 were very similar to those for a-Se, provided the delay time t_d between the application of bias and arrival of the xenon pulse was not excessively long ($\gtrsim$2 ms). The time constant of the exponential decay observed in the photocurrent was assigned to a deep trapping time τ_h as before. This assignment is probably only correct for short delay times since for $t_d \gtrsim 2$ ms, 'τ_h' decreased with t_d and eventually when $t_d \gtrsim 0.1$s the transient current decayed 'quickly' with no apparent transit time t_T. This effect is shown in

Fig. 5.19 as log 'τ_h' vs t_d, Clearly without this test against t_d, the hole photocurrents might have been misinterpreted as trap-limited.

Fig. 5.20 shows the room temperature field dependence of the drift mobility, $\mu_h(F)$, and Fig. 5.21 shows the temperature dependence, $\mu_h(T)$, at three different applied voltages for 30 ppm and 40 ppm Cℓ doped Se.

The field dependence, $\mu_h(F)$, seems to follow eqn. (5.12) with the index s increasing with Cℓ content. Since the mobility data exhibits scaling with thickness variation from L = 42 to 81 μm for a-Se with 30 ppm Cℓ and from L = 53 to 62 μm for a-Se with 40 ppm Cℓ, we can be reasonably confident that the observed $\mu_h(F)$ represents an intrinsic behaviour rather than a dispersive effect.

As apparent from Fig. 5.21, the hole drift mobility in 40 ppm Cℓ doped a-Se exhibits a well defined thermally activated behaviour from room temperature down to the lowest temperature accessed (∿238K). In 30 ppm Cℓ doped a-Se, the mobility activity energy $E_\mu(F)$ at a given field was well defined at low temperatures, $T \lesssim 270K$, but tended to decrease at high temperatures, $T \gtrsim 270K$. This behaviour in $\mu_h(T)$ for Se + 30 ppm Cℓ is similar to that for pure Se in which the critical temperature was ∿250K.

The low temperature mobility activation energy E_μ was found to decrease linearly with the applied field F as shown in the left inset (a) of Fig. 5.21. Using

$$E_\mu = E_\mu^0 - aeF \tag{5.30}$$

we find that both 30 and 40 ppm Cℓ doped samples have $E_\mu^0 \approx 0.45$ eV and $a \approx 40$ nm. Clearly in Cℓ doped a-Se, E_μ is strongly field dependent.

Eqn. (5.30) suggests that the drift mobility at a given temperature has an exponential dependence on the field of the form in eqn. (2.21), i.e.

$$\mu(F) = \mu^0 \exp \frac{eaF}{kT} \tag{5.31}$$

where $\mu^0 = \mu(0)$ and a is a temperature dependent constant usually called the 'activation length'. The right inset (b) in Fig. 5.21 shows some typical

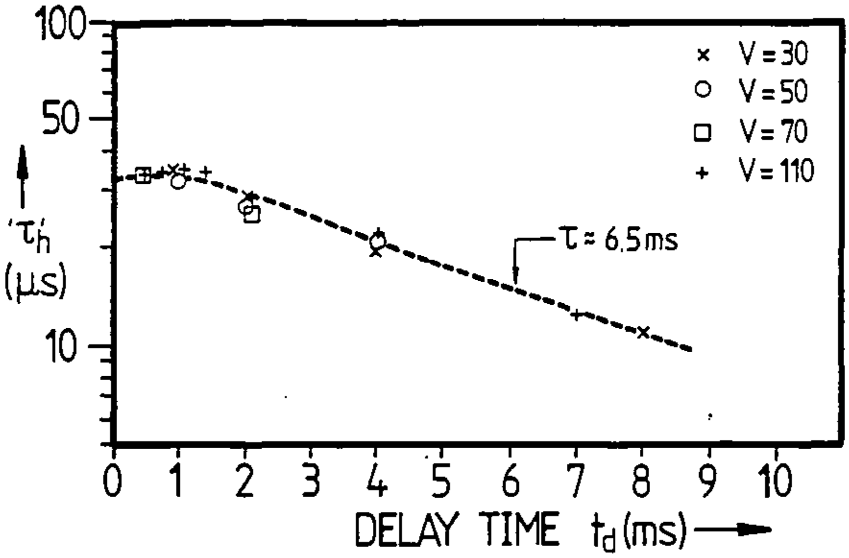

Fig. 5.19: Log 'τ_h' vs delay time t_d of optical excitation for a-Se + 40 ppm Cℓ, 'τ_h', the 'apparent lifetime' is the time constant obtained from the decay of the hole photocurrent for $t \lesssim t_T$.

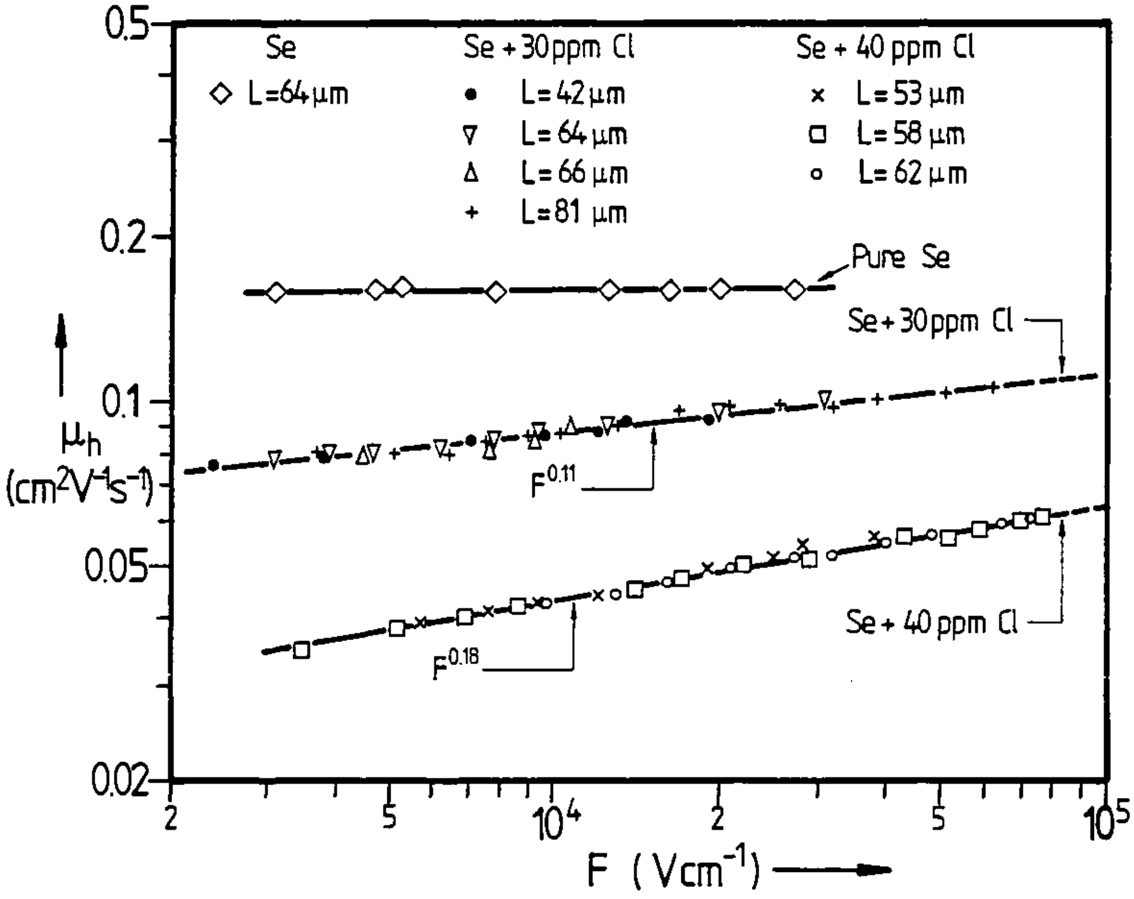

Fig. 5.20: Log-log plots of hole drift mobility μ_h vs applied electric field F for a-Se + y ppm Cℓ at room temperature.

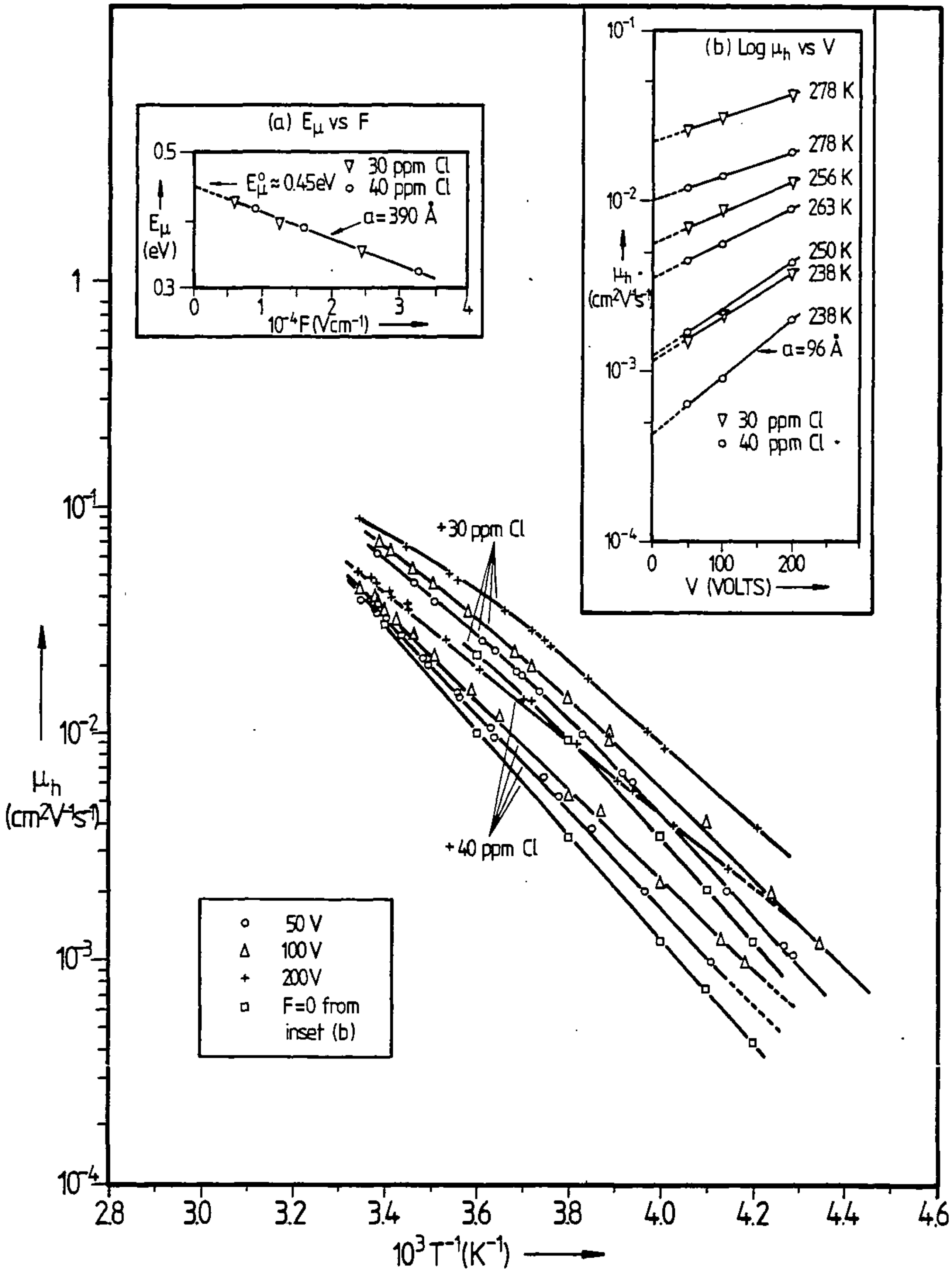

Fig. 5.21: Temperature dependence of hole drift mobility in a-Se + 30 ppm Cℓ and a-Se + 40 ppm Cℓ at various applied fields. The insets show (a) low temperature activation energy E_μ vs applied field F and (b) log μ_h vs V at different temperatures.

log μ_h vs V plots at various 'low' temperatures for both 30 and 40 ppm Cℓ doped Se. It can be seen that with only three $\mu_h(F)$ points it is not difficult to confirm eqn. (5.31) and thus obtain the zero field mobility μ_h^o. The log μ_h vs T^{-1} plots in Fig.5.21 at F = 0 have been obtained by using such extrapolated $\mu_h^o(T)$ data.

Effects of adding chlorine on hole drift parameters are shown in Fig. 5.22 for the drift mobility at $F \approxeq 5 \times 10^3 V\ cm^{-1}$, its 'low field' or zero field activation energy E_μ^o, the lifetime τ_h for two different batches and the Schubweg $s_p = \mu_h \tau_h F$ at $F \cong 5 \times 10^3\ V\ cm^{-1}$ for these two batches.

As apparent from Fig. 5.22, the hole range $r_h = \mu_h \tau_h$ at low fields seems to have been relatively unaffected in one batch,(B), whereas in the other batch,(A), it has shown an improvement. Note that the increase in the mobility with the field (Fig. 5.20) indicates longer range values at higher fields. This suggestion, however, may not be justified inasmuch as it assumes that τ_h remains constant at its low field value. If τ_h is, for example, described by eqn. (5.5) then it should decrease with F so as to maintain $r_h = \mu_h \tau_h$ constant. It is important to remember that although the drift mobility μ_h can be evaluated accurately from the transit time, the determination of the lifetime τ_h involves analysing the shapes of hole photocurrents or transient voltages at low fields (where $\tau_h \lesssim t_T$) and hence its value can only be approximate

(B) Electron Transport

There was no electron transport observable in any of the Cℓ doped samples (y = 30 and 40 ppm) which in the past (e.g. Tabak and Hillegas 1972) has been attributed to trap limited transport, i.e. $\tau_e \ll t_T$. The d.c. conduction levels with negative bias in these samples were found to be several orders of magnitude higher than that in pure a-Se. This suggests that it is quite possible that the TOF technique itself may no longer be operable, say, due to one of the contacts becoming highly injecting. It may be useful in this connection to note that high substrate temperatures are known to give a thin layer of crystalline structure at the

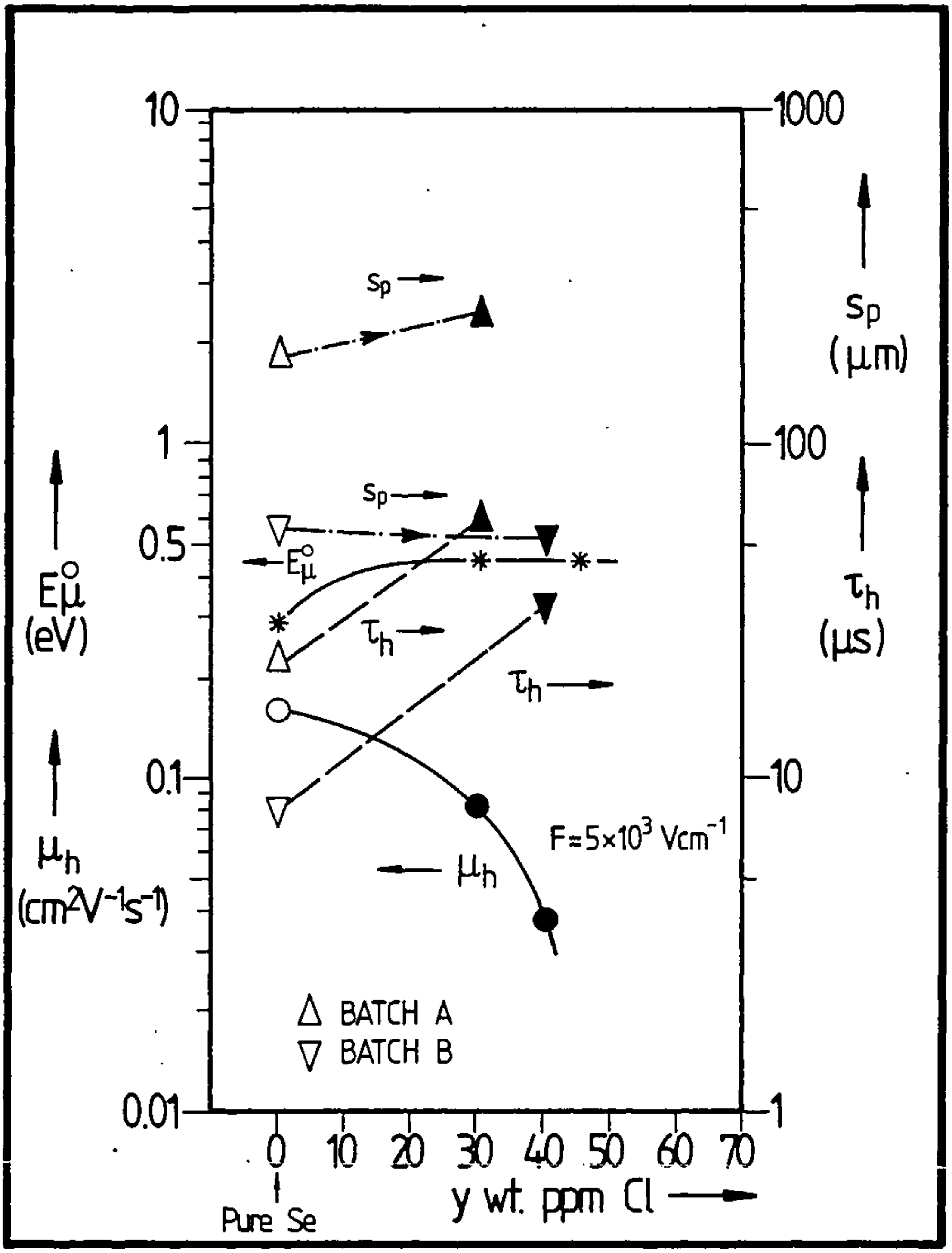

Fig. 5.22: Hole transport parameters in a-Se + y ppm Cℓ. E_μ^o is the 'zero field' or low field mobility activation energy. Note that τ_h depends on the batch, viz. (△) batch A and (▽) batch B. The Schubweg s_p is evaluated at $F = 5 \times 10^3$ V cm^{-1}. Only filled-in points (● ▲ ▼) have Cℓ.

Se-Aℓ interface (Petretis et al 1975, Montrimas and Petretis, 1973 and Cℓ doped Se is believed to be n-type (Twadell et al 1972).

5.3.2 Detailed Discussion and Interpretation

(A) Hole Transport

General Interpretation

The fall in the drift mobility and the enhancement of the hole lifetime are in general qualitative agreement with the trap controlled transport mechanism if we assume longer residence in the shallow traps, say due to an increase in E_t and/or N_t. In fact, it can be shown that the increase in E_t is more than that required to account for the fall in μ_h, hence implying a decrease in N_t.

Consider the well defined thermally activated behaviour of $\mu_h(T)$ in 40 ppm doped Cℓ. From the log μ_h vs T^{-1} plot at F = 0 in Fig. 5.21 and eqn. (5.28) we can determine the zero field μ_0' values. For example, at $T = 263.2K, \mu_h^0 = 3.5 \times 10^{-3}\ cm^2\ V^{-1}\ s^{-1}$, $E_\mu^0 = 0.45$ eV and eqn. (5.28) gives $\mu_0' = 1.29 \times 10^6\ cm^2\ V^{-1}\ s^{-1}$. Similar calculations† over the temperature range $T = 238 \rightarrow 294K$ show that μ_0 is temperature independent as expected from well defined E_μ^0 in Fig. 5.21.

In the trap controlled transport mechanism μ_0' is given by

$$\mu_0' = \mu_0 \frac{N_v}{N_t} \tag{5.32}$$

If Cℓ doping does not appreciably affect the microscopic mobility μ_0, then taking $\mu_0 \approx 0.3\ cm^2\ V^{-1}\ s^{-1}$ gives $N_t/N_v \approx 2.3 \times 10^{-7}$ or $N_t \approx 1.2 \times 10^{13}\ cm^{-3}$ (i.e. 3.5×10^{-4} at ppm). Thus the assumption that Cℓ modifies only the existing shallow traps leads to the inference that their density is diminished by a factor of ∿260. In addition, their distance in energy from E_v is increased by ≈0.16 eV.

---

†For example at T = 238K, $\mu_0' = 1.28 \times 10^6$ and at 40K higher temperature $\mu_0' = 1.29 \times 10^6\ cm^2\ V^{-1}\ s^{-1}$.

If, on the other hand, there was a change in the mode of microscopic channelling to hopping then the increase of 0.16 eV could be associated with the hop energy. This model, however, requires $N_t/N_v = 7.8 \times 10^{-9}$ since μ_o for hopping is $\sim 10^{-2}$ cm^2 V^{-1} s^{-1}.

Suppose that Cℓ doping introduces an additional set of shallow traps. The effective drift mobility μ_h in the presence of two sets of discrete monoenergetic traps may be expected to be of the form[#]

$$\frac{\mu_o(T)}{\mu_h(T)} = 1 + \frac{N_{t1}}{N_v} \exp \frac{E_{t1}}{kT} + \frac{N_{t2}}{N_v} \exp \frac{E_{t2}}{kT} \qquad (5.33)$$

where E_{t1} and E_{t2} are the depths in energy of the traps from the transport states (i.e. E_v) and N_{t1} and N_{t2} are their respective densities. We may tentatively associate the traps at E_{t1}, type 1 traps, with the Se atoms, and the traps at E_{t2}, type 2 traps, with the Cℓ atoms. In other words type 1 traps are intrinsic to the a-Se structure whereas type 2 traps are Cℓ induced. Interpretation of the $\mu_h(T)$ data for Se + 40 ppm Cℓ in Fig. 5.21 via eqn. (5.33) implies that, $E_{t2} = 0.45$ eV and $N_{t2}/N_v \approx 2.3 \times 10^{-7}$. It also requires that

$$\frac{N_{t2}}{N_v} \exp \frac{E_{t2}}{kT} \gg \frac{N_{t1}}{N_v} \exp \frac{E_{t1}}{kT} \qquad (5.34)$$

Using $E_{t1} \approx 0.29$ eV, $E_{t2} \approx 0.45$ eV, $N_{t2}/N_v = 2.3 \times 10^{-7}$ gives $N_{t1}/N_v \ll 1.1 \times 10^{-4}$. Since, in undoped Se, $N_t/N_v \approx 6 \times 10^{-5}$, which satisfies this inequality, we cannot conclude that Cℓ doping destroys type 1 traps.

Turning to the mobility-temperature data of Se + 30 ppm Cℓ, it is apparent that at high temperatures above $T \approx 270$K, the mobility activation energy E_μ decreases with temperature. At low temperatures it is well defined; $E_\mu^o = 0.45$ eV.

In the temperature range $T < 270$K, applying eqn. (5.28) we find μ_o' (at $F = 0$) $= 3.6 \times 10^6$ cm^2 V^{-1} s^{-1} which is a factor of ≈ 2.8 larger than that for 40 ppm doped Se. In other words, assuming that $\mu_o \approx 0.3$ cm^2 V^{-1} s^{-1} remains

---

[#] assuming thermal equilibrium concepts.

unaffected with Cℓ doping, the density of the transport controlling shallow traps (type 2) at $E_{t2} \gtrsim 0.45$ eV increases with Cℓ content.

The high temperature ($T \gtrsim 270$K) behaviour of $\mu_h(T)$ in Fig. 5.21 can readily arise when the densities of the two types of traps do not satisfy eqn. (5.34). At low temperatures the second exponential term in eqn. (5.33) may dominate the right hand side whereas at high temperatures the two exponential terms may be of comparable magnitude.

To quantify this argument we can curve fit eqn. (5.33) onto the $\mu_h(T)$ data of Se + 30 ppm Cℓ in Fig. 5.21. The curve fit analysis may be achieved by writing eqn. (5.33) in the form

$$\left(\frac{Mx}{y} - 1\right) x^{-3/2} \exp\left(-\frac{E_{t1}x}{A'}\right) = m \exp \frac{(E_{t2}-E_{t1})x}{A'} + c \qquad (5.35)$$

i.e.

$$Y(x,y,M,E_{t1}) = mX(x,E_{t1},E_{t2}) + c \qquad (5.36)$$

where the nature of the functions Y and X are obvious from eqn. (5.35), $x \equiv T^{-1}$, $y \equiv \mu_h(T)$, $\mu_o = MT^{-1} = Mx$, $A' \equiv e/k = 8.63 \times 10^{-5}$ and the slope m and the intercept c are defined by

$$\frac{N_{t2}}{N_v} = mT^{-3/2} \quad \text{and} \quad \frac{N_{t1}}{N_v} = cT^{-3/2} \qquad (5.37)$$

Notice that the microscopic mobility was assumed to be proportional to T^{-1} and $N_v \sim T^{3/2}$. E_{t1} and E_{t2} in eqn. (5.35) are in eV.

Table T5.5 summarizes the essential results obtained from curve fitting eqn. (5.35) onto the $\mu_h(T)$ data of Se + 30 ppm Cℓ. The analysis was carried out by setting E_{t2} and E_{t1} to the low temperature activation energy E_μ in pure Se and 30 ppm doped Se respectively at the field of interest. M was taken as 90 (see Table T5.3).

It can be seen that eqn. (5.33) provides a meaningful interpretation of the drift mobility-temperature data. Cℓ doping introduces a new set of traps, type 2, at an energy $E_{t2} \approx 0.45$ eV above E_v. The microscopic mobility μ_o and the density of type 1 traps, which control hole transport in undoped

Table T5.5: Hole Transport in a-Se + y ppm Cℓ

y [wt.ppm]	E_{t1} [eV]	N_{t1}/N_v	E_{t2} [eV]	N_{t2}/N_v	M $[cm^2V^{-1}s^{-1}K]$	Comment
0	0.26	$(4\text{-}6)\times10^{-5}$	?	?	90	At $F \cong 6.1\times10^3 V\ cm^{-1}$. $E_{t1} = E_\mu(F)$ from Fig. 5.11. See also T5.3
30	0.26	30×10^{-5}	0.43	1.32×10^{-7}	90	Eqn. (5.33) onto $\mu_h(T)$ data at $F \cong 6.1\times10^3 V\ cm^{-1}$. Best E_{t1}, N_{t1}/N_v.
30	0.26	-8.5×10^{-6}?	0.42	4.91×10^{-8}	30	Eqn.(5.33) with $\mu_{oh} \cong 0.1\ cm^2V^{-1}\ s^{-1}$
40	0.29?	$<<10^{-4}$	0.45	2.30×10^{-7}	90	Eqns. (5.28) and (5.32) with log μ_h^o vs T^{-1} plot in Fig. 5.21

<u>NOTES:</u> It is assumed that $\mu_o = MT^{-1}$. E_t values represent the effective trap depths which include the influence of the field.

Se, seem to be relatively unaffected. In fact, trying M = 30 ($\mu_0 \approx 0.1$ cm^2 V^{-1} s^{-1}) in curve fitting, (eqn. (5.33)) gives incompatible results. The density of type 2 traps increases with Cℓ content thus supporting the initial hypothesis that they are Cℓ induced. Since for Se + 40 ppm (i.e. 89 at. ppm) Cℓ there are ∿3.5 x 10^{-4} at. ppm type 2 traps, it takes one in every ∿2.5 x 10^{5} Cℓ atoms to generate a trap of this type.

Inasmuch as the drift mobility activation energy has a strong field dependence suggests that these Cℓ induced traps may be charged centres; perhaps isolated charged Cℓ atoms, i.e. $C\ell_0^-$.The univalent nature of Cℓ means that it can terminate a Se chain either by chain breaking or by substitution for the C_1^- centre. In this context it will be extremely useful to have ESR experiments to examine the nature of Cℓ produced centres in Se + Cℓ. If Cℓ does substitute for C_1^- then it will produce a neutral Cℓ chain end and an an electron (Mott and Davis, Ch. 10). The electron may go to another Cℓ atom to produce an unbonded $C\ell^-$ ion, which may act as a hole trap.

Deep Trapping

The improvement in the hole range observed in batch A a-Se + Cℓ is in agreement with Tabak's (1971) report[#] that Cℓ addition to a-Se promotes hole transport. In eqn. (5.5) this means that τ_0 is probably increased with Cℓ doping. Since the exact nature of deep hole traps is still unresolved it is not possible to describe the specific mechanism by which Cℓ affects τ . If the deep hole traps are indeed microcrystalline Se inclusions (see above section 5.2.2(A)) in the amorphous structure then the increase in τ implies either a decrease in their concentration or their size. This is possible because Cℓ addition in small quantities (≲40 ppm) has been found, by one group of researchers, to retard crystallization (Janjua et al 1970).

[#] This is a conference report in the form of an abstract without any quantitative details of the measurements.

(B) Electron Transport

It is interesting to notice that both O and Cℓ are highly electronegative elements and both seem to destroy electron transport in a-Se. Arsenic which has a smaller electronegativity than Se on the other hand promotes electron transport (§5.4) by enhancing the lifetime τ_e.

§5.4 a-Se/0.5% As + y ppm Cℓ

5.4.1 Results and Discussion

(A) Hole Transport

Fig. 5.23 shows a typical set of hole drift mobility results, $\mu_h(T)$, as a function of temperature at different applied fields for type B a-Se/0.5% As. The inset shows the dependence of the low temperature activation energy E_μ on $V^{\frac{1}{2}}$ for two different batches of Se. Fig. 5.24 displays typical drift mobility-temperature data at various biases on the system a-Se/0.5% As + 30 ppm Cℓ. The inset has the low temperature E_μ vs $V^{\frac{1}{2}}$ plot obtained from the log μ_h vs T^{-1} lines.

It can be seen that the temperature dependence of the hole drift mobility in a-Se/0.5% As and a-Se/0.5% As + 30 ppm Cℓ is very similar to that in pure a-Se (Fig. 5.11). Not only the room temperature magnitude of the drift mobility, $\mu_h \approx 0.16\ \mathrm{cm^2\ V^{-1}s^{-1}}$, but also its high temperature and zero field low temperature mobility activation energies, ≈ 0.20 eV and ≈0.29 eV respectively, seem to be unaffected by the addition of 0.5% As. Effects of As alloying a-Se on the hole drift parameters are shown in Fig. 5.25(a). Notice that the hole lifetime τ_h and the hole Schubweg $s_p = \mu_h\tau_h F$ show consistent deterioration with As addition to both A and B type of a-Se. Similar findings have also been reported by Tabak and Hillegas 1972.

When As and Cℓ are used in simultaneously doping a-Se the resulting hole transport, shown in Fig. 5.25(b) has some very interesting features. The mobility and its low temperature activation energy data obtained by varying the As and Cℓ content in Se/As + Cℓ alloys constitute two complementary triangles

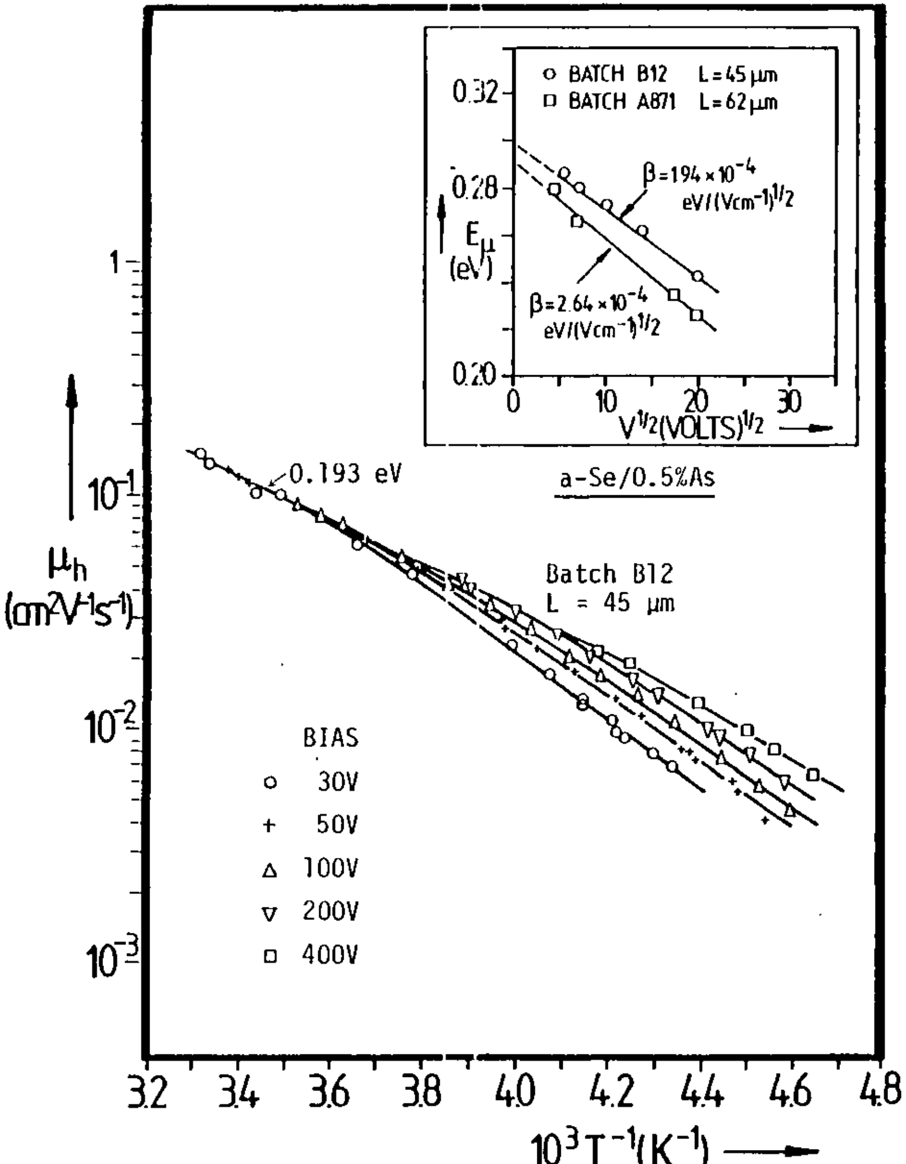

Fig. 5.23: Temperature dependence of hole drift mobility in a-Se 0.5%As at various applied fields. The inset shows the low temperature activation energy E_μ vs $V^{\frac{1}{2}}$. Also shown in the inset is E_μ vs $V^{\frac{1}{2}}$. for another batch sample.

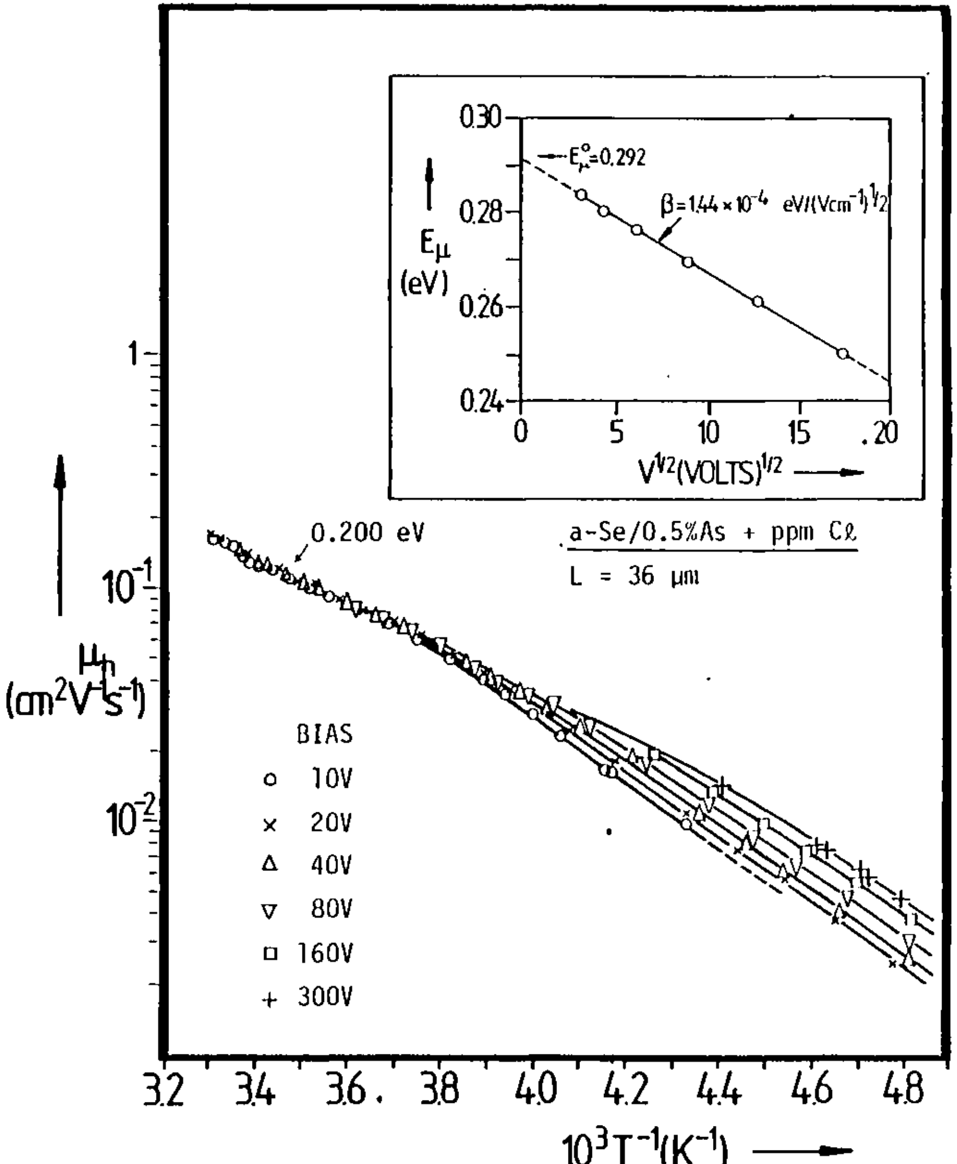

Fig. 5.24: Temperature dependence of hole drift mobility in ~30 ppm Cℓ doped a-Se/0.5%As at various applied fields. The inset shows low temperature activation energy E_μ vs $V^{\frac{1}{2}}$.

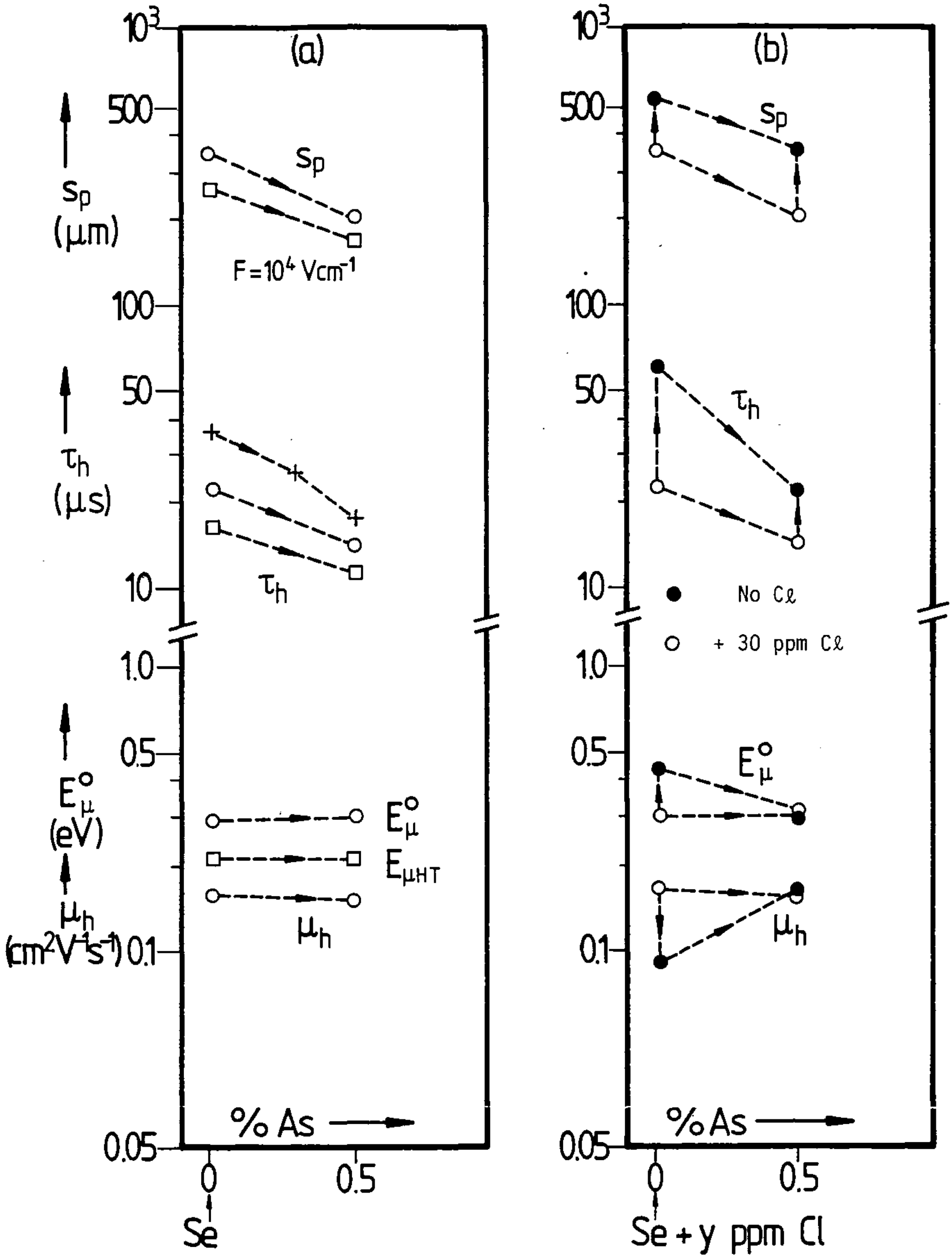

Fig. 5.25(a): Hole transport parameters in the a-Se/As alloy vs As content in wt.%, where $E_{\mu HT}$ is the high temperature ($T \gtrsim 250K$) and E_μ^0 is the 'low field', low temperature activation energy. + ○ □ indicate different batches for τ_h and s_p; (b) hole transport parameters in the system a-Se/x%As+y ppm Cℓ vs As content in wt.%. Filled in points have ~30 ppm Cℓ.

which we call mobility and activation energy triangles[†]. These two complementary triangles suggest that the low temperature hole transport in the system Se/x%As + y ppm Cℓ is controlled by the introduction and/or compensation of traps.

Consider the modulation of the mobility activation energy with As and Cℓ addition. Doping pure Se with Cℓ introduces a new set of traps at $E_{t2} \approx 0.45$ eV which causes an effective increase in E_μ. Alloying with 0.5%As then reduces E_μ to $E_{t1} \approx 0.29$ eV by compensating for Cℓ induced traps. The drift mobility is hence restored.

The lifetime values obtained can be used to construct a 'lifetime parallelogram', as in Fig. 5.25(b), which shows how the hole deep trapping time may be controlled by combinational doping. Addition of Cℓ improves the lifetime whereas As addition shortens it. The Schubweg parrallelogram tends to follow the behaviour of the lifetime parallelogram.

(B) Electron Transport

The results of the electron drift mobility measurements on a-Se/0.5%As at room temperature as a function of the applied field are shown in Fig. 5.26(a) for various batches.

Although the magnitude of the mobility varies from batch to batch its general field dependence is similar to that observed for a-Se (Fig. 5.16). Notice that As addition has reduced the electron mobility by at least a factor of two.

The field dependence of the electron mobility, $\mu_e(F)$, at room temperature in the system a-Se/0.5%As + 30 ppm Cℓ is shown in Fig. 5.26(b) for two batches of Se. It can be seen that the batch to batch variation in μ_e has disappeared with Cℓ addition to Se/0.5%As. This remarkable result could not have been predicted from μ_e(F) data or from any other previous transport measurements on the constituent systems, i.e. a-Se, a-Se/0.5%As and Se + 30 ppm Cℓ.

[†] Obviously the construction of the triangles also involves data from Figs. 5.21 and 5.22 of previous section §5.3.

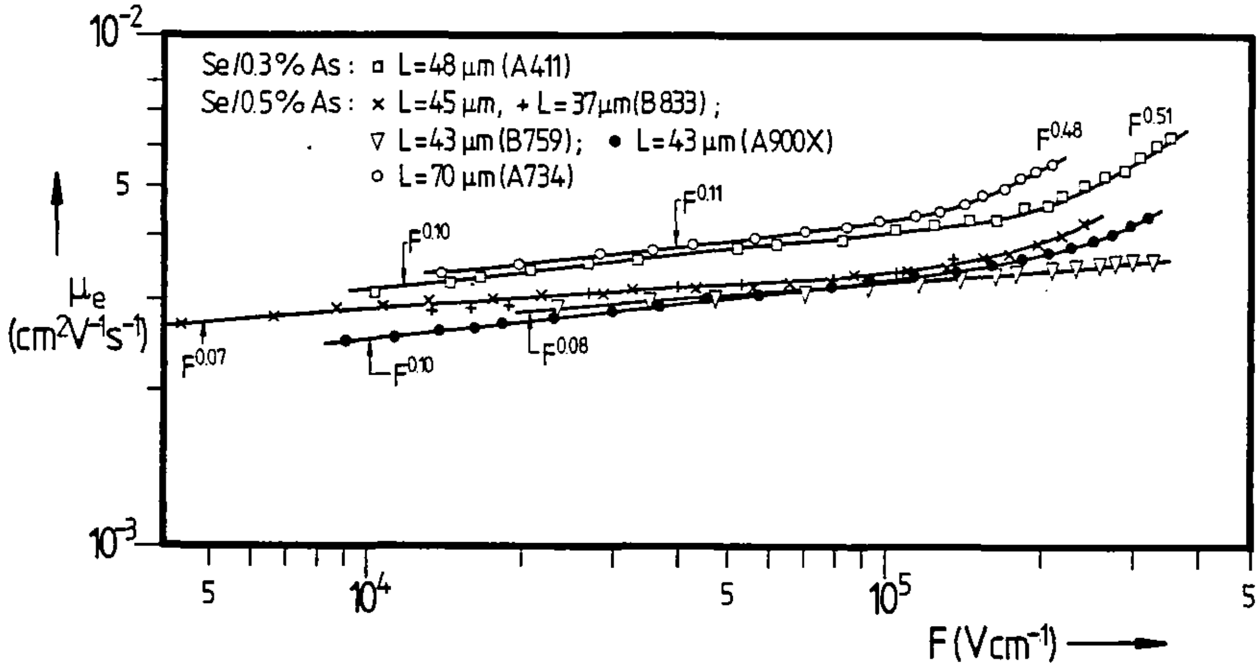

(a) Log μ_e vs log F for a-Se/0.5%As

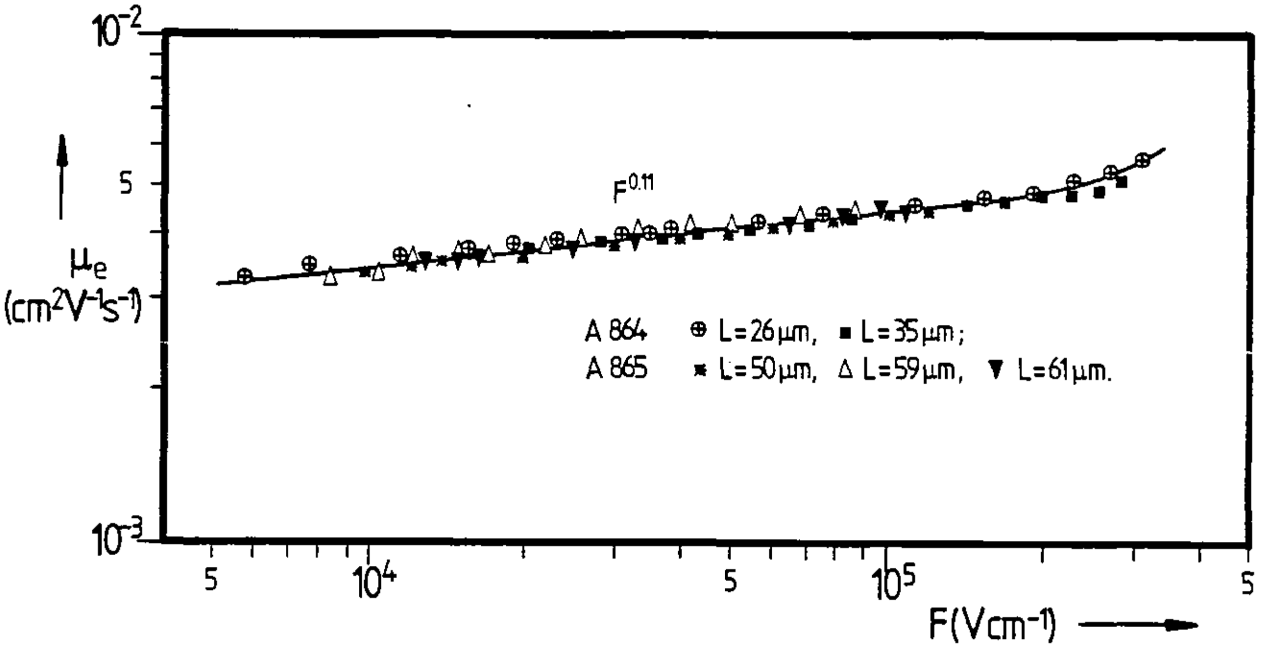

(b) log μ_e vs log F for a-Se/0.5%As + 30 ppm Cℓ

Fig. 5.26: Electric field dependence of electron drift mobility at room temperature in a-Se/%As + y ppm Cℓ.

It should be apparent from Fig. 5.26(a) and (b) that $\mu_e(F)$ data for a given batch show reasonable scaling with thickness to enable interpretation as a meaningful transport coefficient.

The TOF electron photocurrents in the a-Se/0.5%As + y ppm Cℓ (y = 0 and 30) system were very similar to those observed for pure a-Se (Fig. 5.13). The time constant of the exponential decay in I(t) was assigned to an electron lifetime τ_e as described above in section 5.2.1 (B). Fig. 5.27 shows a typical log τ_e vs $V^{\frac{1}{2}}$ plot for two Se/0.5%As samples from identical batches but with Au and Pd as top constants. It can be seen that although τ_e falls with the applied field in a Poole-Frenkel manner, eqn. (5.13), the β coefficient is smaller than that expected (β_{PF} in eqn. (5.9 b)). Table T5.2 summarizes the experimental β, i.e. β_{exp}, and τ_e^o, the extrapolated zero field lifetime, obtained for a-Se, a-Se/0.5%As and a-Se/0.5%As + 30 ppm Cℓ from such log τ_e vs $V^{\frac{1}{2}}$ plots as in Fig. 5.27.

It can be seen that β_{exp} values for a-Se and a-Se/0.5%As vary considerably between batches. For example, it has been as low as by a factor of ≈3 and as high as by a factor of ≈1.4. Notice that for the two batches of a-Se/0.5%As + 30 ppm Cℓ, β_{exp} is about $\frac{1}{2}\beta_{PF}$ and that the two batches have τ_e^o not substantially different from each other.

Figs.5.28 and 5.29 show clearly that the electron drift mobility in a-Se/0.3%As and a-Se/0.5%As is thermally activated. The activation energy E_μ for the 0.3%As doped sample is about 0.39 eV and relatively field independent, whereas E_μ for the 0.5% As doped sample decreases linearly with the applied field as shown in the left inset (a) of Fig. 5.29 in the form E_μ vs V. At a given bias, however, E_μ is well defined and independent of temperature. The zero field value, $E_\mu^o \approx 0.46$ eV is equal to E_μ at $F = 8 \times 10^4$ V cm^{-1} found by Pai 1974 but considerably higher than $E_\mu \simeq 0.33$ eV (at F = ?) reported by Schottmiller et al 1970.

The right inset (b) in Fig. 5.29 shows the field dependence of the drift mobility as log μ_h vs V at various temperatures. These plots were obtained

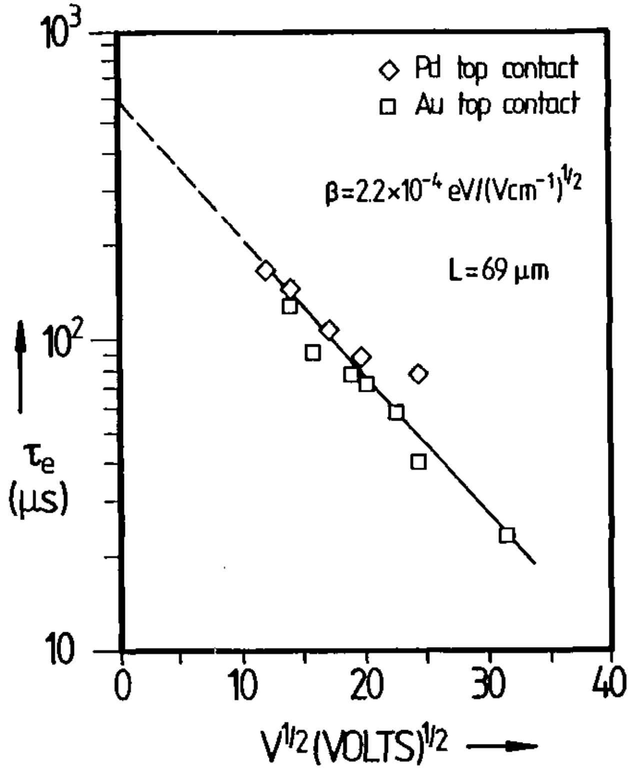

Fig. 5.27: Log τ_e vs $V^{\frac{1}{2}}$ for two different top contacts to a-Se. τ_e is the time constant of exponential decay of electron current transient.

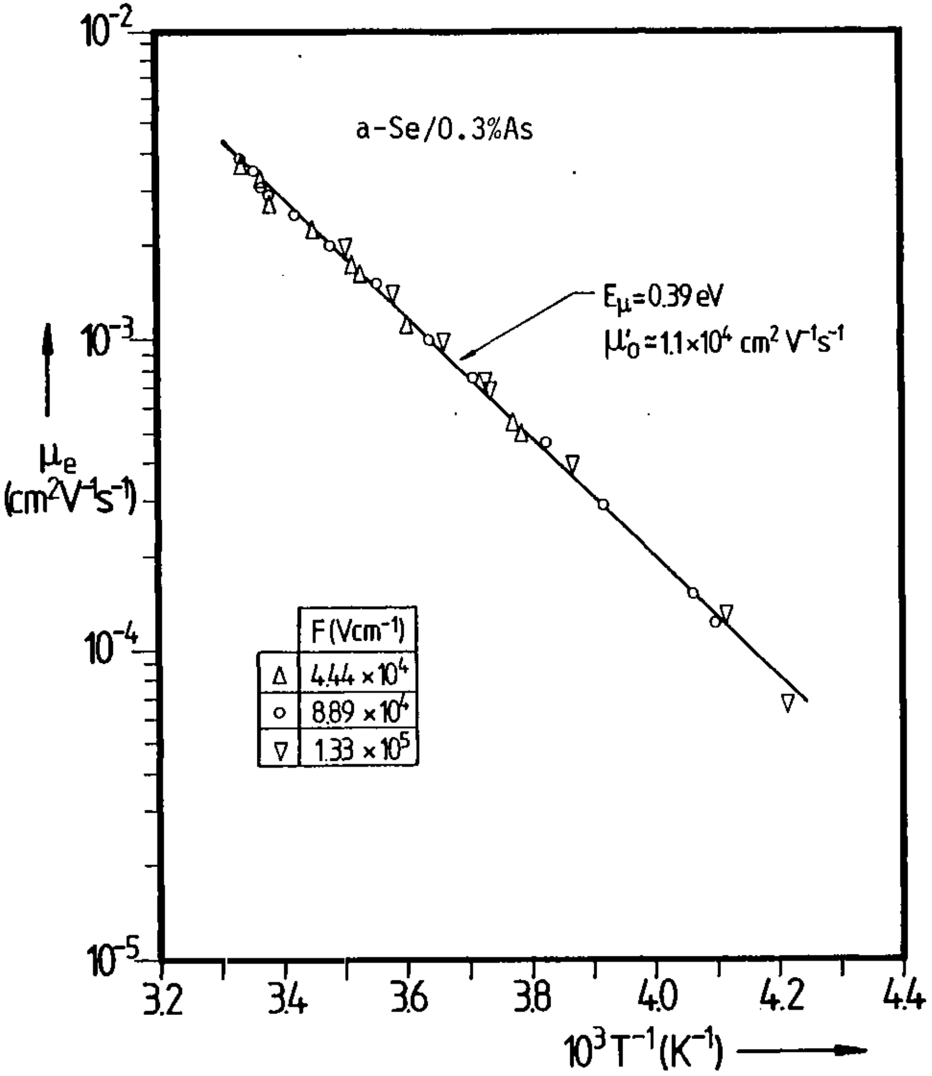

Fig. 5.28: Temperature dependence of the electron drift mobility in a-Se/0.3%As.

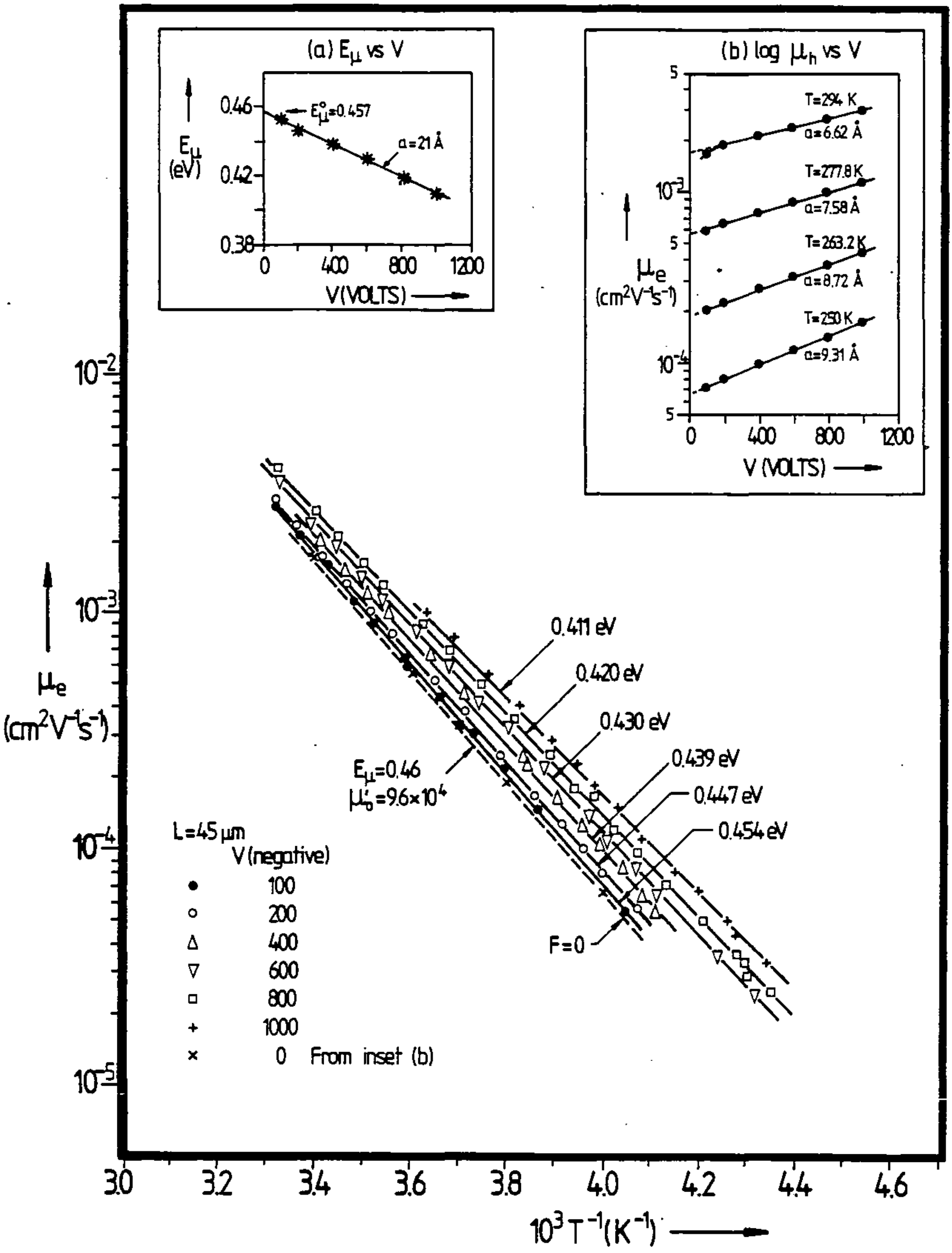

Fig. 5.29: Temperature dependence of electron drift mobility in a-Se/0.5%As at various electric fields. The insets show (a) E_μ vs $V^{\frac{1}{2}}$ and (b) log μ_e vs $V^{\frac{1}{2}}$ obtained from log μ_e vs T^{-1} plots.

from the log μ_e vs T^{-1} lines at different fields. It can be seen that the drift mobility seems to obey eqn. (5.31) in which a decreases with temperature. Notice that the a value obtained from the field dependence of μ_e, i.e. eqn. (5.31), is smaller than that obtained from the field dependence of E_μ, i.e. eqn. (5.30). The zero field mobility μ_e^o obtained by extrapolating eqn. (5.31) to F = 0, as expected, is thermally activated with $E_\mu = 0.46$ eV.

Fig. 5.30 shows the temperature dependence of the electron mobility in a-Se/0.5%As + 30 ppm Cℓ. The left inset (a) displays the activation energy E_μ vs $V^{\frac{1}{2}}$ whereas the right inset (b) has log μ_h vs V at various temperatures. At a given field the thermal activation energy is well defined as in the case with no Cℓ. The zero field activation energy E_μ^o from the inset (a) is 0.42 → 0.43 eV; slightly smaller than that for Se/0.5%As. Although the reduction in E_μ is proportional $F^{\frac{1}{2}}$, thus indicating a Poole-Frenkel type of behaviour, the experimental β coefficient from the E_μ vs $V^{\frac{1}{2}}$ data is about β_{PF} /2.9.

The field dependence of μ_e seems to follow eqn. (5.11) with experimental β values nearly an order of magnitude smaller than eqn. (5.9b) and decreasing with temperature. The extrapolated zero field mobility $\mu_e^o(T)$ was also thermally activated with $E_\mu^o \approx 0.44$ eV.

Fig. 5.31 summarizes the effects of combinational doping of a-Se with As and Cℓ on the electron transport parameters, viz. μ_e, τ_e, $s_n = \mu_e\tau_eF$ and E_μ^o. It should be apparent that the addition of 0.5%As reduces the electron mobility but enhances the electron lifetime. Doping with Cℓ then reduces the electron lifetime but leaves the mobility unaffected. The behaviour of s_n seems to be dominated mainly by that of τ_e.

5.4.2 Detailed Discussion and Interpretation

(A) Hole Transport

Since the magnitude of the hole drift mobility in a-Se and its temperature dependence, $\mu_h(T)$, are relatively unaffected by the addition 0.5%As and 0.5%As + 30 ppm Cℓ we may be justified to employ the same

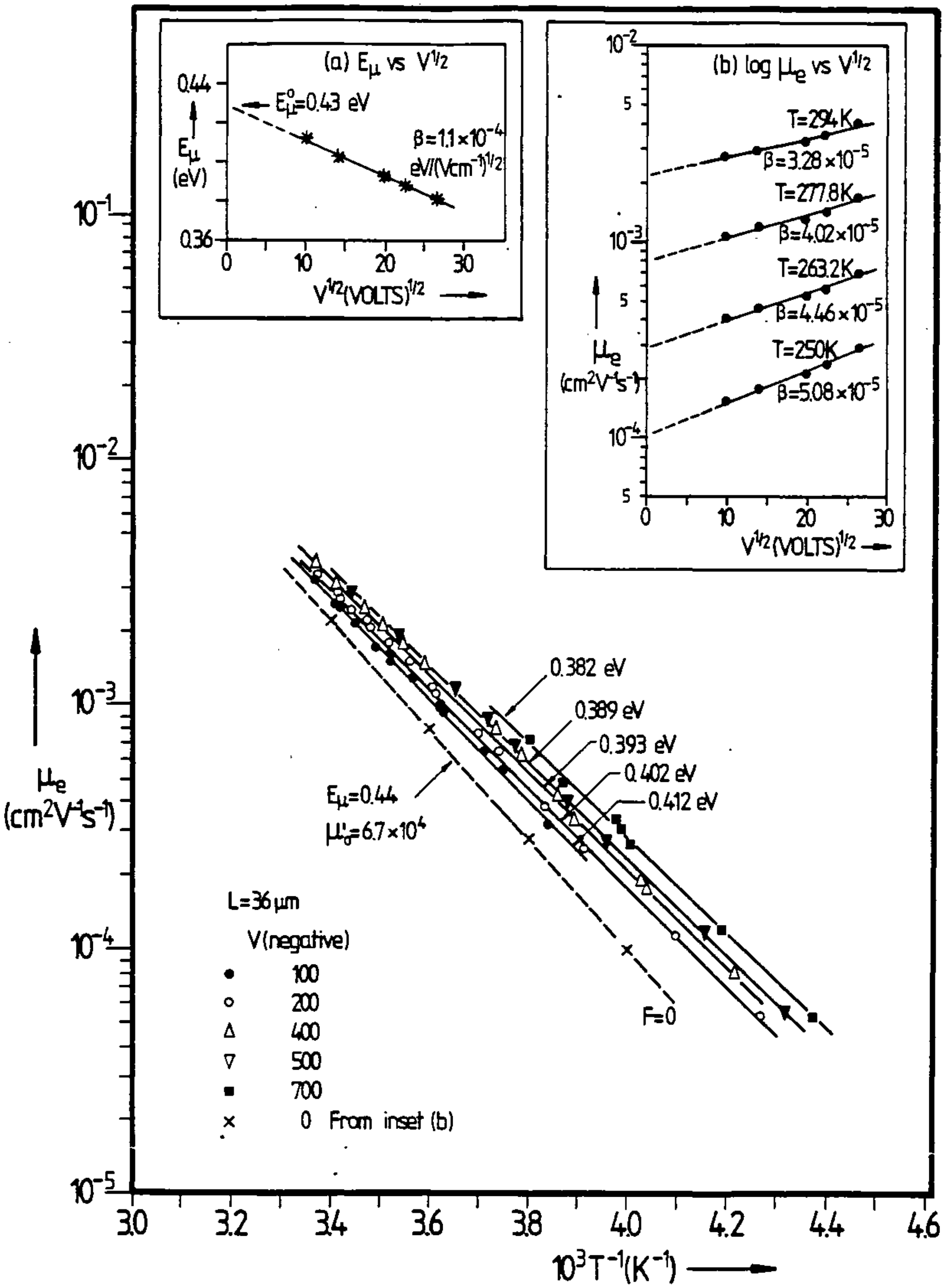

Fig. 5.30: Temperature dependence of electron drift mobility in ~30 ppm Cℓ doped a-Se/0.5%As at various electric fields. The insets show (a) E_μ vs $V^{\frac{1}{2}}$ and (b) log μ_e vs $V^{\frac{1}{2}}$ obtained from log μ_e vs T^{-1} plots.

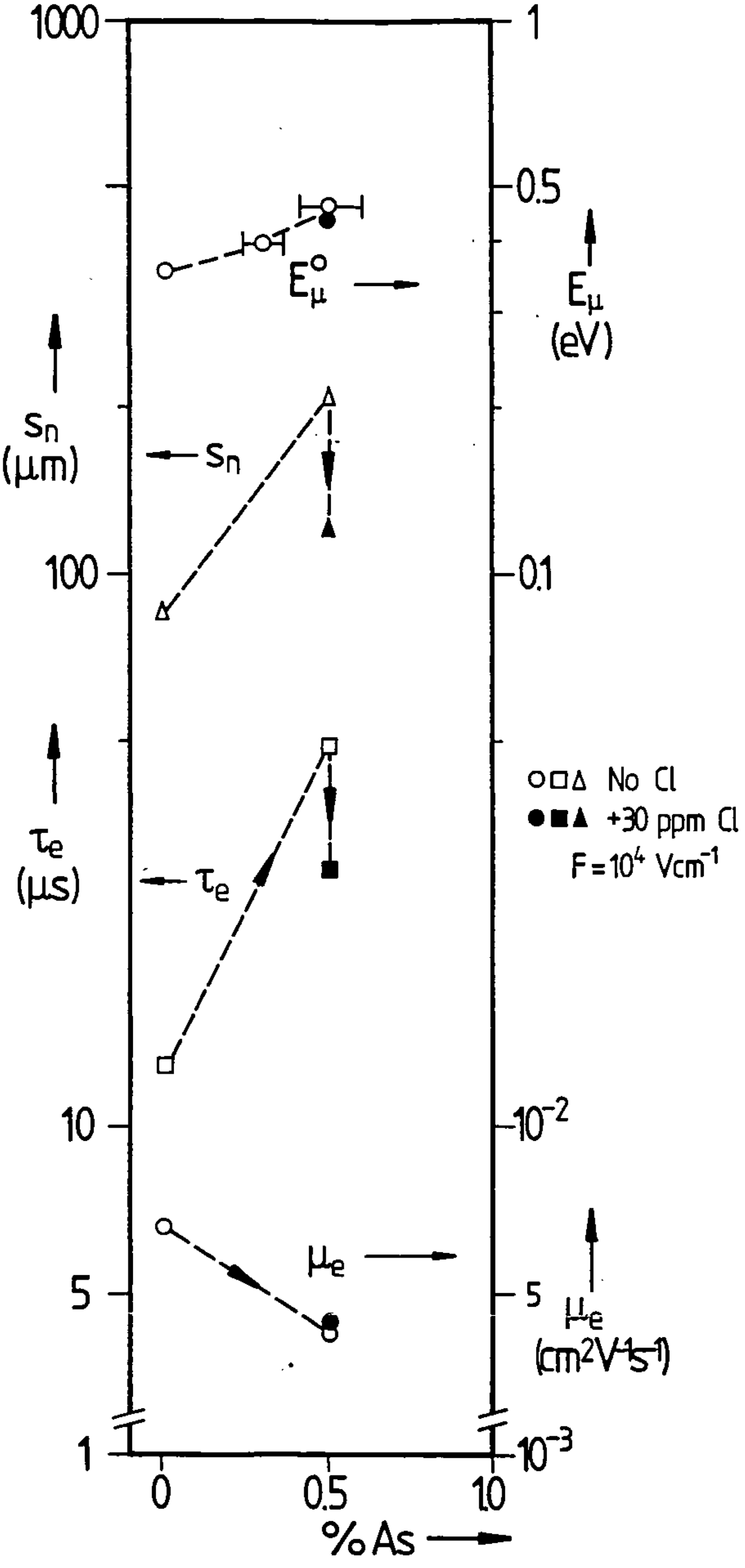

Fig. 5.31: Electron transport parameters in the system a-Se/x%As + y ppm Cℓ. Only filled-in points have Cℓ(~30 wt.ppm)

interpretation for hole transport in a-Se/0.5%As + y ppm Cℓ ($y \leq 40$) as that in pure a-Se, i.e. trap controlled diffusion motion in extended states near E_v. Notice, however, that the field dependence of E_μ in a-Se/0.5%As + y ppm Cℓ is weaker. β_{exp} values are smaller than β_{PF} and for y = 30, $\beta_{exp} \approx \frac{1}{2}\beta_{PF}$. As mentioned in section 5.2.2 (A), the Poole-Frenkel expression in eqn. (5.10) for the escape probability of a trapped carrier was based on considering thermal emission in the field direction. The field lowers the potential barrier for release by an amount $\delta E = \beta_{PF}F^{\frac{1}{2}}$ where β_{PF} is given in eqn. (5.9a). The probability of escape P(F) at a field F is then

$$\frac{P(F)}{P(0)} = \exp \frac{\beta F^{\frac{1}{2}}}{kT} \qquad (5.38)$$

where $\beta = \beta_{PF}$.

When possible emissions in other directions are also incorporated into the total probability of escape then the resulting expressions are usually complicated (see Hartke 1968, Hill 1971b, Ieda et al 1971, Adamec and Calderwood 1975 and review by Kao and Hwang 1981, Ch. 5). For example, Adamec and Calderwood 1975 considered six mutually perpendicular directions to calculate the density of detrapped charge carriers. From their studies we can write†

$$\frac{P(F)}{P(0)} = \left[\frac{2 + \cosh(\beta F^{\frac{1}{2}}/kT)}{3}\right]^2 \qquad (5.39)$$

where $\beta = \frac{1}{2}\beta_{PF}$ is half the β_{PF} coefficient.

Another expression for the probability of field ionization of a donor is given by the Onsager theory (Onsager 1934, see also Pai 1975, Pai and Enck 1975) which considers the electronic escape process to be diffusion controlled. The carrier escapes by executing a Brownian motion under the influence of the attractive coulombic force and the ionizing applied field. The field enhanced probability of escape is given by the Onsager expression;

---

† Under steady state conditions, i.e. $dn/dt = 0$, $P(F)/P(0) = [n(F)/n(0)]^2$ where n is the density of free carriers generated by the donors and $n \ll N_d$, density of donors (see Pai 1975).

$$\frac{P(F)}{P(0)} = 1 + \frac{1}{2!}\left(\frac{\alpha^2}{4}\right) + \frac{1}{2!3!}\left(\frac{\alpha^2}{4}\right)^2 + \frac{1}{3!4!}\left(\frac{\alpha^2}{4}\right)^3 + \ldots \qquad (5.40)$$

where $\alpha = \beta_{PF} F^{\frac{1}{2}}/kT$. It is instructive to note that the Onsager expression predicts lower escape probabilities (at a given field) than eqn. (5.38). . Morever,.if eqn. (5.40) is represented on a log $[P(F)/P(0)]$ vs $F^{\frac{1}{2}}$ plot, the slope† $\beta'(F)$ depends on the applied field F. For small and moderate fields ($F \lesssim 10^5$ V cm^{-1}), β' increases with the field. Its value for $F \lesssim 10^5$ V cm^{-1} is smaller than β_{PF}. For example, at $F = 5 \times 10^4$ V cm^{-1}, $\beta' \approx 0.57\ \beta_{PF}$; and at $F = 1 \times 10^5$ V cm^{-1}, $\beta' = 0.73\ \beta_{PF}$. At high fields ($F > 10^5$) $\beta' \to \beta_{PF}$. (see Fig. 1 in Pai 1975). It is interesting to remark that according to Adamec and Calderwood 1977, at high fields ($e^3F/(8\pi\varepsilon_r\varepsilon_0\, k^2T^2) > 10$) the Onsager expression has an approximate form nearly identical to their three-dimensional field enhanced thermionic emission probability in eqn. (5.39).

It can be seen that β_{exp} values smaller than β_{PF}, e.g. $\beta_{exp} \approx \frac{1}{2}\beta_{PF}$, do not necessarily imply that the field enhanced thermionic emission is unlikely. The Onsager theory, which has already been applied to a-Se (see Pai and Enck 1975), to explain the field, temperature and wavelength dependence of the photogeneration efficiency via geminate (initial) recombination, seems more appropriate. This will be particularly important when the conduction mean free path is much smaller than the capture radius r_c as in many amorphous semiconductors. Note that $\mu_0 \sim 0.4$ cm^2 V^{-1} s^{-1} for a-Se implies a 'mean free path' $\bar{\ell} \sim 0.5$ Å.

We already suggested a plausible interpretation for the mobility activation energy triangle in Fig. 5.25(b) by supposing that Cℓ doping of pure Se introduces a new set of traps at $E_{t2} \cong 0.45$ eV which are subsequently annihilated or 'compensated' by As addition. Cℓ doping effects, discussed in §5.3, strongly suggested a new set of charged centres arising from $C\ell_0^-$ (or some other Cℓ associated centre). In a-Se + 40 ppm Cℓ, for example, these $C\ell_0^-$ centres were more effective in controlling hole transport than the C_1^- centres which were alleged to control transport in undoped a-Se.

Addition of As, because it restores not only the magnitudes of μ_h and E_μ but also the general field dependence of $E_\mu(F)$, indicates that $C\ell_0^-$ centres

---

† $\frac{\beta'}{kT} \equiv d\ell n\,[P(F)/P(0)]/dF^{\frac{1}{2}}$

are ineffective in the Se/0.5%As + Cℓ system. Either As introduction annihilates these Cℓ centres thus diminishing N_{t2} or it neutralizes the negative charge on $C\ell_0^-$ thus converting it to a neutral centre. Note that the latter case is tantamount to increasing the type 2 trap capture time τ_{c2} by an order of magnitude or more in the equivalent expression of eqn. (5.33) in the form

$$\frac{\mu_o}{\mu_h} = 1 + \frac{\tau_{r1}}{\tau_{c1}} + \frac{\tau_{r2}}{\tau_{c2}} \tag{5.41}$$

where τ_{ri} and τ_{ci} are release and capture times of type i trap (i = 1 or 2). A large increase in τ_{c2} would make type 1 traps more dominant.

Addition of 0.5%As to a-Se was found to worsen to hole lifetime τ_h by approximately a factor of ~ 2. From the discussions of deep trapping in a-Se in §5.2.2 it should be apparent that only a very few (e.g. 1 in $\sim 10^6$) of the As atoms in the Se/0.5%As alloy must be acting as deep traps. It is therefore suggested that because some (or a small fraction of) As atoms in the a-Se/As structure would be undercoordinated and thus yield As_2^- centres, the latter are the deep hole traps. As_2^0 has a dative bond which can interact with a lone pair on a C_2^0 atom to form a As_2^- and C_3^+ pair. a-Se/As alloy will hence have three types of charged defect centres, C_3^+, C_1^- and As_2^- inasmuch as As_4^+ is unlikely.

The increase in the hole lifetime τ_h with Cℓ addition to a-Se/0.5%As indicates a reduction in the density of As_2^- centres. It seems that Cℓ doping of Se/As has dininished $[As_2^-]$ whereas As addition to Se + Cℓ has diminished $[C\ell_0^-]$. This is an important conclusion which may have been predicted from charge neutrality considerations.

(B) Electron Transport

The room temperature field dependence of the electron drift mobility $\mu_e(F)$ (Fig.5.26(a)and (b)) in the a-Se/0.5%As and a-Se/0.5%As + 30 ppm Cℓ systems seems to be of algebraic form (eqn. (5.14)) with the index $n \sim 0.1$ remaining constant up to high fields ($F \gtrsim 1.5 \times 10^5$ V cm^{-1}) where $\mu_e(F)$ for some batches increases more sharply with F. The behaviour of $\mu_e(F)$ in Fig .5.26 (a) and (b) is very similar to that in Fig. 5.16 for a-Se. The fact that $\mu_e(F)$ in cases for $n \neq 0$ does not have an 'ohmic' region (i.e. μ_e = constant) down to the lowest fields accessed ($\sim 4 \times 10^3$ V cm^{-1}) has been a common and important feature of electron transport in evaporated a-Se and a-Se/0.5%As + y ppm Cℓ systems. Notice that the high field behaviour of $\mu_e(F)$ is different from batch to batch. In some batches $\mu \sim F^n$ has extended to the highest fields ($\sim 3 \times 10^5$ V cm^{-1}) with n remaining constant throughout.

The observed fall in the electron drift mobility μ_e with As composition can although be explained qualitatively in terms of As induced increase in the activation energy E_μ, quantitatively it also implies a slight increase in the pre-exponential factor μ_o' in eqn. (5.28). For example, to account for the fall in μ_e with 0.3%As (Fig. 5.28) we need to increase μ_o' by a factor of ≈1.6. For Se/0.5%As + y ppm Cℓ the increase in μ_o' is about ∿10.

In the trap controlled transport mechanism this requires either an enhancement of μ_o in eqn. (5.33) or a reduction in the density N_t ($\sim 10^{15}$ cm^{-3}) of shallow electron traps. The latter case is more plausible since μ_o is unlikely to increase with As induced compositional disorder.

It is important to point out that there are a number of charge transport mechanisms which yield a thermally activated drift mobility besides those which have already been discussed in section 5.2.2. Consider, for example, extended state transport which is trap controlled by the tail of localized states below E_c. Suppose that the density N(E') of the localized tail states is described by

$$N(E') = N_c\ [(E_t - E')/E_t]^n \qquad E' \leq E_t \qquad (5.42a)$$

$$= 0 \qquad E' > E_t \qquad (5.42b)$$

where E' is energy measured from E_c and E_t, in this case,is the extent of the tail, i.e. $E_t = E_c - E_A$. Then assuming thermal equilibrium conditions,the drift mobility is of the form

$$\mu = \mu_o [1 + (\frac{E_t}{kT})^{-n} \exp(\frac{E_t}{kT})]^{-1} \qquad (5.43)$$

or

$$\mu \cong \mu_o(\frac{E_t}{kT})^n \exp(-\frac{E_t}{kT}) \quad ; \text{ at low T } (kT << E_t) \qquad (5.44)$$

Cleary a rise in E_t, from eqn. (5.44), is also accompanied by an increase in the pre-exponential factor $\mu_o' \equiv \mu_o (\frac{E_t}{kT})^n$.

Applying eqn. (5.44) to the $\mu_e(T)$ data of a-Se in Fig. 5.18 with $\mu_o(300K) \approx 0.32$ cm^2 V^{-1} s^{-1} (Dresner, 1964) we find $n \cong 3.84$. For a-Se/0.3%As in Fig. 5.28, with the same μ_o, we find $n \cong 3.86$, in excellent agreement with that for pure Se.

The calculation of n for Se/0.5%As + y ppm Cℓ however is more difficult inasmuch as μ_e and E_μ exhibit field dependence. From the log μ_e^o vs T^{-1} plots in Figs. 5.29 and 5.30, for Se/0.5%As and 30 ppm doped Se/0.5%As we have μ_o' (F = 0) $\approx 9.6 \times 10^4$ and 6.7×10^4 cm^2 V^{-1} s^{-1} respectively. The corresponding n values are 4.39 and 4.36 provided μ_{oe} is still ≈ 0.32 cm^2 V^{-1} s^{-1}. Note that if μ_{oe} is diffusion controlled then n values greater than unity would introduce a temperature dependence to μ_o', which may be too weak to be noticeable in log μ vs T^{-1} plots.

It can be seen that eqn. (5.43) can explain not only electron transport in undoped a-Se but also in the system a-Se/x%As + y ppm Cℓ ($x \lesssim 0.5$, $y \lesssim 30$) if we allow the localized tail states below E_c to be of the form in eqn. (5.42) with $n \sim 4$. Thus, one plausible mechanism for electron transport is motion in extended states which is trap controlled by the localized tail states below E_c. The extent of these localized states increases continuously with As alloying for $x \lesssim 0.5$ wt.% (Fig. 5.31).

The appearance of field dependence in μ_e and E_μ when the As content is increased to 0.5% is difficult to account for in the above model since the localized tail states would be expected to be neutral. Note that the observed field dependence is, in fact, weak, e.g. for Se/0.5%As + 30 ppm Cℓ, $\mu_e(F)$ data gives $\beta_{exp} \sim \beta_{PF}/8$. Also note that at room temperature the mobility is of the form of eqn. (5.14) whereas as at lower temperatures it seems to be dominated by the field dependence of the exponent in eqn. (5.28). In other words at room temperatures the mobility activation energy E_μ is relatively insensitive to the field. $\mu_e(F)$ behaviour at room temperature probably arises from that of μ_o.

Consider now the time constant of photocurrent decay τ_e. If this is the quantity in eqn. (5.29) then the increase in τ_e with 0.5% As addition can be explained by the fall in the drift mobility μ_e and reduction in the bulk space charge density ρ. Suppose that τ_e is the true electron lifetime. Then the data implies a reduction in the deep trap population by As alloying. If the deep traps arise from C_3^+ centres then As addition may be expected to reduce $[C_3^+]$ by direct substitution and hence enhance τ_e. The fall in τ_e with Cℓ addition to Se/0.5% As can be explained by noting that unbonded (neutral) Cℓ atoms are highly electronegative and would act as electron traps.

§5.5 a-$Se_{1-x}Te_x$ + y ppm Cℓ

5.5.1 Results and Discussion

(A) Hole Transport

The room temperature hole drift mobility $\mu_h(F)$ values in the a-Se/x%Te system up to 5%Te are shown in Fig. 5.32(a) as a function of the field, F. Notice that alloying with Te drastically reduces the hole mobility. Effects of Cℓ doping a-Se/Te alloys on the hole drift mobility $\mu_h(F)$ are shown in Fig. 5.32(b). The highest Te composition was 12.5% and the largest Cℓ doping was 40 ppm. It can be seen that the drift mobility has an algebraic field dependence of the form in eqn. (5.12) with the index s increasing with Te composition or Cℓ doping. s was also found to depend on the batch for a given composition. It is interesting to note that the general behaviour, including

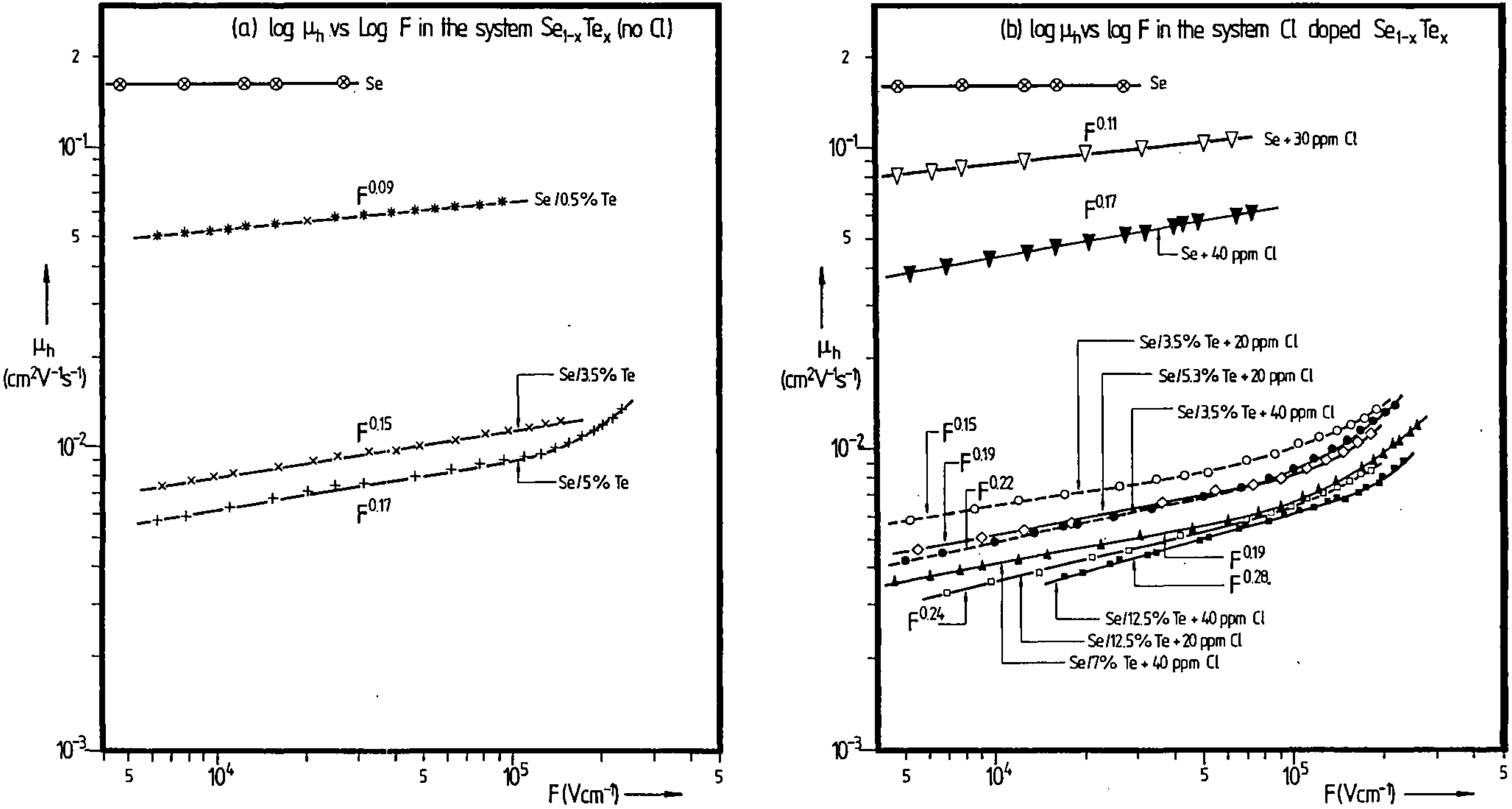

Fig. 5.32: Electric field dependence of hole drift mobility at room temperature in the amorphous systems (a) $Se_{1-x}Te_x$ and (b) $Se_{1-x}Te_x$ + y ppm Cℓ.

the order of magnitude, of the hole drift mobility in the system a-Se/x%Te ($x \gtrsim 1$) + y ppm Cℓ seems to be very similar to that of the electron drift mobility in a-Se (Fig. 5.16).

Fig. 5.33 shows the dependence of the hole drift mobility μ_h (at $F = 10^4$ V cm^{-1}) and the hole lifetime[†] τ_h on the Te and Cℓ contents. The lifetime values were limited to 'low' fields ($F < 10^4$ V cm^{-1}) and small Te compositions ($\lesssim$5%Te). It can be seen that the drift mobility in $Se_{1-x}Te_x$ with no Cℓ drops sharply with Te composition, the fall being more rapid for small Te concentrations. Addition of Cℓ then reduces the mobility further. The lifetime however seems to behave in an inverse fashion to the mobility. Both Te and Cℓ enhance the lifetime. The composition effects on the hole Schubweg s_p at $F = 10^4$ V cm^{-1} are shown in the lower inset of Fig. 5.33. It can be seen that, although s_p initially falls with the Te density and then rises above that of pure Se, the data can also be viewed as s_p remaining unaffected by Te alloying by virtue of τ_h values being only approximate. Addition of Cℓ to $Se_{1-x}Te_x$ seems to promote the hole Schubweg. This is expected from Cℓ doping effects described in §5.3.

Figs. 5.34 and 5.35 show typical hole drift mobility-temperature, $\mu_h(T)$, data for a-Se/5%Te and a-Se/3.5%Te + 40 ppm Cℓ plotted as log μ_h vs T^{-1} at various applied fields. The temperature dependence of the mobility in a-Se/5%Te is, in general appearance, similar to that for a-Se. At low temperatures, $T \lesssim 270$K, the mobility activation energy $E_\mu(F)$ is well defined and larger than that corresponding to $E_\mu(F)$ in a-Se. At high temperatures, $T \gtrsim 270$K, the activation energy E_μ is still relatively well defined (∿0.35 eV), less sensitive to the field, and its value at a given field seems to be lower than the corresponding value at low temperatures. The $\mu_h(T)$ behaviour in the Se/3.5%Te alloy was essentially very similar to that for Se/5%Te whereas for the Se/0.5%Te alloy, the $\mu_h(T)$ data were only collected over a limited temperature range ($T \approx 263 \rightarrow 300$K)

[†] It was also found necessary to use $t_d \lesssim 10$ ms in TOF measurements to obtain meaningful τ_h values probably for the same reasons as those discussed for a-Se+Cℓ.

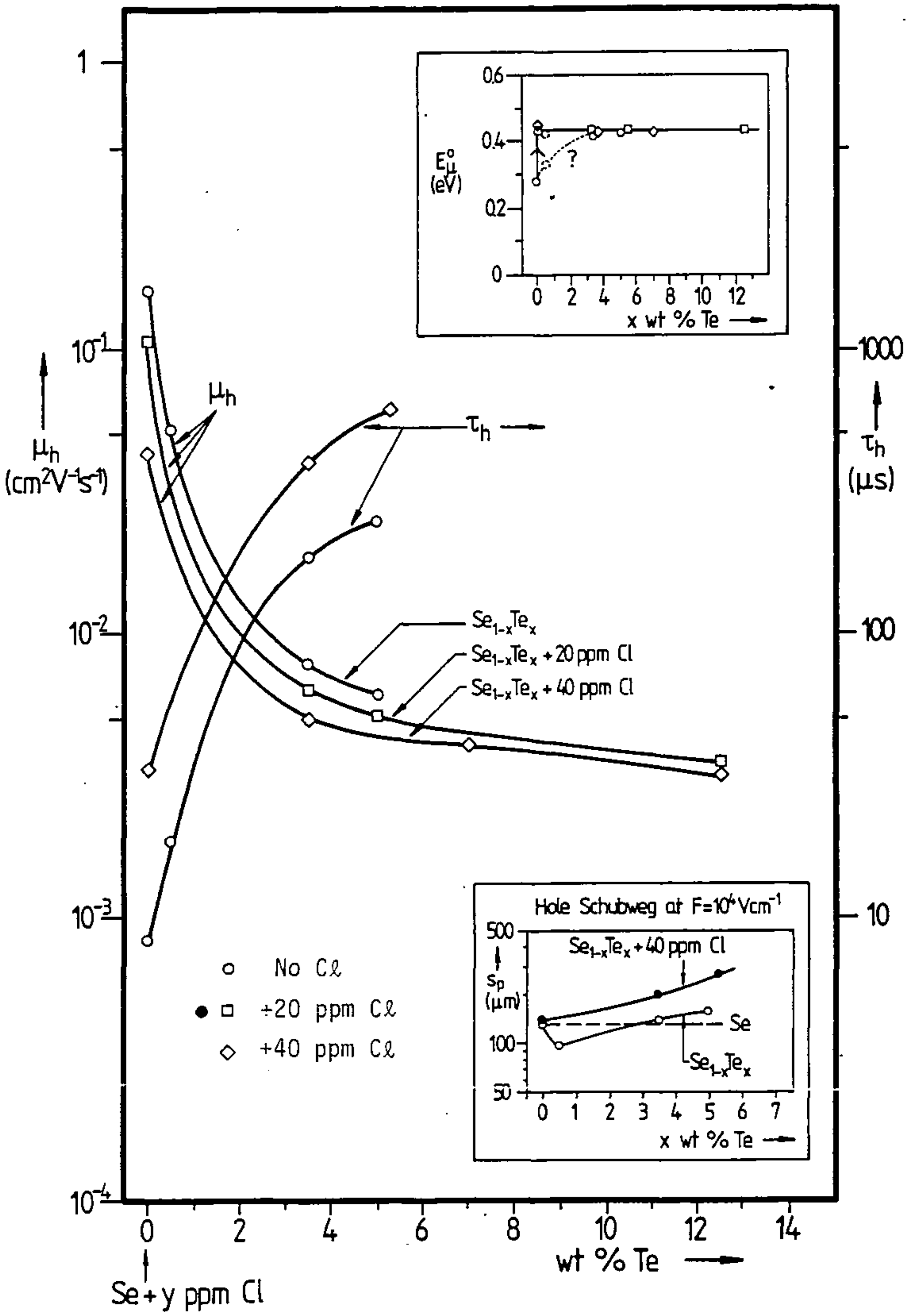

Fig. 5.33: Hole transport data in a-$Se_{1-x}Te_x$ + y ppm Cℓ. Mobility μ_h and lifetime τ_h vs Te content in wt.%. The upper inset shows the 'zero field' mobility activation energy E_μ^o against the Te concentration. The lower inset displays the effect of Te and Cℓ on the Schubweg.

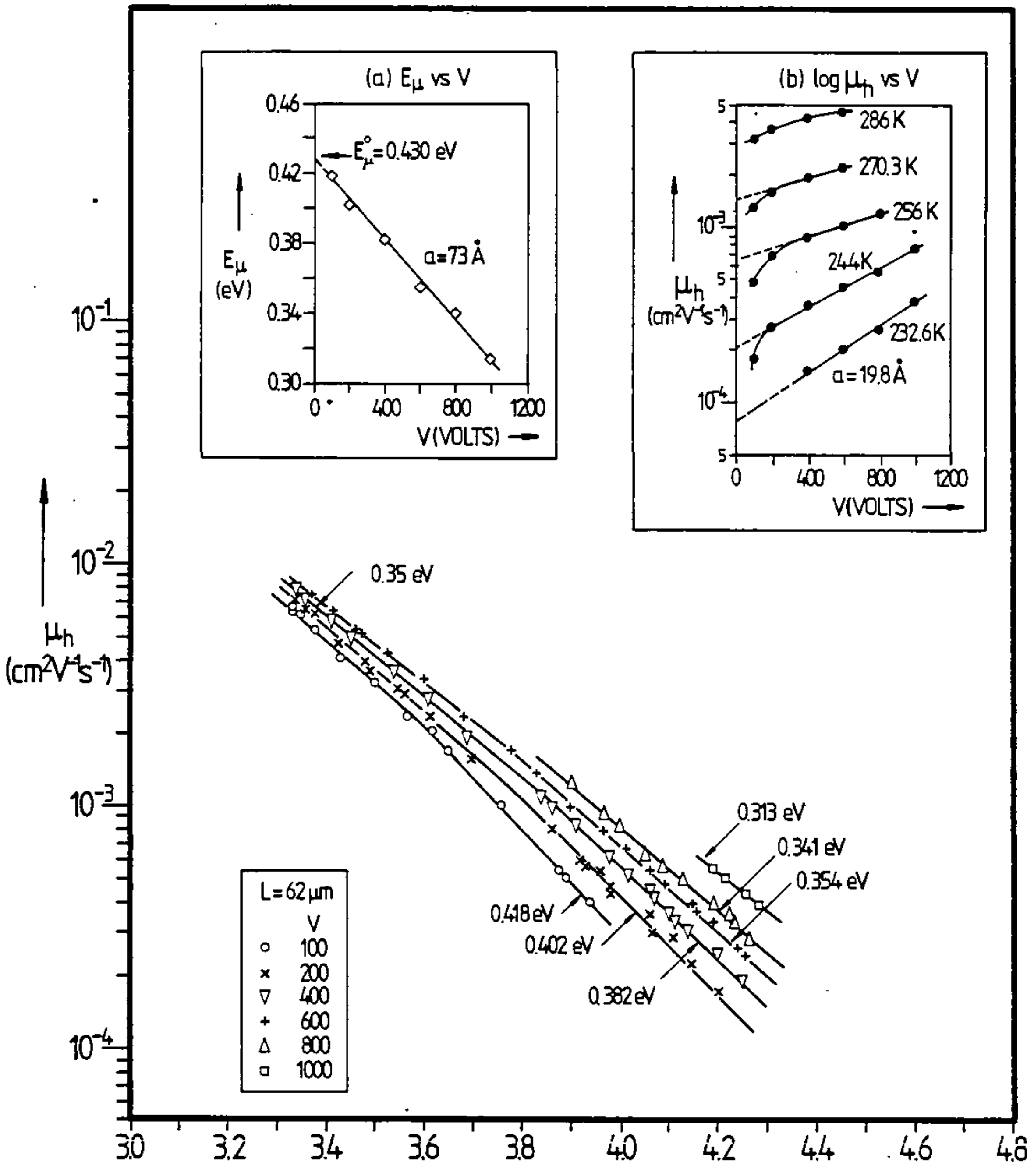

Fig. 5.34: Temperature dependence of hole drift mobility in a-Se/5%Te at various applied fields. The insets show (a) low temperature activation energy E_μ vs V and (b) log μ_h vs V at different temperatures.

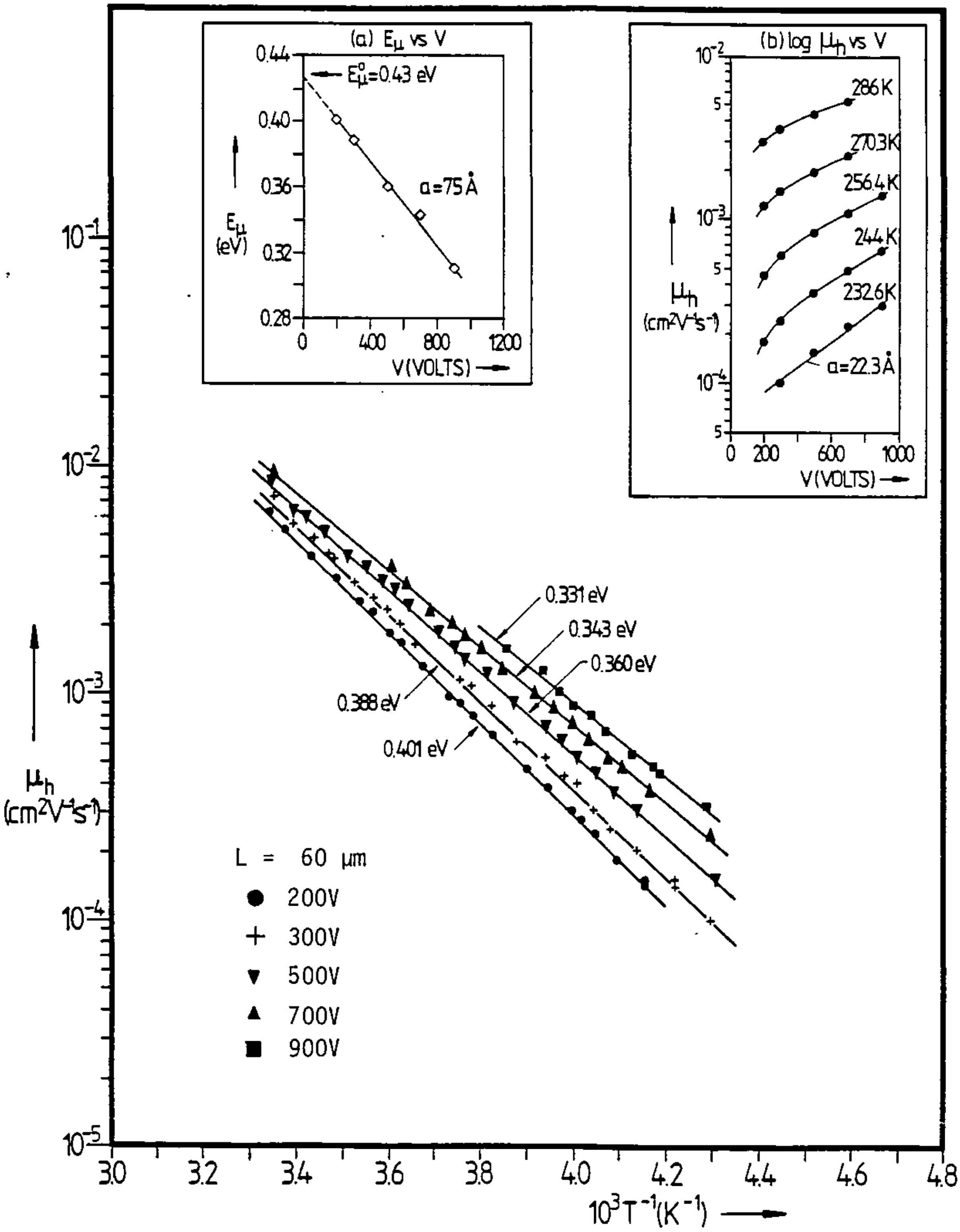

Fig. 5.35: Temperature dependence of hole drift mobility in a-Se/3.5%Te + 40 ppm Cℓ at various applied fields. The insets show (a) E_μ vs V and (b) μ_h vs V, obtained from the log μ_h vs T^{-1} plots.

and hence its behaviour was difficult to identify.

The insets (a) and (b) in Fig. 5.34 show respectively the dependence of the low temperature activation energy E_μ on the applied voltage and log μ_h vs V data at various temperatures, obtained from the log μ_h vs T^{-1} plots. Clearly E_μ decreases linearly with F following eqn. (5.30). At low temperatures the drift mobility μ_h seems to have an exponential field dependence of the form in eqn. (5.31) with a $\sim$20Å. At high temperatures however the drift mobility deviates from eqn. (5.31), particularly at low fields. The zero field activation energy E_μ^0 was about 0.42 eV for Se/3.5%Te and 0.43 eV for Se/5%Te.

The well defined thermally activated behaviour of $\mu_h(T)$ in the 40 ppm Cℓ doped Se/3.5%Te, shown in Fig. 5.35, clearly extends over the whole temperature range accessed (from 300K down to $\sim$230K) and should be compared with the two temperature regions in Fig. 5.34. Recall that log μ_h vs T^{-1} plots for a-Se + 40 ppm Cℓ in Fig. 5.21 also evinced well defined activation energies $E_\mu(F)$ over the temperature range employed. The insets (a) and (b) in Fig. 5.35 display the E_μ vs V and log μ_h vs V data obtained from the log μ_h vs T^{-1} plots. Apparently, Cℓ doping Se/Te alloys does not change the general field dependence of E_μ, i.e. E_μ follows eqn. (5.30). The zero field activation energy E_μ^0 is still about 0.43 eV. At low temperatures and/or high fields the drift mobility $\mu_h(F)$ seems to obey eqn. (5.31) with a $\sim$ 20Å. Notice the deviation in $\mu_h(F)$ from eqn. (5.31) at the lowest fields.

The upper inset in Fig. 5.33 shows how E_μ^0 is affected by Te alloying and Cℓ doping. It is apparent that E_μ^0 increases with both Te and Cℓ content, but saturating at a value between 0.43-0.45 eV.

Table T5.6 summarizes the essential hole transport parameters, viz. μ_h (300K), s in $\mu_h \sim F^s$, E_μ^0 and a in eqn. (5.30) in the system Se/x%Te + y ppm Cℓ.

Since the room temperature field dependence of the drift mobility (Fig. 5.32) was of algebraic form, i.e. eqn. (5.12), it will be instructive to investigate whether at lower temperatures eqn. (5.12) can still describe the $\mu_h(F)$ behaviour. Fig. 5.36 shows typical log μ_h vs log F data at various

Table T5.6: Typical Hole Drift Mobility Data in the System a-Se/x%Te + y ppm Cℓ

x%Te	μ_h(300K) at $F \cong 10^4$ V cm^{-1} [cm^2 V^{-1} s^{-1}]	s(300K) in $\mu_h \sim F^s$	E_μ^o [eV]	a in eqn. (5.30) [Å]	Comment
		$Se_{1-x}Te_x$			
0	1.6×10^{-1}	0.00	0.29	?	$E_\mu = E_\mu^o - \beta F^{\frac{1}{2}}$; $T \lesssim 250K$
0.5	5.2×10^{-2}	0.09	0.33	80	$T \gtrsim 230K$
3.5	8.0×10^{-3}	0.15	0.42	47	$T \lesssim 260K$
5.0	6.2×10^{-3}	0.17	0.43	73	$T \lesssim 270K$
		$Se_{1-x}Te_x$ + 20 ppm Cℓ			
0	1.1×10^{-1}	0.09	0.39		(Fig. 5.22)
3.5	6.5×10^{-3}	0.15	0.44	42	
5.3	5.1×10^{-3}	0.17	0.44	56	
12.5	3.6×10^{-3}	0.24	0.44	52	
		$Se_{1-x}Te_x$ + 40 ppm Cℓ			
0	4.3×10^{-2}	0.18	0.45	390	
3.5	5.0×10^{-3}	0.22	0.43	74	
7.0	4.1×10^{-3}	0.22	0.43	44	
12.5	3.2×10^{-3}	0.28			

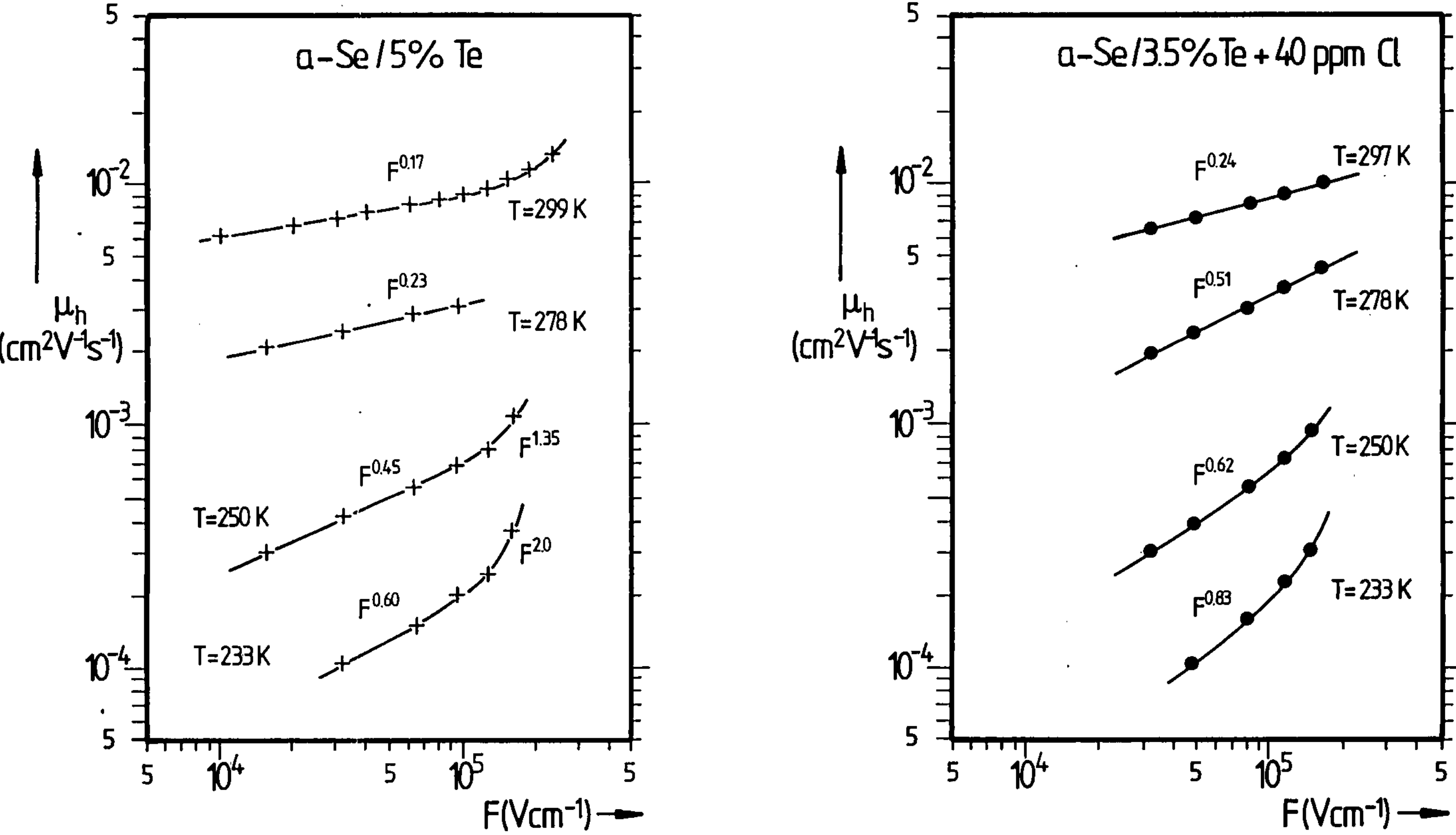

Fig. 5.36: Field dependence of hole drift mobility at various temperaturesin the amorphous systems Se/5%Te and Se/3.5%Te + 40 ppm Cℓ. Data represented as log μ_h vs log F

temperatures for Se/5%Te and Se/3.5%Te + 40 ppm Cℓ. It can be seen that at fields below $F \sim 10^5$ V cm^{-1}, $\mu_h \sim F^s$ type of behaviour persists down to ∿233K and that s increases with the fall in temperature. At high fields ($F \gtrsim 10^5$V cm^{-1}) however either s is larger or $\mu_h(F)$ has an exponential field dependence (see insets of Figs. 5.34 and 5.35). Notice that as the temperature is lowered, $\mu_h \sim F^s$ type of behaviour is restricted to smaller fields.

It is useful to compare the hole drift data of this work on the system $Se_{1-x}Te_x$ with those reported previously by Schottmiller et al 1970, Pai 1974, Tomura and Maekawa 1977 and Takahashi 1979. Although little information has been given on the experimental details, e.g. Te homogeneity, effects of t_d on photocurrents, the observed fall in the hole drift mobility μ_h with Te content is common to all the reports. There are, however, quantitative differences between the various authors' $\mu_h(F,T)$ data.

Schottmiller et al (Fig. 2.27) find the hole lifetime τ_h unaffected up to compositions Se/5.4 at.%Te (i.e. 8.7 wt.%) which does not agree with τ_h vs Te content data in Fig. 5.33. The increase in E_μ with Te (Figs. 2.26 and 2.27) in the works of Schottmiller, Pai and Takahashi is, however, qualitatively in accord with that in the upper inset of Fig. 5.33. Tomura and Maekawa investigated the field dependence of the hole mobility and found it depended on the preparation method. An algebraic field dependence, $\mu_h \sim F^s$, could not be ruled out over the fields accessed, $F = 2 \times 10^4 \rightarrow 8 \times 10^4$ V cm^{-1}.

There are no reported drift mobility measurements on the Cℓ doped $Se_{1-x}Te_x$ system.

(B) Electron Transport

The results of the room temperature electron drift mobility measurements on the system a-Se/x%Te, x = 0, 0.5 and 3.5 (no Cℓ), as a function of the electric field are shown in Fig. 5.37. Clearly, the electron mobility is adversely affected by Te alloying. The field dependence, $\mu_e(F)$, was of the form of eqn. (5.14) with the index n increasing with Te composition. As before $\mu_e \sim F^n$ behaviour indicated no low field cut-off down to $F \sim 10^4$ V cm^{-1}.

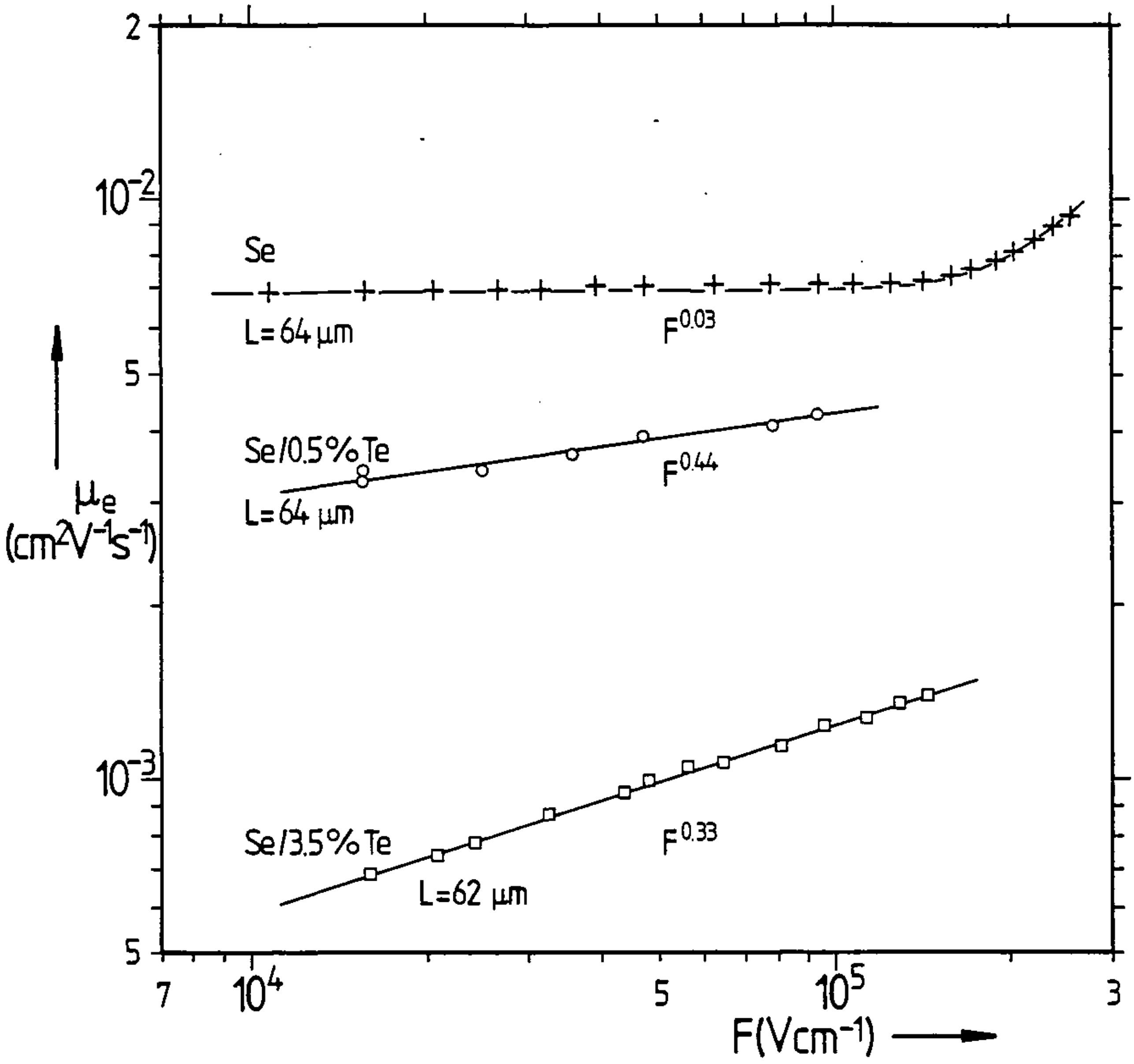

Fig. 5.37: Log-log plots of electron drift mobility μ_e vs applied field F for a-$Se_{1-x}Te_x$ at room temperature.

The temperature dependence of the drift mobility $\mu_e(T)$ in Se/3.5%Te is shown in Fig. 5.38. At a given field, $\mu_e(T)$ below ∿290K exhibits a well defined thermally activated behaviour. Above ∿290K, E_μ decreases with temperature indicating a possible saturation in μ_e. A similar behaviour for $\mu_e(T)$ in a-Se (Fig. 5.18) occurs at ∿280K in a less sharp manner. The mobility activation energy E_μ (for $T \lesssim 290K$) has a slight field dependence as shown in the inset of Fig. 5.38 of the type $E_\mu = E_\mu^o - aeF$ with $E_\mu^o \approx 0.50$ eV and $a \approx 30\mathring{A}$.

The shapes of the TOF electron signals at room temperature for Se/3.5%Te and Se/0.5%Te were also examined. Fig. 5.39(a) shows a typical electron photocurrent waveform for Se/3.5%Te plotted as log I(t) vs log t. The transient current I(t) for $t < t_T$ and $t > t_T$ was found to follow an algebraic time dependence of the form in eqn. (3.84) with $\alpha \equiv \alpha_i$ for $t < t_T$ and $\alpha \equiv \alpha_f$ for $t > t_T$ (see eqn. (2.19)) depending on the applied voltage as in Fig. 5.39(b). α_i increases whereas α_f decreases with the field. There is, therefore, no scaling in the log $\frac{I(t)}{I(t_T)}$ vs log $\frac{t}{t_T}$ plots with respect to the applied field.

The shape of the electron photocurrent in Se/0.5% Te however conformed neither to eqn. (5.2) nor to eqn. (2.19). Fig. 5.40 shows typical current transients plotted as (a) log I(t) vs log t and (b) log I(t) vs t. From the latter plot it is apparent that I(t) evinces an initial fast decay followed by an exponential decay. Recall that similar waveforms for hole transport were observed at lower temperatures in a-Se as described in section 5.2.1(A) (see Fig. 5.9). If we use eqn. (5.4) to describe the waveform in Fig. 5.40 in the domain $t < t_T$ then eqn. (5.4) generates $n = 0.02$ (i.e. $\alpha = 0.98$) and $\tau_e \cong 34.6$ μs. The time constant of the exponential decay following the initial fast component in Fig. 5.40(b) is $\tau_e \cong 34.2$ μs. Fig. 5.41 displays the dependence of such τ_e values on the applied voltage in a log τ_e vs $V^{\frac{1}{2}}$ plot. It can be seen that the $\tau_e(F)$ data for a-Se and a-Se/0.5%Te overlap. The slope gives a β_{exp} value only slightly larger than eqn. (5.9b).

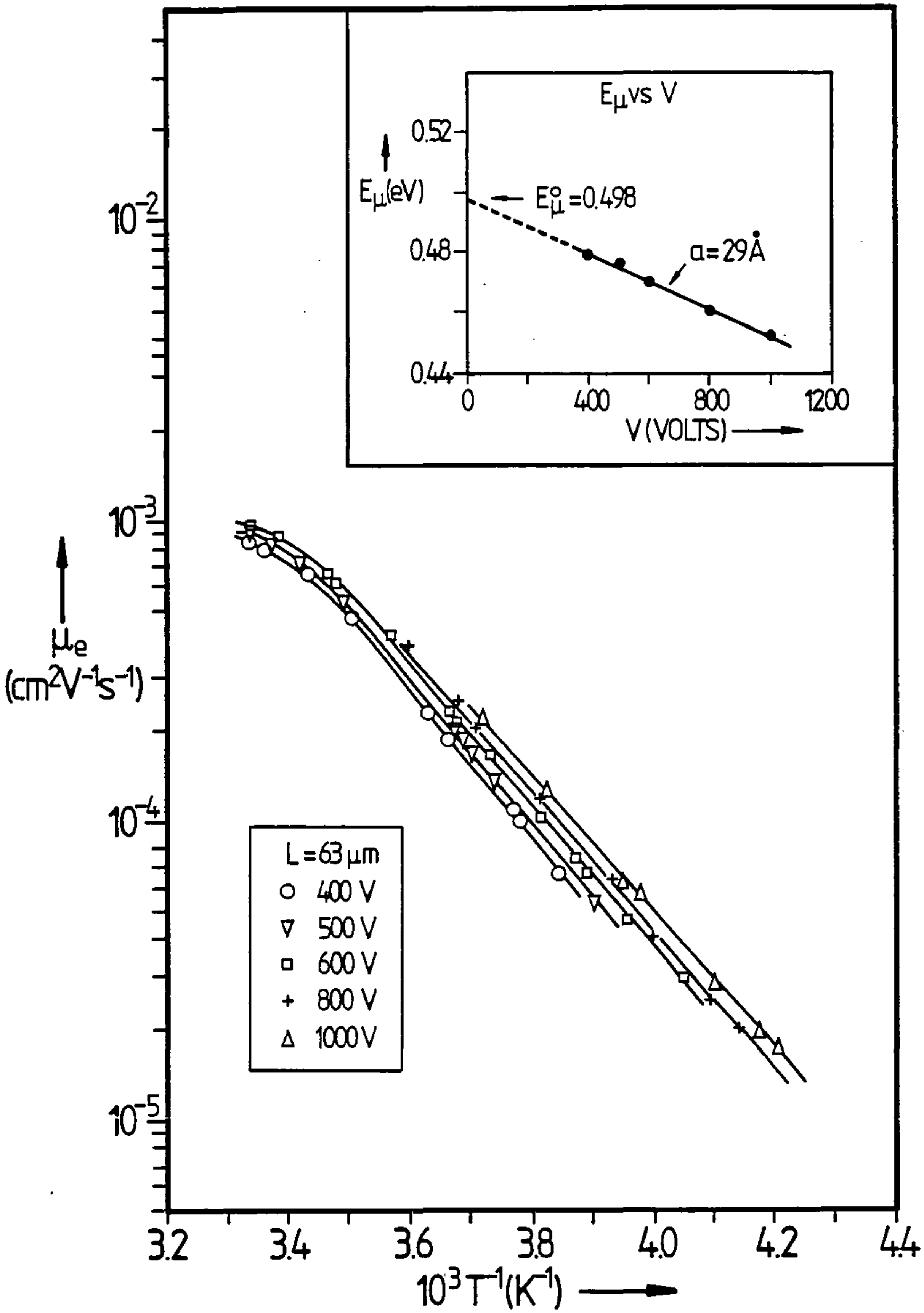

Fig. 5.38: Temperature dependence of electron drift mobility in a-Se/3.5%Te at various electric fields. The inset shows the low temperature activation energy E_μ vs V.

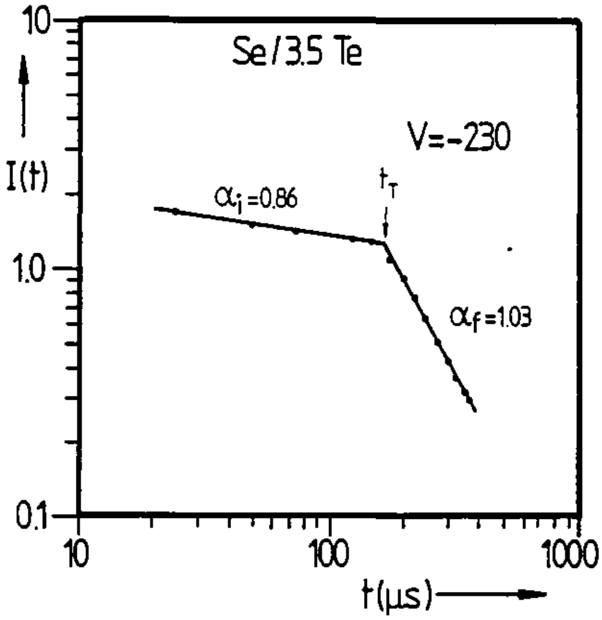

(a) Log I vs log t plot of the electron current transient for a-Se/3.5%Te. I(t) is in arbitrary units.

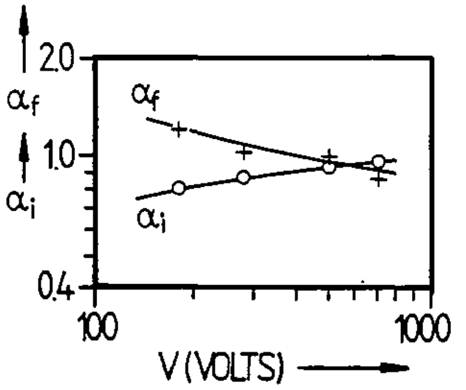

(b) Log-log plot of the voltage dependence of the dispersion parameters α_i and α_f.

Fig. 5.39: Dispersive electron transport in a-Se/3.5%Te

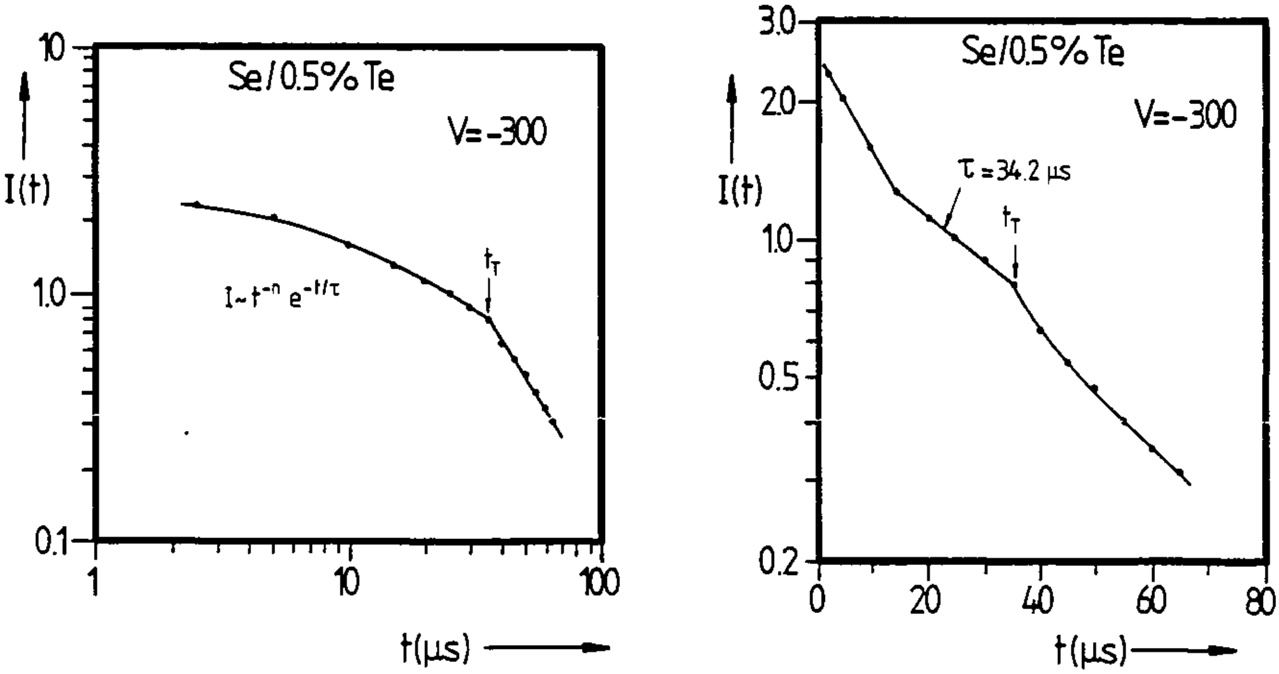

(a) Log I vs Log t

(b) Log I vs t

Fig. 5.40: Electron current transient in a-Se/0.5%Te. I(t) is in arbitrary units.

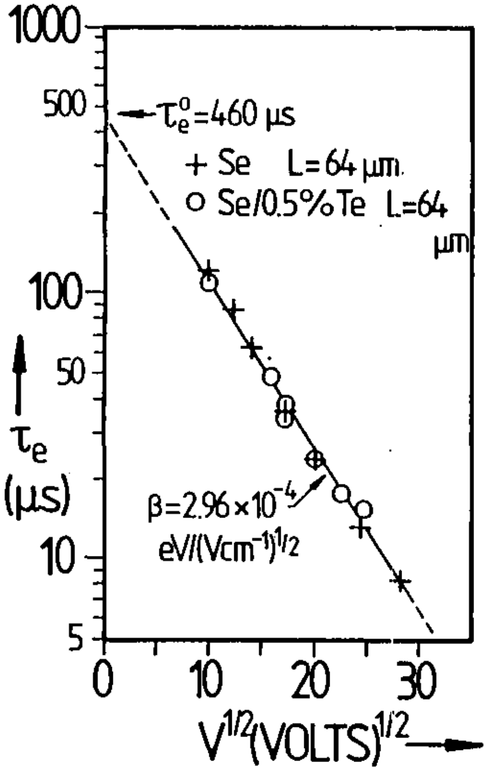

Fig. 5.41: Log (Electron lifetime) vs $\sqrt{\text{(applied voltage)}}$ for a-Se (+) and a-Se/0.5%Te (o).

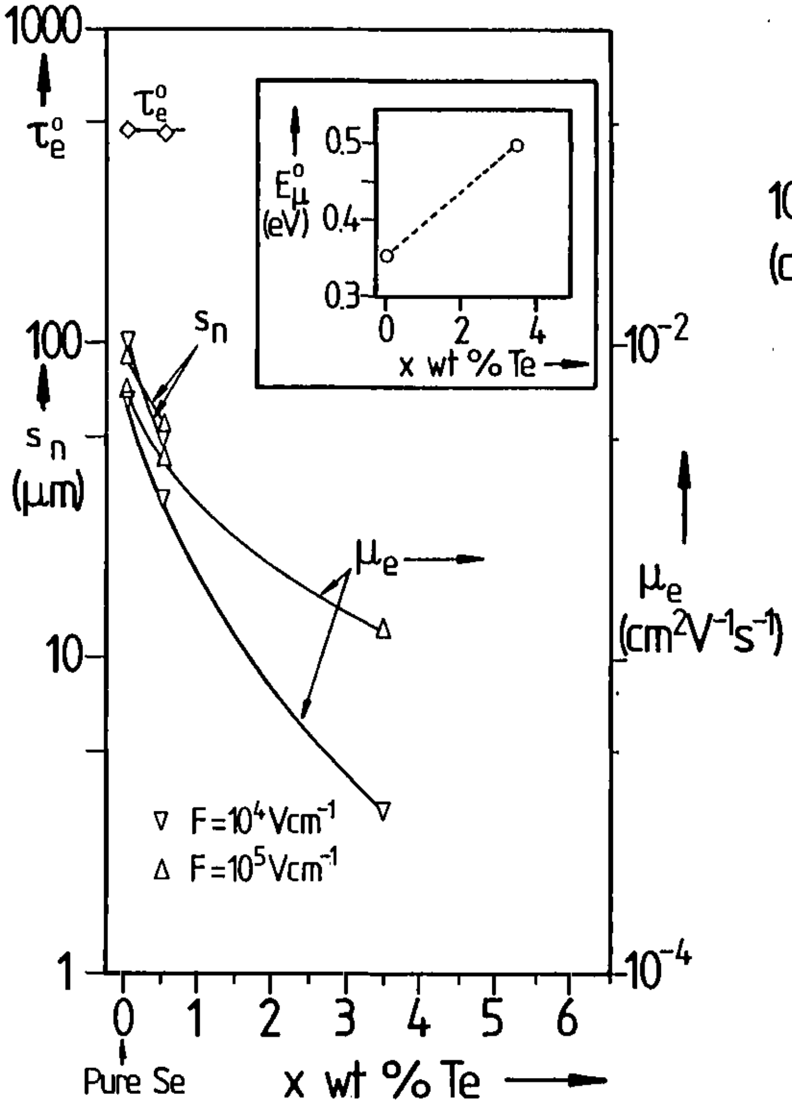

Fig. 5.42: Electron transport parameters, μ_e, τ_e^0, s_n and E_μ^0 vs Te content in a-$Se_{1-x}Te_x$.

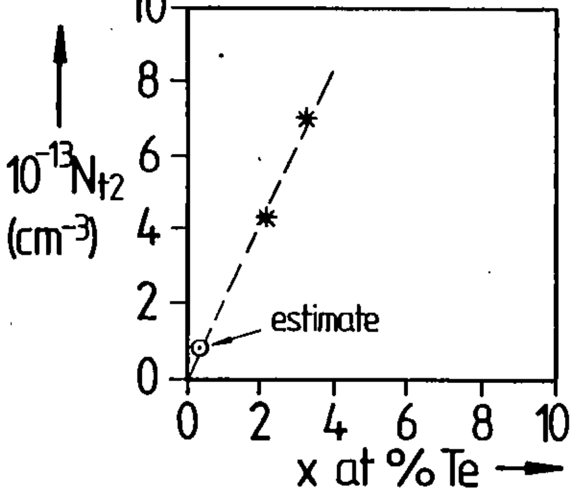

Fig. 5.43: Density of type 2 traps, N_{t2} vs at.%Te in a-$Se_{1-x}Te$.

Fig. 5.42 shows the effects of alloying a-Se with Te on the drift mobility μ_e, 'zero field' lifetime τ_e^o, the Schubweg $s_n(F) \equiv \mu_e(F)\tau_e(F)F$ and the zero field mobility activation energy E_μ^o. In fact, the latter appears in the inset. τ_e^o data could not be extended beyond the Se/0.5%Te composition due to the appearance of dispersive type of photocurrents. Notice that the fall in the Schubweg with Te density arises from that of the drift mobility.

There was no electron TOF signal detectable in 20 or 40 ppm doped a-Se/x%Te alloys up to x ≅ 12.5%, probably for the same reasons as those discussed in section 5.3.1(B) for a-Se + Cℓ.

Previous electron transport measurements on the system $Se_{1-x}Te_x$ have been reported by Schotmiller et al 1970 and Takahashi 1979 (see section 2.5.4(ii) and Figs.2.26 and 2.27). Schottmiller et al found μ_e and τ_e to decrease with the Te composition and $E_\mu \approx 0.33$ eV to remain unchanged up to ∿1 at.%Te (i.e. 1.6 wt.%Te). Takahashi,on the other hand,observed a decrease in E_μ from 0.29 eV in pure Se to 0.25 eV in Se/2.7 at.%Te (Se/4.4 wt.%Te). The temperature range used in the latter work was, however, too limited (≈ 260 → 300K) to allow any meaningful comparisons.

5.5.2 Detailed Discussion and Interpretation

(A) Hole Transport

$Se_{1-x}Te_x$

From Fig. 5.33 it is apparent that although alloying Se with Te reduces the hole drift mobility, the lifetime is enhanced and their product, shown as Schubweg in the lower inset of Fig. 5.33, remains, within experimental errors, unaffected. This suggests that the deep trapping process in these alloys is diffusion controlled by virtue of eqn. (5.5) which requires $\tau_h \sim 1/\mu_h$. As a corollary we may infer that the density of deep traps $N_d(\sim 10^{14}\ cm^{-3})$ remains unchanged with Te composition.

Note that the increase in τ_h with Te content in the manner of $\tau_h \sim 1/\mu_h$ can also arise through eqn. (5.29) which attributes the decay in the hole photocurrent to unneutralized trapped electrons in the bulk.

We may expect the Te addition to modify the already existing shallow traps and/or to introduce a new set of traps. As mentioned above the mobility-temperature data for Se/5%Te in Fig. 5.34 show that it is possible to identify two regions in the log μ_h vs T^{-1} plots. Suppose that alloying with Te introduces an additional set of shallow traps. The effective drift mobility μ_h in the presence of two sets of discrete monoenergetic traps may be expected to be of the form in eqn. (5.33);

$$\frac{\mu_o(T)}{\mu_h(T)} = 1 + \frac{N_{t1}}{N_v} \exp\frac{E_{t1}}{kT} + \frac{N_{t2}}{N_v} \exp\frac{E_{t2}}{kT} \qquad (5.33)$$

where E_{t1} and E_{t2} are the depths in energy of the traps from the transport states at E_v, and N_{t1} and N_{t2} are their respective densities.

We may tentatively associate the traps at E_{t1}, type 1 traps, with the Se atoms and the traps at E_{t2}, type 2 traps, with the Te atoms. In other words, type 1 traps are intrinsic to the a-Se structure, whereas type 2 traps are Te induced[†].

To investigate the 'goodness' of eqn. (5.33) in describing the mobility-temperature data for Se/Te alloys, eqn. (5.33) was rearranged as (see eqn. (5.35)),

$$Y = mX(\alpha) + c \qquad (5.45)$$

with

$$Y = \left(\frac{Mx}{y} - 1\right) x^{-3/2} \exp - \frac{\beta x}{A'} \qquad (5.46)$$

and

$$X = \exp\frac{(\alpha-\beta)x}{A'} \qquad (5.47)$$

where $x \equiv T^{-1}$, $y \equiv \mu_h(T)$, $\mu_o = MT^{-1} = Mx$, $\alpha \equiv E_{t1}$ (or E_{t2}) in eV, $\beta \equiv E_{t2}$ (or E_{t1}) in eV, $A' \equiv \frac{e}{k} = 8.63 \times 10^{-5}$, and m and c are defined by $\frac{N_{t1}}{N_v} = cT^{-3/2}$ and $\frac{N_{t2}}{N_v} = mT^{-3/2}$ respectively. Notice that the microscopic mobility was assumed to be proportional to T^{-1} and $N_v \sim T^{3/2}$.

[†] In section 5.3.2, type 2 traps were Cℓ induced. Here they are Te induced. The reason for labelling the two different sets of traps as type 2 is that they both appear around the same location in energy; $E_{t2} = 0.43 - 0.45$ eV.

Table T5.7 summarizes the essential results of two parameter (best m and c for α fixed) and three parameter (best m, c and α) curve fitting analyses of eqn. (5.33) onto the $\mu_h(T)$ data of Se/3.5%Te and Se/5%Te. In two parameter curve fitting we assigned reasonable values to $\alpha = E_{t1}$, $\beta = E_{t2}$ and M (or μ_o at a given T which sets M) whereas in three parameter curve fitting only E_{t2} and M required values[#].

For the alloy Se/5%Te Table T5.7 also shows the results of curve fitting eqn. (5.19) for a single set of shallow traps onto the mobility-temperature data. It can be seen that the use of eqn. (5.19) to describe the $\mu_h(T)$ data in Fig. 5.34 leads to $\mu_o \cong 0.02$ cm^2 V^{-1} s^{-1} at 300K and $N_{t1}/N_v \approx 3.6 \times 10^{-7}$ which are nearly two orders of magnitude lower than their respective values in pure Se. $\mu_o \approx 0.02$ cm^2 V^{-1} s^{-1} suggests hopping transport for the microscopic channelling and the factor of $\sim$100 reduction in N_t implies that Te atoms hinder defect production[†]. According to Adler and Yoffa 1977, however, charged defect centres, e.g. C_3^+, C_1^-, are more readily formed from Te atoms than from Se atoms.

Curve fitting eqn. (5.33) onto the $\mu_h(T)$ data was carried out by letting E_{t2} equal to the low temperature mobility activation energy E_μ. E_{t1} was chosen to coincide with that for pure a-Se (at the same field). Two M values were used, corresponding to μ_o (300K) $\approx$ 0.3 and 0.1 cm^2 V^{-1} s^{-1}.

It should be apparent that the best $\frac{N_{t1}}{N_v}$ value is sensitive not only to the choice of μ_o (300K) but also to E_{t1}. $\mu_o \approx 0.3$ cm^2 V^{-1} s^{-1} leads to N_{t1} values at least an order of magnitude greater than those for pure a-Se. If we take $\mu_o \approx 0.1$ cm^2 V^{-1} s^{-1} then the best N_{t1} and E_{t1} are comparable to those in pure a-Se. For example, with $\mu_o \approx 0.1$ cm^2 V^{-1} s^{-1}, $N_{t1} \approx 2.2 \times 10^{15}$ and 3.4×10^{15} cm^{-3} in a-Se/3.5%Te and a-Se/5%Te respectively, whereas N_{t1} (i.e. N_t) in a-Se is 2×10^{15} cm^{-3} (T5.3).

[#] Best E_{t1} was found by starting with an initial guess for E_{t1} and then searching in increments for the best E_{t1}, corresponding to the highest correlation coefficient.

[†] It is assumed that the shallow traps are structural defects as discussed in section 5.2.2(A).

Table T5.7: Hole Transport in a-$Se_{1-x}Te_x$. Results of Curve Fit Analyses onto Mobility-Temperature Data

Composition	μ_o(300 K) [$cm^2V^{-1}s^{-1}$]	N_{t1}/N_v(300K)	N_{t2}/N_v(300K)	E_{t1} [eV]	E_{t2} [eV]	Analysis	Comment
Pure Se	0.27	4.0×10^{-5}	0	0.254	?	Eqn. (5.19)	Best μ_o, $\frac{N_{t1}}{N_v}$ at $F = 1.7 \times 10^4$ Vcm^{-1}
Se/3.5%Te	0.30	8.4×10^{-4}	3.4×10^{-6}	0.260	0.401	Eqn. (5.33)	Best $\frac{N_{t1}}{N_v}$, $\frac{N_{t2}}{N_v}$, E_{t1}
	0.10	6.5×10^{-4}	1.2×10^{-6}	0.230	0.401	Eqn. (5.33)	Best $\frac{N_{t1}}{N_v}$, $\frac{N_{t2}}{N_v}$
	0.10	4.4×10^{-5}	8.5×10^{-7}	0.306	0.401	Eqn. (5.33)	Best $\frac{N_{t1}}{N_v}$, $\frac{N_{t2}}{N_v}$, E_{t1}
Se/5%Te	0.02	3.6×10^{-7}	0	0.402	?	Eqn. (5.19)	Best μ_o, $\frac{N_{t1}}{N_v}$
	0.30	2.3×10^{-3}	5.2×10^{-6}	0.23	0.402	Eqn. (5.33)	Best $\frac{N_{t1}}{N_v}$, $\frac{N_{t2}}{N_v}$
	0.30	1.9×10^{-3}	5.2×10^{-6}	0.236	0.402	Eqn. (5.33)	Best $\frac{N_{t1}}{N_v}$, $\frac{N_{t2}}{N_v}$, E_{t1}
	0.10	5.7×10^{-4}	1.6×10^{-6}	0.230	0.402	Eqn. (5.33)	Best $\frac{N_{t1}}{N_v}$, $\frac{N_{t2}}{N_v}$
	0.10	6.7×10^{-5}	1.4×10^{-6}	0.292	0.402	Eqn. (5.33)	Best $\frac{N_{t1}}{N_v}$, $\frac{N_{t2}}{N_v}$, E_{t1}

The slight increase in N_{t1} with Te is expected by virtue of eqn. (2.7) if the traps at E_{t1} are indeed C_1^- type. We know from our DSC data (Fig. 4.12) of Ch. 4 that T_g increases with Te composition.

From T5.7 it can be seen that the density N_{t2} of type 2 traps at $E_{t2} \sim 0.4$ eV is much smaller than N_{t1} and that as expected N_{t2} increases with the Te content. For example, $N_{t2} \approx 4.3 \times 10^{13}$ and 7×10^{13} cm^{-3} for Se/3.5%Te (2.2 at.%) and Se/5%Te (3.2 at.%) respectively. Clearly, N_{t2} seems to be nearly proportional to the number of Te atoms; $N_{t2} \propto x$(at.). Fig. 5.43 shows a linear plot of N_{t2} vs x at.%Te. The straight line drawn to pass through the origin contains both N_{t2} values and thus confirms the starting assumption that the type 2 traps are Te induced.

There is also a slight increase in E_{t1} with the Te content. This may be due to the disorder induced modulation of E_v away from the gap. Alloying a-Se with Te, in addition to the structural disorder present, would also introduce compositional disorder.

The $\mu_h(T)$ data for the Se/0.5%Te composition were collected over a limited temperature range ($T \approx 263 \rightarrow 300$K) in comparison with the temperatures normally accessed for the other compositions. Thus the E_μ^o value for Se/0.5%Te in the upper inset of Fig. 5.33 needs to be considered with caution. It probably corresponds to some fictitious E_t which is neither E_{t1} nor E_{t2} but respresents the transition region between the two exponential regimes in eqn. (5.33). Curve fitting eqn. (5.33) onto the $\mu_h(T)$ data of Se/0.5%Te with the assumption $E_{t2} \approx 0.40$ eV ($F \approx 3 \times 10^4$ V cm^{-1}) and $\mu_o(300\text{K}) \approx 0.3$ cm^2 V^{-1} s^{-1} gives $E_{t1} \approx 0.29$ eV, $N_{t1}/N_v \approx 4.9 \times 10^{-5}$ and $N_{t2}/N_v \approx 1.4 \times 10^{-7}$ (i.e. $N_{t2} \approx 7 \times 10^{12}$ cm^{-3}). Although E_{t1} is larger than that in pure Se, N_{t1}/N_v is in close agreement with that in pure Se and the N_{t2} value falls on the line $N_{t2}(x)$ vs x at.%Te in Fig. 5.43. This means that the hole mobility data of Se/0.5%Te can still be explained by two sets of shallow traps, i.e. eqn. (5.33).

Since the low temperature mobility activation energy decreases with the field we may suspect the type 2 traps to be charged centres, similar to type 1 traps. Under-coordinated charged Te atoms, i.e. Te_1, are probably the most obvious candidates for the type 2 traps.

$Se_{1-x}Te_x + C\ell$

Addition of $C\ell$ between 20-40 ppm $C\ell$ to Se/Te alloys was found to reduce the hole drift mobility, μ_h, and enhance the hole lifetime, τ_h. The increase in the latter was more than that required by eqn. (5.5) inasmuch as the hole Schubweg s_p in $C\ell$ doped $Se_{1-x}Te_x$ alloys was longer with respect to that in undoped $Se_{1-x}Te_x$ (see lower inset in Fig. 5.33). This suggests that $C\ell$ doping probably annihilates a fraction of the deep hole traps since $C\ell$ induced increase in μ_o is unlikely in view of the reduction in μ_h even in high Te composition (e.g. Se/12.5%Te) samples.

$C\ell$ doped Se and $Se_{1-x}Te_x$ both have well defined thermally activated hole drift mobilities from room temperature down to the lowest temperatures employed (see Figs. 5.21 and 5.35). This means that a double exponential expression of the form in eqn. (5.33) resulting from two types of traps is not a useful description of the $\mu_h(T)$ data. Alternatively, we can assume N_{t1} in eqn. (5.33) is too small to allow type 1 traps to influence the transport in comparison with the influence of type 2 traps.

Taking a reasonable value for μ_o, say ≈ 0.1 $cm^2\ V^{-1}s^{-1}$ at 300K, we can estimate the shallow traps responsible for the thermally activated behaviour of $\mu_h(T)$. For example, for Se/3.5%Te + 40 ppm $C\ell$ (Fig. 5.35), $\mu_h \approx 6.4 \times 10^{-3}$ $cm^2\ V^{-1}s^{-1}$ at T = 300K and F = 3.3×10^4 V cm^{-1}, and E_μ (at same F) = 0.401 eV in eqn. (5.28) with $\mu_o \approx 0.1$ $cm^2V^{-1}s^{-1}$ gives $\mu_o' = \mu_o \frac{N_v}{N_t} \approx 3.2 \times 10^4$ $cm^2\ V^{-1}s^{-1}$ and $\frac{N_t}{N_v} \approx 1.7 \times 10^{-6}$. This trap density is about a factor of 2 higher than that for Te induced traps in the undoped Se/3.5%Te (T5.7) but a factor of ∿20 lower than that for a-Se. Suppose, however, we assume that although $C\ell$ doping may diminish type 1 traps it would not, in ppm amounts, affect type 2 traps which are due to Te atoms. Then μ_o must be ≈ 0.03 $cm^2\ V^{-1}s^{-1}$, an order of magnitude less than that in pure Se.

It can be seen that Cℓ doping, in the shallow trap controlled transport mechanism, leads either to a reduction in μ_o and/or N_{t1} or leads to an introduction of Cℓ induced additional traps at $E_{t2} \simeq 0.44$ eV. The latter conclusion would explain qualitatively not only the $\mu_h(T)$ data on Se + y ppm Cℓ but also those on $Se_{1-x}Te_x$ + y ppm Cℓ. The Cℓ induced traps may be $C\ell_o^-$ centres which are unbound charged Cℓ atoms.

Thus, the results of the mobility-temperature measurements indicate that adding Te and Cℓ to a-Se introduces additional sets of shallow hole traps; one set is due to Te atoms and is at ≈0.43 eV above E_v and the other set is Cℓ induced and is at $\simeq$ 0.45 eV above E_v.

It is important to remark that the possibility of a single set of shallow traps at 0.43 - 0.45 eV induced either by Te or by Cℓ addition, within experimental errors, cannot be ruled out. It would be useful to test the latter interpretation by introducing As to a-$Se_{1-x}Te_x$ + Cℓ inasmuch as As was found to compensate for the effects of Cℓ.

(B) Electron Transport

The fall in the electron drift mobility μ_e with the Te concentration in the Se/Te alloy system with no Cℓ seems to be accompanied by an increase in its activation energy as shown in Fig. 5.42. It is not difficult to show from eqn. (5.28) that the expected fall in μ_e from an increase in E_μ alone is a factor of ∿10 more than that actually observed in Fig. 5.38; a situation similar to As addition effects on electron transport discussed in section 5.4.2(B). Thus Te addition not only increases E_μ but also the pre-exponential factor μ_o' in eqn. (5.28).

The increase in E_μ and μ_o' in eqn. (5.28) with Te addition can be attributed to a shallow trap controlled transport in which the shallow traps are the localized tail states below E_c. The drift mobility is then given by eqns. (5.43) or (5.44) provided the density vs energy spectrum of the transport controlling tail states is of the form of eqn. (5.42), i.e. $N(E) \sim (E_t-E')^n$

where E' is measured from E_c. Using as before $\mu_{oe} \approx 0.32$ cm^2 V^{-1}s^{-1} (at room temperature) and $\mu_o' \approx 1 \times 10^5$ cm^2 V^{-1} s^{-1} obtained from Fig. 5.38 we find $n \sim 4.37$, approximately the same value as that for a-Se/0.5%As + y ppm Cℓ.

It can be seen that the effects of Te addition, as in the case for As addition, may be interpreted by an increase in the extent of the localized tail states. This may occur if as a result of increased compositional disorder either E_c moves away from the mobility gap and thereby increases $E_c - E_A \equiv E_t$ (in this model), or the tail states extend further into the gap.

Transport controlled by a monoenergetic set of traps at an energy E_t below E_c cannot, however, be ruled out if Te addition diminishes their density N_t by a factor of $\sim$10.

We can on the other hand following the discussions in part (A) above suspect that alloying with Te induces additional traps, say at $E_{t2} \sim 0.5$ eV, below E_c whose density N_{t2} is sufficiently large to influence electron transport. At low temperatures, $T \lesssim 286$ K, these Te induced, type 2, traps probably dominate transport whereas at high temperatures, the already existing type 1 traps at $E_{t1} \sim 0.35$ eV have a more pronounced effect. Thus the effective mobility is given by eqn. (5.33).

When eqn. (5.33) is curve fitted onto the $\mu_e(T)$ data in Fig. 5.38 as described in part (A) above we obtain the best (N_{t1}/N_c) and (N_{t2}/N_c) values for fixed M (or μ_o at a given T), $E_{t1} = E_\mu$ for a-Se and $E_{t2} = E_\mu(F)$ at $T \lesssim 286$K. For example, $\mu_o \approx 0.1$ cm^2 V^{-1}s^{-1} at 300K, $E_{t1} = 0.35$ eV for a-Se (Fig. 5.18) and $E_{t2} = 0.479$ eV at $F = 6.4 \times 10^4$ V cm^{-1} (Fig. 5.38) gives $N_{t1}/N_c \approx 8.3 \times 10^{-5}$ and $N_{t2}/N_c \approx 4.1 \times 10^{-7}$. Clearly, the N_{t1} estimate is slightly larger than that in pure Se and the N_{t2}/N_c estimate, to within a factor of 2, is nearly equal to N_{t2}/N_v for the Te induced hole traps. This may be taken to mean that hole and electron traps are generated in pairs.

It can be seen that it is reasonable to describe the effects of Te alloying Se on charge transport by the introduction of additional hole and electron traps of nearly equal density. Hole traps are at $\sim$0.43 eV above E_v

whereas electron traps are at $\sim$0.5 eV below E_c. It also seems reasonable to identify these traps with charged overcoordinated and undercoordinated Te atoms, i.e. Te_3^+ and Te_1^- centres. Notice that the mobility activation energy for both hole and electron transport in Se/Te alloys is field dependent in the form of eqn. (5.30).

The 'lifetime' τ_e seems to remain unaffected with 0.5%Te addition to a-Se. This is surprising because the fall in the drift mobility μ_e may be expected to enhance τ_e either via eqn. (5.5) (if τ_e is a diffusion controlled trapping time) or via eqn. (5.29). If τ_e represents a capture time given by eqn. (3.9) with ($\bar{v} = v_{thermal}$ then τ_e is not expected to depend on the drift mobility. The latter interpretation however implies $\bar{\ell} > r_c$ where r_c is the capture radius of the trap. Furthermore, eqn. (3.9) with $\bar{v} = v_{thermal}$ can only account for the field dependence of τ_e if the capture cross section S_d increases with the field which is unlikely (see pp. 185-186). It can be seen that the interpretation of τ_e as an electron lifetime may not be valid.

CHAPTER 6

FINAL COMMENTS AND CONCLUSIONS

Although there have been extensive investigations into the various properties of a-Se, as discussed in Ch.2, details of the charge transport mechanism and the physical models for the structure of a-Se were still unresolved. The structure aspect was highlighted in §4.7 where the DSC data of this work could not conclusively rule out the existence of Se_8 rings in the a-Se structure. It should, however, be remembered that the main interpretation of the DSC data in §4.7 was based on the polymeric nature of a-Se (see Conclusions in section 4.7.4, p. 152). For example, the explanations for the behaviour of crystallization and glass transition with Te composition in a-$Se_{1-x}Te_x$ were based on copolymer notions.

The results and discussions of charge transport measurements were presented in the previous chapter. The measurement of drift mobility involved determining the transit time on the TOF signal whereas the measurement of lifetime required the analysis of the shape of signal waveform. At room temperatures for lightly alloyed a-Se both the hole and electron transient current evinced an exponential decay. Two possible causes for the observed exponential waveforms are:

(i) the loss of carriers from the propagating charge packet as described in §3.2, and

(ii) the presence of a uniform distribution of unneutralized bulk space charge of opposite polarity as described by Scharfe and Tabak (1969).

In the former case the time constant of the transient current decay is equal to the carrier deep trapping time[†], whereas in the latter case the time constant is related to the density of bulk space charge ρ_o via eqn. (5.29) (Scharfe and Tabak);

$$\tau = \frac{\varepsilon_o\varepsilon_r}{\mu\rho_o} \tag{6.1}$$

where μ is the drift mobility of the drifting charge packet. It is assumed that the bulk space charge has opposite polarity to the drifting charge.

For hole transport the observed decay in the photocurrent at low fields was attributed to cause (i) above and the time constant was taken to represent the hole lifetime. For electron transport however the evidence was not conclusive. The main problem was the decrease in τ_e with the applied field. If τ_e is the parameter in eqn. (6.1) and not the lifetime, then ρ_o is the density of trapped holes in the bulk. These holes would have to be injected from the Se/Aℓ interface.

Since we may expect the amount of hole injection to increase with the applied field, the observed τ_e - F behaviour is at least qualitatively reasonable. The saturation in τ_e occurs probably because at high fields there is ample hole injection from the Se/Aℓ interface to fill all the hole traps, i.e. $\rho_o \approx eN_d$ where N_d is the density of deep hole traps which operate over the time scale $\sim t_d$. In fact, taking $N_d \gtrsim 10^{14}$ cm^{-3} in eqn. (6.1) gives $\tau_e \lesssim 4$ μs which would account for the absence of electron TOF signal in most A type a-Se samples. In other words, the observed differences between electron photocurrents for different batches of a-Se are due to the hole injection behaviour of the Se/Aℓ contact.

[†] provided there is one single deep trapping time.

[#] Note that for τ_h, cause (ii) cannot be completely ruled out if all the deep electron traps are filled before the arrival of the xenon pulse (i.e. before time = t_d). If this is the case then τ_h is given by eqn. (6.1) with $\rho_o = eN_d$ where N_d is the density of deep electron traps (cf. eqn. (5.5) in which N_d is the density of coulombic hole traps).

It is useful to summarize the main findings and conclusions of this project according to material composition.

(1) a-Se

Hole Transport:

Hole drift mobility μ_h is thermally activated. At low temperatures, $T \lesssim 250K$, the mobility activation energy, E_μ, is well defined and decreases with the applied field in a Poole-Frenkel fashion. Its extrapolated zero field value, E_μ^o, is about 0.29 eV. Above $T \sim 250K$, E_μ seems to decrease with temperature.

Mobility-temperature data, $\mu_h(T)$, indicate a shallow trap controlled extended state transport mechanism as described by eqn. (3.31) in section 3.3.1. At temperatures above $T \sim 250K$, the drift mobility μ_h tends to saturate towards the microscopic mobility μ_o, i.e. $\mu_h \rightarrow \mu_o$ as T increases in eqn. (3.31a).

The shallow monoenergetic traps are probably charged defect centres, e.g. C_1^-, at 0.29 eV above the valence band mobility edge. Their density is $\sim 3 \times 10^{15}$ cm^{-3} (i.e. 0.1 ppm).

The microscopic transport seems to be a diffusive motion in the extended states. The microscopic mobility at room temperature is ~ 0.3 cm^2 V^{-1} s^{-1}.

The hole lifetime τ_h is sensitive not only to the origin (batch) of Se but also to preparation conditions. Deep hole traps are probably structural in origin, e.g. microcrystalline inclusions. Their density is at most $\sim 10^{14}$ cm^{-3}.

Lifetime temperature data is consistent with the diffusion controlled trapping mechanism inasmuch as τ_h is then given by eqn. (5.5). Note, however, that $\tau_h(T)$ data can also be interpreted via eqn. (5.29) which assumes that the decay in the hole photocurrent is due to the presence of uniformly distributed trapped electrons in the bulk.

Electron Transport:

Electron drift mobility μ_e is thermally activated with a well defined activation energy $E_\mu \approx 0.35$ eV below T ~ 278K. Above T ~ 278K, μ_e tends to saturate.

For electric fields not in excess of ~1.5×10^5 V cm^{-1} the drfit mobility is relatively field insensitive down to T ~ 219K. For fields in excess of 1.5×10^5 V cm^{-1}, μ_e tends to increase with F.

Both the drift mobility μ_e and the lifetime τ_e are sensitive to the origin of Se. Moreover, τ_e seems to be particularly sensitive to oxygen impurity.

Mobility-temperature data indicate a shallow trapped controlled diffusive motion in extended states. The microscopic mobility at room temperature is likely to be 0.1-0.2 cm^2 V^{-1} s^{-1}.

Given that the electron shallow traps are monoenergetic then their density is ~10^{15} cm^{-3}, i.e. comparable with the density of shallow hole traps. ($E_t = 0.35$ eV).

Effects of As alloying on electron drift mobility-temperature data, on the other hand, suggest that the shallow traps are probably the localized tail states below E_c whose density-energy profile is of the form (eqn. (5.42))

$$\begin{aligned} N(E') &= N_c\, [E_t - E')/E_t]^n \;; & E' \leqslant E_t \\ &= 0 \;; & E' > E_t \end{aligned} \qquad (6.2)$$

where E' is energy measured 'downwards' from E_c, $E_t \equiv E_c - E_A$ and, from the $\mu_e(T)$ data, n ~ 4.

It must be remarked that both types of shallow traps, a discrete set at E_t and a tail below E_c can, in principle, operate simultaneously to generate the observed $\mu_e(T)$ data.

(2) a-Se + y ppm Cℓ

Hole Transport:

Cℓ doping a-Se up to 40 wt. ppm reduces the hole drift mobility but promotes the lifetime. The range seems to be improved due to a decrease in the deep trap population.

The drift mobility has a well defined thermally activated behaviour with a low temperature zero field activation energy $E_\mu^o \simeq 0.45$ eV. E_μ decreases linearly with the applied field.

The transport mechanism is still shallow trap controlled. There is, however, an additional set of Cℓ induced shallow traps at ~0.45 eV above E_V whose density increases with Cℓ content. These traps are coulombic in origin and are most likely to be $C\ell^-$ ions.

Fig. 5.22 (p. 203) summarizes the behaviour of hole transport in a-Se + y ppm Cℓ.

Electron Transport:

There was no detectable electron transport either because the transport is trap-limited or one of the contacts becomes highly injecting and the TOF technique is no longer applicable.

(3) a-Se/0.5 wt.% As + y ppm Cℓ

Hole Transport:

Alloying a-Se with As up to 0.5 wt.% causes the hole lifetime and hence the Schubweg to deteriorate. The drift mobility and its general temperature dependence seems to be relatively unaffected (Fig. 5.25a, p.211). The additional deep hole traps are probably As_2^- centres.

Doping a-Se/0.5% As with Cℓ up to 30 wt. ppm Cℓ (Fig. 5.25b, p.211) restores the hole lifetime by reducing the concentration of As induced deep traps and/or the density of deep traps intrinsic to a-Se. The drift mobility and its temperature dependence is relatively unchanged, although the field dependence of E_μ is slightly weaker. An alternative conclusion is that 0.5% As addition to a-Se + 30 ppm Cℓ compensates for the Cℓ induced (e.g. $C\ell_0^-$) traps at ~0.45 eV above E_v. Compensation is probably achieved by neutralizing some of $C\ell_0^-$ centres and hence diminishing $[C\ell_0^-]$. Thus As and Cℓ addition to a-Se have 'compensating' effects.

Electron Transport:

As addition to a-Se up to 0.5 wt.% decreases the drift mobility but enhances the lifetime (Fig. 5.31, p.219). The result is a longer electron Schubweg.

The electron drift mobility activation energy increases with As addition, e.g. for a-Se/0.5% As $E_\mu^o \approx 0.45$ eV. Electron transport is believed to be shallow trap controlled, probably, by the localized tail states below E_c whose density-energy profile is of the form in eqn. (6.2) with E_t and n (= 3.8 → 4.4) increasing with As content.

Cℓ doping a-Se/0.5% As up to ~30 wt.ppm does not affect the electron transport. The lifetime, however, is reduced probably due to highly electronegative neutral Cℓ atoms acting as electron traps.

(4) $a\text{-}Se_{1-x}Te_x$ + y ppm Cℓ

Hole Transport:

Alloying a-Se with Te up to ~5wt.% reduces the drift mobility but enhances the lifetime (Fig. 5.33, p.228). Their products seems to be relatively unaffected which is consistent with the shallow trap controlled transport mechanism provided the deep trap density is not altered.

Drift mobility-temperature data indicate that hole transport in $a\text{-}Se_{1-x}Te_x$ is controlled by two sets of distrete shallow traps. The

The first set is that already present in a-Se, i.e. at ~ 0.29 eV above E_V and density ~10^{15} cm^{-3}, whereas the second set is Te induced and appears at ~0.43 eV above E_V. The concentration of the Te induced traps was found to increase linearly with Te content. They are probably associated with the Te_1^- centres.

Doping a-$Se_{1-x}Te_x$ with Cℓ up to 40 wt. ppm was found to promote the Schubweg. Cℓ doping thus diminishes the population of deep traps as concluded in (2) above. There is a slight reduction in the drift mobility which is due to some additional Cℓ induced shallow traps at ~0.45 eV above E_V, i.e. around the same energy as Te_1^- traps.

Electron Transport:

The drift mobility μ_e in a-$Se_{1-x}Te_x$ (no Cℓ) was found to fall sharply with Te content. The current transient for high Te compositions ($x \gtrsim 0.5$ wt.%) was dispersive whereas for low Te compositions ($x \lesssim 0.5$ wt.%) it was best described by eqn. (5.4). The lifetime τ_e determined by the use of eqn. (5.4) indicated that Te addition leaves the deep electron traps undisturbed.

The drift mobility at low temperatures ($T \lesssim 290K$) had a well defined thermally activated behaviour with a zero field activation energy $E_\mu^o \approx 0.50$ eV.

The electron transport is believed to be shallow trap controlled by Te induced electron traps which are probably Te_3^+ centres.

There was no detectable electron transport in Cℓ doped a-$Se_{1-x}Te_x$ probably for the same reasons as in (2) above.

GENERAL CONCLUSIONS AND SUGGESTIONS FOR FUTURE WORK:

It can be seen that hole and electron drift mobility-temperature data on the various Se based amorphous systems can be readily interpreted by shallow trap controlled transport mechanisms. For hole transport the shallow traps probably constitute discrete sets. For electron transport, on the other hand, evidence suggests that the localized tail states below E_C play an important role, although in Se/Te alloys the data suggested an additional discrete set of shallow traps.

The field dependence of hole and electron drift mobility at high fields and/or low temperatures was essentially determined by the field dependence of the activation energy. At the lowest fields and/or high temperatures the drift mobility for both holes and electrons showed an algebraic field dependence;

$$\mu \sim F^n \tag{6.3}$$

An interesting feature of this behaviour was that, not only μ showed no low field cut-off or saturation, but also the index n increased consistently with temperature and impurity addition.

It would be useful to investigate further the field dependences of hole and electron drift mobilities by, for example, obtaining μ-F behaviour under constant temperature conditions. The fact that the observed μ-F behaviour of the form in eqn. (6.3) scaled with thickness (see, e.g. Fig. 5.20) indicates that this is an intrinsic property rather than a TOF effect. In the shallow trapped controlled transport mechanism it probably reflects the field dependence of the microscopic mobility μ_o.

As pointed out above the assignment of the measured decay time constant, τ_e, in the electron photocurrent to the electron lifetime may not be valid. This intepretation obviously needs further work. It would be useful, for example, to examine whether τ_e depends on the substrate material or on preparation conditions. Recall that in the case of hole transport in a-Se + Cℓ it was shown that the measured time constants for 'long' delay times t_d did not represent the true hole deep trapping time.

It was concluded in (3) above that As and Cℓ in a-Se seem to act in a compensating manner in controlling charge transport. It would, therefore, be useful to investigate charge transport in the amorphous system $Se_{1-(x+y)}As_xTe_y$ + z ppm Cℓ to find out whether As would compensate for the effects of Cℓ when there is also Te present.

Although the behaviour of the hole and electron drift mobilities and lifetimes with temperature were also extended to the glass transition region, the collected data was insufficient to provide reliable conclusions for charge transport around T_g. It would obviously be instructive to carry out systematic drift mobility and/or lifetime measurements in the T_g region[†]. For example, one study would be lifetime-temperature cycles for different isothermal annealing times to see whether the behaviour is similar to that of the drift mobility, reported by Abkowitz 1979. Another study may involve μ-T measurements around T_g for different heating rates and impurities to examine the nature of the 'dip' in the mobility at T_g (see Fig. 5.10). Such studies would be instructive not only towards understanding the glass transition phenomenon but also towards characterizing charge tranport in finer detail.

[†] See, for example, Abkowitz 1979, Abkowitz and Pai 1978, Herms et al 1974, Juska et al 1974, Juska and Vengris 1973.

APPENDIX A1

nth Order Transition Reaction in a DSC Thermogram

Consider the crystallization reaction [eqn. (4.9]

$$\text{a-Se} \rightarrow \gamma\text{- Se} \quad ; \quad \Delta H_c$$

where ΔH_c is the crystallization enthalpy in, say, cal mole^{-1}.

If m is the mass of a-Se before any crystallization and x is the fraction of crystallized material then the ordinate Y(T) in a DSC thermogram is

$$Y(T) \equiv [\partial \Delta H/\partial t]_T = \frac{m}{M} \Delta H_c \dot{x} \tag{a1}$$

where M is the atomic mass (≅79) of Se and $\dot{x} \equiv \frac{dx}{dt}$.

This is a maximum at $T = T_c$ when $\frac{\partial}{\partial T} Y = 0$, i.e. when

$$\dot{x} \frac{\partial \Delta H_c}{\partial T} + \frac{1}{r} \Delta H_c \ddot{x} = 0 \tag{a2}$$

where $r = \frac{dT}{dt}$, the heating rate, is assumed constant.

The first term, $\frac{\partial \Delta H_c}{\partial T} = C_p(\gamma\text{-Se}) - C_p(\text{a-Se}) \approx 0$, may now be neglected so that the maximum in Y(T) is at

$$\frac{d^2x}{dt^2} = 0 \tag{a3}$$

Assuming an nth order reaction, i.e. eqn. (4.13),

$$\dot{x} = c_0 \exp(-\frac{\Delta h}{RT}) (1-x)^n . \tag{a4}$$

in the condition (a3) gives

$$\ell n \left[\frac{r}{T_c^2 Y_c^{\frac{n-1}{n}}} \right] = \ell n \left[\frac{n c_0 R}{\Delta h \gamma^{\frac{n-1}{n}}} \right] - \frac{\Delta h}{nR} \left(\frac{1}{T_c}\right) \tag{a.5}$$

where $\gamma \equiv \frac{m}{M} \Delta H_c$ and $Y_c \equiv Y(T_c)$.

Substituting n = 1, Y_c and γ disappear and (a5) reduces to eqn. (4.10) used in §4.7.3

FIGURE NUMBER INDEX

REFERENCES

Proceedings of conferences are referenced under the editing authors and year published.

Abdullaev, G.B., Asadov, Y.G. and Mamedov, K.P., 1969, p. 179 in Cooper. (editor)

Abkowitz, M., 1979, p. 210 in Gerlach and Grosse (editors).

Abkowitz, M. and Enck, R.C., 1981, J. de Phys. (France), Colloque C4, 42, C4-443 (see Chakraverty and Kaplan editors).

Abkowitz, M. and Enck, R.C., 1982, Phys. Rev. B, 25 (4), 2567.

Abkowitz, M. and Pai, D.M., 1977, Phys. Rev. Lett., 38, 1412.

Abkowitz, M. and Pai, D.M., 1978, Phys. Rev. B., 18 (4), 1741.

Abkowitz, M. and Scher, H., 1977, Phil. Mag., 35 (6), 1585.

Abkowitz, M., Pochan, D.F., and Pochan, J.M., 1980, J. Appl. Phys., 51 (3), 1539.

Adamec, V. and Calderwood, J.H., 1975, J. Phys. D., 10 L79.

Adler, D., 1971, "Amorphous Semiconductors", pub. by Butterworths, London (1971).

Adler, D., 1977, Scientific American, 236 (5), 36.

Adler, D., 1980, J. Non-Cryst. Solids 42, 315.

Adler, D., 1981, p. 14 in Yonezawa (editor).

Adler, D. and Yoffa, E.J., 1976, Phys. Rev. Lett. 36, 1197.

Adler, D. and Yoffa, E.J., 1977, Can. J. Chem., 55, 1920.

Agarwal, S.C., 1973, Phys. Rev. B, 7, 685.

Akutagawa, W.M. and Zanio, K., 1968, I.E.E.E. Trans. Nuc. Sci., NS15 (3), 266.

Alben, R., Galison, P., London, M. and Connell, G.A.N., 1976, p. 194 in Lucovsky and Galeener (editors).

Allan, R., 1977, I.E.E.E. Spectrum, 14 (May), 41.

Allen, G., 1975, Contemp. Phys. 16 (1), 35.

Allison, J., 1971, "Electronic Engineering Materials and Devices", pub. by McGraw-Hill, London.

Allison, J. and Thomson, M.J., 1976, Radio and Electronic Engineer, 46, 11.

Anderson, P.W., 1958, Phys. Rev. 109, 1492.

Arkhipov, V.I. and Rudenko, A.I., 1977, Phys. Lett. A, 61, 55.

Arkhipov, V.I. and Rudenko, A.I., 1982, Phil. Mag., 45 (2), 189.

Atkins, P.W., 1978, "Physical Chemistry", pub. by Oxford University Press, Oxford.

Audiere, J.P., Mazieres, C. and Carballes, J.C., 1978, J. Non-Cryst. Solids, 27, 411.

Avrami, M., 1939, J. Chem. Phys., 7, 1103.

Bagley, B.G., 1970, Solid State Commun., 8, 345.

Bartenev, G.M. and Lukianov, I.A., 1955, Zh. Fiz. Khim., 29, 1486.

Baru, V.G. and Temnitskii, Yu, N., 1972, Sov. Phys. Semicond. 5 (11), 1862.

Bauer, H.H., Christian, G.G. and O'Reilly, J.E., 1978, editors, "Instrumental Analysis", pub. by Allyn and Bacon Inc., Boston, U.S.

Billmeyer, F.W., 1971, "Textbook of Polymer Science", second edition, John Wiley & Sons Inc., N.W., U.S.A.

Bishop, S.G., Strom, U. and Taylor, P.C., 1975, Phys. Rev. Lett., 34, 1346.

Bishop, S.G., Strom, U. and Taylor, P.C., 1976, Phys. Rev. Lett. 36, 543.

Bishop, S.G., Strom, U. and Taylor, P.C., 1979, p. 193, in Gerlach and Grosse (editors).

Blakemore, J.S., 1974, "Solid State Physics", pub. by W.B. Saunders Company, Philadelphia, P.A.

Blakney, R.M. and Grunwald, H.P., 1967, Phys. Rev., 159 (3), 658.

Blakney, R.M. and Grunwald, H.P., 1967, Phys. Rev., 159 (3), 664.

Brenig, W., 1974, p. 31 in Stuke and Brenig (editors).

Briegleb, G., 1929, Z. Phys. Chem. A144, 321 and 340.

Bolotov, I.E. and Komarova, L.I., 1975, Sov. Phys. Solid State, 17 (3), 478.

Bonch-Bruevich, V.L. and Landsberg, E.G., 1968, Phys. Stat. Sol. 29, 9.

Bond, W.L., 1954, J. Opt. Soc. Am. 44 (6), 429.

Brodsky, M.H., Gambino, R.J., Smith, J.E. and Yacoby, Y., 1972, Phys. Stat. Sol. A 52, 609.

Brower, W.E. and Capo, D.J., 1976, J. Vac. Sci. Technol. 13 (5), 1066.

Brown, F.C., 1955, Phys. Rev. 97 (2), 355.

Campbell, W.J., 1978, Ch. 14, "X-ray Spectroscopy", pp. 408-410 in Bauer, Christian and O'Reilly (editors).

Carles, D., Touraine, A. and Vautier, C., 1971, C.R. Acad. Sci. Paris (serie B),273, 392 (see also Touraine et al 1972).

Carles, D., Vautier, C., 1972, C.R. Acad. Sci. Paris (serie B), 274, 357.

Carles, D., Vautier, C. and Touraine, A., 1972, Thin Solid Films 9, 219.

Carles, D., Vautier, C. and Viger C., 1973, Thin Solid Films 17, 67.

Carlson, C.F., 1938, "Electrophotography", U.S. Patent No. 2, 221, 776.

Caywood, J.M. and Mead, C.A., 1970, J. Phys. Chem. Solids 31, 983.

Chakraverty, B.K. and Kaplan, D., 1981, editors, "Proceedings of the Ninth International Conference on Amorphous and Liquid Semiconductors", Grenoble, France, pub. in J. de Physique (France), Colloque C4, 42, (supplement au no 10).

Champness, C.H. and Hoffmann, R.H., 1970, J. Non-Cryst. Solids 4, 138.

Champness, C.H. and McLaughlin, C.R., 1971, p. 267 in Klein et al (editors).

Champness, C.H., Griffiths, C.H. and Sang, H., 1969, p. 349 in Cooper (editor).

Chandler, G.G., Barrow, R.F., Meyer, B., 1966, Phil. Trans. Roy. Soc. London 260A, 395.

Chang, R. and Romo, P., 1967, Acta Cryst. 23, 700.

Clement, R., Carballes, J.C. and de Cremoux, B., 1974, J. Non-Cryst. Solids 15, 505.

Cohen, M.H., 1970, J. Non-Cryst. Solids 4, 391.

Cohen, M.H., Fritzsche, H. and Ovshinsky, S.R., 1969, Phys. Rev. Lett. 22, 1065.

Cohen, M.H. and Turnbull, D., 1959, J. Chem. Phys. 31, 1164.

Condon, E.U., 1926, Phys. Rev. 28, 1182 and Phys. Rev. 32, p. 858 (1928).

Cooper, W.C., 1969, editor, "The Physics of Selenium and Tellurium", pub. by Pergamon Press, In., N.Y.

Cooper, W.C., Bennett, K.G. and Broxton, F.C., 1974, pp. 1-31, in Zingaro and Cooper (editors).

Coughlin, M.C. and Wunderlich, B., 1973, J. Polym. Sci. 11, 1735.

Dalrymple, R.J.F., and Spear, W.E., 1972, J. Phys. Chem. Solids, 33, 1071.

Daniels, T., 1973, "Thermal Analysis", pub. by Kogan Page Ltd., London.

Das, G.C., Bever, M.B., Uhlmann, D.R. and Moss, S.C., 1972, J. Non-Cryst. Solids 7, 251.

Davey, J.E. and Pankey, T., 1965, J. Appl. Phys., 36 (8), 2571.

Davis, E.A., 1970, J. Non-Cryst. Solids, 4, 107.

Davis, E.A., 1971, p. 175 in Klein et al (editors).

Davis, E.A., 1973, Ch. 13 (p. 425) in LeComber and Mort (editors).

Davis, E.A. and Mott, N.F., 1970, Phil. Mag. 22, 903.

De Neufville, J.P., 1975, p. 437 in Seraphin (editor).

Dolezalek, F.K., 1976, Ch. 2 (p. 27) in Mort and Pai (editors).

Dolezalek, F.K. and Spear, W.E., 1970, J. Non-Cryst. Solids, 4, 97.

Dresner, J., 1964, J. Phys. Chem. Solids, 25, 505.

Dresner, J. and Stringfellow, G.B., 1968, J. Phys. Chem. Solids, 29, 303.

Dussel, G.A. and Böer, K.W., 1970, Phys. Stat. Sol. B., 39, 375.

Dussel, G.A. and Bube, R.H., 1966, J. Appl. Phys. 37, 2797.

Dzhalilov, S.U., 1965, Russian J. Phys. Chem., 39 (10), 1376.

Dzhalilov, S.U. and Rzaev, K.I., 1967, Phys. Stat. Sol., 20, 261.

Eisenberg, A. and Tobolsky,A.V., 1960, J. Polym. Sci., 46, 19.

Eisenberg, A. and Tobolsky, A.V., 1962, J. Polym. Sci., 61, 483.

El-Mously, M.K., Wafik, A.H. and Saleh, S.A., 1976, Indian J. of Tech., 4, 565

El-Mously, M.K. and El-Zaidia, M.M., 1978, J. Non-Cryst. Solids, 27, 265.

Emin, D., 1976, p. 461 in Mitra (editor).

Enck, R.C., 1974, Bull. Am. Phys. Soc., 211, 19 (see also Enck, R.C., Phys. Rev. Lett. 31, 220, 1976, and Enck and Pfister 1976).

Enck, R.C. and Pfister, G., 1976, Ch. 7 (p. 297) in Mort and Pai (editors).

Ferry, D.K., Barker, J.R., Jacoboni, C., 1980, editors, "Physics of Nonlinear Transport in Semiconductors", Proceedings of the NATO Advanced Study Institute on Physics of Nonlinear Electron Transport at Urbino, Italy, 1979; pub. by Plenum Press, N.Y. (1980).

Fleming, R.J., 1979, J. Appl. Phys. 50 (12), 8075.

Fleury, G., Viger, C., Vautier, C. and Lhermitte, C., 1981, J. de Phys.(France), Colloque C4, 42, C4-947 (see Chakraverty and Kaplan, editors).

Fox, T.G. and Loshaek, S., 1955, J. Polym. Sci., 15, 371.

Fox, S.J. and Locklar, Jr., H.C., 1972, J. Non-Cryst. Solids, 8-10, 552.

Frank, J., 1926, Trans. Faraday Soc. 21, 536.

Frenkel, J., 1938, Phys. Rev., 54, 647 [also, Tech. Phys. (USSR), 5, 685].

Fritzsche, H., 1971, J. Non-Cryst. Solids 6, 49.

Fritzsche, H., 1973a, Ch. 18 (p. 557) in LeComber and Mort (editors).

Fritzsche, H., 1973b, Ch. 2 (p. 55) in LeComber and Mort (editors).

Fritzsche, H., 1977, Chinese J. Physics, 15 (2), 73.

Fritzsche, H., 1981, p. 1 in Yonezawa (editor).

Gee, G., 1970,Contemp. Phys.,11 (4), 313.

Geller, I.K., Kolomiets, B.T. and Popov, A.I., 1975, Izv. Akad. Nauk, Neorg. Mater. 11 (11), 1936.

Geller, I.K., Karalyunets, A.V., Kolomiets, B.T., and Popov, A.I., 1975, Sov. Tech. Phys. Lett. 1 (12), 460.

Gerlach, E. and Grosse, P., 1979, editors, "The Physics of Selenium and Tellurium", Proceedings of the International Conference on the Physics of Selenium and Tellurium, Königstein, Fed. Repub. Germany; pub. by Springer-Verlag, N.Y. (1979).

Gibbons, D.J. and Papadakis, A.C., 1968, J. Phys. Chem. Solids, 29, 115.

Gobrecht, H., Gawlik, D. and Mahdjuri, F., 1971, Phys. Condens, Matter, 13, 156.

Gobrecht, H., Mahdjuri, F. and Gawlik, D., 1971, J. Phys. C: Solid State Physics, 4, 2247.

Goodman, C.H.L., 1973, Ch. 17 (p. 549) in LeComber and Spear (editors).

Gorman, M. and Solin, S.A., 1976, Solid State Commun., 18, 1401.

Grant, A.J. and Davis, E.A., 1974, Solid State Commun., 15, 563.

Grenet, J., Larmagnac, J.P. and Michon, P., 1980, Thin Solid Films 67, L17.

Grenet, J., Larmagnac, J.P., Michon, P. and Vautier, C., 1981, Thin Solid Films, 76, 53.

Griffiths, C.H. and Fitton, B., 1969, in Cooper (editor).

Grigorovici, R., 1973, Ch. 5 (p. 191) in LeComber and Spear (editors).

Gross, G., Stephens, R.B. and Turnbull, D., 1976, J. Appl. Phys. 48 (3), 1139.

Grunwald, H.P. and Blakney, R.M., 1968, Phys. Rev. 165 (3), 1006.

Hamada, S., Sato, T. and Shirai, T., 1967, Bull. Chem. Soc. Japan, 40 (4), 864.

Hansen, F.Y., Knudsen, T.S. and Carneiro, K., 1975, J. Chem. Phys. 62 (4), 1556.

Hartke, J.L., 1962, Phys. Rev., 125 (4), 1177.

Hartke, J.L., 1968, J. Appl. Phys., 39, 4871.

Hartke, J.L. and Regensburger, P.J., 1965, Phys. Rev. A., 139, 970.

Heading, J., 1971, "Mathematical Methods in Science and Engineering", 2nd. ed., pub. by Edward Arnold Ltd., London.

Heaton, J.L., Hammond, G.H., Goldner, R.B., 1972, Appl. Phys. Lett. 20 (9), 333.

Hecht, K., 1932, Z. Physik, 77, 235.

Henderson, S.T. and Marsden, A.M., "Lamps and Lighting", second edition, pub. by Edward Arnold (Publishers) Ltd., U.K. (1972) (see Ch.15).

Henninger, E.H., Buschart, R.C., and Heaton, L., 1967, J. Chem. Phys., 46, 586.

Herms, W., Karsten, H. and Zerrenthin, U., 1974, Phys. Stat. Sol. (A), 23, 479.

Hill, R.M., 1971a, Phil. Mag., 24, 1307.

Hill, R.M., 1971b, Phil. Mag., 23, 59.

Hill, R.M., 1974, Phys. Stat. Sol. (A), 24, 433.

Hindley, K.N., 1970, J. Non-Cryst. Solids, 5, 17.

Hirsch, J., 1979, J. Phys. C: Solid State Phys. 12, 321.

Holstein, T., 1959, Ann. Phys., 8, 343.

Ieda, M., Sawa, G. and Kato, S., 1971, J. Appl. Phys. 42, 3737.

Ioffe, A.F. and Regel, A.R., 1960, Prog. Semicond. 4, 237.

Isaev, A.I. and Abdinov, D. Sh., 1975, Izv. Akad. Nauk. AzSSR, Ser. Fiz.-Tekh. Mat. Nauk., No. 4, p. 77.

Isaev, A.I., Mekhtieva, S.I. and Abdinov, D.Sh., 1976, Izv. Akad. Nauk. AzSSR, Ser. Fiz.-Tekh. Mat. Nauk., No. 1, p. 31.

Jain, V.K., 1975, J. Scient. Ind. Res. 34, 140.

Janjua, M.B.I., Toguri, J.M. and Cooper, W.C., 1971, Can. J. Phys. 49, 475.

Jespersen, N., 1978, Ch. 17 (p.487) in Bauer, Christian and O'Reilly (editors).

Joannopoulos, J.D., Schlüter, M. and Cohen, M.L., 1975, Phys. Rev. B., 11 (6), 2186.

Juška, G., Matulionis and Viščakas, J., 1969, Phys. Stat. Sol. 33, 533.

Juška, G. and Vengris, S., 1973, Phys. Stat. Sol. A. 16, K27.

Juška, G., Vengris, A. and Viščakas, J., 1974, p. 363 in Stuke and Brenig, 1974.

Juška, G., Vengris, S. and Arlauskas, K., 1978, Phys. Stat. Sol. A., 48, K149.

Kalade, J., Montrimas, E. and Pazera, A., 1972, Phys. Stat. Sol. (A), 13, 187 (see also Dienys, R., Kalade, J., Montrimas, E. and Pazera, A., Liet. Fiz. Rink. 11 (10), 653, 1971).

Kao, K.C. and Hwang, H., 1981, "Electrical Transport in Solids", pub. by Pergamon Press, Oxford.

Kaplow, R., Rowe, T.A. and Averbach, B.L., 1968, Phys. Rev., 168, 1068.

Kastner, M., 1972, Phys. Rev. Lett. 28, 355.

Kastner, M., 1977, p. 504 in Spear (editor).

Kastner, M., 1978, J. Non-Cryst. Solids, 31, 223.

Kastner, M., Adler, D., and Fritzsche, H., 1976, Phys. Rev. Lett., 37, 1504.

Kauzmann, W., 1948, Chem. Rev. 43, 219.

Kawarada, M. and Nishina, Y., 1975, Jap. J. Appl. Phys., 14 (10), 1519.

Kawarada, M. and Nishina, Y., 1977a, Jap. J. Appl. Phys. 16 (9), 1525.

Kawarada, M. and Nishina, Y., 1977b, Jap. J. Appl. Phys. 16 (9), 1531.

Ke, B., 1964, "Newer Methods of Polymer Characterization", Interscience Publishers, N.Y.

Keezer, R.C. and Geils, R.H., unpublished work quoted by Lukovsky, 1979.

Keezer, R.C., Lucovsky, G. and Martin, R.M., 1975, Bull. Am. Phys. Soc. 20, 323.

Kepler, R.G., Phys. Rev. 119, 1226.

Kim, K.S. and Turnbull, D., 1973, J. Appl. Phys., 44, 5237.

Kireev, P.S., 1978, "Semiconductor Physics", Mir Publishers, Moscow.

Kissinger, H.E., 1957, Analy. Chem. 29, 1702.

Klein, N., Tannhauser, D.S. and Pollak, M., 1971, editors, "Conduction in Low Mobility Materials", Proceedings of the Second International Conference, Eilat, Israel, pub. by Taylor & Francis Ltd., London, 1971.

Kolomiets, B.T., 1964, Phys. Stat. Sol. 7, 359, 713.

Kolomiets, B.T. and Lebedev, E.A., 1966, Sov. Phys., Solid State 8, 905.

Kolomiets, B.T. and Lebedev, E.A., 1973, Sov. Phys. Semicond., 7 (1), 134.

LaCourse, W.C., Twaddell, V.A. and Mackenzie, J.D., 1970, J. Non-Cryst. Solids, 3, 234.

Lakatos, A.I. and Abkowitz, M., 1971, Phys. Rev. B., 3 (6), 1791.

Lakin, W.D., Marks, I.M., Noolandi, J., 1977, Phys. Rev. B., 15 (12), 5834.

Lampert, M.A. and Mark, P., 1970, "Current Injection in Solids", Academic Press, N.Y.

Langevin, P., 1903, Ann. Chim. Phys. 28, 287, 433.

Lanyon, H.P.D., 1963, Phys. Rev. 130 (1), 134.

Larmagnac, J.P., Grenet, J. and Michon, P., 1981a, J. Non-Cryst. Solids, 45, 157.

Lax, M., 1960, Phys. Rev. 119 (5), 1502.

Le Blanc, O.H., 1959, J. Chem. Phys., 30, 1443.

Le Blanc, O.H., 1960, J. Chem. Phys. 33, 626.

Le Comber, P.G. and Spear, W.E., 1970, Phys. Rev. Lett., 25, 505.

Le Comber, P.G. and Mort, J., 1973, editors, "Electronic and Structural Properties of Amorphous Semiconductors", Proceedings of the Thirteenth Session of the Scottish Universities Summer School in Physics 1972), pub. by Academic Press, London (1973).

Lemercier, C., 1971a, p. 251 in Klein et al (editors).

Lemercier, C., 1971b, Phys. Stat. Solidi (B), 46, K35.

Long, M., Galison, P., Alben, R. and Connell, G., 1976, Phys. Rev. B., 13, 1821.

Lucovsky, G., 1969, p. 255 in Cooper,(editor).

Lucovsky, G., 1979, p. 178 in Gerlach and Grosse (editors).

Lucovsky, G. and Galeener, F.L., 1976, editors, "Structure and Excitations of Amorphous Solids", (Williamsburg, Va.), Am. Inst. Phys., N.Y.

Lucovsky, G. and Galeener, F.L., 1980, J. Non-Cryst. Solids 35-36, 1209.

Lucovsky, G., Keezer, R.C. and Burstein, E., 1967, Solid State Commun., 5, 439.

Lucovsky, G., Mooradian, A., Taylor, W., Wright, G.B. and Keezer, R.C., 1967, Solid State Commun., 5, 113.

Lucovsky, G. and Tabak, M.D., 1974, Ch. 6 (p.788), Zingaro and Cooper (editors).

Mackenzi, R.C., 1970, editor, "Thermal Analysis", vol. 1, Academic Press, London.

Mackenzi, R.C. and Mitchell, B.D., 1970, Ch.3 in Mackenzi (editor).

Mamedov, K.P. and Nurieva, Z.D., 1964, Kristallografiya, 9, 271.

Many, A. and Rakavy, G., 1962, Phys. Rev. 126, 1980.

Marshall, J.M., 1977, p. 541 in Spear (editor).

Marshall, J.M. and Owen, A.E., 1972, Phys. Stat. Sol. (A) 12, 181.

Marshall, J.M. and Miller, G.R., 1973, Phil. Mag., 27, 1151.

Marshall, J.M., Fisher, F.D. and Owen, A.E., 1974, Phys. Stat. Sol. (A) 25, 419

Martin, R.M., Lucovsky, G. and Helliwell, 1976, Phys. Rev. B. 13 (4), 1383.

Martini, M., Mayer, J.W. and Zanio, K.R., 1972, p. 181 in Wolfe, (editor).

Matsuura, M. and Suzuki, K., 1979, J. Material Sci., 14, 395.

Mayer, J.W., Zanio, K.R., Martini, M., Fowler, I.L., 1970, I.E.E.E. Trans. Nucl. Sci., NS17 (3), 221.

Meek, P.E., 1976, Phil. Mag., 34 (5), 767.

Mehra, R.M., Mathur, P.C., Kathuria, A.K., Shyam, R., 1977, Phys. Stat. Sol. (A), 41, K189.

Mehra, R.M., Mathur, P.C., Mathuria, A.K., Shyam, R., 1978, J. Phys. Chem. Solids, 39, 295.

Mehra, R.M., Shyam, R. and Mathur, P.C., 1979, Phys. Rev. B., 19 (12), 6525.

Mell, H. and Stuke, J., (1967), Phys. Stat. Sol. (A), 24, 183.

Miller, A. and Abrahams, S., 1960, Phys. Rev. 120, 745.

Mitra, S.S., 1976, editor, "Physics of Structurally Disordered Solids", Plenum Press, N.Y. and London.

Montrimas, E. and Petretis, B., 1973, Phys. Stat. Sol. (A), 15, 361.

Montrimas, E. and Petretis, B., 1973, Liet. Fiz. Rink., 13 (2), 273.

Montrimas, E. and Petretis, B., 1974, J. Non-Cryst. Solids, 15, 96.

Montrimas, E. and Petretis, B., 1975, Liet. Fiz. Rink., 15 (5), 799.

Moore, W.J., 1976, "Physical Chemistry", (fifth edition), pub. by Longman Group Ltd., London.

Mort, J., 1967, Phys. Rev. Lett., 1967, 540.

Mort, J., 1973a, Ch. 20 (p. 589) in LeComber and Mort, (editors).

Mort, J., 1973b, Ch. 15 (p.493) in LeComber and Mort, (editors).

Mort, J., 1981, J. de Physique (France), Colloque C4, 42, C4-433 (see Chakraverty and Kaplan, editors).

Mort, J. and Lakatos, A.I., 1970, J. Non-Cryst. Solids, 4, 117.

Moscinky, J., Renninger, A. and Averbach, B.L., 1973, Phys. Lett. A., 42, 453.

Mott, N.F., 1967, Adv. Phys. 16, 49.

Mott, N.F., 1968, Phil. Mag., 17, 1259 and J. Non-Cryst. Solids, 1, 1.

Mott, N.F., 1969, Phil. Mag., 19, 835.

Mott, N.F., 1972, J. Non-Cryst. Solids 8-10, 1.

Mott, N.F., 1973, p. 1 in LeComber and Mort, (editors).

Mott, N.F., 1977a, Contemp. Phys. 18 (3), 225.

Mott, N.F., 1977b, Revue de Physique Applique, 12, 619.

Mott, N.F., 1981, J. de Physique (France), Colloque C4, supplément au 42 (10), C4-27 (see Chakraverty and Kaplan, editors).

Mott, N.F. and Davis, E.A.,1979, "Electronics Processes in Non-Crystalline Materials", (second edition), Clarendon Press, Oxford.

Mott, N.F., Davis, E.A. and Street, R.A., 1975, Phil. Mag. 32, 961.

Moynihan, C.T., Easteal, A.J., Wilder, J. and Tucker, J., 1974, J. Phys. Chem., 78 (26), 2673.

Moynihan, C.T., Easteal, A.J. and De Bold, M.A., 1976, J. Am. Ceramic Soc., 59 (1-2), 14.

Moynihan, C.T. and Schnaus, V.E., 1970, Mater. Sci. Eng. 6, 277.

Müller, L. and Müller, M., 1970, J. Non-Cryst. Solids 4, 504.

Murphy, C.B., 1970, Ch. 23 (p. 645) in Mackenzie,(editor).

Murphy, K.E., Altman, M.B., Wunderlich, B., 1977, J. Appl. Phys., 48 (10), 4122.

Myers, M.B. and Felty, E.J., 1967, Mater. Res. Bull. 2, 535.

Noolandi, J., 1977a, Phys. Rev. B., 16 (10), 4466 (see also p. 224 in Spear, editor).

Noolandi, J., 1977b, Phys. Rev. B., 16 (10), 4475.

Ohsaka, T., 1975, J. Non-Cryst. Solids, 17, 121.

Okamoto, Y. and Nakamura, K., 1979, Electrophotography (Japan), 17 (3), 26.

Onsager, L., 1934, J. Chem. Phys. 2, 599.

Omar, M.A., 1975, "Elementary Solid State Physics", pub. by Addison-Wesley Publishing Co., Reading, Mass.

Ovshinsky, S.R., 1968, Phys. Rev. Lett. 21, 1450.

Ovshinsky, S.R., 1977, p. 519 in Spear, (editor).

Ovshinsky, S.R. and Adler, D., 1978, Contemp. Phys., 19 (2), 112.

Ovshinsky, S.R. and Fritzsche, H., 1973, I.E.E.E. Trans. Elec. Dev., ED20 (2), 91.

Owen, A.E., 1970, Contemp. Phys. 11 (3), 227.

Owen, A.E., 1974, Ch. 4 (p. 161) in LeComber and Mort, (editors).

Owen, A.E. and Spear, W.E., 1976, Phys. Chem. Glasses, 17 (5), 174.

Owen, A.E. and Marshall, J.M., 1977, p. 529 in Spear, (editor).

Pai, D.M., 1974, p. 355 in Stuke and Brenig, (editors).

Pai, D.M., 1975, J. Appl. Phys. 46, 5122.

Pai, D.M. and Enck, R.C., 1975, Phys. Rev. B, 11 (12), 5163.

Pai, D.M. and Ing, S.W., 1968, Phys. Rev. 173, 729.

Pai, D.M. and Scharfe, M.E., 1972, J. Non-Cryst. Solids 8-10, 752.

Papadakis, A.C., 1967, J. Phys. Chem. Solids, 28, 641.

Pauling, L., 1968, "The Nature of the Chemical Bond" (third edition), Cornell Univ. Press, Ithaca, N.Y.

Pelevin, O.V., 1966, Izv. Akad. Nauk SSR Neorgan. Mater. 2, 942.

Perron, J.C., 1967, Advan. Phys. 16, 657.

Petretis, B., Rogass, H., Satas, A., 1975, Phys. Stat. Sol. (A) 30, K3.

Pfister, G., 1976, Phys. Rev. Lett., 36 (5), 271.

Pfister, G., 1976b, p. 537 in "Physics of Semiconductors", Proceedings of the 13th International Conference, Rome, edited by F.G. Fumi, pub. by North-Holland Pub. Co., Amsterdam.

Pfister, G., 1977, p. 765 in Spear (editor) (see also Phys. Rev. B., 16 (8), 3676).

Pfister, G., 1979, Contemp. Phys., 20 (4), 449.

Pfister, G. and Lakatos, A.I., 1972, Phys. Rev. B., 6 (8), 3012.

Pfister, G. and Scher, H., 1977a, p. 197 in Spear, (editor).

Pfister, G. and Scher, H., 1977b, Phys. Rev. B., 15 (4), 2062.

Pfister, G. and Scher, H., 1978, Adv. Phys. 27 (5), 747.

Plessner, K.W., 1951, Proc. Phys. Soc. 64, 671.

Popov, A.I., 1976, J. Phys. C: Solid State Physics, 9, L675.

Popov, A.I., Geller, I. and Karalunets, A., 1977, in Spear, (editor).

Regiani, L., 1980, in Ferry, Barker and Jacoboni, (editors).

Renninger, A.L. and Averbach, B.L., 1974, Phys. Rev. B., 3, 1507.

Richter, H., 1972, J. Non-Cryst. Solids, 8-10, 388.

Richter, H. and Herre, F., 1958, Z. Naturforschg. 13a, 847.

Ritland, H.N., 1954, J. Am. Ceramic Soc., 37 (8), 370.

Robertson, J., 1976, Phil. Mag. 34 (1), 13.

Rollason, R.M., 1978, Internal Report, Nov. 1978, Gestetner (Byfleet) Ltd., U.K.

Rollason, R.M., 1979, Internal Report, Sept. 1979, Gestetner (Byfleet) Ltd., U.K.

Rose, A., 1951, RCA Review, 12, 362.

Rose, A., 1955, Phys. Rev. 97 (6), 1538.

Rossiter, E.L. and Warfield, G., 1971, J. Appl. Phys. 42, 2527.

Rudenko, A.I., 1975, Sov. Phys. Semicond. 9 (5), 608.

Rudenko, A.I., 1976, J. Non-Cryst. Solids, 22, 215 (see also Rudenko, 1975).

Rudenko, A.I. and Arkhipov, V.I., 1978, J. Non-Cryst. Solids, 30, 163.

Rudenko, A.I. and Arkhipov, V.I., 1982a, Phil. Mag. 45 (2), 177.

Rudenko, A.I. and Arkhipov, 1982b, Phil. Mag. 45 (2), 209.

Sakka, S. and Mackenzie, J.D., 1971, J. Non-Cryst. Solids, 6, 145.

Samantaray, B.K. and Nigam, G.D., 1976, Ind. J. Phys., 50, 45.

Satow, T., Uemera, O. and Oizumi, S., 1978, J. Non-Cryst. Solids 27, 139.

Scharfe, M.E., 1970, Phys. Rev. B., 2, 5025.

Scharfe, M.E., 1973, Bull. Am. Phys. Soc., 18, 454.

Scharfe, M.E. and Tabak, M.D., 1969, J. Appl. Phys. 40 (8), 3230.

Schaffert, R.M., 1975, "Electrophotography", pub. by The Focal Press, London.

Scher, H., 1977, p. 209 in Spear, (editor).

Scher, H. and Montroll, E.W., 1975, Phys. Rev. B., 12 (6), 2455 (see also Scher, H. in

Schmidlin, F.W., 1977, Phys. Rev. B., 16 (6), 2362.

Schottmiller, J.C., 1975, J. Vac. Sci. Technol. 12 (4), 807.

Schottmiller, J.C., Tabak, M.D., Lucovsky, G. and Ward, A., 1970, J. Non-Cryst. Solids, 4, 80.

Seraphin, B.O., 1975, editor, "Optical Properties of Solids - New Developments", North-Holland Pub. Co., Amsterdam.

Shevchik, N.J., 1974, Phys. Rev. Lett. 33 (26), 1572.

Shevchik, N.J., Cordona, M. and Tejeda, J., 1973, Phys. Rev. B., 8 (6), 2833.

Silver, M., Mark, P., Olness, D., Helfrich, W. and Jarnagin, R.C., 1962, J. Appl. Phys. 33 (10), 2988.

Simha, R. and Boyer, R.F., 1962, J. Chem. Phys. 37, 1003.

Smith, R.A., 1978, "Semiconductors" (second edition), Cambridge University Press.

Spear, W.E., 1957, Proc. Phys. Soc. (London), B70, 669.

Spear, W.E., 1960, Proc. Phys. Soc. (London), B76, 826.

Spear, W.E., 1961, J. Phys. Chem. Solids, 21, 110.

Spear, W.E., 1969, J. Non-Cryst. Solids, 1, 197.

Spear, W.E., 1974, Adv. Phys. 23, 523.

Spear, W.E., 1974b, p. 1 in Stuke and Brenig, (editors).

Spear, W.E., 1977, editor, "Amorphous and Liquid Semiconductors", Proceedings of the Seventh International Conference on Amorphous and Liquid Semiconductors, Univ. Edinburgh.

Stephens, R.B., 1976, J. Non-Cryst. Solids, 20, 75.

Stephens, R.B., 1978, J. Appl. Phys., 49 (12), 5855.

Street, R.A. and Mott, N.F., 1975, Phys. Rev. Lett. 35, 1293.

Strella, S., 1963, J. Appl. Poly. Sci. 7, 569.

Stuke, J., 1969, in Cooper 1969 (see also Stuke, J., 1964, Phys. Stat. Sol. 6, 441).

Stuke, J., 1974, Ch. 5 (p. 174) in Zingaro and Cooper, (editors).

Stuke, J., and Brenig, W., 1974, editors, "Amorphous and Liquid Semiconductors", Proceedings of the Fifth International Conference on Amorphous and Liquid Semiconductors (Garmish-Partenkirchen, FDR, 1973), pub. by Taylor & Francis, London, 1974.

Tabak, M.D., 1967, Trans. Metall. Soc., A.I.M.E., <u>239</u>, 330.

Tabak, M.D., 1969, Appl. Opt. Supplement 3: Electrophotography, p. 4.

Tabak, M.D., 1970, Phys. Rev. B., <u>2</u> (6), 2104.

Tabak, M.D., 1971, in Klein et al, (editors).

Tabak, M.D. and Hillegas, 1972, J. Vac. Sci. Technol. <u>9</u> (1), 387.

Tabak, M.D. and Scharfe, M.E., 1970, J. Appl. Phys. <u>41</u> (5), 2114.

Tabak, M.D. and Warter, P.J., 1968, Phys. Rev. <u>173</u> (3), 899.

Tabak, M.D., Ing, S.W. and Scharfe, M.E., 1973, I.E.E.E. Trans. Elec. Dev. <u>ED20</u> (2), 132.

Tabak, M.D., Pai, D.M. and Scharfe, M.E., 1971, J. Non-Cryst. Solids, <u>6</u>, 357.

Tahmasbi, A.R., Hirsch, J. and Kolendowicz, J.Z., 1979, Solid State Commun., <u>29</u>, 847.

Takahashi, T., 1979, J. Non-Cryst. Solids, <u>34</u>, 307.

Tefft, W., 1967, J. Appl. Phys. <u>38</u> (13), 5265.

Thronburg, D.D., 1976, Thin Solid Films, <u>37</u>, 215.

Thornburg, D.D. and Johnson, R.I., 1975, J. Non-Cryst. Solids, <u>17</u>, 2.

Tiedje, T. and Rose, A., 1980, Solid State Commun., <u>37</u>, 49.

Tool, A.Q., 1946, J. Amer. Ceramic Soc., <u>29</u> (9), 240.

Tomura, K. and Maekawa, H., Yoshizawa, M., 1975, Jap. J. Appl. Phys. <u>14</u> (12), 2085.

Tomura, K. and Maekawa, H., 1977, Jap. J. Appl. Phys. <u>16</u>, 655.

Touraine, A., Vautier, C. and Carles, D., 1972, Thin Solid Films <u>9</u>, 229.

Turnbull, D., 1969, Contemp. Phys. <u>10</u> (5), 473.

Twaddel, V.A., LaCourse, W.C. and Mackenzie, J.D., 1972, J. Non-Cryst. Solids, <u>8-10</u>, 831.

Unger, P. and Cherin, P., 1969, p. 223 in Cooper, (editor).

Urbach, F., 1953, Phys. Rev. <u>92</u>, 1324.

Van Hove, 1953, Phys. Rev. <u>89</u>, 1189.

Vautier, C., Carles, D., Touraine, A., 1971, C.R. Acad. Sci. Paris (serie B), <u>273</u>, 475.

Vautier, C., Carles, D., and Viger, C., 1979, p. 219 in Gerlach and Grosse, (editors).

Vengris, S.A., Viscakas, J.K., Sakalas, A.P. and Juska, G., 1972, Sov. Phys. Semicond. 6 (6), 903.

Viscakas, J., Mackus, P. and Smilga, A., 1968, Phys. Stat. Sol. 25, 331.

Vollmann, J., Wobst. M. and Fischer, B., 1973, Phys. Stat. Sol. (A) 17, K165.

Vollmann, W., 1974, Phys. Stat. Sol. (A), 22, 195.

Wallace, C.A. and Ward, R.C.C., 1975, J. Appl. Cryst. 8 (2), 255.

Ward, A.T., 1970, J. Phys. Chem. 74, 4110

Ward, A.T., 1972, Adv. Chem. 110, 163.

Warter, P.J., 1969, Appl. Optics, Supplement 3: Electrophotography, p.65.

Weaire, D., 1976, Contemp. Phys. 17 (2), 173.

Weigl, J.W., 1977, Angew. Che. Int. Ed. Engl. 16, 374.

Wert, C.A. and Thomson, R.M., 1970, "Physics of Solids", McGraw-Hill Book Co.

Wendlandt, W.W.M., 1964, "Thermal Methods of Analysis", Interscience Publishers, N.Y.

Williams, M.L., Landel, F.R. and Ferry, J.D., 1955, J. Am. Ceramic Soc. 77, 3701.

Wolfe, R., 1972, editor, "Advances in Materials and Device Research", vol. 3, Academic Press.

Yarwood, J., 1967, "High Vacuum Technology", pub. by Chapman and Hall and Science Paperbacks.

Yashiro, M. and Nishina, Y., 1979, p.207 in Gerlach and Grosse, (editors).

Yonezawa, F., 1981, "Fundamental Physics of Amorphous Semiconductors", Proceedings of the Kyoto Summer Institute, Kyoto, Japan, Sept. 1980, pub. by Springer-Verlag, N.Y., 1981.

Yonezawa, F. and Cohen, M.H., 1981, p. 119 in Yonezawa, (editor).

Zachariasen, W.H., 1932, J. Amer. Chem. Soc., 54, 3841.

Zanio, K.R., Akutagawa, W.M. and Kikuchi, R., 1968, J. Appl. Phys. 39 (6), 2818.

Zallen, R. and Lucovsky, G., Ch. 4 (p.148) in Zingaro and Cooper, (editors).

Zingaro, R.A. and Cooper, W.C., 1974, editors, "Selenium", pub. by Van Nostrand Reinhold Co., N.Y.

NOTES/ERRATA

Diffusive Motion: The use of this phrase in the thesis implies diffusive motion in extended states (p.15).

Diffusive Motion in Extended States: Carrier transport in extended states near E_c as described in p.15. The carrier transport is similar to Brownian motion and the mobility is given by eqn. (1.9).

Diffusion Controlled Trapping: The use of this phrase in the thesis implies that the mean free path, $\bar{\ell} \ll$ capture radius r_c of the trap.